Physics Reports 738 (2018) 1–76

Contents lists available at ScienceDirect

Physics Reports

journal homepage: www.elsevier.com/locate/physrep

The BCS–BEC crossover: From ultra-cold Fermi gases to nuclear systems

Giancarlo Calvanese Strinati [a,b,*], Pierbiagio Pieri [a,b], Gerd Röpke [c], Peter Schuck [d,e], Michael Urban [d]

[a] School of Science and Technology, Physics Division, Università di Camerino, 62032 Camerino (MC), Italy
[b] INFN, Sezione di Perugia, 06123 Perugia (PG), Italy
[c] Institut für Physik, Universität Rostock, 18051 Rostock, Germany
[d] Institut de Physique Nucléaire, CNRS-IN2P3 and Université Paris-Sud, 91406 Orsay cedex, France
[e] Laboratoire de Physique et de Modélisation des Milieux Condensés, CNRS and Université Joseph Fourier, BP 166, 38042 Grenoble cedex 9, France

ARTICLE INFO

Article history:
Accepted 15 February 2018
Available online 23 February 2018
Editor: A. Schwenk

ABSTRACT

This report addresses topics and questions of common interest in the fields of ultra-cold gases and nuclear physics in the context of the BCS–BEC crossover. By this crossover, the phenomena of Bardeen–Cooper–Schrieffer (BCS) superfluidity and Bose–Einstein condensation (BEC), which share the same kind of spontaneous symmetry breaking, are smoothly connected through the progressive reduction of the size of the fermion pairs involved as the fundamental entities in both phenomena. This size ranges, from large values when Cooper pairs are strongly overlapping in the BCS limit of a weak inter-particle attraction, to small values when composite bosons are non-overlapping in the BEC limit of a strong inter-particle attraction, across the intermediate unitarity limit where the size of the pairs is comparable with the average inter-particle distance.

The BCS–BEC crossover has recently been realized experimentally, and essentially in all of its aspects, with ultra-cold Fermi gases. This realization, in turn, has raised the interest of the nuclear physics community in the crossover problem, since it represents an unprecedented tool to test fundamental and unanswered questions of nuclear many-body theory. Here, we focus on the several aspects of the BCS–BEC crossover, which are of broad joint interest to both ultra-cold Fermi gases and nuclear matter, and which will likely help to solve in the future some open problems in nuclear physics (concerning, for instance, neutron stars). Similarities and differences occurring in ultra-cold Fermi gases and nuclear matter will then be emphasized, not only about the relative phenomenologies but also about the theoretical approaches to be used in the two contexts. Common to both contexts is the fact that at zero temperature the BCS–BEC crossover can be described at the mean-field level with reasonable accuracy. At finite temperature, on the other hand, inclusion of pairing fluctuations beyond mean field represents an essential ingredient of the theory, especially in the normal phase where they account for precursor pairing effects.

After an introduction to present the key concepts of the BCS–BEC crossover, this report discusses the mean-field treatment of the superfluid phase, both for homogeneous and inhomogeneous systems, as well as for symmetric (spin- or isospin-balanced) and asymmetric (spin- or isospin-imbalanced) matter. Pairing fluctuations in the normal phase are then considered, with their manifestations in thermodynamic and dynamic quantities. The last two Sections provide a more specialized discussion of the BCS–BEC crossover in ultra-cold Fermi gases and nuclear matter, respectively. The separate discussion in the

* Corresponding author at: School of Science and Technology, Physics Division, Università di Camerino, 62032 Camerino (MC), Italy.
E-mail address: giancarlo.strinati@unicam.it (G.C. Strinati).

https://doi.org/10.1016/j.physrep.2018.02.004

two contexts aims at cross communicating to both communities topics and aspects which, albeit arising in one of the two fields, share a strong common interest.

Contents

1. Introduction

1.1. Historical background

The idea behind the BCS–BEC crossover dates back just after the birth of the BCS theory in 1957 [1]. The authors of this theory made a point to emphasize the differences between their theory for superconductors based on strongly-overlapping Cooper pairs and the Schafroth–Butler–Blatt theory [2] resting on non-overlapping composite bosons which undergo Bose–Einstein condensation at low temperature. Subsequently, the interest in these two different situations has been kept disjoint for some time, until theoretical interest arose for unifying them as two limiting (BCS and BEC) situations of a single theory where they share the same kind of broken symmetry. In this way, the physical system passes through an intermediate situation, where the size of the pairs is comparable to the average inter-particle spacing. (For a short-range (contact) interaction, this intermediate situation is nowadays referred to as the "unitary" regime.) Pioneering work in this sense was done by the Russian school, motivated by the exciton condensation in semiconductors [3] or simply by intellectual curiosity [4]. The theory of the BCS–BEC crossover took shape initially through the work by Eagles [5] with possible applications to

superconducting semiconductors, and later through the works by Leggett [6] and Nozières and Schmitt-Rink [7] where the formal aspects of the theory were developed at zero temperature and above the critical temperature, respectively.

The interest in the BCS–BEC crossover grew up with the advent of high-temperature (cuprate) superconductors in 1987, in which the size of the pairs appears to be comparable to the inter-particle spacing [8–15]. Related interest in the BCS–BEC crossover soon spread to some problems in nuclear physics [16], but a real explosion of this activity appeared starting from 2003 with the advent of the fully controlled experimental realization essentially of all aspects of the BCS–BEC crossover in ultra-cold Fermi gases (see Refs. [17] and [18] for an experimental and theoretical overview, respectively). This realization, in turn, has raised the interest in the crossover problem especially of the nuclear physics community, as representing an unprecedented tool to test fundamental and unanswered questions of nuclear many-body theory. The Fermi gas at the *unitary limit* (UL), where fermions of opposite spins interact via a contact interaction with infinite scattering length, was actually introduced as a simplified model of dilute neutron matter [19,20], and the possibility to realize this limit with ultra-cold atoms was hence regarded as extremely important for this field of nuclear physics.

In nuclear physics there is the paradigmatic example of a proton–neutron bound state (the deuteron) for which in symmetric or asymmetric nuclear matter, as a function of density, one may find a transition from BEC to BCS [16,21–23] (see also Ref. [24] for the density-induced BCS–BEC crossover). Such a scenario may be realized in expanding nuclear matter generated from heavy ion collisions [16] or in proto-neutron stars [25]. More recently, this density driven crossover has been studied together with the competing liquid–gas phase transition [26]. Deuteron condensation also heavily competes with alpha-particle condensation, which is somehow related to *pairing of pairs* discussed also in condensed-matter physics. Nuclear physics is a precursor of the theory for quartet condensation [27], but theoretical studies of quartets came up later also in the area of ultra-cold atoms [28]. Alpha-particle condensation is presently very much discussed in finite nuclei (Hoyle state) [29]. It was also predicted that in the non-condensed phase, the deuterons give rise to a pseudo-gap formation [30]. With today's ultra-cold atoms experiments, it has become possible to test such theories [31–33]. For neutrons, no bound state exists, but rather a virtual state at almost zero energy. As a consequence, a dilute gas of neutrons, as it exists in the inner crust of neutron stars, is almost in the unitary limit mentioned above. Recent studies of the dilute neutron gas, from (almost) unitarity at low density to the BCS limit at high density, were done within BCS theory [34], Quantum-Monte-Carlo calculations [35,36], and the Nozières–Schmitt-Rink approach [37]. One can say that the equation of state and pairing properties of very dilute neutron matter, although inaccessible in experiments, are now known thanks to the analogy with ultra-cold atoms.

As these examples show, there are several aspects of the BCS–BEC crossover which are of broad joint interest to both ultra-cold atoms and nuclear communities. This paper is thus meant to provide a comprehensive review which focuses mainly on these common aspects of ultra-cold atoms and nuclear physics. Along these views, this paper provides also a pedagogical review of the main essential aspects of the BCS–BEC crossover. In the process of writing, we have mostly adopted the quantum many-body diagrammatic techniques in line with our own technical expertise, and we have mainly focused on the topics to which we have provided original contributions over the last several years. Accordingly, for readers interested in complementary theoretical approaches to the problem we refer to other reviews which cover various aspects of the BCS–BEC crossover. In particular, we can refer to reviews on the application to strongly-interacting Fermi gases (in particular, at unitarity) of Quantum Monte Carlo methods [38,39], functional-renormalization-group techniques [40], epsilon [41] and virial [42] expansions. For the application of functional-integral approaches (in particular, to the superfluid phase) we refer instead to the original research works of Refs. [43–45].

In addition, it should be mentioned that further reviews cover a number of aspects on the BCS–BEC crossover which share a partial overlap with the material discussed here. Specifically, the unitary limit of Section 4.3 and the Tan contact of Section 4.5 have been of most interest in other reviews owing to the widespread recent interest in these topics, which have been treated in Refs. [18,46–48]. The Fano–Feshbach resonances of Section 4.1, which are at the heart of the interaction-induced crossover, have been discussed in Refs. [46–50]. Polarized Fermi gases (considered here in Sections 2.6 and 3.7) have also been treated in Refs. [18,47,50–53]. The topic of the single-particle spectral function and pseudo-gap of Section 3.3 can be found discussed also in Refs. [46,48,54]. Also some aspects of pairing in nuclear systems discussed in Section 5 can be found in the reviews of Refs. [55–57]. Finally, Refs. [47] and [57] cover also some introductory material treated here in Sections 1.2, 2.1, 2.4, 3.4, 4.7, 4.8 and 5.1. However, it should be remarked that no other reference thus far has emphasized the aspects of the BCS–BEC crossover common to ultra-cold atoms and nuclear physics as we have done here.

1.2. The BCS wave function and its BEC limit

The starting point is the BCS ground-state wave function, of the form [1,58]

$$|\Phi_{\rm BCS}\rangle = \prod_{\mathbf{k}} \left(u_{\mathbf{k}} + v_{\mathbf{k}} c^{\dagger}_{\mathbf{k}\uparrow} c^{\dagger}_{-\mathbf{k}\downarrow} \right) |0\rangle \, . \tag{1}$$

In this expression, $|0\rangle$ is the vacuum state, $c^{\dagger}_{\mathbf{k}\sigma}$ is a fermionic creation operator for wave vector $\mathbf{k}$ and spin projection $\sigma = (\uparrow, \downarrow)$, and $u_{\mathbf{k}}$ and $v_{\mathbf{k}}$ are probability amplitudes given by:

$$v^2_{\mathbf{k}} = 1 - u^2_{\mathbf{k}} = \frac{1}{2} \left(1 - \frac{\xi_{\mathbf{k}}}{E_{\mathbf{k}}} \right) \tag{2}$$

where $\xi_{\mathbf{k}} = \mathbf{k}^2/(2m) - \mu$ (m being the fermion mass and μ the chemical potential) and $E_{\mathbf{k}} = \sqrt{\xi_{\mathbf{k}}^2 + |\Delta_0|^2}$ where Δ_0 is the BCS order parameter (sometimes referred to as the superconducting gap) here taken at zero temperature. For simplicity, we have assumed that Δ_0 is independent of the wave vector, as it is the case for a contact interaction. More generally, Δ_0 in the expression of $E_{\mathbf{k}}$ will be replaced by the wave-vector (and temperature) dependent value $\Delta_{\mathbf{k}}$. [Throughout this paper, we use units where the reduced Planck constant $\hbar$ and the Boltzmann constant k_B are set equal to unity.]

The BCS wave function (1) has the important property that it is the vacuum to the so-called quasi-particle operators $\alpha_{\mathbf{k}} = u_{\mathbf{k}} c_{\mathbf{k}\uparrow} - v_{\mathbf{k}} c^\dagger_{-\mathbf{k}\downarrow}$ (see Eq. (28) and Ref. [59]), that is, $\alpha_{\mathbf{k}}|\Phi_{\rm BCS}\rangle = 0$. This relation facilitates considerably the evaluation of expectation values. One can readily show that $\langle\Phi_{\rm BCS}|c^\dagger_{\mathbf{k}\sigma} c_{\mathbf{k}\sigma}|\Phi_{\rm BCS}\rangle = v^2_{\mathbf{k}}$ is the occupation number $n_{\mathbf{k}}$ which goes over to the Fermi step in the limit as Δ_0 tends to zero, and that $\langle\Phi_{\rm BCS}|c_{-\mathbf{k}\downarrow} c_{\mathbf{k}\uparrow}|\Phi_{\rm BCS}\rangle = u^*_{\mathbf{k}} v_{\mathbf{k}}$ is the so-called anomalous density $\phi_{\mathbf{k}}$ (known also as the "pairing tensor" $\kappa_{\mathbf{k}}$ in nuclear physics) which characterizes the BCS wave function.

With reference to the BCS–BEC crossover, it has long been known that the BCS wave function (1) contains the Bose–Einstein condensation of composite bosons as a limit. This is because, upon setting $g_{\mathbf{k}} = v_{\mathbf{k}}/u_{\mathbf{k}}$, the expression (1) can be rewritten in the form (see, e.g., Ref. [59]):

$$|\Phi_{\rm BCS}\rangle = \left(\prod_{\mathbf{k}'} u_{\mathbf{k}'}\right) \exp\left[\sum_{\mathbf{k}} g_{\mathbf{k}} c^\dagger_{\mathbf{k}\uparrow} c^\dagger_{-\mathbf{k}\downarrow}\right]|0\rangle \tag{3}$$

since $(c^\dagger_{\mathbf{k}\sigma})^2 = 0$ owing to Pauli principle. Here, the operator $b^\dagger_0 \equiv \sum_{\mathbf{k}} g_{\mathbf{k}} c^\dagger_{\mathbf{k}\uparrow} c^\dagger_{-\mathbf{k}\downarrow}$ contains fermion pairs but it is not a truly bosonic operator, to the extent that the commutator $[b_0, b^\dagger_0] = \sum_{\mathbf{k}} |g_{\mathbf{k}}|^2 (1 - \hat{n}_{\mathbf{k}\uparrow} - \hat{n}_{-\mathbf{k}\downarrow})$ is not a c-number but explicitly contains the fermionic operators $\hat{n}_{\mathbf{k}\sigma} = c^\dagger_{\mathbf{k}\sigma} c_{\mathbf{k}\sigma}$. However, under some circumstances one may consider that $[b_0, b^\dagger_0] \cong 1$ for all practical purposes, provided $\langle\Phi_{\rm BCS}|\hat{n}_{\mathbf{k}\sigma}|\Phi_{\rm BCS}\rangle = v^2_{\mathbf{k}} \ll 1$ for all $\mathbf{k}$ of physical relevance. As a consequence, $|\Phi_{\rm BCS}\rangle = \exp(b^\dagger_0)|0\rangle$ represents a bosonic coherent state (that is, a Bose–Einstein condensate) with a non-vanishing broken-symmetry average $\langle\Phi_{\rm BCS}|b_0|\Phi_{\rm BCS}\rangle = \sum_{\mathbf{k}} |g_{\mathbf{k}}|^2 \neq 0$.

It is clear from Eq. (2) that the condition $v^2_{\mathbf{k}} \ll 1$ can be satisfied for *all* $\mathbf{k}$ provided the fermionic chemical potential μ becomes large and negative. This condition can be achieved when a bound-state with binding energy $\varepsilon_0 = (m a_F^2)^{-1}$ occurs for the two-body problem *in vacuum* with positive scattering length a_F, and the coupling parameter $(k_F a_F)^{-1}$ becomes large such that $\varepsilon_0/E_F \gg 1$. In this limit, μ approaches the value $-\varepsilon_0/2$, which amounts to saying that all fermions are paired up in tight (composite) bosons with a vanishing residual interaction among the bosons. This result for the BEC limit of the fermionic chemical potential μ can directly be obtained from the mean-field gap equation (at zero temperature), which in the case of a wave-vector dependent interaction $V_{\rm eff}(\mathbf{k}, \mathbf{k}')$ reads:

$$\Delta_{\mathbf{k}} = -\int \frac{d\mathbf{k}'}{(2\pi)^3} V_{\rm eff}(\mathbf{k}, \mathbf{k}') \frac{\Delta_{\mathbf{k}'}}{2E_{\mathbf{k}'}} \tag{4}$$

where now $E_{\mathbf{k}} = \sqrt{\xi^2_{\mathbf{k}} + |\Delta_{\mathbf{k}}|^2}$. (In the case of a contact potential, $V_{\rm eff}(\mathbf{k}, \mathbf{k}')$ and $\Delta_{\mathbf{k}}$ reduce, respectively, to the coupling constant v_0 of Eq. (7) and to the constant gap Δ_0 given by the gap equation (8).) Using $\phi_{\mathbf{k}} = \Delta_{\mathbf{k}}/(2E_{\mathbf{k}})$, $n_{\mathbf{k}} = v^2_{\mathbf{k}}$, and Eq. (2), one can rewrite Eq. (4) in the form:

$$2\xi_{\mathbf{k}}\phi_{\mathbf{k}} + (1 - 2n_{\mathbf{k}}) \int \frac{d\mathbf{k}'}{(2\pi)^3} V_{\rm eff}(\mathbf{k}, \mathbf{k}')\, \phi_{\mathbf{k}'} = 0\,. \tag{5}$$

Provided $n_{\mathbf{k}} \ll 1$ for all $\mathbf{k}$, Eq. (5) is just the Schrödinger equation for the relative motion of two particles of equal mass m which are mutually interacting via the potential $V_{\rm eff}$. The negative eigenvalue 2μ of this equation thus corresponds to (minus) the two-body binding energy ε_0 as stated above.

More generally, as we shall see below, it is the fermionic chemical potential μ that takes the key role of the driving field which enables the system to pass from the BCS to the BEC limits of the BCS–BEC crossover. As an illustration, Fig. 1 shows the occupation number $n_{\mathbf{k}} = v^2_{\mathbf{k}}$ at zero temperature for different (from positive to negative) values of the chemical potential μ, which correspond to increasing values of the gap parameter Δ_0. Note that only when $\mu > 0$ the curves have an inflection point at $\varepsilon_{\mathbf{k}} = \mu$, which highlights the presence of an underlying Fermi surface even for a system with attractive inter-particle interaction. As a consequence, when μ becomes negative, the Fermi sea gets completely dissolved and the occupation number becomes quite small for all $\mathbf{k}$.

1.3. Pairing correlations

The BCS wave function (1), or its equivalent form (3), treats all fermion pairs on the same footing to the extent that a single wave function $g_{\mathbf{k}}$ is assigned to each pair. This *mean-field* type of approach is appropriate to describe a system of fermions with a mutual attractive interaction when the inter-particle correlations extend much beyond the average inter-particle distance, in such a way that many pairs are contained within the size of a given pair and different pairs strongly overlap with each other. This is definitely the case for the (BCS) weak-coupling limit, to which the BCS theory of superconductivity was originally meant to apply [1]. When considering the BCS–BEC crossover, however, the range of the inter-particle correlations can decrease down to the size of the bound pair, which, in turn, can be much smaller than

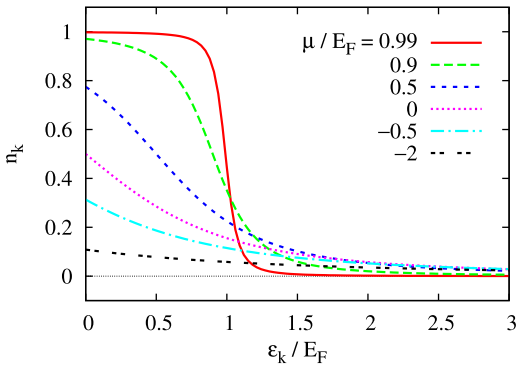

Fig. 1. BCS occupation number $n_{\mathbf{k}} = v_{\mathbf{k}}^2$ at zero temperature vs the energy $\varepsilon_{\mathbf{k}} = k^2/(2m)$ in units of the Fermi energy $E_F = (3\pi^2 n)^{2/3}/(2m)$ where n is the density, for various values of the chemical potential ranging from $\mu = 0.99E_F$ to $\mu = -2E_F$ [the corresponding values of the gap are $\Delta_0/E_F =$(0.09, 0.32, 0.76, 1.05, 1.24, and 1.59), from top to bottom].

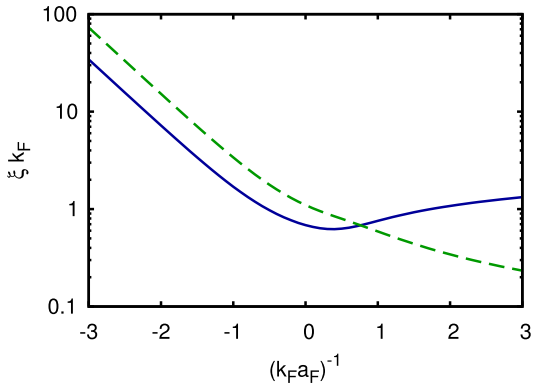

Fig. 2. Zero-temperature intra-pair coherence length $\xi_{\rm pair}$ at the mean-field level (dashed line) vs the coupling parameter $(k_F a_F)^{-1}$. The full line gives the corresponding evolution of the inter-pair coherence (healing) length ξ, to be discussed extensively in Section 3.2. Note that the two lengths differ by an irrelevant numerical factor in the BCS limit owing to their independent definitions.
Source: Reproduced from Ref. [60].

the inter-particle distance. Under these circumstances, the gas of composite bosons becomes dilute and one accordingly anticipates that *pairing fluctuations* beyond mean field can acquire a major role, especially at finite temperature when they are accompanied by thermal fluctuations.

Fig. 2 shows the evolution throughout the BCS–BEC crossover of the zero-temperature *pair coherence length* $\xi_{\rm pair}$ (dashed line) calculated for the BCS ground state (1). This quantity provides information about the intra-pair correlation established between fermions of opposite spins [14] and, at the mean-field level, corresponds to the spatial extension of the order parameter $\phi_{\mathbf{k}}$. Since $\phi_{\mathbf{k}}$ can, in turn, be interpreted as a wave function as shown by Eq. (5), the r.m.s. radius $\xi_{\rm pair}$ of the pairs can be obtained from the expression:

$$\xi_{\rm pair}^2 = \frac{\int d\mathbf{r}\, \mathbf{r}^2\, |\phi(\mathbf{r})|^2}{\int d\mathbf{r}\, |\phi(\mathbf{r})|^2} \tag{6}$$

where $\phi(\mathbf{r})$ is the Fourier transform of $\phi_{\mathbf{k}}$. [For later convenience, Fig. 2 shows also the corresponding evolution of the *healing length* ξ (full line), that instead provides information about the inter-pair correlation [43] and requires the inclusion of pairing fluctuations beyond mean field — see Section 3.2]. In Fig. 2, the average inter-particle distance k_F^{-1} is used as the unit for $\xi_{\rm pair}$, where k_F is the Fermi wave vector related to the particle density via the relation $n = k_F^3/(3\pi^2)$. In Fig. 2 and throughout this paper, the quantity $(k_F a_F)^{-1}$ plays the role of the *coupling parameter* of the theory. Depending on the sign of a_F, this parameter ranges from $(k_F\, a_F)^{-1} \lesssim -1$ characteristic of the weak-coupling BCS regime when $a_F < 0$, to $(k_F\, a_F)^{-1} \gtrsim +1$ characteristic of the strong-coupling BEC regime when $a_F > 0$, across the value $(k_F\, a_F)^{-1} = 0$ at unitarity when $|a_F|$ diverges. In practice, the "crossover region" of most interest, to be discussed throughout this paper, turns out to be approximately limited to the interval $-1 \lesssim (k_F\, a_F)^{-1} \lesssim +1$.

Pairing fluctuations play a particularly important role in the normal phase above the critical temperature T_c where the order parameter vanishes (the generalization of the BCS approach to finite temperature will be considered in Section 2). This is because, a "local" order is expected to survive above T_c if the system is fluctuating, even though the long-range order

characteristic of the superfluid phase is lost. These considerations have led people to associate pairing fluctuations with the occurrence of a *pseudo-gap* above T_c (as seen, for instance, by a depression of the single-particle density of states about the chemical potential), in a similar way to what occurs in the superfluid phase below T_c when the order parameter is instead nonvanishing. Such an analogy (between the order parameter below T_c and the pseudo-gap above T_c) has been carried to the point that even the pseudo-gap state occurring in copper-oxide superconductors has been interpreted from the point of view of a BCS–BEC crossover scenario [54].

In this context, it can be useful to consider the similarity between the pseudo-gap physics resulting from pairing fluctuations above T_c and the persistence of (damped) spin waves, which are present over regions of limited extent in the normal phase of ferromagnetic (or antiferromagnetic) materials when a strict long-range order is absent [61]. Through this analogy, pseudo-gap phenomena in a Fermi system with an attractive inter-particle interaction are attributed to the persistence of a "local pairing order" above the superfluid temperature T_c, which occurs even though the (off-diagonal) long-range order is absent. This local order, which is built up by pairing fluctuations above T_c, makes the single-particle excitation spectrum to resemble that below T_c, although with a frequency broadening due to the decay of the local excitations which cannot propagate over long distances in the absence of long-range order.

In addition, it is relevant to point out that, when raising the temperature and approaching T_c from below, pairing correlations turn out to persist over a finite distance even within mean field, without the need of considering pairing fluctuations beyond mean field. Indeed, explicit calculations of the temperature dependence of the pair correlation function within mean field show that $\xi_{\rm pair}$ maintains a finite value at T_c^- [62], a result which remains true irrespective of coupling across the BCS–BEC crossover [63]). This remark, too, points out the importance of including pairing fluctuations in the normal phase above T_c, in order to obtain a meaningful finite value of $\xi_{\rm pair}$ even when approaching T_c from above. Otherwise, $\xi_{\rm pair}$ would be discontinuous when passing from T_c^- to T_c^+, since above T_c fermions become non-interacting within the BCS (mean-field) approximation. We shall return to this point more extensively in Section 3.2.

2. BCS mean field

2.1. The homogeneous infinite matter case for a contact interaction

The BCS theory of superconductivity considers an effective *attractive* interaction $V_{\rm eff}(\mathbf{r}-\mathbf{r}')$ between otherwise free fermions of two different species (conventionally referred to as spin $\uparrow$ and $\downarrow$), which are embedded in a continuous medium at a distance $|\mathbf{r}-\mathbf{r}'|$ [1,58]. This attractive interaction, albeit weak, is responsible for the formation of Cooper pairs in the medium [64]. In condensed matter (like in metallic superconductors), detailed knowledge of the form of the attractive interaction is not required for most purposes and one may accordingly consider the simple form of a "contact" (zero-range) potential $V_{\rm eff}(\mathbf{r}) = v_0\,\delta(\mathbf{r})$, where v_0 is a negative constant. This model interaction fully applies to ultra-cold Fermi gases (at least in the presence of a broad Fano–Feshbach resonance as discussed in Section 4.1), but does not apply to nuclear systems discussed in Section 5 for which a finite-range interaction should in principle be retained. In order to reduce the numerical difficulties, however, even in the treatment of nuclear superfluids the finite-range interaction is often approximated by a zero-range one, which requires one to introduce a density-dependent coupling constant (see, e.g., Ref. [65]). This approach has further been elaborated (for instance, in Refs. [66,67]) with the introduction of an efficient regularization scheme for finite systems (as discussed in Section 2.4). Here, like in most part of the paper, we consider the case of equal populations $N_\uparrow = N_\downarrow$, while the new features arising under the more general condition $N_\uparrow \neq N_\downarrow$ will be explicitly considered in Section 2.6.

The price to pay for the use of a contact interaction is that, when dealing with a homogeneous system, integrals over the wave vector $\mathbf{k}$ may diverge in the ultraviolet since the Fourier transform $V_{\rm eff}(\mathbf{k}) = v_0$ is a constant (in what follows, we shall consider a three-dimensional system). This difficulty can be simply overcome by introducing a cut-off, given for metallic superconductors by the Debye frequency and for nuclei by a phenomenologically adjusted cut-off energy that reflects the range of the effective force. For ultra-cold gases, on the other hand, one can exploit the fact that a similar divergence affects also the two-body problem *in vacuum*, whereby the fermionic scattering length a_F is obtained from the relation [68]:

$$\frac{m}{4\pi a_F} = \frac{1}{v_0} + \int_{|\mathbf{k}|\le k_0} \frac{d\mathbf{k}}{(2\pi)^3}\,\frac{m}{\mathbf{k}^2} \tag{7}$$

with an ultraviolet cutoff k_0. This regularization procedure entails the limits $v_0 \to 0^-$ and $k_0 \to \infty$ to be taken simultaneously, in such a way that a_F is kept at the desired value. Replacing the parameter v_0 with the physical quantity a_F is especially relevant in the context of ultra-cold gases, where the natural cut-off given by the inverse of the interaction range would be orders of magnitude larger than all wave vectors of physical interest and where a_F can be experimentally controlled [69]. As we shall see in Section 3.1, the regularization (7) is also of help when dealing with the many-body problem based on this two-body interaction, to the extent that it greatly reduces the number of many-body diagrams that survive in the limit $v_0 \to 0$.

In this way, the BCS mean-field equations for the order (gap) parameter Δ at the temperature T and for the density n become [58]:

$$-\frac{m}{4\pi a_F} = \int \frac{d\mathbf{k}}{(2\pi)^3}\left(\frac{1-2f(E_\mathbf{k})}{2E_\mathbf{k}} - \frac{m}{\mathbf{k}^2}\right) \tag{8}$$

$$n = \int \frac{d\mathbf{k}}{(2\pi)^3} \left(1 - \frac{\xi_{\mathbf{k}}}{E_{\mathbf{k}}} (1 - 2f(E_{\mathbf{k}}))\right) \tag{9}$$

where $f(E) = (e^{E/T} + 1)^{-1}$ is the Fermi function and $E_{\mathbf{k}} = \sqrt{\xi_{\mathbf{k}}^2 + |\Delta|^2}$. Note that the quantity Δ that enters Eqs. (8) and (9) plays the dual role of the order parameter (which is non-vanishing between $T = 0$ and $T = T_c$) and of the minimum value of the single-particle excitation energy $E_{\mathbf{k}}$ at $|\mathbf{k}| = \sqrt{2m\mu}$ when $\mu > 0$. [The extension to finite temperature of the gap equation (4) with a finite-range interaction will be considered in Section 5.1 - cf. Eq. (115).]

For a *weak* attractive interaction, a_F is small and negative such that $(k_F a_F)^{-1} \ll -1$. This limit characterizes what is called the "conventional" BCS theory [1]. In this limit, the Fermi surface of non-interacting fermions is only slightly perturbed by the presence of the interaction, and the chemical potential μ at $T = 0$ coincides with the Fermi energy $E_F = k_F^2/(2m)$. This is actually the limit where the mean-field approximation is expected to work best, to the extent that the size $\xi_{\rm pair}$ of a Cooper pair is much larger than the average inter-particle distance k_F^{-1} and a large number of pairs is contained within the size of $\xi_{\rm pair}$ [58].

2.2. Solution at $T = 0$ for a contact potential

For a generic value of the coupling $(k_F a_F)^{-1}$ that ranges between the BCS and BEC limits, the values of Δ_0 and μ_0 at $T = 0$ are determined by solving the coupled equations (8) and (9), where one sets $f(E_{\mathbf{k}}) = 0$ since $E_{\mathbf{k}}$ is always positive. Although a numerical solution of the ensuing equations is possible [70], it was found independently that the three-dimensional integrals over the wave vector occurring in these equations can be expressed either in terms of the complete elliptic integrals [71] or in terms of the Legendre function [72], in such a way that closed-form expressions for Δ_0 and μ_0 are obtained. In Ref. [71], the results were expressed in terms of the parameter $x_0 = \mu_0/\Delta_0$ that ranges from $-\infty$ (BEC limit) to $+\infty$ (BCS limit), while in Ref. [72] the inverse of this parameter was used.

In Ref. [71], the following results were obtained:

$$\frac{\Delta_0}{E_F} = \frac{1}{(x_0 J(x_0) + I(x_0))^{2/3}}\,, \tag{10}$$

$$\frac{\mu_0}{E_F} = x_0 \frac{\Delta_0}{E_F}\,, \tag{11}$$

$$\frac{1}{k_F a_F} = -\frac{4}{\pi} \frac{x_0 I(x_0) - J(x_0)}{(x_0 J(x_0) + I(x_0))^{1/3}}\,, \tag{12}$$

where

$$I(x_0) = \frac{1}{2(1 + x_0^2)^{1/4}} F\left(\frac{\pi}{2}, \kappa\right) \tag{13}$$

and

$$J(x_0) = (1 + x_0^2)^{1/4} E\left(\frac{\pi}{2}, \kappa\right) - \frac{1}{4y_0(1 + x_0^2)^{1/4}} F\left(\frac{\pi}{2}, \kappa\right)\,. \tag{14}$$

In these expressions, $F\left(\frac{\pi}{2}, \kappa\right)$ and $E\left(\frac{\pi}{2}, \kappa\right)$ are the complete elliptic integrals of the first and second kind, respectively, and

$$y_0 = \frac{\sqrt{1 + x_0^2} + x_0}{2}\,, \qquad \kappa^2 = \frac{y_0}{\sqrt{1 + x_0^2}}\,. \tag{15}$$

In Ref. [72], on the other hand, Eq. (12) was equivalently expressed in the form:

$$\frac{1}{k_F a_F} = \left(\frac{1 + x_0^2}{x_0^2}\right)^{1/4} P_{1/2}\left(-|x_0|\,(1 + x_0^2)^{-1/2}\right) \tag{16}$$

where P_α denotes the Legendre function. In addition, analytic expressions for the pair coherence length $\xi_{\rm pair}$ and the condensate fraction were obtained in Refs. [71] and [73], respectively.

Analytic approximations can be readily obtained in the BCS and BEC limits. In the BCS limit where $x_0 \gg 1$, one obtains $\kappa^2 \simeq 1 - 1/(4x_0^2) \approx 1$ in Eq. (15). One can thus approximate $\Delta_0/E_F \simeq 1/x_0$, $\mu_0/E_F \simeq 1$, and $1/(k_F a_F) \simeq -(2/\pi)\ln(8x_0/e^2)$, in such a way that:

$$\Delta_0 = \frac{8E_F}{e^2} \exp\left(\frac{\pi}{2k_F a_F}\right)\,. \tag{17}$$

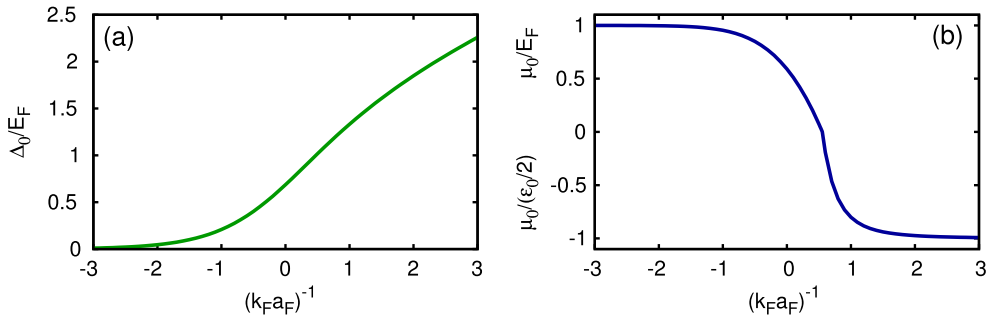

Fig. 3. (a) Gap Δ_0 and (b) chemical potential μ_0 at the mean-field level vs $(k_F a_F)^{-1}$ for a homogeneous system at $T = 0$. *Source:* Reproduced from Ref. [60].

In the BEC limit, on the other hand, $x_0 < 0$ and $|x_0| \gg 1$ such that $\kappa^2 \simeq 1/(4x_0^2) \approx 0$. One thus finds:

$$\frac{1}{k_F a_F} \simeq \left(\frac{16}{3\pi}\right)^{1/3} |x_0|^{2/3}, \tag{18}$$

$$\frac{\Delta_0}{E_F} \simeq \left(\frac{16}{3\pi}\right)^{2/3} |x_0|^{1/3} \simeq \left(\frac{16}{3\pi}\right)^{1/2} \left(\frac{1}{k_F a_F}\right)^{1/2}, \tag{19}$$

$$\frac{\mu_0}{E_F} \simeq -\left(\frac{16}{3\pi}\right)^{2/3} |x_0|^{4/3} \simeq -\frac{1}{2}\frac{\varepsilon_0}{E_F}. \tag{20}$$

The full expressions (10), (11), and (12) interpolate *smoothly* between the above (BCS and BEC) limits through the crossover region $k_F|a_F| \gtrsim 1$. Plots of Δ_0 and μ_0 as functions of $(k_F a_F)^{-1}$ are readily obtained from these equations, as shown in Fig. 3(a) and (b). Note, in particular, that the chemical potential: (i) In the BCS limit equals the Fermi energy E_F; (ii) In the crossover region $-1 \lesssim (a_F k_F)^{-1} \lesssim +1$ gradually decreases and eventually changes its sign; (iii) In the BEC limit reaches the asymptotic value $-\varepsilon_0/2$. It is just this behavior of the chemical potential that drives the BCS–BEC crossover, as it was anticipated in Section 1.2.

2.3. Extension to finite temperature

At finite temperature, the presence of the Fermi function in the gap equation (8) and density equation (9) makes it impossible to find an analytic solution and one has then to resort to a numerical solution of these equations. An exception occurs, however, upon approaching the critical temperature T_c from below, where analytic results can be obtained both in BCS and BEC limits (see, e.g., Ref. [74]).

At the mean-field level, the critical temperature T_c is defined by the vanishing of the BCS gap parameter Δ. Eqs.(8) and (9) are thus replaced by:

$$-\frac{m}{4\pi a_F} = \int \frac{d\mathbf{k}}{(2\pi)^3} \left(\frac{\tanh(\xi_{\mathbf{k}}/2T_c)}{2\xi_{\mathbf{k}}} - \frac{m}{\mathbf{k}^2}\right) \tag{21}$$

$$n = 2\int \frac{d\mathbf{k}}{(2\pi)^3} \frac{1}{\exp(\xi_{\mathbf{k}}/T_c) + 1}. \tag{22}$$

In the weak-coupling limit where $(k_F a_F)^{-1} \ll -1$, Eq. (22) yields the value of the chemical potential of a Fermi gas, which is only slightly smaller than the zero-temperature result $\mu = E_F$ provided $T_c \ll E_F$. Correspondingly, Eq. (21) gives the following expression for T_c:

$$T_c = \frac{8e^{\gamma} E_F}{\pi e^2} \exp\left(\frac{\pi}{2k_F a_F}\right) \tag{23}$$

where γ is Euler's constant (such that $\Delta_0/T_c = \pi/e^{\gamma} \simeq 1.764$ with reference to the result (17) that holds in the same limit). Since in the weak-coupling regime a_F is negative and $k_F|a_F| \ll 1$, Eq. (23) yields $T_c \ll E_F$ consistently with our assumptions.

In the strong-coupling limit where $(k_F a_F)^{-1} \gg +1$, the role of the two Eqs. (21) and (22) is reversed. If we assume that $T_c \ll |\mu|$, we may set $\tanh(\xi_{\mathbf{k}}/2T_c) \simeq 1$ in Eq. (21), making it to reduce to the bound-state equation and yielding $\mu \simeq -\varepsilon_0/2$ at the leading order. The same kind of approximation, however, cannot be used in Eq. (22) since n has to remain finite. In this equation, we set instead $(\exp(\xi_{\mathbf{k}}/T_c) + 1)^{-1} \simeq \exp(-\xi_{\mathbf{k}}/T_c)$ and obtain

$$\frac{\mu}{T_c} \simeq \ln\left[\frac{n}{2}\left(\frac{2\pi}{mT_c}\right)^{3/2}\right], \tag{24}$$

a result which coincides with the expression of the classical chemical potential at temperature T_c. Using at this point the value $\mu(T_c) \simeq -\varepsilon_0/2$ as determined from Eq. (21), we can solve the expression (24) iteratively for T_c yielding [68]:

$$T_c \simeq \frac{\varepsilon_0}{2\ln\left(\frac{\varepsilon_0}{E_F}\right)^{3/2}} \tag{25}$$

at the leading order in $E_F/\varepsilon_0 \ll 1$. Although $T_c \ll |\mu|$ consistently with our assumptions, the expression of T_c given by Eq. (25) diverges in the BEC limit *at fixed density*, instead of approaching as expected the finite value $T_{\rm BEC} = \frac{\pi}{m}\left(\frac{n/2}{\zeta(3/2)}\right)^{2/3}$ at which the Bose–Einstein condensation of an ideal gas of composite bosons with mass $2m$ and density $n/2$ occurs ($\zeta(3/2) \approx 2.612$ being the Riemann ζ function of argument 3/2). Physically, the mean-field temperature (25) corresponds to the *dissociation* of composite bosons, with the ln factor in the denominator originating from entropy effects. It is thus appropriate to associate the mean-field result (25) with the "pair dissociation temperature" of the composite bosons, which is completely unrelated to the BEC temperature $T_{\rm BEC}$ at which quantum coherence is established among the composite bosons. The reason for this failure is that only the internal degrees of freedom of the composite bosons are taken into account by the mean-field expressions (21) and (22), thereby leaving aside the translational degrees of freedom of the composite bosons. To include these, pairing fluctuations beyond mean field need to be considered. The corresponding analysis will be discussed in Section 3.1.

2.4. Bogoliubov–de Gennes and Hartree–Fock–Bogoliubov equations for inhomogeneous Fermi systems

The BCS wave function (1), for the ground state of a *homogeneous* Fermi gas with an attractive inter-particle interaction, is a variational wave function with an associated gap parameter Δ_0 at zero temperature, which extends to the superfluid phase the Hartree–Fock approximation for the normal phase by retaining also operator averages of the type $\langle c^\dagger_{\mathbf{k}\uparrow} c^\dagger_{-\mathbf{k}\downarrow}\rangle$ that do not conserve the particle number.

At finite temperature, the "mean-field" character of the BCS gap equation (8) for Δ and of the associated coherence factors $u_{\mathbf{k}}$ and $v_{\mathbf{k}}$ given by the expressions (2), is better captured by an alternative procedure, whereby a mean-field (or Hartree–Fock-type) decoupling is directly performed at the level of the Hamiltonian by including particle non-conserving averages. Accordingly, one replaces the grand-canonical Hamiltonian $K = H - \mu N$ by its mean-field approximation as follows

$$\begin{aligned} K &= \sum_{\mathbf{k}\sigma} \xi_{\mathbf{k}}\, c^\dagger_{\mathbf{k}\sigma} c_{\mathbf{k}\sigma} + v_0 \sum_{\mathbf{k}\mathbf{k}'\mathbf{q}} c^\dagger_{\mathbf{k}+\mathbf{q}/2\uparrow} c^\dagger_{-\mathbf{k}+\mathbf{q}/2\downarrow} c_{-\mathbf{k}'+\mathbf{q}/2\downarrow} c_{\mathbf{k}'+\mathbf{q}/2\uparrow} \\ &\to \sum_{\mathbf{k}\sigma} \xi_{\mathbf{k}}\, c^\dagger_{\mathbf{k}\sigma} c_{\mathbf{k}\sigma} - \sum_{\mathbf{k}} \left(\Delta^*\, c_{-\mathbf{k}\downarrow} c_{\mathbf{k}\uparrow} + \Delta\, c^\dagger_{\mathbf{k}\uparrow} c^\dagger_{-\mathbf{k}\downarrow}\right) - \frac{\Delta^2}{v_0} \end{aligned} \tag{26}$$

where, for simplicity, we have considered the case of a zero-range interaction with strength v_0 (the generalization to finite-range interactions will be considered below). The parameter Δ in Eq. (26) thus satisfies the condition

$$\Delta = -v_0 \sum_{\mathbf{k}} \langle\, c_{-\mathbf{k}\downarrow} c_{\mathbf{k}\uparrow}\,\rangle \tag{27}$$

where the thermal average $\langle \dots \rangle$ is self-consistently determined through the mean-field Hamiltonian itself. The quadratic form (26) can be readily diagonalized by the canonical transformation

$$c_{\mathbf{k}\uparrow} = u^*_{\mathbf{k}}\, \alpha_{\mathbf{k}} + v_{\mathbf{k}}\, \beta^\dagger_{-\mathbf{k}}\,, \qquad c_{\mathbf{k}\downarrow} = -v_{\mathbf{k}}\, \alpha^\dagger_{-\mathbf{k}} + u^*_{\mathbf{k}}\, \beta_{\mathbf{k}}\,, \tag{28}$$

where $u_{\mathbf{k}} = u_{-\mathbf{k}}$ and $v_{\mathbf{k}} = v_{-\mathbf{k}}$ are constrained by $|u_{\mathbf{k}}|^2 + |v_{\mathbf{k}}|^2 = 1$ at any given $\mathbf{k}$. In terms of the new operators $\alpha_{\mathbf{k}}$ and $\beta_{\mathbf{k}}$, the mean-field Hamiltonian (26) becomes (see, e.g., Chapt. 6 of Ref. [59])

$$\begin{aligned} K \to & \sum_{\mathbf{k}} \left(\alpha^\dagger_{\mathbf{k}}\alpha_{\mathbf{k}} + \beta^\dagger_{\mathbf{k}}\beta_{\mathbf{k}}\right)\left[\xi_{\mathbf{k}}\left(u^2_{\mathbf{k}} - v^2_{\mathbf{k}}\right) + 2\Delta u_{\mathbf{k}} v_{\mathbf{k}}\right] + \sum_{\mathbf{k}} \left(\alpha^\dagger_{\mathbf{k}}\beta^\dagger_{-\mathbf{k}} + \beta_{-\mathbf{k}}\alpha_{\mathbf{k}}\right)\left[2\xi_{\mathbf{k}} u_{\mathbf{k}} v_{\mathbf{k}} - \Delta\left(u^2_{\mathbf{k}} - v^2_{\mathbf{k}}\right)\right] \\ & + 2\sum_{\mathbf{k}} \left(\xi_{\mathbf{k}} v^2_{\mathbf{k}} - \Delta u_{\mathbf{k}} v_{\mathbf{k}}\right) - \frac{\Delta^2}{v_0} \end{aligned} \tag{29}$$

(here, for simplicity, all quantities are assumed to be real). Provided that $u_{\mathbf{k}}$ and $v_{\mathbf{k}}$ are solutions to the equation

$$\begin{pmatrix} \xi_{\mathbf{k}} & \Delta \\ \Delta & -\xi_{\mathbf{k}} \end{pmatrix} \begin{pmatrix} u_{\mathbf{k}} \\ v_{\mathbf{k}} \end{pmatrix} = E_{\mathbf{k}} \begin{pmatrix} u_{\mathbf{k}} \\ v_{\mathbf{k}} \end{pmatrix}\,, \tag{30}$$

whereby $u^2_{\mathbf{k}} = 1 - v^2_{\mathbf{k}} = (1 + \xi_{\mathbf{k}}/E_{\mathbf{k}})/2$ and $E_{\mathbf{k}} = \sqrt{\xi^2_{\mathbf{k}} + \Delta^2}$, the coefficient $[2\xi_{\mathbf{k}} u_{\mathbf{k}} v_{\mathbf{k}} - \Delta(u^2_{\mathbf{k}} - v^2_{\mathbf{k}})]$ of the second term on the right-hand side of Eq. (29) vanishes identically, while the coefficient $[\xi_{\mathbf{k}}(u^2_{\mathbf{k}} - v^2_{\mathbf{k}}) + 2\Delta u_{\mathbf{k}} v_{\mathbf{k}}]$ of the first term equals $E_{\mathbf{k}}$. Correspondingly, the self-consistent condition (27) for Δ reduces to:

$$\Delta = -v_0 \sum_{\mathbf{k}} u_{\mathbf{k}} v_{\mathbf{k}}\,[1 - 2f(E_{\mathbf{k}})] \tag{31}$$

with $u_{\mathbf{k}}v_{\mathbf{k}} = \Delta/(2E_{\mathbf{k}})$. Note further that the last term of Eq. (29), which can be written as $\sum_{\mathbf{k}}(\xi_{\mathbf{k}} - E_{\mathbf{k}}) - \Delta^2/v_0$ with the help of Eq. (30), corresponds to the (grand-canonical) ground-state energy associated with the BCS state.

What is relevant here is that the above procedure can be readily generalized to situations in which $\Delta \to \Delta(\mathbf{r})$ depends on the spatial position $\mathbf{r}$, owing, for instance, to the presence of an external potential (like a trapping potential or a barrier), or of a magnetic field, or of the self-consistent mean field in finite nuclei, which introduce spatial inhomogeneities in the system. In this case, the algebraic matrix equation (30) is replaced by a pair of coupled Schrödinger-like equations for a two-component single-particle fermionic eigenfunction, of the form [75]:

$$\begin{pmatrix} \mathcal{H}(\mathbf{r}) & \Delta(\mathbf{r}) \\ \Delta^*(\mathbf{r}) & -\mathcal{H}(\mathbf{r}) \end{pmatrix} \begin{pmatrix} u_\nu(\mathbf{r}) \\ v_\nu(\mathbf{r}) \end{pmatrix} = E_\nu \begin{pmatrix} u_\nu(\mathbf{r}) \\ v_\nu(\mathbf{r}) \end{pmatrix} \tag{32}$$

where $\mathcal{H}(\mathbf{r}) = -\nabla^2/(2m) + V_{\rm ext}(\mathbf{r}) - \mu$ contains the external potential $V_{\rm ext}(\mathbf{r})$ (in addition, in the presence of an external vector potential $\mathbf{A}(\mathbf{r})$ the gradient operator $\boldsymbol{\nabla}$ in the kinetic energy is replaced as usual by $\nabla - i\mathbf{A}(\mathbf{r})$). Note that the Hartree term is absent in the diagonal elements of the matrix (32), owing to the use of a contact inter-particle interaction which makes this term to vanish in the limit $v_0 \to 0$. [In weak coupling, however, one often introduces in $\mathcal{H}(\mathbf{r})$ a Hartree-like-term of the form $\frac{4\pi a_F}{m}\frac{n}{2}$ [76,77].] These equations, known as the Bogoliubov–de Gennes (BdG) equations, have to be solved up to self-consistency for the local gap parameter $\Delta(\mathbf{r})$, which acts like an off-diagonal pair potential and satisfies the local condition:

$$\Delta(\mathbf{r}) = -v_0 \sum_\nu u_\nu(\mathbf{r}) v_\nu^*(\mathbf{r}) \left[1 - 2f(E_\nu)\right] . \tag{33}$$

In addition, the eigenfunctions $\{u_\nu(\mathbf{r}), v_\nu(\mathbf{r})\}$ obey the orthonormality condition:

$$\int d\mathbf{r} \left[u_\nu^*(\mathbf{r}) u_{\nu'}(\mathbf{r}) + v_\nu^*(\mathbf{r}) v_{\nu'}(\mathbf{r})\right] = \delta_{\nu\nu'} \tag{34}$$

where the Kronecker delta on the right-hand side is readily generalized to account for continuous eigenvalues. Physical quantities like the local number density, the current density, and the energy density can all be expressed in terms of the eigenfunctions and eigenvalues of Eq. (32) [75].

Note that the complex character of $\Delta(\mathbf{r})$ (as well as of the eigenfunctions $\{u_\nu(\mathbf{r}), v_\nu(\mathbf{r})\}$) has been restored in Eqs. (32)–(34), to allow for the presence of a particle current. Note also that it is the particle–hole mixing characteristic of the BCS pairing to be responsible for the coupling of the two components $(u_\nu(\mathbf{r}), v_\nu(\mathbf{r}))$ of the eigenfunctions of Eq. (32), in contrast to the normal Fermi gas where particle- and hole-excitations are separately good quasi-particles.

When solving the BdG equations for a contact inter-particle interaction with coupling constant v_0 (which is the case of ultra-cold Fermi gases), technical problems arise from the need to regularize the self-consistency condition (33) for the gap parameter $\Delta(\mathbf{r})$ since the sum over ν therein diverges in the ultraviolet. In the homogeneous case with a uniform gap parameter Δ_0 this regularization can be readily implemented with the help of Eq. (7), by expressing the bare coupling constant v_0 that enters the gap equation in terms of the scattering length a_F of the two-body problem [cf. Eq. (8)]. This procedure, however, cannot be utilized when the gap parameter $\Delta(\mathbf{r})$ has a spatial dependence, and a new strategy is required. A first generalization of the regularization procedure for fermions on the BCS side of the crossover trapped in a harmonic potential was given in Ref. [76] in terms of a pseudo-potential method in real space, but it turns out that this method is not easily implemented in numerical calculations. A numerically more efficient regularization procedure was described in Ref. [77] for the solution of the BdG equations (32) in a harmonic oscillator basis, which for practical purposes has to be truncated at some energy cutoff E_c. Following Refs. [66,67], the contribution of states above the cutoff is included within the Thomas–Fermi approximation. In this way, one obtains the following *regularized version of the gap equation*:

$$\Delta(\mathbf{r}) = -g_{\rm eff}(\mathbf{r}) \sum_\nu^{E_\nu < E_c - \mu} u_\nu(\mathbf{r}) v_\nu(\mathbf{r})^* \left[1 - 2f(E_\nu)\right] , \tag{35}$$

where the numerical solution of the BdG equations (32) is explicitly performed only for eigenvalues E_ν up to $E_c - \mu$ that appear on the right-hand side of Eq. (35). The pre-factor $g_{\rm eff}(\mathbf{r})$ plays the role of a (cutoff dependent) effective coupling constant and is given by

$$\frac{1}{g_{\rm eff}(\mathbf{r})} = \frac{m}{4\pi a_F} - \mathcal{R}(\mathbf{r}) \tag{36}$$

where

$$\mathcal{R}(\mathbf{r}) = \frac{m}{2\pi^2}\left[k_c(\mathbf{r}) - \frac{k_\mu(\mathbf{r})}{2} \ln \frac{k_c(\mathbf{r}) + k_\mu(\mathbf{r})}{k_c(\mathbf{r}) - k_\mu(\mathbf{r})}\right] . \tag{37}$$

The position-dependent wave vectors $k_\mu(\mathbf{r})$ and $k_c(\mathbf{r})$ are related to the chemical potential μ and energy cutoff E_c by $\mu = k_\mu^2(\mathbf{r})/(2m) + V_{\rm ext}(\mathbf{r})$ and $E_c = k_c^2(\mathbf{r})/(2m) + V_{\rm ext}(\mathbf{r})$. As noticed in Refs. [66,77], Eq. (37) can also be used for negative values of $\mu - V_{\rm ext}(\mathbf{r})$ by allowing for imaginary values of $k_\mu(\mathbf{r})$.

This approach was extended in Ref. [78] to the whole BCS–BEC crossover and generic inhomogeneous situations, by combining the introduction of the cutoff E_c in the quasi-particle energies such that $E_\nu < E_c - \mu$ with the derivation of the Gross–Pitaevskii equation for composite bosons in the BEC limit that was done in Ref. [79] (cf. Section 2.5). Under the assumption that the energy cutoff E_c is the largest energy scale in the problem (such that $\Delta(\mathbf{r})/E_c \ll 1$, $T/E_c \ll 1$, and $E_F/E_c \ll 1$, where E_F is the Fermi energy associated with the mean density — conditions that can be somewhat relaxed in the weak-coupling limit), the regularized version of the gap equation reads eventually [78]:

$$\left\{-\frac{m}{4\pi a_F}+\mathcal{R}(\mathbf{r})-\left[\frac{1}{2}\mathcal{I}_{02}(\mathbf{r})-\frac{1}{3}\mathcal{I}_{13}(\mathbf{r})\right]\frac{\nabla^2}{4m}+2V_{\rm ext}(\mathbf{r})\frac{1}{4}\mathcal{I}_{02}(\mathbf{r})+\frac{1}{4}\mathcal{I}_{03}(\mathbf{r})|\Delta(\mathbf{r})|^2\right\}\Delta(\mathbf{r}) = \sum_{\nu}^{E_\nu<E_c-\mu} u_\nu(\mathbf{r})v_\nu(\mathbf{r})^*\left[1-2f(E_\nu)\right]. \tag{38}$$

The quantities $\mathcal{I}_{ij}(\mathbf{r})$ that enter the left-hand side of this equation are defined as follows:

$$\mathcal{I}_{ij}(\mathbf{r}) = \int_{|\mathbf{k}|>k_c(\mathbf{r})}\frac{d\mathbf{k}}{(2\pi)^3}\frac{\left(\frac{\mathbf{k}^2}{2m}\right)^i}{\left(\frac{\mathbf{k}^2}{2m}+V_{\rm ext}(\mathbf{r})-\mu\right)^j}. \tag{39}$$

The right-hand side of Eq. (38), which results from an explicit numerical integration of the BdG equations over the reduced energy range $E_\nu < E_c - \mu$, acts as a *source term* on the non-linear differential equation for $\Delta(\mathbf{r})$ associated with the left-hand side. By implementing the numerical calculation of the BdG equations for an isolated vortex embedded in a uniform superfluid, it was shown in Ref. [78] that the inclusion of the various terms on the left-hand side of Eq. (38) [from the linear (Δ) term, to the linear plus cubic ($\Delta+\Delta^3$) terms, and finally to the linear plus cubic plus Laplacian ($\Delta+\Delta^3+\nabla^2$) terms] plays an increasingly important role in reducing the total computational time and memory space at any coupling throughout the BCS–BEC crossover, by decreasing the value of the cutoff E_c up to which the eigenfunctions of the BdG equations have to be explicitly calculated [78].

In practice, the BdG equations have been solved numerically up to self-consistency only for relatively simple geometries since their numerical solution becomes rapidly too demanding due to computational time and memory space. For ultracold Fermi gases, the BdG equations have been solved to account for the spatial dependence of the order parameter in balanced [76,77,80] and imbalanced [81,82] trapped gases, as well as for the microscopic structure of a single vortex at zero temperature on the BCS side [83] and across the BCS–BEC crossover [84], and also at finite temperature across the BCS–BEC crossover [78]. The microscopic structure of a single vortex for the unitary Fermi gas has been analyzed in Ref. [85] with BdG-like equations resulting from the superfluid local-density approximation of Ref. [86], which has later been used also to calculate the profile of the order parameter in balanced trapped gases [87] or in the FFLO phase of imbalanced Fermi gases throughout the BCS–BEC crossover [88] (see Section 2.6). In addition, the BdG equations have been used to determine the occurrence of vortex lattices in a rotating trap on the BCS side of the crossover [89,90]. A study of the Josephson effect with a one-dimensional barrier throughout the BCS–BEC crossover at zero temperature [60] will be reported in Section 4.6.

In nuclear physics, where in the most sophisticated cases finite-range (instead of zero-range) forces are used in the mean-field and gap equations (a famous example in this context being the Gogny-force [91]), both matrix elements in (32) become non-local. The corresponding equations, usually referred to as the Hartree–Fock–Bogoliubov (HFB) equations, are thus more general than the BdG equations and read (for simplicity, we do not write down the spin and isospin structure):

$$\int d\mathbf{r}'\begin{pmatrix}\mathcal{H}(\mathbf{r},\mathbf{r}') & \Delta(\mathbf{r},\mathbf{r}')\\ \Delta^*(\mathbf{r},\mathbf{r}') & -\mathcal{H}^*(\mathbf{r},\mathbf{r}')\end{pmatrix}\begin{pmatrix}u_\nu(\mathbf{r}')\\ v_\nu(\mathbf{r}')\end{pmatrix} = E_\nu\begin{pmatrix}u_\nu(\mathbf{r})\\ v_\nu(\mathbf{r})\end{pmatrix} \tag{40}$$

where

$$\mathcal{H}(\mathbf{r},\mathbf{r}') = \left[-\frac{\nabla^2_{\mathbf{r}}}{2m}+\Gamma_{\rm H}(\mathbf{r})\right]\delta(\mathbf{r}-\mathbf{r}')+\Gamma_{\rm F}(\mathbf{r},\mathbf{r}') \tag{41}$$

and

$$\Delta(\mathbf{r},\mathbf{r}') = -V_{\rm eff}(\mathbf{r}-\mathbf{r}', n(\tfrac{\mathbf{r}+\mathbf{r}'}{2}))\sum_\nu u_\nu(\mathbf{r})v_\nu(\mathbf{r}')^*[1-2f(E_\nu)]. \tag{42}$$

In the above expressions, $\Gamma_{\rm H}(\mathbf{r}) = \int d\mathbf{r}' V_{\rm eff}(\mathbf{r},\mathbf{r}')\,n(\mathbf{r}')$ and $\Gamma_{\rm F}(\mathbf{r},\mathbf{r}') = -V_{\rm eff}(\mathbf{r},\mathbf{r}')\,n(\mathbf{r},\mathbf{r}')$ are the Hartree and Fock fields, respectively, with the density matrix given by $n(\mathbf{r},\mathbf{r}') = \sum_\nu v_\nu(\mathbf{r})v_\nu^*(\mathbf{r}')$ (such that $n(\mathbf{r}) = n(\mathbf{r},\mathbf{r})$ is the number density). In nuclear physics, the phenomenological effective forces are generally density dependent, also in the pairing channel, as indicated in the argument of $V_{\rm eff}$ in Eq. (42).

The non-local HFB equations (40), that hold for finite nuclei, are numerically much harder to solve than the local BdG equations (32). Yet, they are almost routinely solved even for deformed and rotating nuclei, in general the results of the calculations being in excellent agreement with experiments (see Refs. [92,93] for reviews). Owing to the high numerical cost to solve these equations, however, approximate local approximations have been developed for the mean-field terms of Eq. (41) (such as the Skyrme Energy Density Functionals (EDF) [94]) and for the pairing interaction of Eq. (42).

The need to regularize the gap equation arises also for the nuclear problem. In this context, it is worth mentioning that the renormalization scheme of Eq. (35) discussed above was originally developed in Refs. [66,67] for the nuclear problem, in the case when the gap equation reduces to a local form. In this case, Eqs. (36) and (37) are replaced by an effective coupling constant which takes the form:

$$\frac{1}{g_{\rm eff}(\mathbf{r})} = \frac{1}{g(\mathbf{r})} - \frac{m^*(\mathbf{r})}{2\pi^2}\left[k_c(\mathbf{r}) - \frac{k_\mu(\mathbf{r})}{2}\ln\frac{k_c(\mathbf{r})+k_\mu(\mathbf{r})}{k_c(\mathbf{r})-k_\mu(\mathbf{r})}\right]. \tag{43}$$

Here, in contrast to Eqs. (36) and (37), the effective mass $m^*(\mathbf{r})$ and the bare coupling constant $g(\mathbf{r})$ are now position dependent through the value of the local density, which can be fitted such that Δ_0 as a function of k_F reproduces the gap obtained with the Gogny force [65] in infinite matter. In addition, the wave vectors $k_\mu(\mathbf{r})$ and $k_c(\mathbf{r})$ are now related to the chemical potential μ and energy cutoff E_c by $\mu = \frac{k_\mu^2(\mathbf{r})}{2m^*(\mathbf{r})} + U(\mathbf{r})$ and $E_c = \frac{k_c^2(\mathbf{r})}{2m^*(\mathbf{r})} + U(\mathbf{r})$, where $U(\mathbf{r})$ is the self-consistent mean-field potential (given, for instance, by the Skyrme EDF) which takes the place of the trapping potential $V_{\rm ext}(\mathbf{r})$ of Eqs. (36) and (37)

Finally, it is worth mentioning that the information contained in the BdG and HFB equations [Eqs. (32) and (40), respectively] can be cast in an integral form in terms of the (single-particle) Gor'kov propagators, from which one can better appreciate also the particle–hole mixing characteristic of the pairing theory. These propagators read:

$$\hat{\mathcal{G}}(\mathbf{r},\mathbf{r}';\omega_n) = \sum_\nu \begin{bmatrix} u_\nu(\mathbf{r}) \\ v_\nu(\mathbf{r}) \end{bmatrix} \frac{1}{i\omega_n - E_\nu} \left[u_\nu^*(\mathbf{r}'), v_\nu^*(\mathbf{r}')\right] + \sum_\nu \begin{bmatrix} -v_\nu^*(\mathbf{r}) \\ u_\nu^*(\mathbf{r}) \end{bmatrix} \frac{1}{i\omega_n + E_\nu} \left[-v_\nu(\mathbf{r}'), u_\nu(\mathbf{r}')\right] \tag{44}$$

where $\omega_n = (2n+1)\pi T$ (n integer) is a fermionic Matsubara frequency and the sums are limited to $E_\nu > 0$. In the matrix (44), the diagonal (off-diagonal) elements correspond to the normal (anomalous) Gor'kov propagator [95]. Upon taking the analytic continuation $i\omega_n \to \omega + i\eta$ ($\eta = 0^+$) to the real frequency ω, the two terms on the right-hand side of the expression (44) give rise to the particle and hole components of the spectral function, which are peaked about the poles at $\omega = +E_\nu$ and $\omega = -E_\nu$, respectively, and have their weights expressed in terms of $u_\nu(\mathbf{r})$ and $v_\nu(\mathbf{r})$. We shall return to this issue in Section 3.3.

2.5. Ginzburg–Landau and Gross–Pitaevskii equations

There are cases when the BdG equations (32) can be replaced by suitable non-linear differential equations for the gap parameter $\Delta(\mathbf{r})$, which are somewhat easier to solve numerically and conceptually more appealing than the BdG equations themselves. These non-linear differential equations for $\Delta(\mathbf{r})$ are the Ginzburg–Landau (GL) equation for the Cooper-pair wave function and the Gross–Pitaevskii (GP) equation for the condensate wave function of composite bosons. As a matter of fact, it turns out that the GL and GP equations can be microscopically derived from the BdG equations in two characteristic limits; namely, the GL equation in the weak-coupling (BCS) limit close to T_c [96] and the GP equation in the strong-coupling (BEC) limit at $T = 0$ [79]. In both cases, the integral form (44) of the (single-particle) Gor'kov propagators associated with the solutions of the BdG equations provides the starting point for the microscopic derivation of these non-linear differential equation for $\Delta(\mathbf{r})$.

In particular, one obtains the GL equation for strongly overlapping Cooper pairs through an expansion of the expression (44) in terms of the small parameter $|\Delta(\mathbf{r})|/T_c$ [96], in the form:

$$\left\{\frac{(i\nabla + 2\mathbf{A}(\mathbf{r}))^2}{4m} + \frac{6\pi^2 T_c^2}{7\zeta(3)E_F}\left[\left(1 - \frac{\pi}{4k_F a_F}\right)\frac{V_{\rm ext}(\mathbf{r})}{E_F} - \left(1 - \frac{T}{T_c}\right)\right]\right\}\Delta(\mathbf{r}) + \frac{3}{4E_F}|\Delta(\mathbf{r})|^2\Delta(\mathbf{r}) = 0 \tag{45}$$

where $\zeta(3) \approx 1.202$ is the Riemann ζ function of argument 3. [For the meaning of the vector potential $\mathbf{A}$, see below.] In the presence of the trapping (harmonic) potential $V_{\rm ext}(\mathbf{r})$, the values of the critical temperature T_c and of the Fermi wave vector k_F correspond to those of a uniform system with density equal to that at the center of the trapped system. This extra term did not appear in the original Gor'kov derivation of the GL equation [96] and was first considered in Ref. [97]. A simple way to derive it is by following the method of Ref. [98] and adopting a local-density approximation in the expression of the regularized particle–particle bubble given by Eq. (82). Upon replacing in this expression $E_F \to (E_F - V_{\rm ext}(\mathbf{r}))$ and expanding to linear order in the small quantity $V_{\rm ext}(\mathbf{r})/E_F$, one readily recovers both terms within parentheses that multiply $V_{\rm ext}(\mathbf{r})/E_F$ in Eq. (45).

In addition, from the BdG equations one also obtains the GP equation for a gas of dilute composite bosons of mass $2m$ through an expansion of the expression (44) in terms of the small parameter $|\Delta(\mathbf{r})/\mu|$ [79], in the form:

$$\frac{(i\nabla + 2\mathbf{A}(\mathbf{r}))^2}{4m}\Phi(\mathbf{r}) + 2V_{\rm ext}(\mathbf{r})\Phi(\mathbf{r}) + \frac{8\pi a_F}{2m}|\Phi(\mathbf{r})|^2\Phi(\mathbf{r}) = \mu_B\Phi(\mathbf{r}). \tag{46}$$

Here, $\Phi(\mathbf{r}) = \sqrt{\frac{m^2 a_F}{8\pi}}\Delta(\mathbf{r})$ is the condensate wave function expressed in terms of the gap parameter $\Delta(\mathbf{r})$ and μ_B is the residual chemical potential of the composite bosons, defined by $2\mu = -\varepsilon_0 + \mu_B$ with $\mu_B \ll \varepsilon_0 = (ma_F^2)^{-1}$ in the relevant BEC limit ($a_F > 0$). Note in this context that the GP equation (46) could also be obtained from the regularized gap equation (38) discussed in Section 2.4, in the BEC limit when $|\mu|$ is the largest energy scale in the problem such that E_c (and thus k_c)

can be taken to vanish. In this limit, the source term on the right-hand side of Eq. (38) can be neglected while the coefficients on the left-hand side become $\mathcal{R} = \frac{m}{4\pi a_F} - \frac{m^2 a_F}{8\pi}\,\mu_B, \mathcal{I}_{02} = \frac{m^2 a_F}{2\pi}, \mathcal{I}_{13} = \frac{3m^2 a_F}{8\pi}$, and $\mathcal{I}_{03} = \frac{m^3 a_F^3}{4\pi}$, such that Eq. (46) with $\mathbf{A}(\mathbf{r}) = 0$ is recovered from Eq. (38).

Since we are here concerned with superfluidity of neutral particles, in Eqs. (45) and (46) the vector potential $\mathbf{A}(\mathbf{r})$ is meant to describe rotating systems and is accordingly given by $\mathbf{A}(\mathbf{r}) = m\,\boldsymbol{\Omega} \times \mathbf{r}$ where $\boldsymbol{\Omega}$ is the angular velocity of the rotating trap. [In this case, the quadratic term in $\mathbf{A}(\mathbf{r})$ should be omitted from the kinetic energy.] At the same time, the factor of 2 in front of the vector potential $\mathbf{A}(\mathbf{r})$ in Eqs. (45) and (46) (as well as of the external (trapping) potential $V_{\rm ext}(\mathbf{r})$ in Eq. (46)) reflects the composite nature of Cooper pairs and bosons in the two (GL and GP) situations. In practice, the independent solutions of the GL and GP equations (45) and (46) represent useful benchmarks for the numerical results of the BdG equations for the local gap parameter $\Delta(\mathbf{r})$, in the respective (BCS and BEC) limits of the BCS–BEC crossover.

2.6. Spin-imbalanced (polarized) systems

The effect of spin-population imbalance ("polarization") on superconductivity was first addressed shortly after the formulation of BCS theory [99–103]. In these works, the spin-population imbalance was assumed to be produced by an external magnetic field acting only on the spins of the electrons, while the orbital effects were completely neglected. This assumption requires quite stringent conditions on superconductors, which, in practice, have made the experimental study of this issue in condensed-matter systems an extremely difficult task (see Ref. [104] for a review). In nuclear matter, the problem of pairing in population-imbalanced Fermi gases naturally arises because most of the heavier nuclei have more neutrons (n) than protons (p), and the same is true for nuclear matter in proto-neutron stars. In nuclear physics, one quite generally refers in this context to *asymmetric nuclear matter*. In the context of deuteron-like Cooper pairs, several works deal with this problem also with respect to the BCS–BEC crossover [21,23,105] (cf. Section 5.2). This problem has also been studied in the context of dense quark matter [106,107].

Recently, great interest in population-imbalanced Fermi gases has been prompted by experiments with two-component ultra-cold Fermi gases, for which the populations of different "spin" states (that correspond to different atomic hyperfine states) can be controlled independently of orbital effects. In addition, and similarly to the situation in nuclear matter, these populations are separately conserved, owing to the long relaxation time associated with the processes that change the hyperfine state of an atom. The first two experiments with imbalanced ultra-cold Fermi gases [108,109] have stimulated a large theoretical activity on these systems over the last several years. Detailed reviews of the recent theoretical and experimental activity on population-imbalanced ultra-cold Fermi gases can be found in Refs. [52] and [53]. Below, we will first describe the historical approaches to the problem of an imbalanced Fermi gas as related to conventional (weak-coupling) superconductors, and then we will deal with the more recent connection of this problem to the BCS–BEC crossover for arbitrary couplings.

The BCS mean-field approximation, that was discussed in the previous Sections for a balanced system, can be readily generalized to the presence of different spin populations (and thus of different chemical potentials). For a contact interaction, the gap equation (8) is modified as follows

$$-\frac{m}{4\pi a_F} = \int \frac{d\mathbf{k}}{(2\pi)^3}\left(\frac{1 - f(E^+_{\mathbf{k}}) - f(E^-_{\mathbf{k}})}{2E_{\mathbf{k}}} - \frac{m}{\mathbf{k}^2}\right), \tag{47}$$

while the number equation (9) splits into an equation for the total density

$$n_\uparrow + n_\downarrow = \int \frac{d\mathbf{k}}{(2\pi)^3}\left(1 - \frac{\xi_{\mathbf{k}}}{E_{\mathbf{k}}}\left[1 - f(E^+_{\mathbf{k}}) - f(E^-_{\mathbf{k}})\right]\right) \tag{48}$$

and an equation for the difference between the two densities:

$$n_\uparrow - n_\downarrow = \int \frac{d\mathbf{k}}{(2\pi)^3}\left[f(E^+_{\mathbf{k}}) - f(E^-_{\mathbf{k}})\right]. \tag{49}$$

Here, $E_{\mathbf{k}} = \sqrt{\xi^2_{\mathbf{k}} + |\Delta|^2}$ with $\xi_{\mathbf{k}} = (\xi_{\mathbf{k}\uparrow} + \xi_{\mathbf{k}\downarrow})/2$, and $E^\pm_{\mathbf{k}} = E_{\mathbf{k}} \pm \delta\xi_{\mathbf{k}}$ with $\delta\xi_{\mathbf{k}} = (\xi_{\mathbf{k}\uparrow} - \xi_{\mathbf{k}\downarrow})/2$, where $\xi_{\mathbf{k}\sigma} = k^2/(2m) - \mu_\sigma$ is the single particle energy relative to the chemical potential μ_σ for the spin $\sigma = (\uparrow, \downarrow)$. One sees from Eq. (49) that at $T = 0$ the difference $(n_\uparrow - n_\downarrow)$ between the two densities is finite, provided there is a region of $\mathbf{k}$-space where one of the two single-particle excitation energies $E^\pm_{\mathbf{k}}$ becomes negative. In terms of the field $h = (\mu_\uparrow - \mu_\downarrow)/2$ such that $E^\pm_{\mathbf{k}} = E_{\mathbf{k}} \mp h$, one has that $n_\uparrow > n_\downarrow$ provided $h > \min E_{\mathbf{k}}$ (for definiteness, in the following we shall assume $h > 0$ such that spin-$\uparrow$ fermions correspond to the majority species). In addition, it can be verified that at $T = 0$ the above Eqs. (47)–(49) correspond to the following ground-state wave function [23]:

$$|\Phi_{\rm S}\rangle = \prod_{\mathbf{k}\in\mathcal{R}} c^\dagger_{\mathbf{k}\uparrow} \prod_{\mathbf{k}\notin\mathcal{R}} (u_{\mathbf{k}} + v_{\mathbf{k}} c^\dagger_{\mathbf{k}\uparrow} c^\dagger_{-\mathbf{k}\downarrow})\,|0\rangle \tag{50}$$

where $u_{\mathbf{k}}$ and $v_{\mathbf{k}}$ are defined in terms of $\xi_{\mathbf{k}}$ and $E_{\mathbf{k}}$ as in Eq. (2) for the balanced case. In the expression (50), the region $\mathcal{R}$ of $\mathbf{k}$-space with $E^+_{\mathbf{k}} < 0$ is fully occupied by the $\uparrow$-fermions of the majority species, while outside this region Cooper pairing

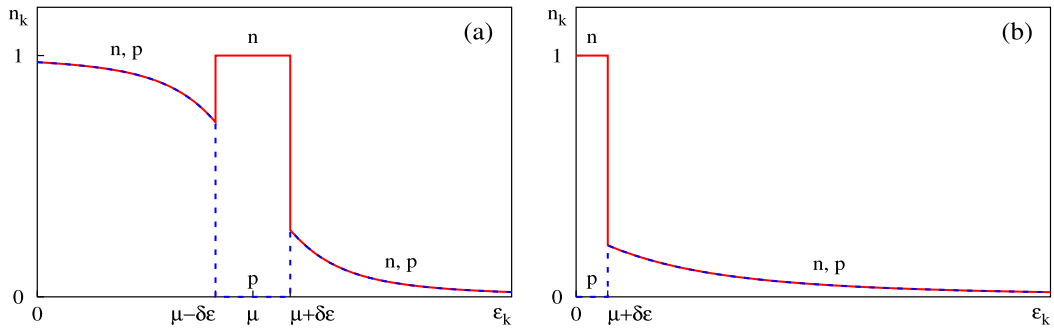

Fig. 4. Schematic representation of the occupation number of neutrons $n =\uparrow$ (full line) and protons $p =\downarrow$ (dashed line) as a function of the energy ε_k in asymmetric ($n_n > n_p$) nuclear matter with proton–neutron pairing, for (a) $\mu > \delta\varepsilon$ and (b) $\mu < \delta\varepsilon$. Here, $\mu = (\mu_\uparrow + \mu_\downarrow)/2$ and $\delta\varepsilon = \sqrt{h^2 - \Delta^2}$, with $h = (\mu_\uparrow - \mu_\downarrow)/2$.

occurs. The fact that the states in the region $\mathcal{R}$ are no longer available for pairing is called "blocking effect" in nuclear physics. The state $|\Phi_S\rangle$ (referred to either as the "Sarma" state from the original work by Sarma [101] or as the "breached-pair" phase from the more recent work of Ref. [110–112]) by Wilczek and co-workers accommodates at the same time superfluidity and a finite population imbalance, through a sort of phase separation in $\mathbf{k}$-space between one region which is unpolarized and superfluid and a second region which is fully polarized and normal. Depending on the value of $\mu = (\mu_\uparrow + \mu_\downarrow)/2$, the normal region $\mathcal{R}$ is enclosed by two (when $\mu > \delta\varepsilon$), or one (when $\mu < \delta\varepsilon$) Fermi surfaces with gapless single-particle excitations, where $\delta\varepsilon = \sqrt{h^2 - \Delta^2}$. The state (50) thus corresponds to a gapless superfluid. As an example of the breached-pair phase, Fig. 4 shows a schematic picture of the occupation number for protons and neutrons in asymmetric nuclear matter (which can be transferred to the case of a spin-imbalanced system by replacing the labels n and p with $\uparrow$ and $\downarrow$, respectively). The two panels of Fig. 4 distinguish the two cases with (a) $\mu > \delta\varepsilon$ and (b) $\mu < \delta\varepsilon$. In both cases, one sees that there is a window of energies with unpaired occupancies for the extra neutrons. This problem will be further elaborated in Section 5.2.

A problem with the Sarma state (50) in weak coupling is that it is energetically unstable, since it corresponds to a local maximum of the variational energy at $T = 0$ [101]. Specifically, by solving the gap equation (47) in the weak-coupling limit one finds that $\Delta(h)$ shows a re-entrant behavior below a certain temperature T_0, while at high enough temperature $\Delta(h)$ decreases monotonically with h and vanishes continuously at a critical value of h. The Sarma state is then associated with this re-entrant branch at $T = 0$. An analogous re-entrant behavior is found for the dependence of the critical temperature on h, which is obtained by letting $\Delta \to 0$ in the gap equation (47) (as shown by the full line in Fig. 5(a)). Comparison between the (grand-canonical) free energies of the normal and superfluid phases shows, however, that below the temperature T_0 (=$0.56T_c^0$ in weak coupling) the transition becomes of first order, with the gap dropping discontinuously to zero at the transition. Correspondingly, the transition curve eliminates completely the re-entrant behavior below T_0 (as shown by the dashed curve in Fig. 5(a)). An analysis along these lines made by Sarma at $T = 0$ [101] recovered the Clogston [99] and Chandrasekhar [100] prediction of a first-order transition at $h = \Delta_0/\sqrt{2}$, from an unpolarized BCS state (when $h < \Delta/\sqrt{2}$) to a polarized normal state (when $h > \Delta_0/\sqrt{2}$).

An alternative solution to the problem of superconductivity (superfluidity) in the presence of spin imbalance was proposed by Fulde and Ferrell (FF) [102] and independently by Larkin and Ovchinnikov (LO) [103]. The basic idea is that a mismatch of the spin-up and spin-down Fermi surfaces due to spin imbalance should favor Cooper pairing for a finite value of the center-of-mass wave vector $\mathbf{Q}$. This is because, by taking $|\mathbf{Q}|$ of the order of $(k_{F\uparrow} - k_{F\downarrow})$, the pairing states $|\mathbf{k} + \mathbf{Q}/2, \uparrow\rangle$ and $|-\mathbf{k} + \mathbf{Q}/2, \downarrow\rangle$ remain in the vicinity of both Fermi surfaces. Specifically, this matching occurs only on one side of the respective Fermi surfaces as determined by $\mathbf{Q}$ itself, while on the other side pairing is completely suppressed. A non-vanishing value of the polarization is then obtained by making these regions completely empty/filled with $\downarrow/\uparrow$ fermions, respectively. In addition, pair condensation at finite $\mathbf{Q}$ leads to a space-dependent order parameter $\Psi(\mathbf{r}) = \langle\psi_\uparrow(\mathbf{r})\psi_\downarrow(\mathbf{r})\rangle$ (where $\psi_\sigma(\mathbf{r})$ is a fermion field operator with spin σ), which is given by a single plane wave $\Psi(\mathbf{r}) = \psi_0 e^{i\mathbf{Q}\cdot\mathbf{r}}$ in the Fulde–Ferrell analysis and by a superposition of plane waves with the same $|\mathbf{Q}|$ in the Larkin–Ovchinnikov analysis (in particular, the solution $\Psi(\mathbf{r}) = \psi_0 \cos(\mathbf{Q}\cdot\mathbf{r})$ was considered).

The above mean-field equations (47)–(49) are readily extended to take into account the FF pairing. By setting $\Delta_{\mathbf{Q}} e^{i\mathbf{Q}\cdot\mathbf{r}} \equiv -\int \frac{d\mathbf{k}}{(2\pi)^3} v_0 \langle c_{-\mathbf{k}+\mathbf{Q}/2\downarrow} c_{\mathbf{k}+\mathbf{Q}/2\uparrow}\rangle$, the gap equation is modified as follows:

$$-\frac{m}{4\pi a_F} = \int \frac{d\mathbf{k}}{(2\pi)^3}\left(\frac{1 - f(E^+_{\mathbf{k},\mathbf{Q}}) - f(E^-_{\mathbf{k},\mathbf{Q}})}{2E_{\mathbf{k},\mathbf{Q}}} - \frac{m}{\mathbf{k}^2}\right) \tag{51}$$

where $E_{\mathbf{k},\mathbf{Q}} = \sqrt{\xi^2_{\mathbf{k},\mathbf{Q}} + |\Delta_{\mathbf{Q}}|^2}$ with $\xi_{\mathbf{k},\mathbf{Q}} = (\xi_{\mathbf{k}+\mathbf{Q}/2\uparrow} + \xi_{-\mathbf{k}+\mathbf{Q}/2\downarrow})/2$, and $E^\pm_{\mathbf{k},\mathbf{Q}} = E_{\mathbf{k},\mathbf{Q}} \pm \delta\xi_{\mathbf{k},\mathbf{Q}}$ with $\delta\xi_{\mathbf{k},\mathbf{Q}} = (\xi_{\mathbf{k}+\mathbf{Q}/2\uparrow} - \xi_{-\mathbf{k}+\mathbf{Q}/2\downarrow})/2$. Similarly to the gap equation (51), the number equations for the FF phase are obtained from the corresponding equations (48) and (49) of the Sarma phase via the replacements $(\xi_{\mathbf{k}}, E_{\mathbf{k}}, E^\pm_{\mathbf{k}}) \to (\xi_{\mathbf{k},\mathbf{Q}}, E_{\mathbf{k},\mathbf{Q}}, E^\pm_{\mathbf{k},\mathbf{Q}})$. And, analogously to the Sarma phase

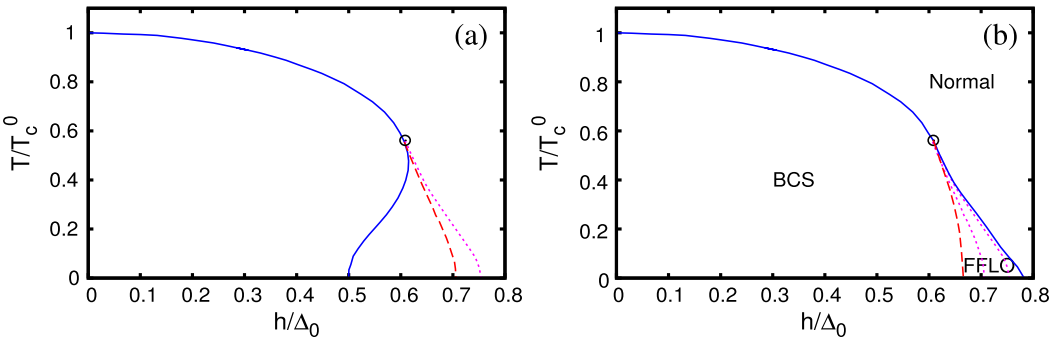

Fig. 5. (a) Phase diagram for the superfluid/normal transition in the (extreme) weak-coupling limit. The temperature is in units of the critical temperature T_c^0 for $h = 0$, and $h = (\mu_\uparrow - \mu_\downarrow)/2$ is in units of the zero-temperature gap Δ_0 at $h = 0$. Full line: solution of the equation for the critical temperature obtained by setting $\Delta = 0$ in the BCS gap equation, which corresponds to a true transition line only above the tricritical point (circle). Dashed line: first-order transition line that separates the BCS superfluid from the normal phase. Dotted line: second-order transition line between the (single $\mathbf{q}$) FF and normal phase. (b) Refined phase diagram for the superfluid/normal transition in weak coupling, where more general solutions in the FFLO phase are considered. Full line: transition line separating the superfluid from the normal phase, which becomes of first order below the tricritical point (circle) and separates the FFLO from the normal phase. Dashed line: second-order transition line that separates the BCS and FFLO phases. The transition lines BCS $\to$ FF and FF $\to$ normal obtained by the simple FF solution are also reported for comparison (dotted lines).

[cf. Eq. (49)], a finite population imbalanced is obtained at $T = 0$ when (at least) one of the two single-particle excitations $E^{\pm}_{\mathbf{k},\mathbf{Q}}$ becomes negative in a region of $\mathbf{k}$-space. Calling $\mathcal{R}_\uparrow$ and $\mathcal{R}_\downarrow$ the regions where $E^{+}_{\mathbf{k},\mathbf{q}}$ and $E^{-}_{\mathbf{k},\mathbf{q}}$ are negative, the FF solution at $T = 0$ then corresponds to the variational wave function (see, e.g., Ref. [113])

$$|\Psi_{\rm FF}\rangle = \prod_{\mathbf{k}\in\mathcal{R}_\uparrow} c^\dagger_{\mathbf{k}+\frac{\mathbf{Q}}{2}\uparrow} \prod_{\mathbf{k}\in\mathcal{R}_\downarrow} c^\dagger_{-\mathbf{k}+\frac{\mathbf{Q}}{2}\downarrow} \prod_{\mathbf{k}\notin\mathcal{R}_{\uparrow,\downarrow}} (u_{\mathbf{k}} + v_{\mathbf{k}} c^\dagger_{\mathbf{k}+\frac{\mathbf{Q}}{2}\uparrow} c^\dagger_{-\mathbf{k}+\frac{\mathbf{Q}}{2}\downarrow})|0\rangle\,, \tag{52}$$

where in the region $\mathcal{R}_\uparrow$ ($\mathcal{R}_\downarrow$) the state $|\mathbf{k} + \mathbf{Q}/2, \uparrow\rangle$ is fully occupied (empty) and the state $|-\mathbf{k} + \frac{\mathbf{Q}}{2}, \downarrow\rangle$ is fully empty (occupied), with the remaining states being available for pairing. A finite population imbalance results when the regions $\mathcal{R}_\uparrow$ and $\mathcal{R}_\downarrow$ have different volumes. Note, however, that no finite value of the current is associated with a finite value of $|\mathbf{Q}|$.

The thermodynamic stability of the FF phase, together with the value of $|\mathbf{Q}|$, are obtained by minimizing the mean-field free-energy. In weak coupling, one obtains that at $T = 0$ the Clogston–Chandrasekhar first-order transition from the BCS state to the normal phase at $h = \Delta_0/\sqrt{2}$ is replaced by a first-order transition BCS $\to$ FF at essentially the same value of h, followed by a second-order transition FF $\to$ normal when h reaches the value $h = 0.754\Delta_0$. Correspondingly, $|\mathbf{Q}|$ changes from $1.28\,(k_{F\uparrow} - k_{F\downarrow})$ at the transition BCS $\to$ FF, to $1.2(k_{F\uparrow} - k_{F\downarrow})$ at the transition FF $\to$ normal [113]. The transition FF $\to$ normal remains of second order also at finite temperature, while the transition BCS $\to$ FF is of first order and corresponds, in practice, to the transition BCS $\to$ normal, since the free energies of the FF and normal phases are quite close in value. The resulting phase diagram is reported in Fig. 5(a), where the three transition lines meet at the tricritical point with $h = 0.61\Delta_0$ and $T = 0.56T_c^0$. It turns out that the region of existence of the FF phase (in the figure delimited by the dashed and dotted lines) is quite narrow.

The assumption of a single wave vector $\mathbf{Q}$ was overcome by the LO approach [103], where a more general superposition of plane waves with the same $|\mathbf{Q}|$ was considered, corresponding in real space to a crystalline order for the order parameter $\Psi(\mathbf{r})$ (or of the gap parameter $\Delta(\mathbf{r})$). The LO analysis was based on an expansion in powers of $\Delta(\mathbf{r})$ of the Gor'kov equations for the normal and anomalous Green's functions in the presence of a Zeeman splitting between the two spin species, and thus holds only near the second-order transition where $\Delta(\mathbf{r})$ vanishes. It was found that near the transition point the solution $\Delta(\mathbf{r}) = 2\Delta\cos(\mathbf{Q}\cdot\mathbf{r})$ has lower energy than the single plane-wave FF solution, and has also the lowest energy among the crystalline solutions. It was further found that the location of the transition to the normal state is unchanged with respect to the FF analysis, since the degeneracy among the possible superpositions of plane waves with the same $|\mathbf{Q}|$ is lifted only inside the superfluid phase.

When dealing with a first-order transition, however, the power expansion of the Gor'kov equations utilized by the LO approach is not appropriate and one should resort to a full solution of the Gor'kov equations (or, equivalently, of the BdG equations) for the polarized Fermi gas. Since this is rather a difficult task, in weak coupling the problem was approached using the Eilenberger quasi-classical equations which are appropriate to this limit [114,115]. These equations have been applied to a three-dimensional polarized Fermi gas in Refs. [116] and [117], where a generic combinations of $\mathbf{Q}$ with the same value of $|\mathbf{Q}|$ was considered. In particular, the analysis of Ref. [117] shows that the transition to the normal phase is of first order from the tricritical point down to $T = 0$, although it remains very close to the standard FFLO second-order transition. At $T = 0$, the critical field for the transition to the normal phase has now the value $h = 0.781\Delta_0$, to be compared with the FFLO value $h = 0.754\Delta_0$ for which a second-order transition was assumed. Similar results were obtained by an alternative approach (valid, in principle, only close to the tricritical point) based on a GL expansion up to sixth order in Δ and

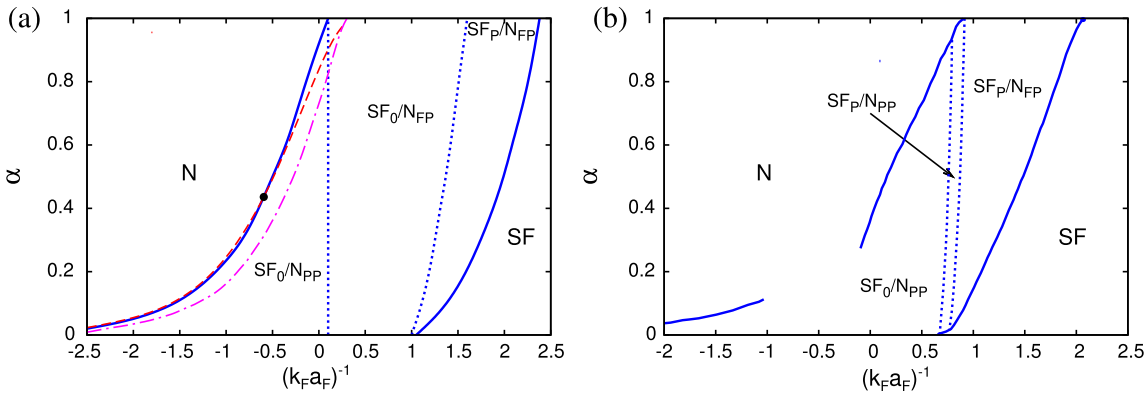

Fig. 6. (a) Mean-field $T = 0$ phase diagram for the population imbalance $\alpha = (n_\uparrow - n_\downarrow)/(n_\uparrow + n_\downarrow)$ vs the coupling parameter $(k_F a_F)^{-1}$, where k_F is determined by the total density $n = n_\uparrow + n_\downarrow$. Full lines: boundaries between the phase separation region and the homogeneous normal (N) and superfluid (SF) phases. Dotted lines: boundaries within the phase separation region between balanced superfluid and partially polarized normal state (SF_0/N_{PP}), balanced superfluid and fully polarized normal state (SF_0/N_{FP}), and polarized superfluid and fully polarized normal state (SF_P/N_{FP}). Dashed line: transition line to the FFLO phase (which does not take into account phase separation). Dashed–dotted line: normal to superfluid transition line for the Sarma phase (which is reported here regardless of its stability). (b) Corresponding phase-diagram obtained in Ref. [132] by fixed-node Quantum Monte Carlo simulations.

fourth order in $|\mathbf{Q}|$ [118–120]. An expansion up to sixth order of the GL energy functional was also considered in Ref. [121] to study the FFLO phase in the context of color superconductivity in QCD (for a review, see Refs. [106] and [107]). Owing to all these results, in weak coupling the description of the FFLO phase near the transition to the normal phase can be considered to be quite accurately described.

A similar degree of accuracy is lacking for the description of the FFLO phase away from the critical line. The reason is that, as one gets inside the superfluid phase, a single value of $|\mathbf{Q}|$ no longer suffices: $\Delta(\mathbf{r})$ remains a periodic function in space, but Fourier harmonics of higher order are required. Insights in this problem are provided by the analytic solution of the BdG equations in one dimension [122–124]. This yields an evolution, from a soliton lattice at the BCS–FFLO transition (for which the gap parameter changes its sign over a region of the order of the coherence length and then remains uniform over a region that gets progressively wider upon approaching the BCS–FFLO transition), to the ordinary LO solution at the FFLO–normal transition. A similar kind of evolution is expected to occur in higher dimensions [116]. In particular, in three dimensions the formation of a one-dimensional soliton lattice, with a period that tends to infinity at the transition point, makes the BCS–FFLO transition continuous and shifts it to lower values of h compared to the FF solution. For instance, at $T = 0$ the BCS–FFLO transition occurs at $h = 0.666\Delta_0$ [116], in contrast with $h = 0.707\Delta_0$ of the FF solution. The complete phase diagram, which takes into account the formation of a soliton lattice at the BCS–FFLO transition and the analysis of Ref. [117] (as elaborated in [53]) at the FFLO–normal transition, is reported in Fig. 5(b). One sees that, although the region for the occurrence of the FFLO phase is now enlarged with respect to the FF solution, the FFLO phase still remains confined to a small corner of the phase-diagram.

The discussion about the Sarma and FFLO phases and their stability was thus far restricted to the weak-coupling limit of the interaction. The question about what happens when this assumption is relaxed was considered only recently, stimulated by the experiments with ultra-cold Fermi gases that we now pass to consider. The first theoretical works on ultra-cold polarized Fermi gases focused on the Sarma solution, initially for weak coupling [125,126] in line with the work on the breached-pair phase of Refs. [110,111] and later on across the BCS–BEC crossover [127–130]. Also in this context, the Sarma phase turns out to be unstable against the FFLO phase or the phase separation between the unpolarized BCS phase and the polarized normal phase. Since in ultra-cold gases the spin populations are separately conserved, here phase separation is a manifestation of the (Clogston–Chandrasekhar) first-order transition discussed above for superconductors as a function of the magnetic field. The stability of the Sarma phase was further checked by looking at the sign of the superfluid density or of the compressibility matrix, which yield the spinodal curves of local stability against the FFLO phases and phase-separation [126,128,130,131].

A more complete mean-field analysis of the ground-state phase diagram for the polarized Fermi gas throughout the BCS–BEC crossover was carried out in Ref. [133], by taking into account the FF phase with a single plane wave as well as the phase-separation, while searching for the global minima of the grand-canonical potential Ω at $T = 0$. This has the form [52]:

$$\frac{\Omega}{V} = -\frac{m}{4\pi a_F}\Delta_{\mathbf{Q}}^2 + \int \frac{d\mathbf{k}}{(2\pi)^3}\left[\xi_{\mathbf{k},\mathbf{Q}} - E_{\mathbf{k},\mathbf{Q}} + \frac{m\Delta_{\mathbf{Q}}^2}{k^2} + E^+_{\mathbf{k},\mathbf{Q}}\Theta(-E^+_{\mathbf{k},\mathbf{Q}}) + E^-_{\mathbf{k},\mathbf{Q}}\Theta(-E^-_{\mathbf{k},\mathbf{Q}})\right] \tag{53}$$

where V is the volume. The resulting phase diagram is reported in Fig. 6(a) and shows that phase separation dominates, especially in the unitary regime of interest for ultra-cold gases. The polarized superfluid (Sarma) phase is stable only on the BEC side of the crossover, where it corresponds to a mixture of composite bosons and excess fermions [134]. The FFLO phase is

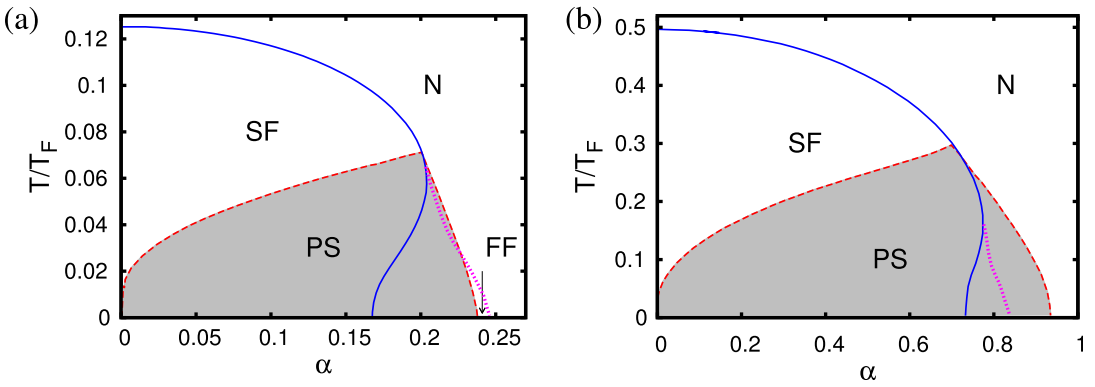

Fig. 7. Mean-field phase diagram for temperature T (in units of the Fermi temperature T_F) vs population imbalance α with the coupling values (a) $(k_F a_F)^{-1} = -1.0$ and (b) $(k_F a_F)^{-1} = 0$, where k_F and T_F are defined in terms of the total density $n = n_\uparrow + n_\downarrow$. Full line: second order transition line obtained by taking $\Delta \to 0$ in the gap equation (47). Dotted line: second order transition line to the FFLO phase. Shaded region enclosed by dashed lines: phase separation (PS) region between the superfluid (SF) and normal (N) phases. Full and dotted lines correspond to true transition lines only outside the phase separation region.
Source: Data reproduced from Refs. [50,138,139].

instead confined to a small region on the BCS side (in between the dashed and full lines on the left of the black dot in Fig. 6(a)). The previous discussion about the FFLO phase in weak coupling suggests, however, that also in this case the region of stability of the FFLO phase could be enlarged by considering more complex solutions than the FF ansatz. Work in this direction was reported in Refs. [135] and [88]. In particular, Ref. [88] suggested the occurrence of an FFLO phase over an extended range of polarizations for the unitary Fermi gas. In addition, inside the region of phase-separation Fig. 6(a) distinguishes (dotted lines) the phases made by: (i) A balanced superfluid and a partially polarized normal state (SF_0/N_{PP}); (ii) A balanced superfluid and a fully polarized normal state (SF_0/N_{FP}); (iii) A polarized superfluid and a fully polarized normal state (SF_P/N_{FP}). All these phases were obtained by minimizing the total energy with respect to different kinds of phase separation and their relative volumes (a procedure equivalent to the Maxwell construction of Ref. [136]).

For comparison, Fig. 6(b) shows the corresponding $T = 0$ phase diagram obtained in Ref. [132] by fixed-node Quantum Monte Carlo simulations (which, however, do not take into account FFLO correlations in the nodal surface of the trial wave functions). This phase diagram is qualitatively similar to that at the mean-field level of Fig. 6(a), with the polarized superfluid being stable as a homogeneous phase only on the BEC side of the crossover (albeit now somewhat closer to unitarity). At unitarity, the critical polarization above which superfluidity disappears is $\alpha_c = 0.39$, in agreement with the (extrapolated) experimental value $\alpha_c \simeq 0.36$ obtained in Ref. [137], but in contrast with the mean-field result $\alpha_c = 0.93$. This reduction of the value of α_c is expected, since the mean-field analysis neglects correlations in the normal phase and thus overestimates the extension of the BCS phase in the coexistence region. A further difference with respect to the mean-field results is the prediction of a region of coexistence between a partially polarized superfluid and a partially polarized normal phase (SF_P/N_{PP}) at the center of the phase separation region, which replaces the SF_0/N_{FP} region found at the mean-field level.

At finite temperature, the analysis of the phase diagram and of the properties of polarized superfluid Fermi gases throughout the BCS–BEC crossover requires one to include (like for a balanced system) pairing fluctuation over and above mean field. This extension will be discussed in detail in Section 3.7. Here, for future reference, Fig. 7 shows the temperature vs population imbalance phase diagram at the mean-field level for the two coupling values $(k_F a_F)^{-1} = (-1.0, 0)$ which are representative of the evolution away from weak coupling. One sees that the curve for T_c obtained by taking $\Delta \to 0$ in the gap equation (47) (and solving simultaneously the number equations (48) and (49)) presents a re-entrant behavior as a function of population imbalance α, in analogy to what was found in Fig. 5(a) in the weak-coupling limit as a function of the magnetic field h. Allowing for the FFLO pairing, but still looking for a second-order transition line by setting $\Delta_{\mathbf{Q}} \to 0$ in Eq. (51), one obtains the curves represented by dotted lines which eliminate the re-entrant behavior (as also found in weak coupling). By further allowing for phase separation between a balanced superfluid phase and a polarized normal phase, the shaded areas of Fig. 7 result [50,138,140]. One sees that, while in the weak-coupling regime of Fig. 5(a) the FFLO instability anticipates the first-order normal–superfluid transition line and merges with it at the tricritical point, as the coupling increases the FFLO second-order transition line is progressively replaced by phase separation, while the tricritical point no longer coincides with the point where the FFLO second-order transition line merges with the BCS transition line (full line in Fig. 7).

3. Pairing fluctuations

Quite generally, a consistent description of the BCS–BEC crossover cannot proceed without proper inclusion of pairing fluctuations. This is true not only in the superfluid phase below T_c where pairing fluctuations are added on top of the BCS

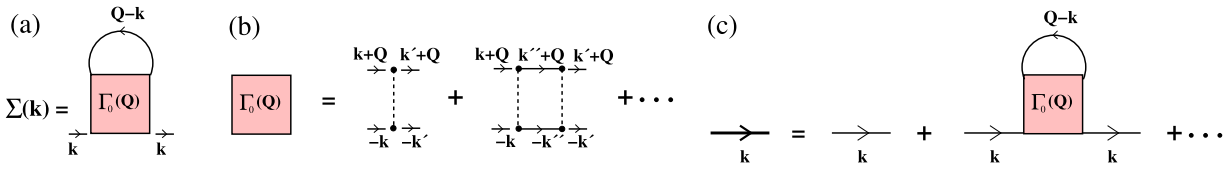

Fig. 8. Graphical representation of (a) the fermionic self-energy $\Sigma(k)$ given by Eq. (54), (b) the particle–particle propagator $\Gamma_0(Q)$ given by Eq. (55), and (c) the fermionic single-particle propagator $G(k)$ that enters the expression (59) for the density. Thick and thin lines represent, respectively, dressed ($G(k)$) and bare ($G_0(k)$) fermionic single-particle propagators, while dashed lines stand for the inter-particle interaction. The colored box identifies the particle–particle propagator $\Gamma_0(Q)$.

mean field, but it is especially relevant in the normal phase above T_c where pairing fluctuations account for important precursor effects. This Section provides a concise overview about the physical phenomena relevant to the BCS–BEC crossover, for which pairing fluctuations turn out to be mostly important.

3.1. Nozières–Schmitt-Rink approach and its extensions

It was already mentioned in Section 2.3 that, to obtain the expected value $T_{\rm BEC}$ of the Bose–Einstein critical temperature in the BEC limit of the BCS–BEC crossover, one has to include the translational degrees of freedom of the composite bosons and account for their dynamics. This, in turn, requires one to include pairing fluctuations beyond the BCS mean-field approximation. Specifically, it was clear from the analysis of Section 2.3 that, to obtain the correct value of the critical temperature T_c in the BEC limit of the BCS–BEC crossover, one needs to modify Eq. (22) for the density. To this end, one can extend the diagrammatic description of the dilute repulsive Fermi gas due to Galitskii [141] to the case of the attractive Fermi gas which undergoes the BCS–BEC crossover, along the lines of the original approach by Nozières and Schmitt-Rink (NSR) [7] (a firm basis for this extension was later discussed in Ref. [142]). In the normal phase above T_c, this amounts to considering the effects of the fermionic self-energy depicted in Fig. 8(a) which is given by the following expression:

$$\Sigma(k) = -\int \frac{d\mathbf{Q}}{(2\pi)^3}\, T \sum_{\nu} \Gamma_0(Q)\, G_0(Q-k)\,. \tag{54}$$

Here, $k = (\mathbf{k}, \omega_n)$ is a four-vector with fermionic Matsubara frequency $\omega_n = (2n+1)\pi T$ (n integer), $Q = (\mathbf{Q}, \Omega_\nu)$ is a four-vector with bosonic Matsubara frequency $\Omega_\nu = 2\pi\nu T$ (ν integer), $G_0(k) = (i\omega_n - \xi_{\mathbf{k}})^{-1}$ is the bare fermionic single-particle propagator, and Γ_0 is the particle–particle propagator (sometimes called the t-matrix or vertex of ladder diagrams) which is depicted in Fig. 8(b) and is given by the expression

$$\Gamma_0(Q) = \frac{-v_0}{1 + v_0\, \chi_{\rm pp}(Q)} = -\frac{1}{\frac{m}{4\pi a_F} + R_{\rm pp}(Q)} \tag{55}$$

where v_0 is the bare coupling constant appearing in Eq. (7),

$$\chi_{\rm pp}(Q) = \int \frac{d\mathbf{k}}{(2\pi)^3}\, T \sum_{n} G_0(\mathbf{k}+\mathbf{Q}, \omega_n + \Omega_\nu)\, G_0(-\mathbf{k}, -\omega_n) \tag{56}$$

is the particle–particle bubble, and

$$R_{\rm pp}(Q) = \chi_{\rm pp}(Q) - \int \frac{d\mathbf{k}}{(2\pi)^3}\frac{m}{\mathbf{k}^2} = \int \frac{d\mathbf{k}}{(2\pi)^3}\left(\frac{1 - f(\xi_{\mathbf{k}+\mathbf{Q}}) - f(\xi_{\mathbf{k}})}{\xi_{\mathbf{k}+\mathbf{Q}} + \xi_{\mathbf{k}} - i\Omega_\nu} - \frac{m}{\mathbf{k}^2}\right) \tag{57}$$

is the regularized version of the particle–particle bubble obtained with the help of Eq. (7). Note that the minus signs in front of the expressions (54) and (55) comply with a standard convention for the Matsubara Green's functions (cf., e.g., Ref. [95]), according to which the value $-v_0$ is associated with each diagrammatic potential line. Sometimes, however, a change of sign is adopted in the definition of Γ_0, such that at the leading order Γ_0 agrees instead with the bare potential v_0; this is, for instance, the convention used in nuclear physics (cf. Section 5).

The self-energy (54) enters the fermionic single-particle propagator

$$G(k) = \frac{1}{G_0(k)^{-1} - \Sigma(k)}\,, \tag{58}$$

in terms of which the fermionic density can be calculated as follows ($\eta = 0^+$):

$$n = 2\int \frac{d\mathbf{k}}{(2\pi)^3}\, T \sum_{n} e^{i\omega_n \eta}\, G(k)\,. \tag{59}$$

In the original NSR approach [7], on the other hand, the density was instead derived from the thermodynamic potential that is obtained by closing the ladder diagrams. As shown in Ref. [68], this corresponds to including Gaussian fluctuations

around the saddle point (the latter corresponding to the BCS mean field approximation), or to calculating the thermodynamic potential to order $1/N$ in a large-N expansion [143]. The same result can also be obtained in the present language, if one calculates the density from Eq. (59) with the additional approximation of truncating the Dyson equation (58) at first order in Σ as depicted in Fig. 8(c), thereby writing:

$$G(k) \simeq G_0(k) + G_0(k)\,\Sigma(k)\,G_0(k)\,. \tag{60}$$

The two above approximations are equivalent when the self-energy corrections are small; however, if the corrections are not small, Eq. (59) might yield a sensible result when the NSR approach does not [144]. We shall discuss below some advantages as well as disadvantages of adopting the NSR (truncated) approach (60) with respect to its extension (58) with the full single-particle propagator.

An argument in favor of the perturbative expansion (60) of the Dyson equation considers the shift of the grand-canonical potential $\Omega(T, V, \mu)$ with respect to the value $\Omega_0(T, V, \mu)$ for the non-interacting system, which quite generally is given by the following expression (cf. Eq. (25.27) of Ref. [95]):

$$\Omega - \Omega_0 = V \int_0^1 \frac{d\lambda}{\lambda} \int \frac{d\mathbf{k}}{(2\pi)^3}\, T \sum_n e^{i\omega_n \eta}\,(i\omega_n - \xi_{\mathbf{k}})\,G^{\lambda}(k)\,, \tag{61}$$

where V is the volume and the single-particle propagator G^{λ} is evaluated with the variable coupling constant λv_0. With the choice of the self-energy (54) and the perturbative expansion (60), Eq. (61) reduces to the following approximate expression

$$\Omega - \Omega_0 \cong V \int \frac{d\mathbf{Q}}{(2\pi)^3}\, T \sum_{\nu} e^{i\Omega_\nu \eta} \ln[1 + v_0\,\chi_{\rm pp}(Q)] \tag{62}$$

where $\chi_{\rm pp}$ is given by Eq. (56), which coincides with the expression derived in the original NSR approach on the basis of a linked-cluster expansion for Ω which sums up ladder diagrams [7]. This shows that the results for the grand-canonical potential, obtained from the single-particle propagator and from the linked-cluster expansion, are consistent with each other, a property which is not obvious for an approximate theory (cf., e.g., the discussion in Section 3.6 of Ref. [145]). As a consequence of this property, the derivative of Eq. (62) with respect to the chemical potential yields:

$$-\frac{\partial}{\partial \mu}\left(\frac{\Omega - \Omega_0}{V}\right)_T = n - n_0 \cong 2 \int \frac{d\mathbf{k}}{(2\pi)^3}\, T \sum_n G_0(k)^2\,\Sigma(k)\,, \tag{63}$$

which coincides with the expression (59) for the density obtained in terms of the single-particle propagator G once this is expanded as in Eq. (60).

A similar argument was made in Ref. [146] with the use of the zero-temperature formalism in the canonical ensemble [95,145]. In this case, the NSR approach corresponds to what in nuclear physics is known as the particle–particle random-phase approximation (pp-RPA) [59]. Here, the correlation energy of the ground-state is obtained from the zero-temperature counterpart of Eq. (61) (cf., e.g., Eq. (7.32) of Ref. [95]), where the expanded Dyson equation (60) is again used. Note, however, that for an attractive inter-particle interaction, the use of the NSR approach at zero temperature is physically meaningful only in the presence of a mechanism that suppresses superfluidity. In finite systems, like nuclei or ultra-small metallic grains, this occurs when the level spacing exceeds a critical value [59]. For infinite systems, on the other hand, this may occur when the system is polarized above a critical value, as discussed in Section 2.6. In this respect, it was shown in Ref. [146] that the NSR approach in the zero-temperature formalism, together with the truncation of the Dyson equation, fulfills the Luttinger theorem (see Section 3.7 for more details). Nevertheless, the truncation of the Dyson equation has some notable drawbacks. For example, within the pp-RPA at $T = 0$ the quasi-particle residue Z (associated with the discontinuity of the Fermi distribution at the Fermi surface) can become negative [147], a feature that does not occur when the self-energy is summed up to all orders. Furthermore, the shape of the single-particle spectral function (cf. Section 3.3) crucially depends on the location of the poles of the single-particle propagator in the complex frequency plane, which is of course different when the full expression (58) or its truncation (60) are adopted.

A definite virtue of the NSR approach (in both its variants) is that it interpolates for the critical temperature between two limiting cases, that is, the free Bose gas and the BCS weak-coupling limit (albeit with the some provisions for the latter case). This is because, in the BEC (strong-coupling) limit whereby $|\mu|/T \gg 1$, the particle–particle propagator Γ_0 acquires the polar form [13,148,149]:

$$\Gamma_0(Q) \simeq -\frac{8\pi}{m^2 a_F}\,\frac{1}{i\Omega_\nu - \frac{\mathbf{Q}^2}{4m} + \mu_B} \tag{64}$$

which (apart from the presence of the residue $-8\pi/(m^2 a_F)$) is equivalent to a bare bosonic propagator with mass $2m$ and chemical potential $\mu_B = 2\mu + \varepsilon_0$, where $\varepsilon_0 = (m a_F^2)^{-1}$ is the dimer binding energy. In this limit, $|\mu|$ is the largest energy scale in the fermionic propagator G_0, in such a way that one can neglect the Q-dependence of G_0 in Eq. (54) and obtain:

$$\Sigma(k) \simeq -\,G_0(-k) \int \frac{d\mathbf{Q}}{(2\pi)^3}\, T \sum_{\nu} e^{i\Omega_\nu \eta}\,\Gamma_0(Q) \qquad (\eta = 0^+)\,. \tag{65}$$

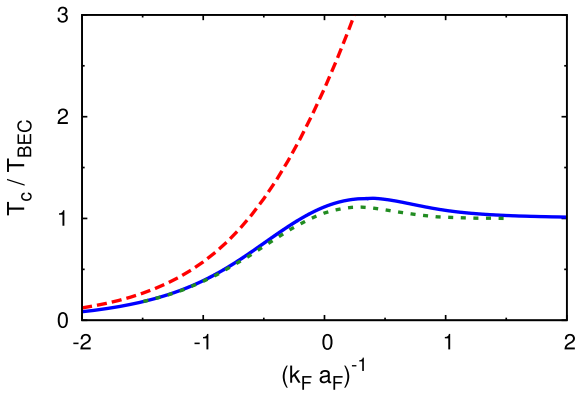

Fig. 9. Critical temperature T_c for the superfluid transition vs the coupling parameter $(k_F a_F)^{-1}$, as obtained by solving the density equation with the fermionic single-particle propagator that includes (full line) or neglects (dashed line) the self-energy (54). The NSR result, where the approximation (60) is further adopted in the density equation, is also reported for comparison (dotted line).

With the approximation (60), one thus ends up with the following expression for the density (59):

$$n \simeq 2\int \frac{d\mathbf{k}}{(2\pi)^3}\, T\sum_n e^{i\omega_n\eta}\, G_0(k) - 2\int \frac{d\mathbf{k}}{(2\pi)^3}\, T\sum_n G_0^2(k)\, G_0(-k)\int \frac{d\mathbf{Q}}{(2\pi)^3}\, T\sum_\nu e^{i\Omega_\nu\eta}\, \Gamma_0(Q) \tag{66}$$

where the first term on the right-hand side can be neglected since $|\mu|/T \gg 1$ (this holds true provided the value of T_c we are after is finite). When substituting the polar form (64) for Γ_0 in the second term on the right-hand side of Eq. (66), one sees that the factor

$$\int \frac{d\mathbf{k}}{(2\pi)^3}\, T\sum_n G_0^2(k)\, G_0(-k) \simeq -\frac{m^2}{8\pi\sqrt{2m|\mu|}} \simeq -\frac{m^2 a_F}{8\pi} \tag{67}$$

cancels the residue of the expression (64). One is thus left with the following Bose-like expression for the density:

$$n \simeq 2\int \frac{d\mathbf{Q}}{(2\pi)^3}\, \frac{1}{\exp(\xi^B_{\mathbf{Q}}/T)-1} \equiv 2\, n_B \tag{68}$$

where $\xi^B_{\mathbf{Q}} = \mathbf{Q}^2/(4m) - \mu_B$, with n_B playing the role of the density of a system of non-interacting composite bosons with mass $2m$. The correct value of the Bose–Einstein temperature $T_{\rm BEC} = 3.31\, n_B^{2/3}/(2m)$ then results by letting $\mu_B \to 0^-$ in the expression (68). In the BCS (weak-coupling) limit, on the other hand, at the leading order the self-energy (54) approaches the mean-field value $\Sigma_0 = \frac{4\pi a_F}{m}\frac{n}{2}$ and the BCS result (23) for T_c is recovered, *provided* the mean-field shift Σ_0 is also self-consistently included in the fermion propagators entering Γ_0 (see Refs. [150–152] for a discussion about the importance of including this shift in the weak-coupling limit). It should be noted that the NSR approach in its original formulation, which does not include the mean-field shift Σ_0, recovers the BCS result (23) for T_c in the weak-coupling limit only with logarithmic accuracy (specifically, it yields the result (23) divided by a "spurious" factor $e^{1/3}$). In this limit, however, particle–hole (rather than particle–particle) effects are known to be important and modify the pre-factor in front of the exponential dependence in (23), as it will be discussed in Section 3.4.

Quite generally, for generic values of the coupling parameter $(k_F a_F)^{-1}$ throughout the BCS–BEC crossover, the density equation (59) with Σ and G given by Eqs. (54) and (58) can be solved numerically in conjunction with Eq. (21), to yield T_c and $\mu(T_c)$ as functions of $(k_F a_F)^{-1}$. Fig. 9 compares the values of T_c obtained by using the full G in the density equation that includes pairing fluctuations through the self-energy Σ of Eq. (54) (full line), and the corresponding mean-field values of T_c where the bare G_0 is instead used in the density equation (dashed line). The two results are seen to strongly deviate from each other on the BEC side of the crossover where $(k_F a_F)^{-1} \gtrsim 1$. If we consider for all couplings (and not only in the BEC limit as we did in Section 2.3) the mean-field critical temperature to represent a sort of "pair dissociation temperature" T^*, the above result indicates that, while in weak coupling fermion pairs form and condense at the same temperature (that is, $T^* \simeq T_c$), in strong coupling pair formation occurs at a temperature higher than the condensation temperature (that is, $T^* \gg T_c$). The difference between T_c and T^*, which naturally arises within a pairing-fluctuation scenario, points to the presence of precursor pairing phenomena (like the pseudo-gap effects to be discussed below in Section 3.3) at temperatures intermediate between T_c and T^*.

A few additional comments on the structure of the particle–particle propagator $\Gamma_0(Q)$ are in order. At any coupling, $\Gamma_0(Q)$ admits a spectral representation of the form [151,153]:

$$\Gamma_0(\mathbf{Q}, \Omega_\nu) = -\int_{-\infty}^{+\infty} \frac{d\omega}{\pi}\, \frac{\mathrm{Im}\,\Gamma_0^R(\mathbf{Q}, \omega)}{i\Omega_\nu - \omega} \tag{69}$$

where the retarded particle–particle propagator (or vertex function) $\Gamma_0^R(\mathbf{Q},\omega)$ is defined by $\Gamma_0(\mathbf{Q},\Omega_\nu)$ given by the expressions (55)–(57) in which one makes the replacement $i\Omega_\nu \to \omega + i\eta$. With this replacement, it appears that the expression (57) has a branch cut in the complex ω-plane for $\omega \geq \frac{\mathbf{Q}^2}{4m} - 2\mu$, whose branch point at $\omega = \frac{\mathbf{Q}^2}{4m} - 2\mu$ is pushed to large positive values in the BEC limit when $-2\mu \to \varepsilon_0 - \mu_B$. In this limit, $\Gamma_0^R(\mathbf{Q},\omega)$ shows a pole at $\omega = \frac{\mathbf{Q}^2}{4m} - \mu_B$, such that $\mathrm{Im}\,\Gamma_0^R(\mathbf{Q},\omega) = \frac{8\pi^2}{m^2 a_F}\delta(\omega - \frac{\mathbf{Q}^2}{4m} + \mu_B)$ and the spectral representation (69) reduces to the previous result (64). Away from the BEC limit, however, the branch cut of $\Gamma_0^R(\mathbf{Q},\omega)$ in the complex ω-plane plays in practice an important role, which is related on physical grounds to the fermionic nature of the constituent particles. This fermionic nature actually manifests itself even in the BEC limit, when calculating the residual interaction which acts among the composite bosons (cf. Section 3.6).

It is also worth emphasizing that, for a zero-range interaction potential, it is the regularization (7) that makes the infinite summation of the particle–particle bubble (56) (which yields eventually the particle–particle propagator Γ_0 of Eq. (55)) to remain finite in the limit $v_0 \to 0$ and $k_0 \to \infty$, because the ultraviolet divergence of the expression (56) is compensated by the simultaneous vanishing of v_0 [149]. An analogous mechanism works also for the normal and anomalous particle–particle bubbles that are present below T_c [154]. As a consequence, the only diagrammatic structures that survive the regularization procedure (7) are those which are built directly on the particle–particle propagator Γ_0 and not on the bare potential v_0 (the only exception to this rule occurs below T_c for the BCS diagram of the gap equation, where the trace of the anomalous single-particle Green's function itself diverges in the ultraviolet [151,153]). In practice, this provides a strong simplification on the classification of the many-body diagrams, and as such has recently been used also to develop a sophisticated re-summation technique known as "bold diagrammatic" Monte Carlo [155]. This simplification, however, cannot be exploited when the interaction potential has a finite range, like in the case of the potentials used in nuclear physics.

As already mentioned, the sum of ladder diagrams that defines the particle–particle propagator Γ_0 of Eq. (55) (together with the ensuing fermionic self-energy Σ of (54)) is sometimes referred to as the t-matrix approximation. The above expressions actually represent the G_0G_0 *version* of this approximation [150], since *all* the fermionic single-particle propagators (that is, both those entering Γ_0 and the one closing the fermion loop in Σ - cf. Fig. 8) are bare (G_0) ones. Different variants of the t-matrix approximation have actually been introduced, which correspond to:

(i) The G_0G *version*, where one G_0 in the particle–particle bubble $\chi_{\rm pp}$ of Eq. (56) is replaced by a full G [54,156–158];
(ii) The *extended t-matrix approximation* (ETMA), where the propagator G_0 closing the loop in Σ [cf. Eq. (54)] is replaced by the full G, but not the propagators in $\chi_{\rm pp}$ [138];
(iii) The *self-consistent Green's function method* (also called Luttinger–Ward method), where all G_0 (including that closing the loop in Σ) are replaced by full G [13,148,159];
(iv) A variant following the approach by Zimmermann and Stolz [160], where the bare G_0 are replaced by quasi-particle propagators (cf. Section 3.5).

These different variants of the t-matrix approximation unavoidably produce different quantitative results when applied to specific problems in the context of the BCS–BEC crossover [161,162]. Mostly for the purpose of illustration, in what follows we shall mainly present the results obtained within the G_0G_0 version of the t-matrix approximation. In this context, one should anyway keep in mind that not always what is believed to be an improvement in the treatment of a given fermionic single-particle propagator necessarily leads to a corresponding improvement in the comparison with the experimental data, nor even in comparison with results of exactly solvable models (see for instance Ref. [163] for the description of a spin-$\downarrow$ impurity in a gas of spin-$\uparrow$ particles).

3.2. Intra- and inter-pair correlations

In Section 3.1 we went through the original argument due to Nozières and Schmitt-Rink [7], according to which considering pairing fluctuations over and above mean field is essential to recover the correct value of the Bose–Einstein critical temperature in the BEC limit of the BCS–BEC crossover. In addition, in Section 1.3 we mentioned that the need to include pairing fluctuations beyond mean field arises even in the BCS limit of the BCS–BEC crossover, where already at the mean-field level one finds that the size $\xi_{\rm pair}$ of the intra-pair correlations between opposite-spin fermions remains finite when approaching T_c from below [62]. In Section 1.3 we have further anticipated that, even at zero temperature, the inclusion of pairing fluctuations is required to calculate the inter-pair coherence (or healing) length ξ, which strongly deviates from the intra-pair coherence length $\xi_{\rm pair}$ upon approaching the BEC limit [43,164], as shown in Fig. 2. On physical grounds, the difference between $\xi_{\rm pair}$ and ξ has the same origin of that occurring between the pair dissociation temperature T^* and the critical temperature T_c, as shown in Fig. 9.

Here, we dwell further on the difference between the two lengths $\xi_{\rm pair}$ and ξ. At zero temperature this difference lies at the very origin of the BCS–BEC crossover, while at finite temperature it gives valuable information about the persistence of pairing above T_c. To this end, we shall rely on the results of Ref. [63] where the t-matrix approximation of Section 3.1 (as well as its extension below T_c [151,153]) was employed to calculate the pair correlation function for opposite-spin fermions (to get $\xi_{\rm pair}$) and the correlation function of the order parameter (to get ξ).

The pair correlation function for opposite-spin fermions is defined by:

$$g_{\uparrow\downarrow}(\boldsymbol{\rho},\mathbf{R}) = \left\langle \psi_\uparrow^\dagger\left(\mathbf{R}+\frac{\boldsymbol{\rho}}{2}\right)\psi_\downarrow^\dagger\left(\mathbf{R}-\frac{\boldsymbol{\rho}}{2}\right)\psi_\downarrow\left(\mathbf{R}-\frac{\boldsymbol{\rho}}{2}\right)\psi_\uparrow\left(\mathbf{R}+\frac{\boldsymbol{\rho}}{2}\right)\right\rangle - \left(\frac{n}{2}\right)^2 \tag{70}$$

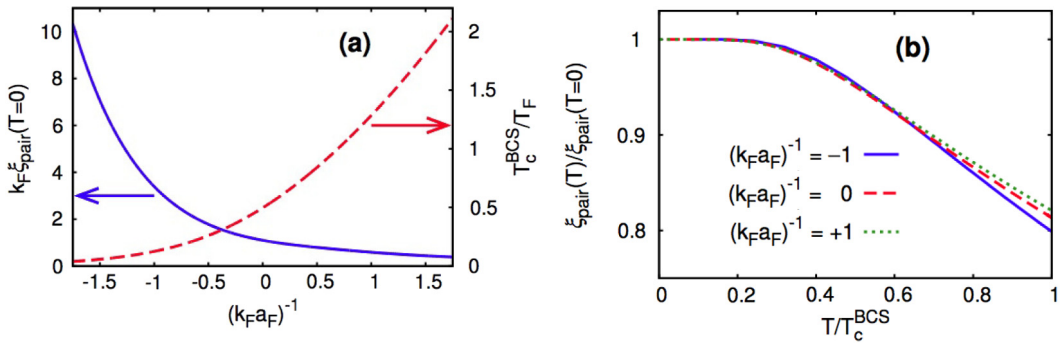

Fig. 10. (a) BCS pair coherence length $\xi_{\rm pair}(T=0)$ at zero temperature in units of the inverse Fermi wave vector k_F^{-1} (full line, left scale) and BCS critical temperature $T_c^{\rm BCS}$ in units of the Fermi temperature T_F (dashed line, right scale) vs the coupling parameter $(k_Fa_F)^{-1}$. (b) BCS pair coherence length $\xi_{\rm pair}(T)$ in units of $\xi_{\rm pair}(T=0)$ vs the temperature T in units of the respective BCS critical temperature $T_c^{\rm BCS}$ at various couplings.
Source: Adapted from Ref. [63].

where $\psi_\sigma(\mathbf{r})$ is a fermion field operator with spin σ, and $\boldsymbol{\rho} = \mathbf{r} - \mathbf{r}'$ and $\mathbf{R} = (\mathbf{r} + \mathbf{r}')/2$ are the relative and center-of-mass coordinates of the pair (the dependence of $g_{\uparrow\downarrow}$ on $\mathbf{R}$ can be dropped for a homogeneous system). The pair coherence length $\xi_{\rm pair}$ is then obtained as follows

$$\xi_{\rm pair}^2 = \frac{\int d\boldsymbol{\rho}\, \boldsymbol{\rho}^2\, g_{\uparrow\downarrow}(\boldsymbol{\rho})}{\int d\boldsymbol{\rho}\, g_{\uparrow\downarrow}(\boldsymbol{\rho})}\,, \tag{71}$$

which generalizes Eq. (6) that is only valid at the mean-field level. [The definition (71) for $\xi_{\rm pair}$ is meaningful only when the integrals therein converge. This is the case at the mean-field level and with the further inclusion of pairing fluctuations within the t-matrix approximation, to be considered below. When going beyond this approximation, a long-range (power-law) tail may appear in $g_{\uparrow\downarrow}(\boldsymbol{\rho})$ which is related to correlations between spin-↑ and spin-↓ belonging to different pairs, such that the integrals in Eq. (71) may not converge. In this case, it should anyway be possible to identify a short-range from a long-range part in $g_{\uparrow\downarrow}(\boldsymbol{\rho})$, in such a way that $\xi_{\rm pair}$ could be isolated by inspection.]

Quite generally, the thermal average of Eq. (70) can be related to the two-particle Green's function by a suitable choice of its space $\boldsymbol{\rho}$, (imaginary) time τ, and spin arguments [63]. The two-particle Green's function, in turn, can be conveniently calculated in terms of many-body diagrams. In particular, at the mean-field level for any temperature below T_c, $g_{\uparrow\downarrow}(\boldsymbol{\rho})$ is given by the square of the anomalous BCS single-particle Green's function:

$$\mathcal{G}_{12}(\boldsymbol{\rho}, \tau = 0^-) = \Delta \int \frac{d\mathbf{k}}{(2\pi)^3}\, e^{i\mathbf{k}\cdot\boldsymbol{\rho}}\, \frac{1 - 2f(E_{\mathbf{k}})}{2E_{\mathbf{k}}}\,. \tag{72}$$

The results of this calculation are shown in Fig. 10. For convenience, Fig. 10(a) reproduces the coupling dependence of $\xi_{\rm pair}$ at $T = 0$ from Fig. 2 and of $T_c^{\rm BCS}$ from Fig. 9. It turns out that, irrespective of coupling, the temperature dependence of $\xi_{\rm pair}$ follows approximately a kind of a "law of corresponding states" (that is, with a common behavior when reduced variables are used as in Fig. 10(b)), provided that $\xi_{\rm pair}(T)$ is expressed in units of $\xi_{\rm pair}(T = 0)$ and T in units of the BCS critical temperature $T_c^{\rm BCS}$ at the given coupling. It turns further out that the temperature dependence of $\xi_{\rm pair}$ from $T = 0$ to $T_c^{\rm BCS}$ is rather weak, not only in the BCS weak-coupling limit (where it was originally pointed out in Ref. [62]) but also at stronger couplings throughout the BCS–BEC crossover [63]. Specifically, in all cases $\xi_{\rm pair}$ reaches a finite value at $T_c^{\rm BCS}$ which is about 80% of its value at $T = 0$, as shown in Fig. 10(b) for various couplings. On physical grounds, as the temperature raises the spatial range of the correlations between spin-↑ and spin-↓ fermions is bound to decrease, because the effect of temperature is to disorder the system over a progressively shorter length scale which sets a limit on the value of $\xi_{\rm pair}$.

Although below T_c pairing fluctuations can be added on top of mean field to improve on the description of the pair correlation function (70) as well as to obtain the correlation function of the order parameter, from a physical point of view it is most interesting to consider the behavior of the intra-pair ($\xi_{\rm pair}$) and inter-pair (ξ) coherence lengths above T_c. In particular, the pair correlation function (70) can be obtained above T_c within the t-matrix approximation of Section 3.1 by the following expression [63]:

$$g_{\uparrow\downarrow}(\boldsymbol{\rho}) = \int \frac{d\mathbf{Q}}{(2\pi)^3}\, T\sum_\nu \Gamma_0(\mathbf{Q}, \Omega_\nu) \int \frac{d\mathbf{k}}{(2\pi)^3}\, e^{i\mathbf{k}\cdot\boldsymbol{\rho}} \left(\frac{1 - f(\xi_{\mathbf{k}+\mathbf{Q}}) - f(\xi_{\mathbf{k}})}{\xi_{\mathbf{k}+\mathbf{Q}} + \xi_{\mathbf{k}} - i\Omega_\nu} \right) \int \frac{d\mathbf{k}'}{(2\pi)^3}\, e^{-i\mathbf{k}'\cdot\boldsymbol{\rho}} \left(\frac{1 - f(\xi_{\mathbf{k}'+\mathbf{Q}}) - f(\xi_{\mathbf{k}'})}{\xi_{\mathbf{k}'+\mathbf{Q}} + \xi_{\mathbf{k}'} - i\Omega_\nu} \right) \tag{73}$$

in terms of which $\xi_{\rm pair}(T)$ results again using the definition (71). Note that the expression (73) has the expected short-range behavior:

$$g_{\uparrow\downarrow}(\boldsymbol{\rho}) \underset{(\rho\to 0)}{\longrightarrow} \left(\frac{m\,\Delta_\infty}{4\pi} \right)^2 \left(\frac{1}{\rho^2} - \frac{2}{a_F\,\rho} + \cdots \right) \tag{74}$$

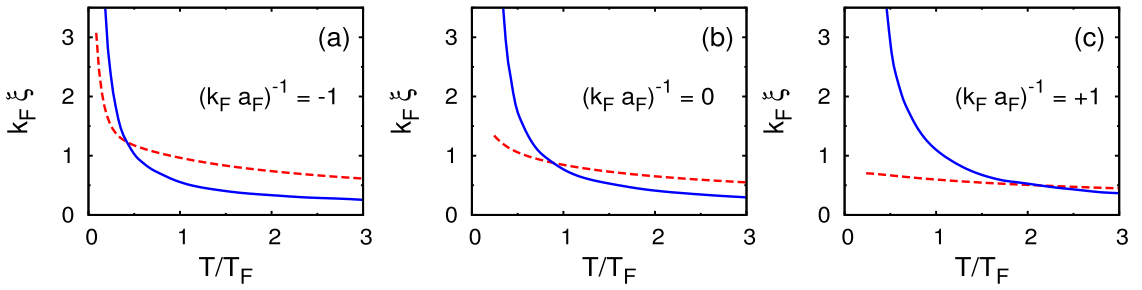

Fig. 11. The temperature dependence of the inter-pair coherence length ξ (full lines) and of the intra-pair coherence length $\xi_{\rm pair}$ (dashed lines) is shown above T_c for three values of the coupling $(k_F a_F)^{-1}$. Each curve terminates at the corresponding value of T_c obtained with the inclusion of pairing fluctuations (cf. the full line of Fig. 9).
Source: Adapted from Ref. [63].

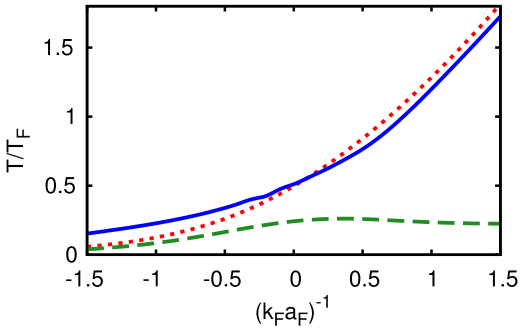

Fig. 12. The coupling dependence of the crossover temperature T^* (full line) is compared with that of the "pair dissociation temperature" obtained at the mean-field level (dotted line). Also shown is the critical temperature T_c obtained within the t-matrix approximation (dashed line).
Source: Reproduced from Ref. [63].

with $\rho = |\boldsymbol{\rho}|$ and the notation

$$\Delta_\infty^2 = \int \frac{d\mathbf{Q}}{(2\pi)^3}\, T \sum_\nu e^{i\Omega_\nu \eta}\, \Gamma_0(\mathbf{Q}, \Omega_\nu)\,. \tag{75}$$

In Section 4.5 we shall identify the quantity $(m\Delta_\infty)^2$ with the form of the Tan contact within the present theory. [Note that below T_c within mean field one ends up with an expression similar to (74) with the BCS gap Δ replacing Δ_∞.]

The correlation function of the order parameter can also be obtained above T_c within the t-matrix approximation of Section 3.1, in the form [63]:

$$F(\mathbf{R} - \mathbf{R}') = \frac{1}{2} \int \frac{d\mathbf{Q}}{(2\pi)^3}\, e^{i\mathbf{Q}\cdot(\mathbf{R}-\mathbf{R}')}\, \Gamma_0(\mathbf{Q}, \Omega_\nu = 0) \tag{76}$$

where only the static ($\Omega_\nu = 0$) component, which corresponds to taking a time averaging of pairing fluctuations, is considered for extracting the spatial dependence of the correlation function. To obtain the value of the inter-pair coherence length ξ from the above expression it is enough to expand $\Gamma_0(\mathbf{Q}, \Omega_\nu = 0)^{-1} = a + b\,\mathbf{Q}^2 + \cdots$ up to quadratic order. The Fourier transform in (76) then yields a Yukawa potential form with range $\xi = \sqrt{b/a}$ [43]. In the limit $T \to T_c$ the propagator $\Gamma_0(\mathbf{Q}, \Omega_\nu)$ then develops the Cooper singularity for $(\mathbf{Q} \to 0, \Omega_\nu = 0)$, in agreement with the Thouless criterion. Accordingly, the coefficient a vanishes like $(T - T_c)$ in the limit $T \to T_c^+$.

The temperature dependence of both lengths $\xi_{\rm pair}$ and ξ is shown in Fig. 11 for three characteristic couplings throughout the BCS–BEC crossover. Owing to the steeper temperature dependence of ξ with respect to $\xi_{\rm pair}$, at a given coupling these curves are bound to cross each other at a characteristic temperature T^*. This temperature, which can thus be obtained at any coupling throughout the BCS–BEC crossover, has the meaning of a "crossover temperature" below which inter-pair correlations are built up out of intra-pair correlations that are already present above this temperature. [The values of $\xi_{\rm pair}$ in Fig. 10 for $T \to T_c^-$ slightly differ from those in Fig. 11 for $T \to T_c^+$, because Fig. 10 is obtained at the mean-field level while Fig. 11 includes the effect of pairing fluctuations.]

The coupling dependence of the crossover temperature T^* obtained in this way is shown in Fig. 12 (full line), where it is compared with the "pair dissociation temperature" (dotted line) obtained in Section 2.3 at the mean-field level (the latter was already reported as the dashed line in Fig. 9). It is rather remarkable that the overall coupling dependences of these two

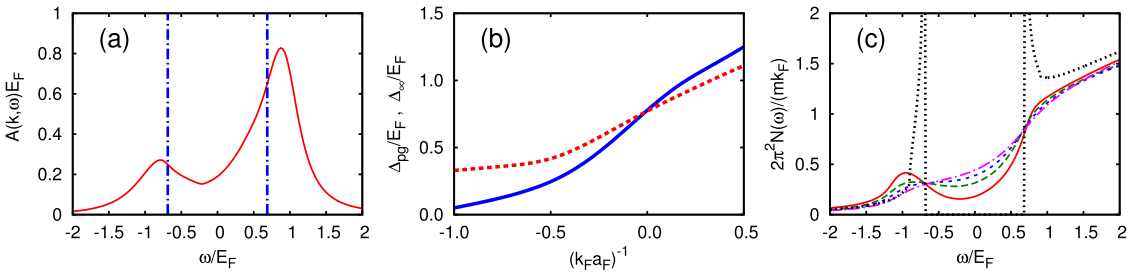

Fig. 13. (a) Single-particle spectral function $A(k, \omega)$ vs ω at unitarity, as obtained at $T = 0$ within mean field (dashed–dotted lines) and at T_c with the inclusion of pairing fluctuations (full line). The corresponding wave vectors are $k = 0.76\, k_F$ and $k = 0.91 k_F$, at which the maximum of the lower branch of the dispersion relation occurs in the two cases. (b) Pseudo-gap Δ_{pg} (full line) and parameter Δ_∞ related to short-distance physics (dashed-line) vs. the coupling $(k_F a_F)^{-1}$ at T_c. (c) Density of states $N(\omega)$ vs ω calculated within the t-matrix approximation at unitarity and various temperatures: T_c (full line), $1.2\, T_c$ (long-dashed line), $1.4\, T_c$ (short-dashed line), and $1.65\, T_c$ (dot-dashed line). The corresponding mean-field result at $T = 0$ is also reported (dotted line). The non-interacting value $N_0 = mk_F/(2\pi^2)$ of the density of states at the Fermi surface is used for normalization.
Source: Adapted from Refs. [166] and [167].

crossover temperatures about coincide with each other, even though they have been obtained through different physical approaches. With the present analysis based on the range of the correlation functions, however, this crossover temperature acquires the more physical meaning for the building up of inter-pair correlations out of intra-pair correlations that develop above this temperature.

For this reason, and as already remarked in Section 3.1, precursor pairing phenomena (like the pseudo-gap energy to be discussed in Section 3.3) are expected to occur in a range of intermediate temperatures, which are above the critical temperature T_c but below the crossover temperature T^*.

3.3. Single-particle spectral function and pseudo-gap

The term pseudo-gap was originally introduced to indicate a minimum in the density of states at the Fermi level [165]. As such, it can be directly related to the shape of the *single-particle spectral function* $A(\mathbf{k}, \omega)$, which embodies the essential information on the single-particle Green's function $G(\mathbf{k}, \omega_n)$ through the spectral representation

$$G(\mathbf{k}, \omega_n) = \int_{-\infty}^{+\infty} d\omega \, \frac{A(\mathbf{k}, \omega)}{i\omega_n - \omega} \tag{77}$$

and to which the following sum rule is associated:

$$\int_{-\infty}^{+\infty} d\omega \, A(\mathbf{k}, \omega) = 1 \, . \tag{78}$$

Analogous considerations apply to the superfluid phase below T_c for a Fermi gas with an attractive inter-particle interaction. In particular, within BCS mean-field one gets:

$$\mathcal{G}_{11}(\mathbf{k}, \omega_n) = \frac{v_{\mathbf{k}}^2}{i\omega_n + E_{\mathbf{k}}} + \frac{u_{\mathbf{k}}^2}{i\omega_n - E_{\mathbf{k}}} \tag{79}$$

with reference to the upper diagonal element of Eq. (44) (once specified to a homogeneous system and using the notation introduced after Eq. (30)). The corresponding single-particle spectral function

$$A(\mathbf{k}, \omega) = v_{\mathbf{k}}^2 \, \delta(\omega + E_{\mathbf{k}}) + u_{\mathbf{k}}^2 \, \delta(\omega - E_{\mathbf{k}}) \tag{80}$$

contains two delta-like peaks symmetrically located about $\omega = 0$ (although with different weights), which correspond to the upper $(+E_{\mathbf{k}})$ and lower $(-E_{\mathbf{k}})$ branches of the BCS dispersion. For values of $k = |\mathbf{k}|$ that satisfy $\xi_{\mathbf{k}} = k^2/(2m) - \mu = 0$ such that $E_{\mathbf{k}} = |\Delta|$, the spacing between these two peaks provides a measure of $2|\Delta|$. This situation is represented by the dashed–dotted lines in Fig. 13(a) for the case of unitarity and $T = 0$. Within the BCS mean-field, when T approaches T_c and $|\Delta|$ vanishes these two peaks merge eventually into a single (free-particle) peak centered at $\omega = 0$.

The situation changes when including pairing fluctuations, which give rise to precursor pairing effects above T_c. Extensive studies along these lines [166] have, in particular, been performed within the t-matrix approximation discussed in Section 3.1, whereby the single-particle Green's function $G(\mathbf{k}, \omega)$ contains the self-energy (54). The formation of a pseudo-gap was studied also in nuclear physics and calculated for nuclear matter in Ref. [30] (cf. Fig. 36 in Section 5.3). As it was already mentioned in Section 3.1, to get the single-particle spectral function $A(\mathbf{k}, \omega)$ it is essential for the self-energy (54) to appear in the denominator of $G(\mathbf{k}, \omega)$ like in Eq. (58) and not in the expanded form (60). Otherwise, the poles of $G(\mathbf{k}, \omega)$ in the complex ω-plane cannot be located in a physically meaningful way. Fig. 13(a) shows the corresponding calculation at unitarity and T_c, where two broad and overlapping peaks now appear in $A(\mathbf{k}, \omega)$ in the place of the two delta-like peaks

obtained at $T = 0$ within mean field. This result evidences how a real gap at $T = 0$ transforms into a pseudo-gap at T_c, through a partial filling of the spectral function in between the two peaks.

As an example, Fig. 13(b) shows the coupling dependence of the pseudo-gap $\Delta_{\rm pg}$ at T_c (full line), which can be extracted from the two-peak structure of $A(\mathbf{k}, \omega)$ shown in Fig. 13(a) [167]. For comparison, Fig. 13(b) also reports the coupling dependence of the parameter Δ_∞, related to short-distance physics, introduced in Section 3.2 (dashed line). Note that the two quantities $\Delta_{\rm pg}$ and Δ_∞ differ considerably from each other over most of the coupling range. Physically, this difference is because $\Delta_{\rm pg}$ is defined at small wave vectors while Δ_∞ is defined at large wave vectors, such that one does not expect them to be correlated with each other. In this respect, the crossing of the two curves near unitarity is to be considered as accidental. This coincidence has sometimes led in the literature to identify the expression (75) for Δ_∞ with the pseudo-gap $\Delta_{\rm pg}$ [54,168,169].

Reference to a specific wave vector can be avoided by performing an average of $A(\mathbf{k}, \omega)$ over all $\mathbf{k}$. In particular, this procedure may support to the presence of a pseudo-gap in cases when the two peaks of $A(\mathbf{k}, \omega)$ strongly overlap each other, at least in some ranges of $\mathbf{k}$. In this way one is led to define the single-particle density of states:

$$N(\omega) = \int \frac{d\mathbf{k}}{(2\pi)^3} A(\mathbf{k}, \omega) . \tag{81}$$

Fig. 13(c) shows plots of $N(\omega)$ at unitarity for several temperatures at and above T_c [166]. Here, the depression of $N(\omega)$ about $\omega = 0$ confirms the existence of a pseudo-gap, which is seen to progressively disappear at temperatures somewhat below the crossover temperature T^* (in the present case, T^* is approximately $2\,T_c$). For comparison, also reported in Fig. 13(c) is the density of states obtained within mean field at $T = 0$, which shows two sharp peaks located at $\pm|\Delta|$. Similar results have also been obtained in two dimensions [170], which are qualitatively similar to the ones shown here in three dimensions. However, the temperature window above T_c in which precursor pairing occurs is wider in two than in three dimensions, owing to the increased importance of fluctuations.

When spanning the BCS–BEC crossover so as to approach the BEC limit, the question naturally arises about *the boundary* between the pseudo-gap (many-body) regime and the molecular (two-body) regime. This is because in the BEC limit when all fermions are bound in pairs, the depression of the single-particle density of states would just reflect the presence of the molecular (two-body) bound state. It is then clear that this molecular regime should not be confused with the pseudo-gap regime of interest, which originates from genuine many-body effects and is not simply a manifestation of two-body binding. This is even more so in two dimensions, where a two-body bound state occurs for any value of the inter-particle coupling. To resolve this issue, a careful analysis is required on the shape of the lower branch of the dispersion relation for given coupling and temperature above T_c. Accordingly, in Ref. [171] the position of the wave vector was determined, at which the maximum of the lower branch occurs and past which the branch eventually backbends, identifying in this way a characteristic wave vector k_L called the Luttinger wave vector. By this analysis, it was found that the value of k_L remains finite (near k_F) even past unitarity where the gas is strongly interacting, thereby signaling the presence of a remnant Fermi surface and the importance of the Fermi statistics to pairing. Afterwards once entering the molecular regime, k_L rapidly decreases towards zero and vanishes at about $(k_F a_F)^{-1} \simeq 0.5$ [171]. The conclusion was that the boundary between the pseudo-gap and molecular regimes resides just where k_L vanishes and the underlying Fermi surface disappears. This criterion generalizes to finite temperature and beyond mean field the zero-temperature mean-field criterion, which identifies the boundary between the BCS and BEC sides of the crossover with the change of the sign of the chemical potential μ [6] (see [170,171] for a discussion of the connections and differences between these two criteria).

3.4. Gor'kov–Melik-Barkhudarov (screening) corrections

In the weak-coupling (BCS) limit, the exponential dependence of Δ_0 and T_c on $(k_F a_F)^{-1}$ (given, respectively, by Eq. (10) and by Eq. (23), whereby $\Delta_0/T_c = \pi/e^\gamma$) leaves open the possibility of the presence of sub-leading contributions in the exponent beyond the leading contribution $(k_F a_F)^{-1}$, which may thus affect the pre-factors in the expressions of Δ_0 and T_c. That this is actually the case was proved by Gor'kov and Melik-Barkhudarov (GMB) [172] not long after the BCS result, by introducing corrections to the BCS mean field. We provide here a slightly different derivation of their original result, by focusing specifically on the correction to T_c for which one can exploit the pairing fluctuations approach of Section 3.1 valid for the normal phase.

We recall that the expression (23) for the superfluid critical temperature T_c can be alternatively obtained by approaching T_c from above in terms of the Thouless criterion [173]. According to this criterion, the instability of the normal phase when approaching T_c is signaled by the divergence at $Q = 0$ of the particle–particle propagator (or t-matrix) $\Gamma_0(Q)$ given by Eq. (55). This is equivalent to the condition $m/(4\pi a_F) + R_{\rm pp}(Q = 0) = 0$ in terms of the regularized particle–particle bubble $R_{\rm pp}(Q)$ of Eq. (57). In weak coupling for this quantity one obtains the value:

$$R_{\rm pp}(Q = 0) \simeq N_0 \ln\left(\frac{8 e^\gamma E_F}{\pi e^2 T}\right) \tag{82}$$

where $N_0 = m k_F/(2\pi^2)$, so that the BCS result (23) for T_c is readily recovered.

To go beyond the BCS result for T_c, the above form of the Thouless criterion needs to be modified by including particle–particle (pp) "self-energy" effects in the particle–particle propagator $\Gamma_0(Q)$. In their simplest form, these effects

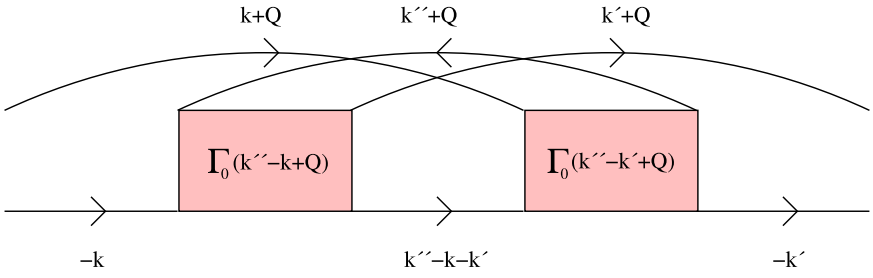

Fig. 14. Graphical representation of the bosonic-like self-energy $\Sigma^{\rm pp}_{\rm GMB}(Q)$ that enters the condition (83) for the critical temperature, according to the GMB approach. Boxes stand for the particle–particle propagator Γ_0 and thin lines for the bare fermionic single-particle propagator $G_0(k)$.

are represented by the crossed-ladder diagram $\Sigma^{\rm pp}_{\rm GMB}(Q)$ depicted in Fig. 14, which was originally identified in Ref. [172] at the lowest significant order in the small parameter $k_F a_F$. In this way, the modified criterion for the critical temperature reads:

$$\Gamma_0(Q=0)^{-1} - \Sigma^{\rm pp}_{\rm GMB}(Q=0) = 0 \tag{83}$$

with $-\Gamma_0(Q=0)^{-1} = m/(4\pi a_F) + R_{\rm pp}(Q=0)$ according to Eq. (55). Note how the criterion (83) resembles the Hugenholtz–Pines condition for the critical temperature of a system of interacting bosons [174].

The quantity $\Sigma^{\rm pp}_{\rm GMB}(Q=0)$ can be readily calculated in the weak-coupling limit $(k_F a_F)^{-1} \ll -1$ through the following steps [172]: (i) Both particle–particle propagators occurring in Fig. 14 are approximated by the constant value $\Gamma_0 \simeq -4\pi a_F/m$, according to a standard result of the Galitskii approach [141]; (ii) Owing to this approximation, the particle–hole (or polarization) bubble $\chi_{\rm ph}(k+k')$

$$\chi_{\rm ph}(k+k') = \int \frac{d\mathbf{k}''}{(2\pi)^3} \frac{f(\xi_{\mathbf{k}+\mathbf{k}'+\mathbf{k}''}) - f(\xi_{\mathbf{k}''})}{\xi_{\mathbf{k}+\mathbf{k}'+\mathbf{k}''} - \xi_{\mathbf{k}''} - i(\omega_n + \omega_{n'})}\,, \tag{84}$$

which is nested in the central part of the diagram of Fig. 14, gets effectively disentangled from the two particle–particle bubbles $\chi_{\rm pp}(Q=0)$ which are present on the sides of the diagram; (iii) To avoid an ensuing ultraviolet divergence in the particle–particle channel, $\chi_{\rm pp}$ is then replaced by its regularized version $R_{\rm pp}$ according to Eq. (57) (in practice, this procedure is equivalent to introducing a cutoff of the order k_F in the integration over $|\mathbf{k}|$); (iv) Correspondingly, in the particle–hole bubble (84) one takes the zero-temperature limit (whereby $\omega_n + \omega_{n'} = 0$), sets $\mu = E_F$, and performs an average over the Fermi sphere, to yield:

$$\bar{\chi}_{\rm ph}(0) = -N_0 \ln(4e)^{1/3}\,; \tag{85}$$

(v) Grouping all the above approximate results, one obtains eventually

$$\Sigma^{\rm pp}_{\rm GMB}(Q=0) \simeq \left(\frac{4\pi a_F}{m}\right)^2 R_{\rm pp}(Q=0)^2\, \bar{\chi}_{\rm ph}(0) \tag{86}$$

in such a way that the condition (83) is approximated by the following expression:

$$\frac{m}{4\pi a_F} + R_{\rm pp}(Q=0) + \left(\frac{4\pi a_F}{m}\right)^2 R_{\rm pp}(Q=0)^2\, \bar{\chi}_{\rm ph}(0) = 0\,; \tag{87}$$

(vi) In weak coupling, one can further approximate $(4\pi a_F/m) R_{\rm pp}(Q=0) \simeq -1$ in the last term on the left-hand side of Eq. (87). In this way, the equation for T_c reduces to the simple form:

$$\frac{m}{4\pi a_F} + R_{\rm pp}(Q=0) + \bar{\chi}_{\rm ph}(0) = 0\,. \tag{88}$$

With the expressions (82) for $R_{\rm pp}(Q=0)$ and (85) for $\bar{\chi}_{\rm ph}(0)$, Eq. (88) yields eventually the result:

$$T_c = \frac{1}{(4e)^{1/3}} \frac{8e^{\gamma} E_F}{\pi e^2} \exp[\pi/(2k_F a_F)] \tag{89}$$

which is smaller by the factor $(4e)^{1/3} \simeq 2.2$ with respect to the BCS result (23). Note that it is for the presence in Eq. (88) of the particle–hole (or polarization) bubble $\chi_{\rm ph}$ (which gives the leading contribution to the screening in an electron gas [95]) that the GMB result is often referred to as a "screening correction" to T_c.

By a similar token, particle–hole corrections affect also the value of the BCS gap, by replacing the term $m/(4\pi a_F)$ on the right-hand side of Eq. (8) with $m/(4\pi a_F) + \bar{\chi}_{\rm ph}(0)$ just like in Eq. (88). At zero-temperature, this yields a reduction of the BCS result $\Delta_0 = (8E_F/e^2)\exp[\pi/(2k_F a_F)]$ by the same factor of 2.2 occurring in Eq. (89), thereby maintaining the value of the ratio $\Delta_0/T_c = \pi/e^{\gamma}$ of the BCS theory.

In the context of the BCS–BEC crossover, it would be of interest [175] to assess whether corrections of the GMB type (as embodied by the diagram of Fig. 14) can still yield significant effects on T_c and Δ, when carried over to the unitary limit $(k_F a_F)^{-1} = 0$ where one knows that a remnant Fermi surface is still active (cf. Section 3.3). A partial answer to this question was provided in Refs. [176,177], where the expression (88) was taken to hold for all couplings across the BCS–BEC crossover, with the only provision of using the appropriate value of the chemical potential (and not simply E_F) when calculating $\bar{\chi}_{\rm ph}(0) = 0$. [A completely different approach was instead followed in Refs. [178–180], where particle–particle and particle–hole fluctuations were included simultaneously in the framework of the functional renormalization-group approach.] To get a complete answer to this question, however, the typical approximations of the weak-coupling (BCS) limit that led to the expression (88) should be abandoned and the full wave-vector and frequency dependence of the particle–particle propagator $\Gamma_0(Q)$ should be retained in the calculation of $\Sigma^{\rm pp}_{\rm GMB}$ in Fig. 14. Work along these lines has recently appeared [181]. In any case, the fact that experimental [182,183] and Quantum Monte Carlo (QMC) [184–186] results for T_c at unitarity are only by about 25% lower than the NSR result indicates that screening effects on top of the t-matrix are less important at unitarity than in the weak-coupling (BCS) regime.

In nuclear physics, the GMB corrections were instead considered for the gap parameter Δ [187]. With more than two species of fermions, the reduction of the gap can turn over into an enhancement [188]. In nuclear and neutron matters, screening of the pairing force has also been considered at higher densities [189]. Not only the particle–hole bubble exchange has been considered, but these bubbles have been summed up to the full RPA. Once polarization effects are no longer treated to the lowest order as within the GMB approach, the problem arises that the screening of the force and the coupling of the single-particle motion to the two-particle excitations have to be treated on the same footing. This introduces a single-particle self-energy energy $\Sigma(\mathbf{k}, \omega)$ that depends on wave vector and frequency, a feature that has to be taken into account because the Fermi step gets reduced by the wave-function renormalization factor

$$Z_{\mathbf{k}}^{-1} = 1 - \left.\frac{\partial \Sigma(\mathbf{k}, \omega)}{\partial \omega}\right|_{\omega=\xi_{\mathbf{k}}}. \tag{90}$$

The gap equation modified in this way reads [190]:

$$\Delta_{\mathbf{k}} = \int \frac{d\mathbf{k}'}{(2\pi)^3} V_{\rm eff}(\mathbf{k}, \mathbf{k}') \frac{Z_{\mathbf{k}} Z_{\mathbf{k}'} \Delta_{\mathbf{k}'}}{2\sqrt{\xi^2_{\mathbf{k}'} + \Delta^2_{\mathbf{k}'}}} \tag{91}$$

where the effective potential $V_{\rm eff}$ contains the RPA screening correction [cf. diagrams (b) and (c) of Fig. 41 in Section 5.5] in addition to the Born term [cf. diagram (a) of Fig. 41 in Section 5.5]. In neutron matter this kind of screening reduces the gap as a function of k_F by about 30%, bringing the results in quite close agreement with QMC calculations [36] (see Section 5.5). In symmetric nuclear matter an anti-screening effect also exists, because in this case attractive density fluctuations become more important than spin fluctuations. This enhancement effect, however, is over-compensated by the particle–phonon coupling in the self-energy, so that in the end the gap becomes even smaller than in the BCS approximation. In the case of symmetric nuclear matter no QMC calculations exist to compare with.

3.5. NSR theory in nuclear physics and the approach by Zimmermann and Stolz

In nuclear physics, too, the t-matrix (sometimes referred to also as T-matrix) approach has a long history, to treat bound state formation and correlations at finite temperatures [191,192]. Based on the work by Zimmermann and Stolz (ZS) [160], an improved Beth–Uhlenbeck equation for hot nuclear matter was treated with the t-matrix [193]. In 1995 the NSR approach was applied to nuclear matter for the treatment of the BEC–BCS transition in the case of proton–neutron pairing, which leads to the bound state of the deuteron in strong coupling [22].

In the ZS approach of Ref. [160], the self-energy Σ is given by the diagram of Fig. 8(a) similar to the NSR approach, albeit with an important difference. The ZS approach is based on a perturbative treatment, where the Dyson equation is truncated at first order in the self-energy like in Eq. (60) for the NSR approach, that is, $G \approx G_0 + G_0^2 \Sigma$ where Σ denotes the self-energy calculated in ladder approximation with single-particle propagators G_0. The difference is that now G_0 is not the bare propagator $1/(i\omega_n - \xi_{\mathbf{k}})$ of the NSR approach, but is a quasi-particle propagator that takes into account a mean-field-like quasi-particle energy shift due to Σ, that is, $G_0 = 1/(i\omega_n - \xi^*_{\mathbf{k}})$ where $\xi^*_{\mathbf{k}} = \xi_{\mathbf{k}} + \Sigma^R(\mathbf{k}, \xi^*_{\mathbf{k}})$ and Σ^R is the retarded self-energy. This is because in nuclear physics it is crucial to include the (Hartree–Fock) mean-field shift in the single-particle energies [26]. Also in the case of a contact interaction, however, the importance of including a mean-field shift was pointed out in Refs. [150,151] for the BCS side of the crossover and in Ref. [194] for the whole BCS–BEC crossover. With the above replacement $\xi \to \xi^*$, one ends up with an expression for the correlated density slightly different from that of the NSR approach, of the form

$$n_{\rm corr} = -\int \frac{d\mathbf{Q}}{(2\pi)^3} \int \frac{d\Omega}{\pi} b'(\Omega) \left(\delta(Q, \Omega) - \frac{1}{2}\sin[2\delta(Q, \Omega)]\right) \tag{92}$$

where $b'(\Omega)$ is the derivative of the Bose function $b(\Omega) = 1/(e^{\Omega/T} - 1)$ with respect to Ω and $\delta(Q, \Omega) = {\rm Im}\ln[R_{\rm pp}(Q, \Omega) + m/4\pi a_F]$ is the in-medium scattering phase shift with $R_{\rm pp}$ given by Eq. (57). In the presence of a bound state (for which $a_F > 0$), $\delta = \pi$ in the energy range between the bound-state energy and the continuum threshold. The expression (92) for

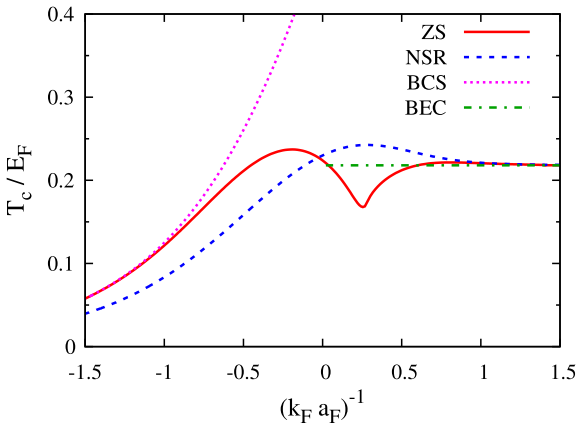

Fig. 15. The dependence of the critical temperature T_c (in units of E_F) on the interaction parameter $(k_F a_F)^{-1}$ is compared for several approximations: ZS approach (solid line); NSR approach (dashed line); BCS result (dotted line); BEC limit (dashed–dotted line). The NSR result of Fig. 9 has been also reported for convenience.
Source: Adapted from Ref. [194].

the correlated density was first used to describe the BCS–BEC crossover in nuclear matter [22,26], and was later used for a contact interaction [194].

Fig. 15 shows the coupling dependence of the critical temperature obtained by the ZS approach, which interpolates between the BCS and BEC limits, and compares it with that obtained by other approaches. Note that, while in the BCS limit the ZS approach converges to the BCS result (23), the NSR approach (which neglects the mean-field shift) converges to the BCS result divided by $e^{1/3}$, as already mentioned in Section 3.1. In Section 5 the ZS approach will be employed to describe the deuteron case in nuclear physics.

3.6. Residual interaction among composite bosons

In the (extreme) BEC limit of the BCS–BEC crossover, all fermions get paired into tight composite bosons (dimers) which interact with each other through a residual (albeit small) interaction. To the extent that this gas of composite bosons is dilute, at low energy the residual interaction can be characterized by the boson–boson scattering length a_B, in a similar fashion as the inter-particle interaction of the original fermionic system was characterized by the fermionic scattering length a_F. It is also clear that a_B is bound to be proportional to a_F with a constant coefficient, in such a way that a_B vanishes simultaneously with a_F in the extreme BEC limit when $(k_F a_F)^{-1} \gg +1$.

From a physical point of view, the progressive loss of fermionic character of the system when approaching the BEC limit becomes apparent by looking at the shape of the single-particle spectral function discussed in Section 3.3. When approaching the BEC limit, the left (hole) peak at negative frequency in the single-particle spectral function looses progressively its weight because all particles are bound in pairs [151,153,166].

In terms of the diagrammatic structure, the above features are reflected in the facts that: (i) The only diagrams that survive the regularization procedure (7) are those which are built directly on the particle–particle propagator Γ_0 given by the expression (55); (ii) In the BEC limit, the particle–particle propagator Γ_0 is proportional to the bare bosonic (dimer) propagator [cf. Eq. (64)]. The correspondence between these two propagators is shown graphically in Fig. 16(a).

To construct the full diagrammatic structure in the BEC limit, one has then to connect different particle–particle propagators Γ_0 with each other through four-leg structures, which, when taken together, correspond to an effective residual interaction between the composite bosons. These structures (which are infinite in number) correspond to all different kinds of virtual processes by which the fermionic character of the constituent particles manifests itself when two composite bosons undergo isolated scattering events. Accordingly, the associated diagrams are calculated in the limit of vanishing density. The collection of all these diagrammatic structures is schematically represented in Fig. 16(b) by a block which connects two incoming and two outgoing composite bosons.

The first two terms contributing to the residual interaction among composite bosons are shown in Fig. 16(b). When evaluated in the limit of vanishing four-vectors, these terms yield the value $8\pi a_F/(2m)$ of the coefficient of the cubic term in the GP equation (46), thereby implying the result $a_B = 2a_F$ between the fermionic and bosonic scattering lengths. This result corresponds to the Born approximation for the dimer–dimer scattering problem [13,68,148]. It turns out that this result can be improved by introducing the dimer–dimer T-matrix which considers a sequence of dimer–dimer scatterings instead of a single scattering, as shown schematically in Fig. 16(c). [Note that here the label T-matrix is meant to distinguish this dimer–dimer sequence from the t-matrix (Γ_0) of the constituent fermions.] The calculation of the dimer–dimer T-matrix (and thus of a_B) is then reduced to the calculation of two infinite perturbation series, namely, the series that builds up the dimer–dimer residual interaction (cf. Fig. 16(b)) and the series that obtains the complete dimer–dimer T-matrix through an infinite

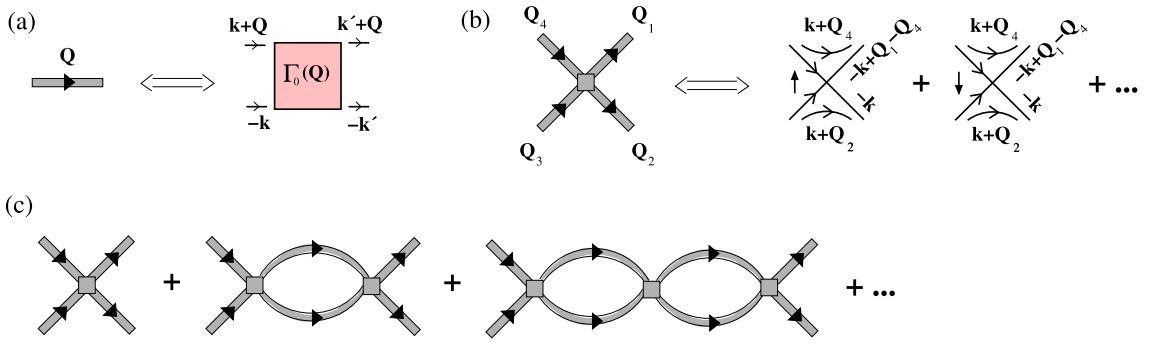

Fig. 16. (a) Correspondence between the bare bosonic propagator (left) and the particle–particle propagator (right). (b) The dimer–dimer residual interaction is represented graphically by a block (where $Q_1 + Q_2 = Q_3 + Q_4$ in four-vector notation). The first two terms of the dimer–dimer residual interaction are explicitly shown (right), where thin lines represent bare fermionic single-particle propagators G_0 and fermionic spin labels are indicated in the internal lines. The dimer–dimer residual interaction contains, in principle, an additional infinite number of terms (dots), where in the intermediate states one of the dimers is broken into its fermionic constituents. (c) T-matrix for the dimer–dimer scattering problem, where successive blocks are connected through a sequence of dimer–dimer bubbles.

sequence of this dimer–dimer residual interaction (cf. Fig. 16(c)). By this scheme, the Born approximation corresponds to the first-order term of both perturbation series.

The dimer–dimer T-matrix beyond the Born approximation was first considered in Ref. [149]. There, only the first two terms of the dimer–dimer residual interaction shown explicitly in Fig. 16(b) were retained and the corresponding diagrammatic series for the dimer–dimer T-matrix of Fig. 16(c) was summed up, obtaining the value $a_B \simeq 0.75 a_F$ for the bosonic scattering length. Later on, a complete treatment was given in Refs. [195,196] for the numerical solution of the corresponding four-body Schrödinger equation, yielding $a_B \simeq 0.60 a_F$. This value of a_B was subsequently confirmed in Refs. [197,198], where a full diagrammatic treatment was given by summing up not only the series for the dimer–dimer T-matrix of Fig. 16(c) but *also* the infinite series for the residual dimer–dimer interaction of Fig. 16(b), and by lattice-effective-field theory-methods [199] which yielded in addition the estimate $r_e \simeq -0.43 a_F$ for the dimer–dimer effective range parameter. This value has recently been corrected to $r_e \simeq 0.13 a_F$ by the four-body calculation of Ref. [200], which has confirmed the previous results of Refs. [201,202]. The problem was recently reconsidered in Ref. [203] for a two-component Fermi mixture in which the two different fermionic species have different masses. It was found that, in the large mass ratio domain, the dominant processes are just the repeated dimer–dimer scatterings considered originally in Ref. [149] (that is, those explicitly depicted in Fig. 16(b) and (c)), with the conclusion that the ensuing approximation is asymptotically correct for large mass ratio (and thus provides, in practice, a good approximation for any mass ratio).

It is worth emphasizing that the presence of the branch cut, which occurs in the BEC limit at sufficiently high energy in the spectral representation (69) of the particle–particle propagator Γ_0, is bound to give an important contribution to the *ab-initio* calculation of the boson–boson scattering length a_B in terms of the scattering length a_F of the constituent fermions. On physical grounds, this feature is expected to occur because the fermionic nature of the constituent particles of the composite bosons has to show up just when these bosons collide against each other, such that energies that are much higher than the kinetic energy of the colliding bosons come into play in the intermediate (virtual) states of the collision. To some extent the logic here is similar to Frank Wilczek's account for the origin of mass [204], when this quantity is calculated from first principles and not merely regarded as a phenomenological parameter by remaining in the low-energy sector where quantum mechanics effectively suppresses the complexity of composite systems.

For all these reasons, the above results for the dimer–dimer scattering obtained in the BEC limit of the BCS–BEC crossover can be considered almost unique, to the extent that it has been possible to obtain from first principles the relevant scattering properties of composite (bosonic) objects in terms of the scattering properties of the constituent (fermionic) particles. Only very recently, it has become possible to describe also deuteron–deuteron scattering by solving the four-body Schrödinger equation for two neutrons and two protons [205]. A corresponding information is not available, for instance, for a gas of bosons like ^{4}He atoms, whose inter-particle potential is commonly modeled by a simplified phenomenological form (like the hard-sphere model) and the bosons are considered to be effectively point-like objects.

The above results for the dimer–dimer scattering were obtained in the limit of vanishing density, which is relevant to an extremely dilute gas of composite bosons in the BEC limit. At higher densities, where the Pauli principle starts to become important and the Fermi functions are no longer negligible, an in-medium corrected four-fermion equation of the following form has to be considered (see Ref. [27]):

$$[E - (\varepsilon_{k_1} + \varepsilon_{k_2} + \varepsilon_{k_3} + \varepsilon_{k_4})]\, \Psi_{k_1 k_2 k_3 k_4} = [1 - f(\xi_{k_1}) - f(\xi_{k_2})] \sum_{k'_1 k'_2} \bar{v}_{k_1 k_2 k'_1 k'_2} \Psi_{k'_1 k'_2 k_3 k_4} + [1 - f(\xi_{k_1}) - f(\xi_{k_3})] \sum_{k'_1 k'_3} \bar{v}_{k_1 k_3 k'_1 k'_3} \Psi_{k'_1 k_2 k'_3 k_4} + \text{permutations}\,. \tag{93}$$

Here, $\bar{v}_{k_1k_2k_3k_4} = \langle k_1k_2|v|k_3k_4\rangle - \langle k_1k_2|v|k_4k_3\rangle$ is the anti-symmetrized matrix element of the two-body force and the indices $k_i = (\mathbf{k}_i, \sigma_i)$ contain momenta and spin (and possibly isospin, like in nuclear physics). The eigenvalue of this Schrödinger type of equation is denoted by E. The phase-space factors $[1 - f(\xi_{k_1}) - f(\xi_{k_2})]$ are the same as in the two particle Bethe–Salpeter equation and take care of the fact that particles cannot scatter into points of phase space which are already occupied. The above in-medium four-fermion equation could be used to study the density dependence of a_B. It will be explicitly employed in Section 5 to reveal quartet condensation (but it could as well be used to investigate bi-exciton versus exciton condensation in semiconductors).

3.7. Pairing fluctuations in polarized Fermi gases

The NSR approach discussed in Section 3.1 is readily extended to the polarized case with different spin populations, by introducing two different chemical potentials μ_σ for the two spin species σ in the bare fermionic single-particle propagators $G_{0\sigma}$ that enter the particle–particle propagator Γ_0 and the self-energy (54) (which thus depends also on σ). This approach, however, breaks down near unitarity, because if one calculates the densities for $\mu_\uparrow > \mu_\downarrow$ one finds $n_\uparrow < n_\downarrow$ in some regions of the phase diagram [140,206]. A warning about this problem exists already in the unpolarized case, where the spin susceptibility becomes negative at temperatures slightly above T_c in a region about unitarity [138,207] (see also Ref. [208]). The size of this region can be significantly reduced by avoiding the expansion (60) of the Dyson equation and using the t-matrix approximation discussed in Section 3.1, although even in this case the spin susceptibility at T_c remains negative in a small region on the BEC side of unitarity [138].

To overcome this problem of a negative spin susceptibility for all temperatures above T_c throughout the whole BCS–BEC crossover, it turns out that it is sufficient to introduce some degree of self-consistency in the self-energy of Fig. 8(a). This has been done either by using the ZS approach of Section 3.5 where a quasi-particle energy shift is introduced in all particle lines of the self energy of Fig. 8(a) [194], or by replacing the bare single-particle propagator that closes the loop in Fig. 8(a) by a dressed one [138,207]. The latter approximation (referred to as the Extended T-Matrix Approximation (ETMA)) was applied to calculate the critical temperature of the polarized gas throughout the BCS–BEC crossover [138]. Specifically, assuming that the transition to the superfluid phase is of second order, in Ref. [138] the Thouless criterion $\Gamma_0(Q = 0)^{-1} = 0$ was solved simultaneously with the number equations $n_\sigma = \int \frac{d\mathbf{k}}{(2\pi)^3} T \sum_n e^{i\omega_n\eta} G_\sigma(k)$, where G_σ is dressed by the ETMA self-energy Σ_σ via the Dyson equation and the particle–particle propagator $\Gamma_0(Q)$ is determined by Eq. (57) for R_{pp} with the replacement $\xi_{\mathbf{k}+\mathbf{Q}} \to \xi_{\mathbf{k}+\mathbf{Q}\uparrow}$ and $\xi_{\mathbf{k}} \to \xi_{\mathbf{k}\downarrow}$. This form of the Thouless criterion corresponds to the vanishing of the gap Δ in the mean-field equation (47) for a polarized superfluid.

At unitarity, the critical temperature obtained in this way decreases for increasing polarization, from the value $T_c/E_F = 0.21$ for balanced populations to the value $T_c/E_F \simeq 0.12$ at a critical polarization $\alpha_c = 0.13$ where the curve develops a re-entrant behavior (cf. the dashed line in Fig. 17), in analogy to what occurs within mean-field (cf. Fig. 7 of Section 2.6). This analogy would suggest one that the re-entrant behavior could be eliminated by taking into account the FFLO instability or phase separation. However, a problem arises at finite temperature with the FFLO instability within the present scheme, because a second-order phase transition to the FFLO phase would require the Thouless criterion to be satisfied for finite value $\mathbf{Q}_0$ of the pair momentum $\mathbf{Q}$ (that is, $\Gamma_0(\mathbf{Q}_0, \Omega_\nu = 0,)^{-1} = 0$) rather than for $\mathbf{Q} = 0$ as usually. This, in turn, implies that $\Gamma_0(\mathbf{Q}, \Omega_\nu = 0)$ diverges like $(|\mathbf{Q}| - |\mathbf{Q}_0|)^{-2}$ when $|\mathbf{Q}| \to |\mathbf{Q}_0|$ (in the present rotationally invariant case Γ_0 depends only on the magnitude $|\mathbf{Q}|$ of the wave vector). This divergence is non-integrable in the expression of the self-energy, in contrast to the standard case where the divergence of Γ_0 when $\mathbf{Q} \to 0$ is compensated by the factor Q^2 resulting from the spherical integration over $\mathbf{Q}$. As a consequence, when $T \to T_c$ the self-energy $\Sigma_\sigma(k)$ would diverge for all wave vectors and frequencies, a result which does not allow for a solution of the number equations. This failure of having a second-order phase transition associated with the FFLO phase within the NSR theory was pointed out in Ref. [209], following a similar conclusion drawn in Refs. [210,211] within a Ginzburg–Landau approach. The above argument appears to be quite general and is thus applicable, at finite temperature, to any version of the t-matrix approximation.

The above argument, on the other hand, will not be applicable if the transition from the normal to the FFLO phase is of *first order*, since in this case the transition occurs before the divergence of the particle–particle propagator will show up. In this respect, it was already mentioned in Section 2.6 that the detailed analysis of Ref. [117] in the weak-coupling limit has shown that the transition from the normal to the FFLO phase is indeed of first order even at the mean-field level. For ultra-cold Fermi gases, for which the two spin populations are separately conserved, this first-order transition corresponds to a phase separation between the polarized normal gas and a polarized FFLO superfluid. In general, this kind of phase separation will compete with the phase separation between the normal phase and a standard BCS superfluid (where Cooper pairs condense with zero center-of-mass wave vector). Finally, we mention some recent work on this matter where an analysis of the stability of the FFLO phase with respect to fluctuations was considered for the superfluid phase at finite temperature. While Refs. [212,213] conclude that low-energy fluctuations act to disorder the FFLO phase at long distances, yielding a phase with an algebraic decay of correlations, the renormalization-group analysis of Ref. [214] points to an instability of the FFLO phase towards phase separation between the normal and the standard BCS superfluid phase.

The experimental phase diagram for the polarized unitary Fermi gas was obtained in Ref. [137] and shows that indeed, beyond a critical polarization $\alpha_{tc} \approx 0.20$, the transition from the normal to the superfluid phase turns from second- to first-order, with a phase separation occurring between a polarized normal gas and a polarized superfluid (with no indication, however, about the BCS or FFLO nature of the superfluid component). This experimental phase diagram is shown in Fig. 17,

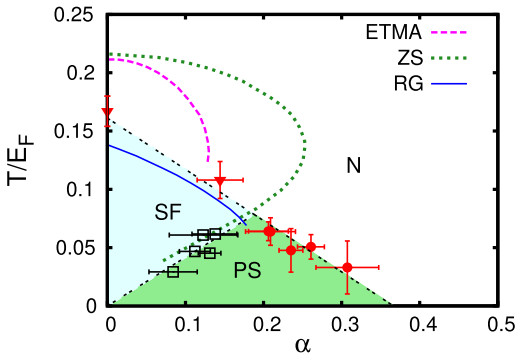

Fig. 17. Phase diagram for a unitary Fermi gas in the plane temperature (in units of T_F) vs polarization α. Symbols correspond to the experimental data from Ref. [137] for $\alpha \neq 0$ and from Ref. [183] for $\alpha = 0$. Circles: boundary between the normal phase (N) and the phase separation (PS) region; Triangles: boundary between the normal phase and the superfluid phase (SF); Squares: boundary between the superfluid phase and the phase separation region. Following Ref. [137], data are interpolated by straight lines to identify the three regions in the phase diagram. The second-order transition lines obtained by the theoretical ETMA [138], ZS [194], and renormalization group (RG) [50] approaches are also reported for comparison.

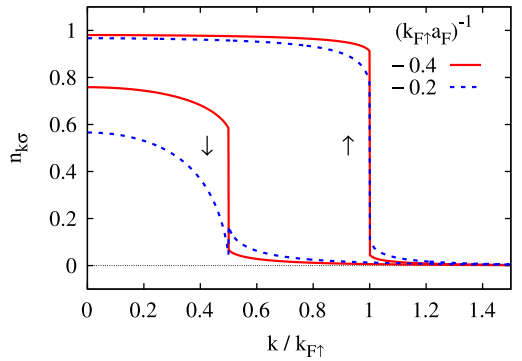

Fig. 18. Occupation numbers for majority (↑) and minority (↓) fermions vs the wave vector k in the normal phase at $T = 0$ when $k_{F\downarrow} = k_{F\uparrow}/2$, obtained within the pp-RPA approach for two values of the interaction strength.
Source: Adapted from Ref. [146].

where the second-order transition lines obtained by three different theoretical approaches are also reported: the ETMA of Ref. [138], the ZS approach of Ref. [194], and the renormalization group (RG) approach of Refs. [50,215]. The theoretical results are physically meaningful only for the part of the curves that precedes the re-entrant behavior, and for this reason the re-entrant branch is only partially reported. The physical branch can instead be compared with the experimental data for the second-order transition to the superfluid phase (triangles). One sees that, although the ETMA and ZS curves are somehow off the experimental data, they still represent an improvement over the mean-field curve of Fig. 7(b). The RG approach curve approximates instead quite well the experimental data for the second-order transition, including also the position of the tricritical point (that corresponds to the end point of the RG curve and to the upper vertex of the experimental PS region). This agreement appears quite remarkable, even though one should warn that there is some arbitrariness in the choice of couplings to be kept in the RG equations and in the way the RG flow is implemented, as pointed out in Ref. [50]. On the other hand, theoretical calculations are still missing for the first-order (N–PS and SF–PS) transition lines of Fig. 17, which would eventually allow for a quantitative comparison with the experimental data. [In this respect, it should be mentioned that the "pseudo-gap" approach of Ref. [216], which at zero temperature reduces to the mean-field approximation discussed in Section 2.6, cannot be used for such a quantitative comparison, while the functional renormalization group results of Ref. [217] are expressed in terms of grand-canonical variables and for this reason they cannot be directly compared with the phase diagram of Fig. 17].

As a final remark, we discuss the relevance of the Luttinger theorem in the context of imbalanced systems. According to this theorem [218], interaction effects in the normal phase do not modify the position of the Fermi step in wave-vector space at $T = 0$. In the polarized case, one has to impose a strong polarization such that the system remains normal even at $T = 0$, in such a way that a jump is expected to occur in the occupation numbers $n_{\mathbf{k}\sigma}$ at the respective Fermi wave vectors $k_{F\sigma} = (6\pi^2 n_\sigma)^{1/3}$. As an illustration, Fig. 18 shows $n_{\mathbf{k}\sigma}$ obtained for $k_{F\downarrow} = k_{F\uparrow}/2$ within the pp-RPA approach at $T = 0$ for two different couplings. It turns out that the depletion of $n_{\mathbf{k}\sigma}$ below $k_{F\sigma}$ due to interaction effects is compensated by the filling of $n_{\mathbf{k}\sigma}$ above $k_{F\sigma}$, in such a way that the Luttinger theorem is satisfied for each σ as shown analytically in Ref. [146]. However, one sees from Fig. 18 that for the stronger coupling $(k_{F\uparrow}a_F)^{-1} = -0.2$ the jump of $n_{\mathbf{k}\downarrow}$ at $k_{F\downarrow}$ is positive instead of

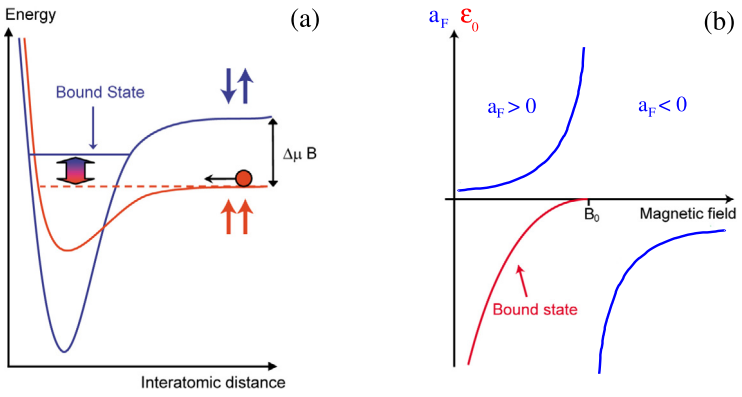

Fig. 19. (a) Coupling of closed and open dimer scattering channels, which can be displaced relative to each other by the coupling to a magnetic field B. (b) The corresponding scattering length vs the magnetic field. When $a_F > 0$, a bound state with binding energy $\varepsilon_0 = (ma_F^2)^{-1}$ sets in.
Source: Adapted from http://cua.mit.edu/ketterle_group.

being negative, resulting in a negative quasi-particle residue $Z_{\mathbf{k}\downarrow}$. This shortcoming signals the breakdown of the perturbative treatment (like in Eq. (60)) of the self-energies Σ_σ in the pp-RPA approach. It is relevant to mention that the $T = 0$ formalism of the pp-RPA approach, where the bare particle propagators are defined in terms of the Fermi wave vectors $k_{F\sigma}$ instead of the chemical potentials μ_σ [95] and in terms of which the results of Fig. 18 have been obtained, has been shown to be equivalent to the ZS approach in the $T \to 0$ limit [146], due to the inclusion of the mean-field-like quasi-particle energy shift (cf. Section 3.5). For this reason, the results obtained above for the Luttinger theorem at $T = 0$ within the pp-RPA approach apply also to the ZS approach reported in the phase diagram of Fig. 17.

4. BCS–BEC crossover in ultra-cold Fermi gases

Ultra-cold Fermi gases have provided a unique opportunity for realizing experimentally the BCS–BEC crossover. This is because a method was found to vary the scattering length a_F of the two-fermion problem, from negative to positive values across the resonance where $a_F = \pm\infty$, while keeping the density of the system (and thus the corresponding Fermi wave vector k_F) fixed. In this way, the experimental data have been associated with and labeled by the value of the dimensionless coupling parameter $(k_F a_F)^{-1}$ which is also used theoretically to drive the BCS–BEC crossover, thereby allowing for a direct and unambiguous comparison between experiments and theory. Below we shall describe the main aspects and achievements of the BCS–BEC crossover that have emerged with ultra-cold Fermi gases during the last several years. We refer to Refs. [51,219] for further reviews on the BCS–BEC crossover with ultra-cold fermionic atoms.

4.1. Fano–Feshbach resonances and the interaction-induced crossover

In the context of ultra-cold Fermi gases, the Fano–Feshbach resonances [220–222] occur via the coupling of alternative scattering channels, when a bound level in a *closed* molecular channel can be displaced continuously with respect to the threshold of an *open* channel. This occurs by exploiting the different Zeeman coupling felt by the two (closed and open) channels in an external magnetic field B [49].

The atom–atom interaction can thus be varied, from a condition when the resonant bound state is embedded in the continuum above threshold, to a condition when a true bound state exists below threshold (cf. Fig. 19(a)). Correspondingly, the scattering length a_F for the low-energy scattering changes from negative to positive values, being associated with attractive or repulsive interactions in the two cases, and diverges when the bound state sets in (cf. Fig. 19(b)).

In particular, for a "broad" Fano–Feshbach resonance (with respect to the variations of B), such that the effective range can be neglected in the expression of the scattering amplitude, the interaction between atoms with different spin labels can be modeled by a contact interaction with a negative strength v_0, where, in turn, v_0 can be eliminated in terms of a_F like in Eq. (7) [223]. What is here meant by "spin" is the quantum number associated with the atomic hyperfine levels that are split apart by the magnetic field itself. The two hyperfine levels of lowest energy are then conventionally referred to as spin $\uparrow$ and spin $\downarrow$, and can be populated independently with $N_\uparrow$ and $N_\downarrow$ atoms (in practice, $N = N_\uparrow + N_\downarrow$ is at most of the order of 10^6). For instance, in ^{6}Li for B large enough the states $|\downarrow\rangle$ and $|\uparrow\rangle$ correspond to $|m_I = 1, m_J = -\frac{1}{2}\rangle$ and $|m_I = 0, m_J = -\frac{1}{2}\rangle$, respectively, where $I = 1$ and $J = \frac{1}{2}$ are the nuclear and electron spin quantum numbers with projections m_I and m_J. In addition, the dependence of a_F on B can be inferred either directly from the experiment [69] (cf. Fig. 20(a)) or from a molecular calculation [49,223] (cf. Fig. 20(b)).

For a Fano–Feshbach resonance, the resonant condition $a_F = \pm\infty$, which occurs when the bound state crosses the threshold of the continuum, corresponds to the "unitarity limit" whereby $(k_F a_F)^{-1} = 0$. While in principle the BCS

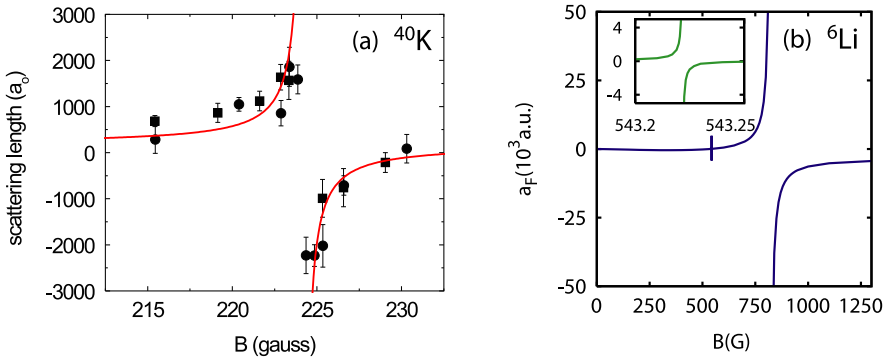

Fig. 20. (a) Measurements of the scattering length (in units of the Bohr radius a_0) vs the magnetic field B near the broad Fano-Feshbach resonance of ^{40}K Fermi atoms. (b) Calculated scattering length a_F (in atomic units) for the collision of two fermionic ^{6}Li atoms vs the magnetic field B (in Gauss), which detunes the scattering from the closed channel. The inset shows the behavior of a_F for the narrow resonance at about 543G.
Source: Panel (a) adapted from Ref. [69]; panel (b) adapted from Ref. [223].

condition of strongly overlapping Cooper pairs corresponds to $(k_F a_F)^{-1} \ll -1$ and the BEC condition for molecular bosons corresponds to $(k_F a_F)^{-1} \gg +1$, it turns out that the evolution from the BCS to BEC limits is best studied in the limited range $-1 \lesssim (k_F a_F)^{-1} \lesssim +1$ for the following reasons. On the one hand, it is found by theoretical calculations that this limited range is sufficient in practice for realizing the BCS–BEC crossover in most physical quantities. On the other hand, the range $-1 \lesssim (k_F a_F)^{-1} \lesssim +1$ is just where the experiments can be realized because: (i) when $(k_F a_F)^{-1} \ll -1$ the experimental signal is usually too weak to be detected; (ii) when $(k_F a_F)^{-1} \gg +1$ the molecules (which are in the highest vibrational state of the interatomic potential) undergo rapid vibrational relaxation via three-body collisions, leading to heating and trap losses which set an upper limit on the value of $(k_F a_F)^{-1}$ up to which the experimental data can be trusted.

4.2. Main experimental results

The distinctive and rather unique feature of the BCS–BEC crossover with trapped ultra-cold Fermi gases is that a variety of targeted experiments have been realized with these systems over the last decade, which have specifically allowed to follow the continuous evolution of the system between the two (BCS and BEC) limits. The large majority of these experiments have been realized with ^{6}Li atoms, using the broad Fano–Feshbach resonance occurring at 832 G to tune the interaction, while the remaining experiments used ^{40}K atoms and the broad Fano-Feshbach resonance at 202.2 G. In both cases, the interaction between fermions can be accurately modeled by the contact potential described in detail in the previous sections. It should be recalled in this context that, initially, most of the theoretical studies of the BCS–BEC crossover with ultra-cold atoms were instead based on a "two-channel" model, which includes explicitly the closed-channel molecules in the Hamiltonian [224–229]. In Ref. [223] it was eventually clarified, however, that for a broad resonance a "single-channel" contact potential is adequate to describe the system in an extended range of magnetic field that spans the whole BCS–BEC crossover. This property of broad Fano-Feshbach resonances is fundamental for using ultra-cold atoms to simulate the BCS–BEC crossover in a universal fashion, independent of the details of the inter-atomic interaction.

An additional aspect to be considered for the use of ultra-cold gases as effective "quantum simulators", is that ultra-cold gases require a trap to hold the neutral atoms together. Most useful in this sense prove to be the *optical traps*, which allow for an independent application of a magnetic field to tune a Fano-Feshbach resonance. In practice, these traps act on the atoms as an external potential proportional to the laser intensity, which has usually the shape of an inverted Gaussian. For most purposes, it is sufficient to expand this inverted Gaussian up to second order around its minimum, leading to an anisotropic harmonic potential of the form

$$V_{\rm ext}(\mathbf{r}) = \frac{1}{2} m \left(\omega_x^2 x^2 + \omega_y^2 y^2 + \omega_z^2 z^2\right) \tag{94}$$

where $\mathbf{r} = (x, y, z)$, with typical values of the frequencies $(\omega_x, \omega_y, \omega_z)$ ranging from tens to thousands of Hz.

When comparing theory and experiments, one thus needs, in general, to consider the effects of the trapping potential (94). This is usually done by relying on a local-density approximation (LDA), whose conditions of validity are normally satisfied in the experiments. By this approximation, the trapped gas is regarded as a (continuous) collection of independent homogeneous systems characterized by a "local" chemical potential $\mu(\mathbf{r}) = \mu_{\rm trap} - V_{\rm ext}(\mathbf{r})$, with a common temperature T and scattering length a_F. [To avoid ambiguities, we have here introduced the chemical potential $\mu_{\rm trap}$ of the trapped system to distinguish it from that of the homogeneous system]. Physical quantities then result by averaging (that is, by integrating) over the contributions at different $\mathbf{r}$. In this context, it is also useful to introduce the trap Fermi energy $E_{F\,\rm trap} = \omega_0 (3N)^{1/3}$ (associated with an ideal balanced Fermi gas at $T = 0$), where $\omega_0 = (\omega_x \omega_y \omega_z)^{1/3}$ is the geometrically averaged trap frequency [230]. In terms of $E_{F\,\rm trap}$, one can also define the Fermi wave vector $k_{F\,\rm trap} = \sqrt{2mE_{F\,\rm trap}}$ for the trap and form the

dimensionless coupling parameter $(k_{F\,\mathrm{trap}}a_F)^{-1}$. [Note, however, that these numbers do *not* coincide with the local values of k_F and $(k_F a_F)^{-1}$ associated with the density of the system at the trap center.] Thermodynamic quantities can be made dimensionless by using appropriate powers of $E_{F\,\mathrm{trap}}$, $k_{F\,\mathrm{trap}}$ and N, in such a way that they depend solely on the interaction parameter $(k_{F\,\mathrm{trap}}a_F)^{-1}$ and the dimensionless temperature $T/E_{F\,\mathrm{trap}}$ (see, e.g,. Refs. [231–233]). Recently, novel experimental methodologies have become available which apply tomographic reconstruction techniques to the bare experimental data by still relying on the above LDA approximation [234,235], thus allowing for a direct extraction of quantities characteristic of the homogeneous gas from the experiments made on the trapped gas.

An impressive series of experiments has been realized with ultra-cold Fermi gases over the last decade, covering a broad number of physical (both thermodynamic and dynamical) quantities. These experiments include:

(i) The initial production of long-lived composite bosons [236–239];
(ii) The condensation of composite bosons [240–242];
(iii) The evidence of a condensate extending also to the BCS side of the crossover [243,244] with the "projection" technique introduced in Ref. [243] (see Refs. [245] and [246] for a theoretical and experimental analysis of this technique, respectively);
(iv) The evidence for a pairing gap with radio-frequency spectroscopy [234,247,248] and its quantitative measurement using a small population imbalance [249];
(v) The study of collective modes in a trap, in particular, the measurement of frequencies and damping rates of breathing [250–254], radial quadrupole [255,256], scissors [254,256], and higher-nodal axial modes [257];
(vi) The measurement of several thermodynamic properties of the unitary Fermi gas across the superfluid transition, including the critical temperature [182,183,258,259], the specific heat and entropy [258,259], the equation of state, chemical potential and pressure [182,183,260,261];
(vii) The precise measurement of the closed-channel contribution in ^{6}Li, that has confirmed the validity of the single-channel model [262];
(viii) The detection of pairing correlations with atom shot noise measurements [263], following the proposal of Ref. [264];
(ix) The observation of vortices throughout the whole crossover [265];
(x) The detection of phase separation [108,109,266] and the measurement of the critical temperature [137,267] and polarization [267–269] in imbalanced Fermi gases;
(xi) The measurement of first- [270] and second-sound [271] velocities;
(xii) The measurement of the critical velocity for the superfluid flow [272,273];
(xiii) The estimate of the Cooper pair size ξ_{pair} [274];
(xiv) The measurement of single-particle spectral features (with evidence of a pseudo-gap) with wave-vector resolved radio-frequency spectroscopy [31,32];
(xv) The measurement of the Tan's contact [275–279] and the verification of universal relations connected with this quantity [275,276];
(xvi) The measurement of the shear viscosity and of its ratio with the entropy density [280–283], to test the "universal minimum" conjectured for this quantity by string-theory methods [284];
(xvii) The measurement of static [285] and dynamic spin [286] and density [279,287] response functions;
(xviii) The evidence for a superfluid quenching of the moment of inertia [288] and the measurement of the superfluid fraction [271];
(xix) The measurement of "current–voltage" characteristic curves for transport through a quantum point contact in the unitary Fermi gas across the superfluid transition [289];
(xx) The detection of the Josephson's oscillations throughout the BCS–BEC crossover [290].

The above experiments have explored rather completely the BCS–BEC crossover in three dimensions. More recently, experimental studies have been conducted for the BCS–BEC crossover also in systems with reduced dimensionality. In particular, for a two-dimensional gas experiments have analyzed pairing effects [291,292] and single-particle spectral features [33], collective modes and the shear viscosity [293], the ground-state pressure [294], the effects of spin imbalance [295], the superfluid critical temperature [296,297], and the equation of state [298,299]. Finally, Ref. [300] has analyzed the phase-separation in a one-dimensional spin-imbalanced Fermi gas, confirming the predictions based on the Bethe-ansatz [301] and providing indirect evidence for the occurrence of FFLO ordering in the system.

4.3. The unitary limit

In the context of ultra-cold Fermi gases, special attention has been devoted to the "unitary limit" of the inter-particle interaction, when the scattering length is infinite. At the two-body level, in this limit the scattering cross section approaches $\sigma(k) = 4\pi/k^2$ at low relative wave vector k, which corresponds to the unitarity bound for the (s-wave) scattering cross section and stems directly from the unitarity condition of the S-matrix (see, e.g., Ref. [302]).

At the many-body level, interest in this limit of the interaction was stimulated by G. Bertsch at the 10th conference on "Recent progress in many-body theories" (see Refs. [19] and [20]). As a challenge to the participants, Bertsch proposed the problem of determining the ground-state properties of a (homogeneous) system of fermions interacting via a contact interaction tuned at infinite scattering length (then referred to as the "unitary Fermi gas"). This case is particularly interesting

also for a dilute neutron gas, where the scattering length is much larger than the inter-particle distance (cf. Section 5). What is intriguing of the unitary limit is that there are no length scales associated with the interaction, paradoxically somehow just like for the non-interacting Fermi gas. The only length scale that remains at zero temperature is the average inter-particle spacing k_F^{-1} which is fixed by the density. More generally, the thermodynamic properties of the unitary Fermi gas depend only on density and temperature. A few universal functions of the dimensionless temperature T/E_F (or, at zero temperature, a few universal numbers) then suffice to characterize the properties of the unitary Fermi gas and for this reason the unitary gas is said to be *universal*. In addition, several nontrivial relationships between thermodynamic observables can be derived [303], which are particularly useful to extract from experiments thermodynamic quantities that cannot directly be measured (or are especially difficult to measure).

For the unitary Fermi gas, the absence of a length scale associated with the interaction has interesting consequences also for trapped systems. For instance, it can be shown [304] that at zero temperature the spatial profile $n(\mathbf{r})$ of the density within LDA is completely specified in terms of the value of a single parameter ξ. This parameter (referred to as the Bertsch parameter) is defined as the ratio between the ground-state energy of the unitary *homogeneous* Fermi gas and that of the non-interacting system (this ratio corresponds also to μ/E_F as a consequence of scale invariance). The argument goes as follows. For a contact potential at $T = 0$, the chemical potential in units of the Fermi energy depends only on the dimensionless coupling $(k_F a_F)^{-1}$, such that for the homogeneous gas $\mu/E_F = F\left((k_F a_F)^{-1}\right)$ where F is a universal function. The LDA then implies that for the trapped system:

$$\mu(\mathbf{r})/E_F(\mathbf{r}) = F\left((k_F(\mathbf{r})a_F)^{-1}\right) \tag{95}$$

with the local quantities $k_F(\mathbf{r}) = (3\pi^2 n(\mathbf{r}))^{1/3}$, $E_F(\mathbf{r}) = k_F(\mathbf{r})^2/2m$, and $\mu(\mathbf{r}) = \mu_{\rm trap} - V_{\rm ext}(\mathbf{r})$. A remarkable feature of the unitary limit is that the "local" dimensionless coupling $(k_F(\mathbf{r})a_F)^{-1}$ does not depend on the position $\mathbf{r}$ in the trap, such that $\mu(\mathbf{r})/E_F(\mathbf{r}) = F(0) \equiv \xi$ as for the homogeneous gas. This relation can be inverted to get $E_F(\mathbf{r}) = \mu(\mathbf{r})/\xi$, thus yielding for the density profile the expression:

$$n(\mathbf{r}) = \xi^{-3/2}[2m(\mu_{\rm trap} - V_{\rm ext}(\mathbf{r}))]^{3/2}/(3\pi^2) \tag{96}$$

which has the same form of the non-interacting Fermi gas apart from the pre-factor $\xi^{-3/2}$. In addition, the expression $N = \int d\mathbf{r}\, n(\mathbf{r})$, once applied alternatively to Eq. (96) and to the corresponding equation for the non-interacting gas, yields the relation $\mu_{\rm trap}/E_{F\,\rm trap} = \xi^{1/2}$, which connects the ratio between the chemical potential $\mu_{\rm trap}$ of the unitary Fermi gas and the Fermi energy $E_{F\,\rm trap} = \omega_0 (3N)^{1/3}$ of the non-interacting Fermi system in the trap, to the corresponding ratio ξ for the homogeneous gas. Eq. (96) also implies that the axial and radial radii of the cloud at unitarity are reduced by a factor $\xi^{1/4}$ with respect to the corresponding values of the non-interacting Fermi gas, a result that was used to obtain some of the first experimental estimates of the Bertsch parameter [305,306]. The spatial invariance of the local coupling strength for the trapped unitary Fermi gas leads also to the relation

$$\Delta(\mathbf{r}) = \frac{\eta}{\xi}\,\mu(\mathbf{r}) \tag{97}$$

for the local gap parameter $\Delta(\mathbf{r})$, where η is the ratio Δ/E_F for the homogeneous unitary Fermi gas at $T = 0$. Also the gap profile of the trapped unitary Fermi gas has thus the form of an inverted parabola.

4.4. Theoretical approaches to the unitary limit and comparison with experiments

The universality of the unitary Fermi gas and the possibility to realize it in experiments with ultra-cold atoms has motivated a number of theoretical studies of this system, and in particular of its ground-state energy characterized by the Bertsch parameter ξ. The first estimate of the Bertsch parameter was given in Ref. [20] by using a Padé-approximant extrapolation of the perturbative expansion of the ground-state energy of a dilute Fermi gas, with the result $\xi = 0.43 \pm 0.13$. Since then, a number of theoretical works have calculated the value of the Bertsch parameter. Analytic or semi-analytic works have improved the simple BCS mean-field estimate $\xi = 0.59$ by including pairing fluctuations in the superfluid phase with diagrammatic [151,159,304] or functional integral approaches [44,45], by using ϵ [307–309] and large-N expansions [310], or by the functional renormalization group approach [311,312]. A few words about these approaches are required.

The ϵ expansion exploits the fact that, in $d = 2$ dimensions the unitary Fermi gas is a non-interacting Fermi gas, while in $d = 4$ it is a gas of non-interacting dimers [313]. By calculating the loop integrals using dimensional regularization, one can perform calculations in arbitrary dimensions near $d = 2$ or $d = 4$ and make expansions in $\bar{\epsilon} = d - 2$ or in $\epsilon = 4 - d$, respectively. To get predictions for the physical case with $d = 3$, one then tries to match these two expansions. Depending on the details of the approximations used for this matching, one obtains $\xi = 0.364$ to 0.391 [308]. The ϵ expansion can also be used for finite temperature calculations [314]. For instance, for the critical temperature this approach gives $T_c/E_F = 0.183 \pm 0.014$.

The large-N expansion provides another way to circumvent the absence of a small expansion parameter in the unitary Fermi gas. Here, one introduces N species ("flavors") of fermions distinguished by an index i ($i = 1, \ldots, N$), each having two spin projections ($\sigma = \uparrow, \downarrow$) and mutually interacting via [310]

$$H_{\rm int} = \frac{g}{N}\sum_{i,j=1}^{N}\int d\mathbf{r}\, \psi_{i\uparrow}^{\dagger}(\mathbf{r})\,\psi_{i\downarrow}^{\dagger}(\mathbf{r})\,\psi_{j\downarrow}(\mathbf{r})\,\psi_{j\uparrow}(\mathbf{r})\,, \tag{98}$$

$\psi_{i\sigma}(\mathbf{r})$ being the field operator for the fermion species i and spin σ and g the coupling constant. Note that the interaction has a Sp($2N$) symmetry and can transform a pair of one species j into a pair of another species i. For this reason, the case $N = 2$ is different from the isospin in nuclear physics, where the numbers of protons and neutrons are instead separately conserved. Note in addition that the number of species N is a purely formal parameter (like the quantity ϵ above) and the physical results correspond to $N = 1$. What is relevant here is that, in the limit $N \to \infty$, the BCS mean-field approximation becomes exact, and corrections in $1/N$ can be calculated by including the RPA on top of it. Including only the leading term and the $1/N$ correction, and then extrapolating the result to $N = 1$, one finds for the Bertsch parameter the value $\xi = 0.28$.

The same ϵ and large-N expansions were used also in Ref. [315], where they have been framed in the standard approach for critical phenomena. In this case, the starting point was the observation that the unitary Fermi gas in the zero-density limit can be interpreted as a quantum multi-critical point at $\mu = (k_F a_F)^{-1} = h = T = 0$, which can be used as the fixed point of a renormalization-group analysis.

Finally, the functional renormalization group starts from a flow equation for the effective-action generating functional. Approximate solutions of the flow equation can be found by using truncations in the space of possible functionals (see Refs. [40,316] for recent reviews of this method).

Before we turn to the fully numerical works, let us mention that at high temperature, the fugacity $e^{\beta\mu}$ can be used as a small expansion parameter, leading to the virial expansion. Of course it cannot be used to compute the universal parameters ξ or η, but it allows for the calculation of the equation of state of the unitary Fermi at high temperatures which has been measured to high precision. While the second-order virial coefficient for a contact interaction was calculated long time ago [317], the virial expansion was pushed to higher order only recently. In particular, the third-order virial coefficient for the unitary Fermi gas was obtained in Refs. [318–320] with different techniques (see Ref. [42] for a review). For the fourth-order virial coefficient, on the other hand, a discrepancy that was found between the theoretical estimates [321,322] and the experimental value [182,183] was resolved only recently by a fully numerical calculation [323] that agrees with the experimental value.

A completely different way of approaching the unitary Fermi gas consists in trying to solve the problem using fully numerical techniques. One can distinguish between studies of particles in a harmonic potential and studies of particles in a box with periodic boundary conditions. Calculations for particles in a harmonic potential are especially interesting because of their similarity with nuclear systems and because they allow one to extract the coefficients of the leading gradient terms (i.e., beyond LDA) in the energy density functional [324]. Such calculations have been done using the direct diagonalization of the Schrödinger equation in the basis of correlated Gaussians (CG) for few particles (up to six in Ref. [325] and up to ten in Ref. [326]), and for larger particle numbers using Green's function [327] and fixed-node diffusion Monte-Carlo (FN-DMC) [325], lattice Monte-Carlo [328], and auxiliary-field Monte-Carlo (AFMC) [324]. The pairing gap, defined as the energy difference between odd and even numbers of particles (corresponding to the lowest quasiparticle energy, which is generally smaller than the local gap at the trap center), was discussed in Refs. [325,327]. Unfortunately, results of different calculations do not agree with each other (see Fig. 10 of Ref. [39]). It should be stressed, however, that while FN-DMC is just a variational method with an unknown error bar a priori, AFMC and lattice Monte-Carlo are in principle exact (and free from the fermionic sign problem for the imbalanced gas). In practice, it turns out to be quite difficult to reach the zero-range interaction limit in this kind of calculations. It is also not clear why the lattice calculations [328] show pronounced shell effects (that is, strongly reduced energies per particle at shell closures $N = 2, 8, 20, 40$) in contrast to all other approaches, where the shell effects seem to be washed out by the strong pairing.

Calculations for particles in a box with periodic boundary conditions are better suited for the extrapolation to a uniform gas, although it remains difficult to control finite size effects. These calculations, too, were performed using different numerical methods. Like in the trapped case, the results show strong variations. The predictions for the Bertsch parameter ξ vary between $\xi = 0.25$ in the first lattice calculation [329] and $\xi = 0.44$ in the first DMC calculation [330]; in later lattice [331] and FN-DMC calculations [332–336] the value of ξ slowly converged over the years (see table VI of Ref. [337]) towards the value $\xi = 0.37$ that was obtained in the latest AFMC [338] and lattice [337] calculations simulating up to 66 particles. (The AFMC technique was also used for neutron matter, see Section 5.5.)

Correspondingly, a number of experimental works has determined ξ with increasing precision [109,183,260,305,306,339–342], culminating with the value $\xi = 0.370 \pm 0.005$ obtained in Ref. [183] (this value takes into account a small systematic-error correction associated with a subsequent more precise determination of the position of the broad Fano-Feshbach resonance of ^{6}Li [343]). This experimental value agrees well with the state-of-the art theoretical results $\xi = 0.372 \pm 0.005$ and $\xi = 0.366^{+0.016}_{-0.011}$ obtained in Refs. [338] and [337], respectively. In addition, the value $\eta = 0.44 \pm 0.03$ for the parameter η of Eq. (97) was determined experimentally in Ref. [249], in good agreement with the QMC result $\eta = 0.45 \pm 0.05$ of Ref. [344]. These comparisons exemplify the high degree of accuracy that is nowadays possible to reach in experiments with ultra-cold Fermi gases, thereby pointing out the effectiveness of these gases as "analog" quantum simulators of many-body problems.

The unitary Fermi gas has been analyzed in detail also at finite temperature. The main experiments that have contributed to the characterization of the thermodynamic and dynamical properties of the unitary Fermi gas have already been mentioned in Section 4.2. On the theoretical side, the (homogeneous) unitary Fermi gas has represented a central issue of finite-temperature QMC calculations, and actually most of the numerical efforts have been focused on this specific coupling value of the BCS–BEC crossover. The auxiliary-field QMC method has extensively been applied to the calculation of thermodynamic quantities, such as the temperature dependence of the chemical potential, energy, and entropy [175,345,346] as well as of the

wave-vector distribution and "contact" constant [347]. In principle, this method is unbiased for thermodynamic quantities, although the effects due to space and time discretization, the finite-size of the sample, and the use of a finite-range interaction introduce significant sources of uncertainty (which are discussed in detail in Ref. [346]). The same method has also been applied to the calculation of dynamical quantities, such as the spectral-weight function [348] and the (frequency dependent) spin susceptibility [349] and shear viscosity [350–352]. It should be recalled, however, that the extraction of dynamical quantities from QMC simulations relies on a numerical solution of the problem of the analytic continuation of a function from the imaginary to the real axis. Such a numerical solution is notoriously an ill-posed problem, which unavoidably requires uncontrolled assumptions on the properties and the overall structure of the function to be continued analytically. For these reasons, the results for dynamical quantities extracted from QMC simulations should be considered with caution.

Alternative Monte Carlo methods based on diagrammatic expansions of the partition function or of the single-particle self-energy have also been applied to the (homogeneous) unitary Fermi gas. The determinant diagrammatic Monte Carlo method has been used in Refs. [184,185,353] and in Ref. [186] for the calculation of the critical temperature, chemical potential, and energy of the unitary Fermi gas. Their results for the critical temperature $T_c/E_F = 0.152 \pm 0.007$ [184,185] and $T_c/E_F = 0.173 \pm 0.006$ [186] slightly disagree with each other, probably because of the different extrapolations to the continuum limit from the lattice model used in the calculations. These results, however, are both consistent with the experimental values $T_c/E_F = 0.157 \pm 0.015$ [182], 0.17 ± 0.01 [261], and 0.167 ± 0.013 [183]. In this respect, it should be noted that a crucial advance of Ref. [183] was the determination of the temperature directly from the density profiles without the use of a fitting procedure or an external thermometer.

In addition, the bold diagrammatic Monte Carlo method [155] was used in Ref. [354] to obtain the equation of state of the unitary Fermi gas in the normal phase. This method is formulated directly in the thermodynamic limit and can thus be applied to the continuum system with a genuine contact interaction. It is based on the idea of sampling stochastically Feynman diagrams for the (imaginary time) self-energy using "bold" (that is, self-consistent) fermionic single-particle propagators G and particle–particle propagators Γ, summing up in this way a huge number of diagrams. The method relies on the assumption that the Feynman series of self-consistent (skeleton) diagrams, possibly regularized with re-summation techniques for diverging series, converges to the physical self-energy Σ. This assumption, however, was challenged in Ref. [355] (see also Ref. [356]), where explicit counter-examples were given. The reported excellent agreement with the experimental data for the unitary Fermi gas [354], on the other hand, seems to indicate *a posteriori* that, at least for the unitary Fermi gas in the normal phase, a good convergence to the physical self-energy can be reached. Clearly, an *a priori* knowledge about the expected range of validity of the method would be desirable. Progress in this direction was recently made in Ref. [357], where a sufficient condition was established for the convergence to the correct result by the self-consistent skeleton scheme.

We conclude by pointing out that, although the unitary Fermi gas has been at the forefront of both theory and experiments in the field of ultra-cold Fermi gases, under the perspective the BCS–BEC crossover the unitary limit $(k_F a_F)^{-1} = 0$ represents just one point (and not necessarily the most significant one) within the intermediate-coupling region. For instance, as discussed in Section 3.3, the boundary between the fermionic (pseudo-gap) and bosonic (molecular) regimes of the BCS–BEC crossover is found to occur past unitarity at about $(k_F a_F)^{-1} \simeq 0.5$ [171]. In addition, the maximum value of the superfluid critical velocity (which signals where superfluidity is most robust) does not occur exactly at unitarity but slightly past it, as obtained by theoretical calculations [358] and measured by experiments [272,273] (see Section 4.6). Finally, in two dimensions, where the unitary gas (that is, a scale-invariant interacting Fermi gas) cannot be defined, the intermediate region of the BCS–BEC crossover is still perfectly meaningful, and the unitary limit can be replaced with alternative concepts characterizing the crossover region [170].

4.5. Tan contact

A major advance in the understanding of the physical properties of many-body systems with short-range interaction (like ultra-cold Fermi gases) has recently come from the introduction of a set of universal relations, expressed in terms of a quantity called the *contact* C, which connect the strength of short-range two-body correlations to the thermodynamics and provide powerful constraints on the behavior of the system irrespective of its state [359–361].

Originally, Tan derived the universal relations for the contact C by a suitable enforcement of the boundary conditions at short inter-particle distance on the many-body Schrödinger wave-function for otherwise non-interacting particles. Later on, these relations were re-derived within quantum field theory methods involving the operator product expansion [362,363], as well as using the Schrödinger formalism in the coordinate representation [364].

From a physical and intuitive point of view, the contact C describes how the two-body problem locally merges into the surrounding many-body problem, by considering the short-distance behavior of the pair correlation function for opposite-spin fermions [359,365]:

$$g_{\uparrow\downarrow}(\boldsymbol{\rho}) \underset{(\rho\to 0)}{\longrightarrow} \frac{C}{(4\pi)^2}\left(\frac{1}{\rho^2} - \frac{2}{a_F \rho} + \cdots\right) \tag{99}$$

which generalizes the expression (74) obtained in Section 3.2 at the level of the t-matrix. Alternatively, the contact can be defined via the large wave-vector tail of the fermionic distributions $n_\sigma(k)$ with $k = |\mathbf{k}|$, which behaves asymptotically as [359]

$$n_\sigma(k) \approx \frac{C}{k^4}\,. \tag{100}$$

With a zero-range inter-particle interaction, both the kinetic and interaction energies diverge but their sum is well-defined, such that the internal energy density E/V and the pressure P can be expressed in terms of the contact C as [359,360]:

$$\frac{E}{V} = \frac{C}{4\pi a_F m} + \int \frac{d\mathbf{k}}{(2\pi)^3} \frac{k^2}{2m} \left(n_\sigma(k) - \frac{C}{k^4} \right) \tag{101}$$

$$P = \frac{2}{3}\frac{E}{V} + \frac{C}{12\pi a_F m} \tag{102}$$

where V is the volume occupied by the system. One can also show that the derivative of the energy (at constant entropy) and of the free energy (at constant temperature) with respect to the scattering length can be related to the contact through the following "adiabatic relations" [360,365]:

$$\left(\frac{\partial E}{\partial a_F^{-1}} \right)_S = -\frac{CV}{4\pi m} \tag{103}$$

$$\left(\frac{\partial F}{\partial a_F^{-1}} \right)_T = -\frac{CV}{4\pi m} \,. \tag{104}$$

Additional quantities depend only on the short-range behavior of the pair correlation function and can therefore be expressed in terms of the contact C. In particular, the high-frequency tail of the radio-frequency (RF) spectrum $I_{\rm RF}(\omega)$ [366] approaches $I_{\rm RF}(\omega) \approx C\omega^{-3/2}/(2^{3/2}\pi^2)$ (where ω is in units of E_F and $\int_{-\infty}^{+\infty} d\omega I_{\rm RF}(\omega) = 1/2$), which holds provided final-state effects in the RF transition can be neglected (see Ref. [367] for a derivation of the high-frequency tail based on a short-time operator product expansion). Another example is the large wave-vector tail of the static structure factor $S(Q) \approx C[1/(8Q) - 1/(2\pi a_F Q^2)]$ where $Q = |\mathbf{Q}|$ [368]. Also the number of closed-channel molecules near a Fano-Feshbach resonance is proportional to the contact [369,370]. For a comprehensive review of the universal relations involving the contact, cf. Ref. [365].

Albeit useful at a formal level, the above relations do not allow one to actually compute the value of the contact C, as a function of coupling and temperature. We now turn to this point, restricting ourselves to the case of a balanced gas. The simplest way to introduce (and calculate) the contact is to consider the large wave-vector behavior of the fermionic distribution $n(k)$ (per spin component). At the mean-field level, $n(k)$ is given by the factor $|v_{\mathbf{k}}|^2 = (1 - \xi_{\mathbf{k}}/E_{\mathbf{k}})/2$ that enters the BCS wave function (1). Upon expanding this factor for large k, one obtains:

$$n(k) = |v_{\mathbf{k}}|^2 \simeq \frac{\Delta^2}{4\,\xi_{\mathbf{k}}^2} \simeq \frac{(m\Delta)^2}{k^4} \tag{105}$$

which allows one to approximate the contact C with the quantity $(m\Delta)^2$ at this level of approximation. In particular, in the BEC limit at $T = 0$, one gets $(m\Delta)^2 = 4\pi n_0/a_F$ from the relation between the gap Δ and the wave function Φ of the Gross–Pitaevskii equation (46), where n_0 is the condensate density within the present approximation. In the BCS regime, on the other hand, Δ is exponentially small in the coupling parameter $(k_F a_F)^{-1}$ and thus the value $(m\Delta)^2$ cannot properly represent the contact in this limit. However, one knows on general grounds that in weak coupling C must reduce to the expression $(2\pi a_F n)^2$ as it can be readily obtained from the adiabatic relation reported above, where $\pi a_F n^2/m$ represents the leading coupling dependence of the free energy at $T = 0$.

Inclusion of pairing fluctuations somewhat modifies the mean-field results and recovers, in particular, the correct value for the contact in weak coupling at $T = 0$. The simplest way to assess the effect of pairing fluctuations is to consider the normal phase above T_c in terms of the non-self-consistent t-matrix approximation. For large $|\mathbf{k}|$ the approximate expressions (65) and (66) hold at any coupling, such that one obtains

$$n(k) \simeq -\,\Delta_\infty^2\; T \sum_n G_0(k)^2\, G_0(-k) \tag{106}$$

for each spin component, where the quantity Δ_∞ was defined in Eq. (75). [Strictly speaking, in the limit of large $|\mathbf{k}|$ to the result (65) one should add the term $-\Gamma_0(k)\, n_F$ where n_F is the particle density due to free fermions. However, this additional term turns out to be irrelevant for the calculation of $n(k)$.] With the further result which holds for large $|\mathbf{k}|$

$$T\sum_n G_0(k)^2\, G_0(-k) \simeq -\frac{1}{4\,\xi_{\mathbf{k}}^2} \simeq -\frac{m^2}{|\mathbf{k}|^4} \,, \tag{107}$$

Eq. (106) becomes $n(k) \simeq (m\Delta_\infty)^2/|\mathbf{k}|^4$ thus identifying $(m\Delta_\infty)^2$ with the contact C within the present approximation, as anticipated in Section 3.2. The identification $C = (m\Delta_\infty)^2$ where Δ_∞ is given by Eq. (75) was originally introduced in Ref. [366] within the non-self-consistent t-matrix, and later generalized in Ref. [371] to include all possible higher-order effects in the particle–particle propagator.

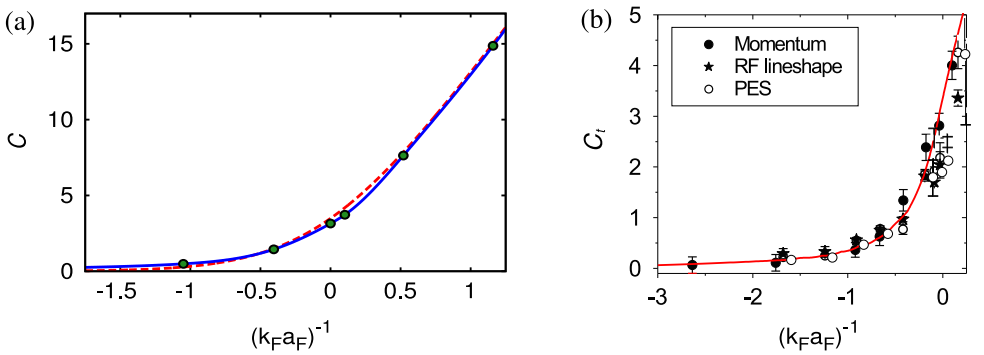

Fig. 21. (a) Coupling dependence of the Tan's contact C at $T = 0$ (in units of $k_F^4/3\pi^2$), obtained in terms of the gap Δ at the mean-field level (dashed line) and with the inclusion of pairing fluctuations in terms of the parameter Δ_∞ given by Eq. (75) (circles and full line). (b) Experimental data of the (trap-averaged) contact C_t (in units of Nk_F, where N is the total number of atoms and k_F is the trap Fermi wave vector) for a gas of ^{40}K atoms vs $(k_F a_F)^{-1}$. Data were obtained alternatively from the tail of the wave-vector (momentum) distribution (full circles), photo-emission spectrometry PES (empty circles), and the high-frequency tail of the RF line-shape (stars).
Source: Panel (a) reproduced from Ref. [63]; panel (b) adapted from Ref. [275].

The quantity Δ_∞^2 can be calculated analytically in the BCS and BEC limits. Starting from the definition (75), in the BCS limit one expands $\Gamma_0(Q)$ given by Eq. (55) to second order in $4\pi a_F/m$, so that $\Gamma_0(Q) \simeq -\frac{4\pi a_F}{m}\left(1 - \frac{4\pi a_F}{m} R_{pp}(Q)\right)$ with $R_{pp}(Q)$ given by Eq. (57). This yields:

$$(m\,\Delta_\infty)^2 \simeq (4\pi a_F)^2 \int \frac{d\mathbf{Q}}{(2\pi)^3}\, T\sum_\nu e^{i\Omega_\nu \eta}\, \chi_{pp}(\mathbf{Q}, \Omega_\nu)$$
$$= (4\pi a_F)^2 \int \frac{d\mathbf{Q}}{(2\pi)^3}\, T\sum_\nu e^{i\Omega_\nu \eta} \int \frac{d\mathbf{k}}{(2\pi)^3}\, T\sum_n G_0(\mathbf{Q}-\mathbf{k}, \Omega_\nu - \omega_n)\, G_0(\mathbf{k}, \omega_n) \;=\; (2\pi a_F n)^2 \tag{108}$$

where χ_{pp} is the particle–particle bubble given by Eq. (56) and n is the (full) particle density. The value (108) vanishes quadratically with $|a_F|$ and is thus dominant with respect to the mean-field value of the contact in the BCS limit, as discussed previously. In the BEC limit, on the other hand, using the approximate form (64) for Γ_0 one obtains:

$$(m\,\Delta_\infty)^2 \simeq -\frac{8\pi}{a_F} \int \frac{d\mathbf{Q}}{(2\pi)^3}\, T\sum_\nu \frac{e^{i\Omega_\nu \eta}}{i\Omega_\nu - \frac{\mathbf{Q}^2}{4m} + \mu_B} = \frac{4\pi n}{a_F}\,. \tag{109}$$

The result (109) formally coincides with that obtained within mean field, with the difference that here n refers to the full and not to the condensate density. This kind of analysis can be extended also to the superfluid phase below T_c. The numerical results for the contact obtained at $T = 0$ throughout the BCS–BEC crossover with the inclusion of pairing fluctuations (circles and full line) and at the mean-field level (dashed line) are shown in Fig. 21(a).

Experimentally, the expected universality of the contact C was demonstrated in Ref. [275] for an ultra-cold gas of trapped fermionic (^{40}K) atoms, where the (trap-averaged) contact C_t was measured at a temperature of about $0.1T_F$ by three independent methods. Specifically, through (i) the large wave-vector tail of the fermionic distribution $n(k)$, (ii) the high frequency tail of the RF spectrum $I_{RF}(\omega)$, as well as (iii) using wave-vector-resolved RF (photo-emission) spectroscopy. The data obtained by these three independent experimental methods are reported in Fig. 21(b). Here, the mutual agreement (obtained within the experimental errors) of the different results can be considered as an empirical proof of the universality of Tan's relations.

Besides the dependence of the contact C on coupling at a given temperature, its dependence on temperature at a given coupling is also of interest. This dependence was first determined analytically in the low- and high-temperature limits in Ref. [372]. It was found that in the low-temperature limit the contact increases like T^4 due to phonons, while in the high-temperature limit the contact decreases like $1/T$, thereby implying that the contact must achieve a maximum at an intermediate temperature (which is expected to be of the order of the Fermi temperature T_F). [Higher orders in a high-temperature expansion were obtained in Ref. [373].] The full temperature dependence of the contact for the homogeneous gas at unitarity was then calculated in Ref. [167] from the large wave-vector tail of the fermionic distribution $n(k)$, both below and above T_c, and is reported Fig. 22 (dashed line). This calculation is based on the non-self-consistent t-matrix approximation of Section 3.1, which is known to become exact in the high-temperature limit [374], and presents an enhancement of the contact C when approaching T_c from above that was attributed to pseudo-gap effects (a broad maximum above T_c was also found by QMC calculations [347]). Above T_c, Fig. 22 shows also an improved calculation (full line) based on an extended version of the non-self-consistent t-matrix [375], which includes correlations among pre-formed pairs that are missing in the t-matrix and which improves on the value of T_c and on the high-temperature behavior of C. The temperature

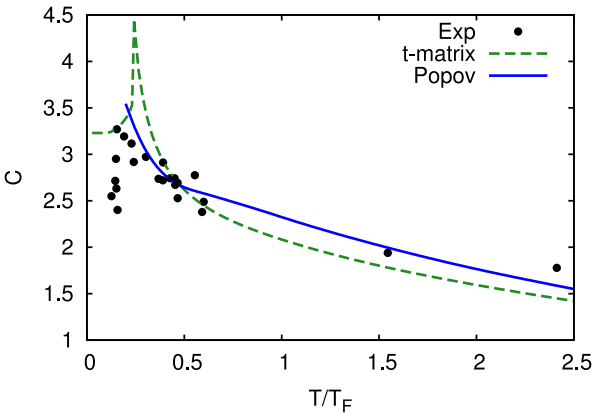

Fig. 22. Temperature dependence of the contact C (in units of $k_F^4/3\pi^2$) for the homogeneous gas at unitarity. The experimental values from Ref. [278] (circles) are compared with the theoretical calculations of Ref. [167] based on the non-self-consistent t-matrix approximation (dashed line) and with an improved approximation based on the work of Ref. [375] that also includes correlations among pre-formed pairs (full line).
Source: Courtesy of F. Palestini.

dependence of the contact for the unitary Fermi gas has further been studied with the self-consistent t-matrix [376], Gaussian pairing-fluctuations [377], and functional renormalization group [378] approaches.

Fig. 22 further reports the experimental measurements of the contact for the homogeneous gas (circles), based on a technique that allows the local properties of the trapped cloud to be probed [278]. These measurements show a gradual decrease of the contact with increasing temperature as predicted by theory, while at the edge of the experimentally attainable temperatures (which is about where the experimental value of T_c is expected to occur) a sharp decrease of the contact is observed. Later on, based on the evidence that the contact gets enhanced near T_c, the question was raised about whether the contact displays a critical behavior near a continuous transition, in spite of the fact that it remains finite even for strongly interacting fermions both in the normal and superfluid phases [379].

In nuclear physics, the range of the interaction is not short enough to allow finding a $1/k^4$ tail in the occupation numbers. Nevertheless, the concept of the contact has been generalized to the nuclear physics context as well (see Section 5.7).

4.6. Josephson effect

The Josephson effect is probably the most striking consequence of the spontaneous symmetry breaking of the phase $\varphi(\mathbf{r})$ of the complex gap (order) parameter $\Delta(\mathbf{r}) = |\Delta(\mathbf{r})|e^{i\varphi(\mathbf{r})}$, which is at the essence of the macroscopic quantum coherence of superconductivity. In its original formulation [380], the Josephson effect is the phenomenon for which a super-current flows indefinitely without any voltage applied across a physical constriction or a junction (which can be either a thin insulating barrier or a point of contact) that weakens the superconductivity in between two superconductors. Such Josephson junctions have important applications in quantum-mechanical circuits [381]. At a microscopic level, the phenomenon amounts to the coherent tunneling of Cooper pairs across a potential barrier placed at the interface between two superconductors. It results in a *characteristic relation* $J(\delta\varphi)$ between the super-current J and the asymptotic phase difference $\delta\varphi$ across the potential barrier, which in its simplest version has the form $J(\delta\phi) = J_0 \sin(\delta\varphi)$ where J_0 is the maximum value of the current attainable with the barrier [381].

The BdG equations (32) can be used to calculate the relation $J(\delta\phi)$ for an arbitrary shape of the potential barrier. And not only in the conventional situations of BCS weak coupling when Cooper pairs tunnel across the barrier, but also under more general conditions when the inter-particle interaction is spanned up to the BEC strong-coupling limit where composite bosons are instead responsible for tunneling. In a recent study of the Josephson effect throughout the BCS–BEC crossover at zero temperature [60,358], a slab geometry was adopted where a potential barrier $V_{\rm ext}(x)$ (either rectangular or Gaussian) is embedded in a homogeneous superfluid that extends to infinity on both sides of the barrier. Accordingly, the order parameter has the form $\Delta(x) = |\Delta(x)|e^{2i[qx+\phi(x)]}$, where $q = Jm/n_0$ is the wave vector associated with the uniform super-current (n_0 being the bulk fermionic number density) and $2\phi(x)$ is the local phase accumulated by the order parameter over and above the reference value $2qx$ in the absence of the barrier, such that $\delta\varphi = 2[\phi(x = +\infty) - \phi(x = -\infty)]$ across the barrier. It turns out that, while a full implementation of self-consistency for the solution of the BdG equations is not required on the BCS side, self-consistency is essential on the BEC side to account for the non-linearity of the GP equation (46) to which the BdG equations reduce in this limit (cf. Section 2.5). Typical Josephson characteristics obtained in this way throughout the BCS–BEC crossover are shown in Fig. 23, where they are seen to depend markedly on the inter-particle coupling $(k_F a_F)^{-1}$ for a given barrier.

For given coupling, the shape of the Josephson characteristics varies also with the width and height of the barrier. In particular, these variations affect the value of the maximum Josephson current J_0 which increases as the ratio V_0/E_F

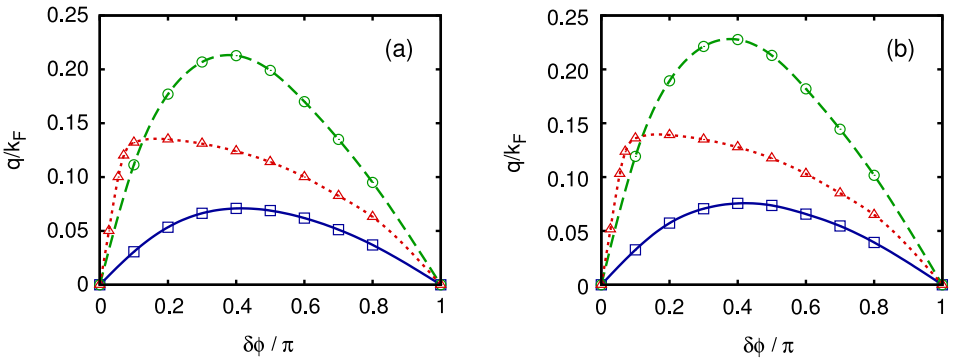

Fig. 23. Josephson characteristics for: (a) A rectangular barrier centered at $x = 0$ of width $Lk_F = 4.0$ and height $V_0/E_F = 0.1$; (b) A Gaussian barrier $V_{\rm eff}(x) = V_0 e^{-x^2/(2\sigma^2)}$ with $\sigma k_F = 1.6$ and the same value of V_0. The three curves correspond to $(k_F a_F)^{-1} = -1.0$ (dotted lines), 0.0 (dashed lines) and $+1.5$ (full lines).
Source: Reproduced from Ref. [60].

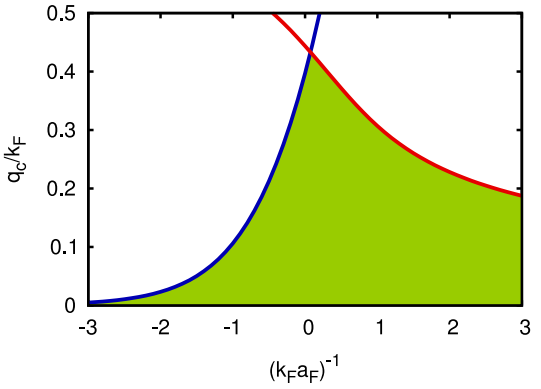

Fig. 24. Critical velocity vs coupling. The shaded region identifies the allowed region outside which the superfluid flow becomes unstable. The left (blue) and right (red) boundary curves are associated with pair-breaking and sound-mode excitations.
Source: Reproduced from Ref. [60].

decreases. For any given coupling, it is thus of interest to determine the maximum allowed value of the Josephson current obtained by progressively lowering the barrier height, which corresponds to an *intrinsic* upper value q_c/m for the velocity of the superfluid flow. On physical grounds, a vanishing small (albeit non zero) barrier acts as an impurity that probes the stability of the homogeneous superfluid flow and plays a similar role to the walls of a container in the context of the *Landau criterion for superconductivity* [382]. In this respect, alternative dissipation mechanisms are active on the two sides of unitarity and are associated with the onset of quasi-particle excitations of a different nature, namely, pair-breaking excitations on the BCS side and sound-mode quanta on the BEC side. In the presence of a barrier, the allowed values of the superfluid flow are thus expected to lie inside the shaded region of Fig. 24, which is bounded by the critical velocities associated with the above two kinds of excitations.

Detailed numerical calculations with the BdG equations have confirmed this expectation, leading one to conclude that the Josephson effect is most robust in the unitary regime where q_c attains its maximum [60,358]. Examples of calculations of the maximum Josephson current for given barrier are reported in Fig. 25. A similar conclusion has also been confirmed experimentally, through a direct measurement of the critical velocity of an ultra-cold superfluid Fermi gas in the BCS–BEC crossover (cf. Fig. 2 of Ref. [272] and Fig. 2 of Ref. [273]).

In terms of the above analysis, by spanning the BCS–BEC crossover it was possible to smoothly connect the Josephson effect conceived originally for fermions [380,381] to the corresponding effect for bosons (as measured, e.g., in Ref. [383]). This connection, in turn, has allowed for a deeper understanding of the Josephson effect [60,358].

4.7. Collective modes and anisotropic expansion

Collective modes and the expansion from an anisotropic trap allow one to obtain interesting information on the dynamical regime of a system. A simple example is a non-interacting Fermi gas in an anisotropic trap with $\omega_x > \omega_y$. When the trap is switched off at $t = 0$, each atom follows its ballistic trajectory $\mathbf{r}(t) = \mathbf{r}(0) + t\,\mathbf{p}(0)/m$, so that after a long time

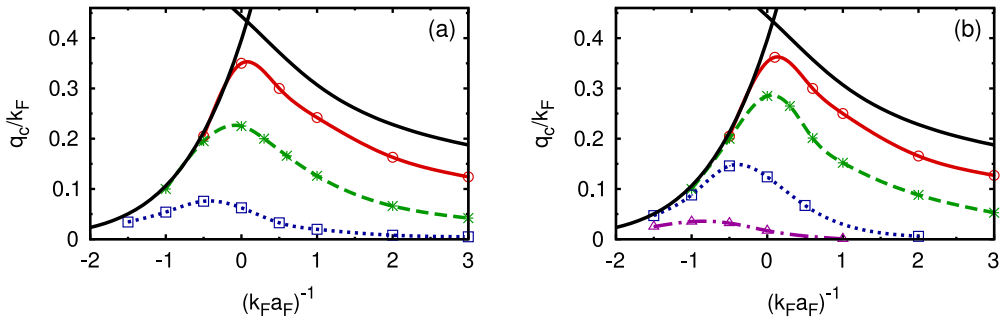

Fig. 25. Maximum velocity q_c/m obtained from the maximum of the Josephson characteristics vs $(k_F a_F)^{-1}$, for several rectangular barriers with: (a) $Lk_F = 2.65$ and $V_0/E_F = (0.02, 0.10, 0.40)$ from top to bottom; (b) $Lk_F = 5.30$ and $V_0/E_F = (0.01, 0.05, 0.20, 0.50)$ from top to bottom. The Landau critical velocity is also reported (full lines without symbols).
Source: Reproduced from Ref. [60].

of flight the cloud profile reflects the spherical shape of the wave-vector distribution at $t = 0$. Accordingly, the aspect ratio $R = \sqrt{\langle x^2\rangle/\langle y^2\rangle}$, which was initially given by $R = \omega_y/\omega_x < 1$, approaches $R = 1$ for long times. The situation is completely different in the hydrodynamic regime. If the cloud is initially in hydrostatic equilibrium, the pressure gradient has to compensate the force of the trap. For the above example, this means that the pressure gradient is stronger in the x than in the y direction, so that when the gas is released from the trap it will be accelerated more strongly in the x than in y direction. Accordingly, during the expansion the aspect ratio will turn from $R < 1$ to $R > 1$.

Differences between the collisionless and hydrodynamic regimes can be observed also in small-amplitude collective oscillations. Among the different modes that have been studied, the radial quadrupole mode exhibits a particularly drastic change. This mode is an oscillation of the gas in a cylindrical trap (with $\omega_x = \omega_y \equiv \omega_r$), which can be excited by squeezing the gas in x direction and simultaneously expanding it in y direction for a short time (so as to keep the volume constant). In this way, the cloud shape oscillates with frequency $\approx 2\omega_r$ in the collisionless regime [384] and $\sqrt{2}\omega_r$ in the hydrodynamic regime [385–387].

The hydrodynamic behavior can be a consequence of superfluidity (the so-called collisionless hydrodynamics). For instance, in the BEC limit the dynamics of the gas at $T = 0$ is described by the time-dependent Gross–Pitaevskii equation for dimers, which can be reduced to the continuity equation

$$\dot{n} + \nabla \cdot (n\mathbf{v}) = 0 \tag{110}$$

and the Euler equation

$$\dot{\mathbf{v}} + \nabla\left(\frac{\mathbf{v}^2}{2} + \frac{V_{\rm ext}}{m} + \frac{\mu_{\rm loc}}{m}\right) = 0 \tag{111}$$

for large particle numbers [388]. Here, $\mathbf{v}(\mathbf{r}, t)$ is the velocity field and $\mu_{\rm loc}(\mathbf{r}, t)$ the local chemical potential calculated from the density $n(\mathbf{r}, t)$. [Note that one can rewrite $\nabla\mu_{\rm loc} = (1/n)\nabla P$ where P is the pressure.] On the BCS side, it can be shown that at $T = 0$ the time-dependent BdG equations, too, can be reduced to the continuity (110) and Euler (111) equations, provided the dynamics is sufficiently slow to avoid pair breaking and the Cooper pair size is sufficiently small compared to the system size [90,389].

The system behaves hydrodynamically also in the normal phase when there occur enough collisions between atoms to maintain local equilibrium (the so-called collisional hydrodynamics). In this case, Eqs. (110) and (111) can be derived from the Boltzmann equation [390]. If the system is very dilute (like at high temperature) or weakly interacting, the normal phase will be in the collisionless regime. In this case, the collision term of the Boltzmann equation (see Eq. (114)) can be neglected and the system dynamics described by the Vlasov equation:

$$\dot{f} + \frac{\mathbf{p}}{m} \cdot \nabla_{\mathbf{r}} f - (\nabla V) \cdot \nabla_{\mathbf{p}} f = 0\,, \tag{112}$$

where $f(\mathbf{r}, \mathbf{p}, t)$ is the distribution function per spin state (we assume $f_\uparrow = f_\downarrow = f$) and $V = V_{\rm ext} + U$ is the potential that takes into account the trap $V_{\rm ext}$ and a mean-field-like potential U. Theoretically, most challenging are the situations when the system cannot be described by the above limiting cases. We discuss two examples where the intermediate regimes have explicitly been studied.

We first consider the $T = 0$ case and discuss how well hydrodynamics reproduces the results of the time-dependent BdG theory. For small-amplitude collective oscillations, the time-dependent BdG equations can be linearized around equilibrium. [In nuclear physics this procedure is referred to as the Quasiparticle Random-Phase Approximation (QRPA), while in condensed matter is known as RPA.] QRPA calculations were performed in the BCS regime for the collective modes of a gas in a spherical trap with $\omega_z = \omega_r$ [391,392]. It was found that hydrodynamics is only valid if the gap Δ (at the trap center)

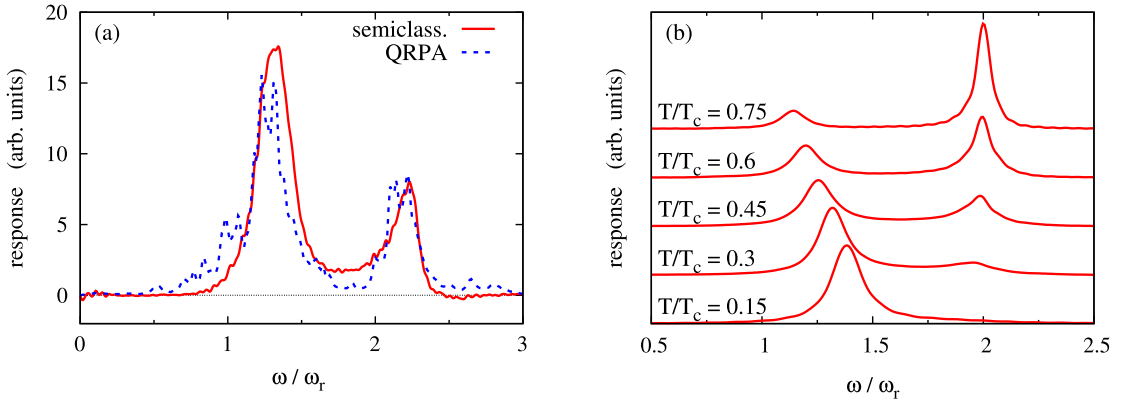

Fig. 26. (a) Quadrupole response function for a gas of 17000 atoms in a spherical trap with $(k_F a_F)^{-1} = -1.5$ and $T = 0.5T_c$. The results of the semiclassical quasi-particle transport theory of Ref. [401] (solid line) are compared to the QRPA results of Ref. [392] (dotted line). (b) Semiclassical results for the quadrupole response of a gas of 400 000 atoms in a cylindrical trap with $(k_F a_F)^{-1} = -1.5$ and various temperatures.
Source: Panel (a) adapted from Ref. [401]; panel (b) adapted from Ref. [402].

is much larger than the level spacing ω_r in the trap; otherwise, the frequency of the collective mode can be significantly smaller than that predicted by hydrodynamics, and the mode gets damped due to its coupling to two-particle excitations (pair breaking). In Ref. [393] this pair-breaking effect was suggested as an explanation for the frequency shift and damping of the radial breathing mode observed experimentally in Ref. [251].

The QRPA equations were also solved for the collective modes in a uniform gas [71,394]. At small wave vector q, the QRPA dispersion $\omega(q)$ of the collective mode follows the linear behavior $\omega = cq$ of the Bogoliubov–Anderson sound [395,396], where $c = \sqrt{(1/n)\partial P/\partial n}$ is the hydrodynamic sound velocity. In the BCS regime (but also at unitarity), for increasing q the dispersion relation $\omega(q)$ approaches the threshold for pair breaking at about 2Δ, and the QRPA dispersion $\omega(q)$ becomes progressively flat with a negative curvature $d^2\omega/dq^2 < 0$. Analogous results were obtained in Ref. [397], where equations similar to the time-dependent BdG equations (albeit adapted to the unitary limit) were solved, as well as in Ref. [398] where the QRPA was solved for neutron matter. On the BEC side where $\mu < 0$, the situation is different since the pair-breaking threshold is no longer flat as a function of q [394]. In this case, the QRPA dispersion $\omega(q)$ has a positive curvature but does not enter the continuum. Deep in the BEC limit, the QRPA reproduces the dispersion $\omega = \sqrt{(cq)^2 + (q^2/2m_B)^2}$ of the Bogoliubov mode which is obtained from the linearized time-dependent GP equation for the condensate of composite bosons with mass $m_B = 2m$ [388]. In this case, the sound velocity $c = \sqrt{8\pi a_F/m_B^2}$ corresponds to the (Born approximation) value $a_B = 2a_F$ of the boson–boson scattering length, as discussed in Section 3.6.

We next consider the regime of sufficiently strong pairing and long wavelength, such that hydrodynamics can be applied at $T = 0$. The question then arises about what happens at finite temperature, when thermal quasi-particle excitations form a normal-fluid component in the superfluid. If the collision rate of the thermal quasi-particles is high enough (that is, much higher than the frequency of the collective oscillation), also this normal component can be treated hydrodynamically and the collective modes can be described in the framework of Landau two-fluid hydrodynamics [399]. In particular, the two-fluid hydrodynamics predicts the existence of second sound (for which normal and superfluid components oscillate out of phase). In a recent experiment with ^{6}Li atoms at unitarity [271], second sound was indeed observed and the temperature dependence of the normal-fluid density was extracted.

In the BCS regime, on the other hand, the normal component is more likely to be in the collisionless regime. In this case, one can again apply the time-dependent BdG theory (or its linearized form QRPA). A simplification, which is computationally less demanding, is provided by a semiclassical quasi-particle transport theory developed initially for clean superconductors in Ref. [400]. It can be derived by a formal expansion of the time-dependent BdG equations in powers of the Planck constant $\hbar$ [389], in analogy to the derivation of the Vlasov equation (112) from the time-dependent Hartree–Fock theory [59]. In this quasi-particle transport theory, the normal component is described in terms of a quasi-particle distribution function $\nu(\mathbf{r}, \mathbf{p}, t)$, which satisfies a Vlasov-like equation of motion

$$\dot{\nu} + (\nabla_{\mathbf{p}} E) \cdot \nabla_{\mathbf{r}} \nu - (\nabla_{\mathbf{r}} E) \cdot \nabla_{\mathbf{p}} \nu = 0\,, \tag{113}$$

where E is the quasiparticle energy in the local rest frame of the superfluid (see Refs. [389,401] for the explicit expressions). The superfluid velocity is obtained by solving the continuity equation for the total (superfluid and normal) density and current at the same time.

Fig. 26(a) shows a comparison of the quadrupole response function (that is, the Fourier transform of the quadrupole moment $\langle x^2 - y^2 \rangle$ after its excitation at $t = 0$) for $T \approx T_c/2$, as obtained within the semiclassical theory and the QRPA. With this set of parameters, hydrodynamics works well at $T = 0$ since in this case the gap at the center of the trap is

$\approx 6\omega_r$. At $T = 0.5T_c$, one sees from this figure that the agreement between QRPA and the semiclassical theory remains satisfactory. The presence of the normal component leads to a strong damping (which is reflected in the width of the peak) of the hydrodynamic mode at $\sqrt{2}\omega_r$, as well as to the presence of a second damped mode with frequency $2\omega_r$ corresponding to the collisionless normal gas.

While the QRPA is limited for computational reasons to spherical traps with small particle numbers, the semiclassical theory can be applied also to realistic geometries and particle numbers [402], as shown in Fig. 26(b). One distinguishes again two peaks, whose strength is shifted for increasing temperature from the hydrodynamic mode at left to the ballistic mode at right. In addition to being broadened, the hydrodynamic mode is also shifted to lower frequencies, which allows for a qualitative explanation of the experimental result of Ref. [253] as shown in Ref. [402].

Finally, it may happen that the effects of collisions in the normal component are not negligible but insufficient to guarantee hydrodynamic behavior. In this case, neither the time-dependent BdG equations nor the Landau two-fluid description are applicable (to our knowledge, this theoretically difficult case has not been studied thus far). The situation becomes much simpler for temperatures $T > T_c$ where the entire system is in the normal phase. In this case, the transition from collisional hydrodynamic to collisionless behavior, which is observed experimentally as function of temperature or coupling [254,256], has been theoretically described in the BCS regime up to unitarity in terms of the Boltzmann equation [254,403–408]:

$$\dot{f} + \frac{\mathbf{p}}{m} \cdot \nabla_{\mathbf{r}} f - (\nabla V) \cdot \nabla_{\mathbf{p}} f = - \int \frac{d\mathbf{p}_1}{(2\pi)^3} \int d\Omega \frac{d\sigma}{d\Omega} \frac{|\mathbf{p} - \mathbf{p}_1|}{m} [ff_1(1 - f_2)(1 - f_3) - f_2 f_3 (1 - f)(1 - f_1)] \,. \tag{114}$$

[This equation is sometimes referred to as the Boltzmann–Nordheim or Boltzmann–Uehling–Uhlenbeck equation.] In the collision integral on the right-hand side, f_i is a short-hand notation for $f(\mathbf{r}, \mathbf{p}_i, t)$, Ω is the solid angle defining the direction of $\mathbf{p}_2 - \mathbf{p}_3 \equiv 2\mathbf{q}$, while the total wave vector and the absolute value of the relative wave vector are determined by the conservation requirements $\mathbf{p}_2 + \mathbf{p}_3 = \mathbf{p} + \mathbf{p}_1 \equiv \mathbf{k}$ and $|\mathbf{p}_2 - \mathbf{p}_3| = |\mathbf{p} - \mathbf{p}_1| \equiv 2q$. The factors $(1 - f)$ and $(1 - f_i)$ in the collision integral underline the occurrence of Pauli blocking, which is absent in the classical Boltzmann equation.

To a first approximation, the cross section $d\sigma/d\Omega = a_F^2/(1 + q^2 a_F^2)$ for the scattering of two atoms in vacuum can be used in Eq. (114). However, the cross section and thus the collision rate may be strongly affected by medium effects. In the medium, the cross section is given by $d\sigma/d\Omega = |m\Gamma^R(\mathbf{k}, \omega)/4\pi|^2$, with $\omega = k^2/4m + q^2/m - 2\mu$. As Γ^R develops a pole at $T = T_c$, $d\sigma/d\Omega$ can be strongly enhanced already at temperatures above but close to T_c. The effect of this enhancement on the viscosity of the gas was studied in Refs. [409,410]. The in-medium t-matrix enters also the left-hand side of Eq. (114), through the mean-field-like contribution to V calculated from the self-energy [403,406].

As an example of the quantitative precision that can be reached with the Boltzmann equation, Fig. 27 compares the solution of the Boltzmann equation, obtained in Ref. [403] for the unitary Fermi gas in the normal phase, with the experimental data. One sees that both (a) the expansion of the cloud from an anisotropic trap and (b) the quadrupole mode are well described by the theory. Unfortunately, these observables are not very sensitive to medium effects, since they give strong weight to parts of the cloud far away from the cloud center (where the local T/T_F is large and medium effects are weak). In addition, the enhanced collision rate and the mean-field-like potential act into opposite directions [403], making the observation of medium effects even more difficult.

4.8. Quantum vortices and moment of inertia

In contrast to superconducting materials, ultra-cold trapped Fermi gases are neutral systems which are well isolated from their surrounding. In addition, all physical properties of these systems are expected to vary smoothly throughout the BCS–BEC crossover, also owing to the presence of the trap. For instance, the fact that the normal and condensed gas clouds have similar size and shape makes it difficult to detect condensation on the BCS side. For this reason, a stringent proof of the superfluid behavior of ultra-cold trapped Fermi gases has long been elusive. In this context, two experiments were performed specifically to reveal the presence of the superfluid phase [265,288], by setting an ultra-cold trapped Fermi gas into rotation. In both experiments, an equal mixture of ^{6}Li atoms in the lowest two atomic (hyperfine) states was prepared in a cigar-shaped trap.

In the first experiment [265], large arrays of vortices were generated at low temperature throughout the BCS–BEC crossover by sweeping a Fano-Feshbach resonance, thereby providing the first direct evidence for the occurrence of the superfluid phase in a *fast* rotating trapped Fermi gas and establishing an analogy with type-II superconductors and neutron stars. This is because the occurrence of a quantized vortex lattice is a direct consequence of the existence of a macroscopic wave function that describes the superfluid, with the gradient of the phase of the wave function being proportional to the velocity field of the superfluid. Fig. 28 shows examples of these vortex lattices, that were detected in Ref. [265] by imaging the cloud after ballistic expansion in order to increase the contrast.

In the second experiment [288], the superfluid behavior was revealed in a *slowly* rotating trapped Fermi gas by the quenching of the moment of inertia Θ, which was measured at unitarity for increasing temperature until the classical rigid-body value $\Theta_{\rm cl}$ of the normal state was reached. The basic idea for a quenched moment of inertia as a signature of superfluidity dates back to more than fifty years ago in nuclear physics, where a moment of inertia below the classical rigid-body value was attributed to superfluidity [59]. In the experiment of Ref. [288], a slow rotation was required to transfer a finite angular momentum L to the system while avoiding at the same time the presence of vortices, which are energetically favored only

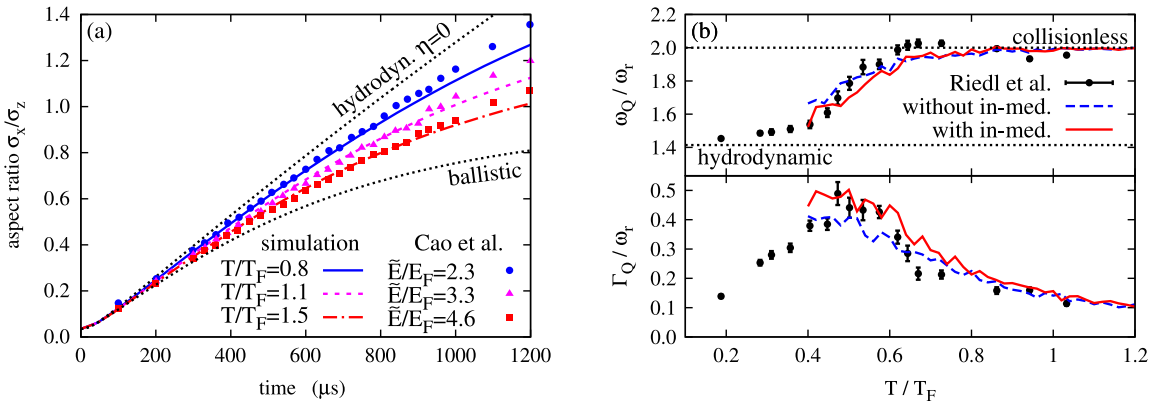

Fig. 27. Comparison of the numerical solutions of the Boltzmann equation for the unitary Fermi gas in the normal phase (lines) with the experimental data (symbols). (a) Time dependence of the aspect ratio during the anisotropic expansion of the cloud for different initial temperatures (experimental data from Ref. [280]). (b) Temperature dependence of the frequency (top) and damping rate (bottom) of the quadrupole mode (experimental data from Ref. [254]).
Source: Adapted from Ref. [403].

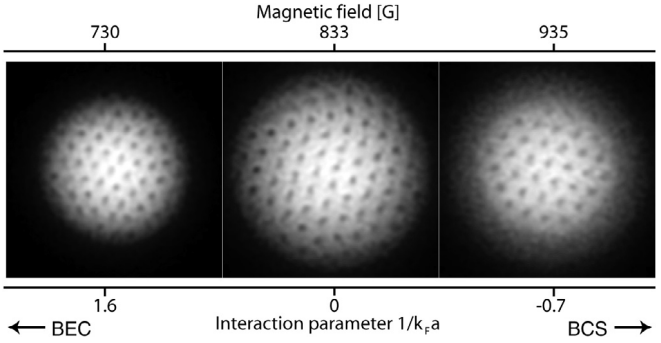

Fig. 28. Observation of vortex lattices across the BCS–BEC crossover.
Source: Reproduced from Ref. [265].

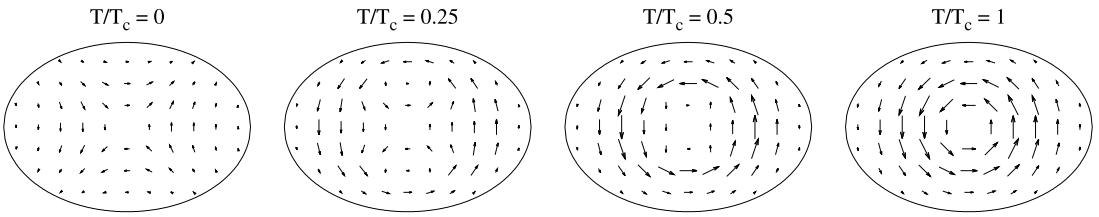

Fig. 29. Current densities in the x–y plane for a gas in the BCS regime at temperatures $T/T_c = 0.0$, 0.25, 0.5, and 1.0 (from left to right), in a trap with $\omega_x/\omega_y = 0.7$ slowly rotating about the z axis.
Source: Adapted from Ref. [414].

above a critical rotation frequency Ω_{c_1} (in this respect, the experiment of Ref. [288] is complementary to the experiment of Ref. [265]).

Theoretically, the slow rotation of a trapped Fermi gas at $T = 0$ was studied in Ref. [411], where it was shown that the moment of inertia of a superfluid gas rotating around the z axis reaches the irrotational value $\Theta_{\rm irrot} = \Theta_{\rm cl}(\omega_x^2 - \omega_y^2)/(\omega_x^2 + \omega_y^2)$ provided the condition $\Delta \gg (\omega_x, \omega_y)$ is satisfied (which coincides with the condition for the validity of superfluid hydrodynamics discussed in Section 4.7). If Δ and (ω_x, ω_y) are instead of the same order of magnitude, the moment of inertia is larger than $\Theta_{\rm irrot}$ and lies between $\Theta_{\rm irrot}$ and $\Theta_{\rm cl}$, as it is the case of atomic nuclei [412]. An early work on this subject was published by Migdal [413].

The temperature dependence of the moment of inertia was studied in Refs. [414,415], where it was shown that in the limit $\Delta \gg (\omega_x, \omega_y)$ the current in the rotating trap can be decomposed as in Landau two-fluid hydrodynamics into a normal component rotating like a rigid body and a superfluid component with an irrotational velocity field. As an example, the resulting current densities in a trap with $\omega_x/\omega_y = 0.7$ are displayed in Fig. 29 at different temperatures, and show how the

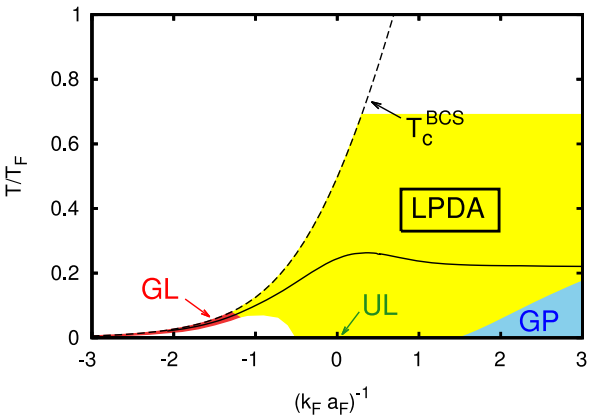

Fig. 30. Temperature vs coupling phase diagram across the unitary limit (UL), in which the regions of validity of the GL, GP, and LPDA equations are schematically indicated by the colored sectors. The critical temperatures of the homogeneous system at the mean-field level (dashed line) and within the t-matrix approximation (full line) are also reported (cf. Fig. 9) to set the relevant boundaries.

irrotational velocity field at $T = 0$ turns continuously into a rigid-body rotation at $T = T_c$. The rotational component, which is proportional to the normal-fluid fraction, is concentrated at the surface at low temperature and penetrates more and more into the trap center upon approaching T_c. As a consequence, the moment of inertia smoothly reaches the rigid-body value at $T = T_c$.

Similar effects as in a slowly rotating gas at finite temperature may appear in a rapidly rotating gas already at zero temperature. In particular, it was suggested in Ref. [416] that it might be possible to put the system into fast rotation without generating vortices by adiabatically increasing the angular velocity. In this case, in the limit of axial symmetry $\omega_x = \omega_y$ it is expected that the system separates into a superfluid phase at rest near the center surrounded by a rotating normal phase. Since in the strongly-coupled regime the normal and superfluid phases have different equations of state, this would have an observable effect on the density profile, which would enable one to determine the difference in energies of the normal and superfluid phases. As pointed out in Ref. [417], however, the rotation itself destroys a certain fraction of Cooper pairs, in analogy to what happens at finite temperature in the two-fluid model. As a consequence, an intermediate layer appears in between the superfluid and normal phases, where the rotational current gradually builds up from the inner superfluid phase to the outer normal phase, and the discontinuity in the density profile is eventually washed out.

Regarding the case of a rapidly rotating system with vortices, as it was observed in the experiment [265], it turns out that this case is theoretically challenging since it requires the description of complex arrays of vortices in a trapped system across the BCS–BEC crossover. Approaches based on the BdG equations discussed in Section 2.4 have so far been limited to a single vortex line [78,83,84] or to vortex lattices in small 2D systems [89,90]. Extending these calculations to vortex lattices in realistic 3D systems appears to be computationally prohibitive, owing to exceeding computation time and memory space. Nevertheless, finding solutions with large vortex patterns has recently become possible in terms of the LPDA equation introduced in Ref. [98], where a "Local Phase Density Approximation" to the BdG equations was obtained by a suitable *double coarse graining* of those equations throughout the BCS–BEC crossover, which deals with the magnitude and phase of the order parameter on a different footing. In this way, the BdG equations were replaced by a single differential equation for $\Delta(\mathbf{r})$ in close analogy with the GL and GP equations discussed in Section 2.5. With the important difference, however, that the LPDA equation holds over an extended region of the temperature-coupling phase diagram of the BCS–BEC crossover, and reduces to the GL and GP equations in appropriate ranges of coupling and temperature as shown schematically in Fig. 30. A full theoretical analysis based on the LPDA equation for the two experiments with rotating traps made in Refs. [265,288] was reported in Ref. [418], where a vector potential $\mathbf{A}(\mathbf{r}) = m\,\boldsymbol{\Omega} \times \mathbf{r}$ was associated to the trap rotating with frequency $\boldsymbol{\Omega}$.

Fig. 31(a) shows a comparison of the LPDA calculation of Ref. [418] with the experimental data of Ref. [265]. In this figure, the experimental values for the number of vortices $\mathcal{N}_v$ have been multiplied by a factor of 4 common to all couplings, because it was also found in Ref. [418] that the Feynman's theorem for the number of vortices for unit area (which is known to apply to an infinite array of vortices [419]) is satisfied here only in (about) 1/4 of the cloud area. Similarly to the Josephson effect discussed in Section 4.6, also in this case by looking at the number of vortices one concludes that superfluidity is most robust in the unitary regime.

Fig. 31(b) shows instead the frequency dependence of the moment of inertia $\Theta = L/\Omega$ obtained in terms of the total angular momentum L at zero temperature for three different couplings, using the trap parameters of Ref. [288]. At unitarity, the number of vortices that enter the cloud are also indicated for a choice of angular frequencies, from which one concludes that not too many vortices are required to stabilize the moment of inertia to its classical value $\Theta_{\rm cl}$. The inset of Fig. 31(b) provides a closer view at the behavior of Θ at unitarity in a narrow frequency range about the critical frequency Ω_{c_1}, at which the first vortex nucleates in the cloud. A smooth increase in Θ is found to occur before the sharp rise at Ω_{c_1}, owing to the finite particle number. In addition, this increase of Θ before Ω_{c_1} has a linear dependence, in line with a general argument discussed in Ref. [420].

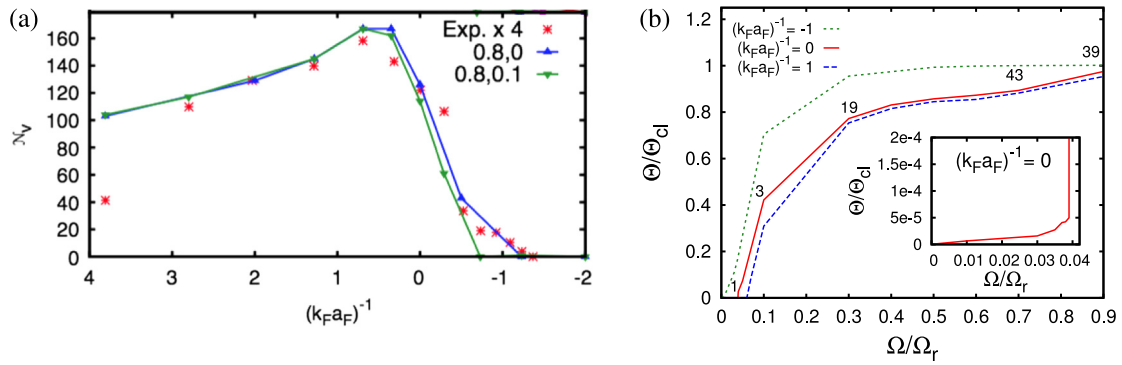

Fig. 31. (a) The experimental values for the number of vortices $\mathcal{N}_v$ from Ref. [265] multiplied by a factor of four (stars) are compared with the results of the calculations of Ref. [418] for $\Omega = 0.8$ (in units of the radial trap frequency Ω_r) and two different temperatures (in units of T_F). The calculations use the same trap parameters of the experiment. (b) Moment of inertia Θ (in units of its classical value Θ_{cl}) vs the angular frequency Ω (in units of Ω_r), for three couplings at zero temperature. The inset shows the tiny increase of Θ at unitarity before its sharp rise at the critical frequency Ω_{c_1}.
Source: Adapted from Ref. [418].

5. BCS–BEC crossover in nuclear systems

Nuclear systems (nuclei, neutron stars, proto-neutron stars, etc.) contain two types of nucleons: protons and neutrons. Consequently, three types of pairing can occur: neutron–neutron (*nn*), proton–proton (*pp*), and proton–neutron (*pn*). Only the latter channel shows a bound state, the deuteron (d or ^{2}H). As a consequence, one can imagine a crossover from a BEC of deuterons to a BCS state of *pn* Cooper pairs.

In contrast to the cold-atom case, where the interaction strength can be varied (leading to the interaction-induced crossover of Section 4.1), the nucleon–nucleon interaction is of course fixed. In nuclear matter the crossover is thus realized by varying the density. At low density, the deuteron is bound, but the binding energy decreases with increasing density. At some stage, the deuteron becomes unbound and turns into a *pn* Cooper pair. The possibility of such a density-induced crossover is actually not limited to nuclear systems. It relies only on the fact that the interaction has a finite range [24], since then the relevant matrix elements of the interaction get small as the momentum transfer, which is of the order of k_F and then increases with density, exceeds the wave-vector range of the interaction.

In ordinary nuclei, *nn* and *pp* pairing win against *pn* pairing because of *n*–*p* asymmetry, i.e., there are usually more neutrons than protons. Since there is no *pp* or *nn* bound state, the BEC regime does not exist for these channels. However, since the *nn* system is "almost" bound, the *nn* scattering length is very large and a situation similar to the unitary limit can be realized in low-density neutron matter.

There is also a completely different way how one can pass from a BEC to a BCS state in nuclear systems. The α particle (^{4}He nucleus made of two protons and two neutrons) is much more strongly bound than the deuteron mentioned above. Therefore, one may think that at low density, a BEC of α particles is energetically more favorable than a BEC of deuterons. But as we will discuss below, an α particle is much more sensitive to the presence of a finite density than a deuteron, and therefore, at some density, the BEC of α particles disappears in favor of a BCS state of *pn* (or *nn* and *pp*) Cooper pairs mentioned above.

Nuclear pairing is, of course, a quite old subject dating back to the even–odd staggering of nuclear binding and the strong reduction of the moment of inertia of deformed nuclei. Those issues, together with their history, are well described in textbooks (see, e.g., Refs. [59,421]). More modern reviews can be found in Refs. [55–57]. Since our aim here is to concentrate on the BCS–BEC crossover and since this phenomenon is so far elusive in finite nuclei (see later), this Section will mainly concentrate on infinite nuclear or infinite neutron matter with only short glimpses on what happens in finite nuclei.

5.1. Deuteron in symmetric nuclear matter and proton–neutron pairing

The deuteron is the only bound state of two nucleons. Its spin is $S = 1$ (spin triplet). To have an antisymmetric wave function, it must be isospin singlet (i.e., $T = 0$), and the orbital angular momentum can take the values $L = 0, 2$ since the total spin of the deuteron is $J^P = 1^+$. It is, indeed, well known that the deuteron has a quadrupole ($L = 2$) component in its wave function as a consequence of the non-central (tensor) force. With $E_B/A = 1.1$ MeV (where $E_B = 2.2$ MeV is the binding energy and $A = 2$ is the number of nucleons), its binding energy is very weak compared to the most bound nucleus ^{56}Fe with $E_B/A = 8.8$ MeV or the α particle with $E_B/A = 7.1$ MeV. Nonetheless, *pn* pairing can exhibit the BCS–BEC crossover phenomenon [16,21,22]. This can be of a certain importance, for instance, to explain the deuteron production in heavy-ion collisions where the expansion of the system after the collision results in low-density nuclear matter [16]. One may also imagine that in collapsing stars or in not completely cooled neutron stars, where a certain fraction of protons still exists, *pn* pairing can play a role.

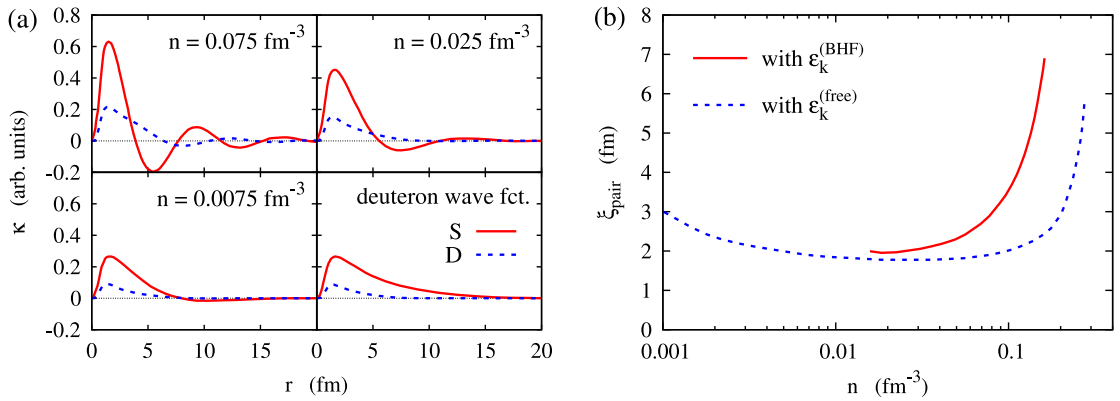

Fig. 32. (a) S and D components of the pairing tensor in coordinate space at $T = 0$ for three different values of the density. The panel at the lower right displays the free deuteron wave function for comparison. (b) Deuteron size as a function of density.
Source: Panel (a) adapted from Ref. [16]; panel (b) adapted from Ref. [423].

The BCS–BEC crossover in nuclear matter has been investigated within the BCS framework in Ref. [16]. At finite temperature, the BCS equation for the wave-vector dependent gap $\Delta_{\mathbf{k}}$ has the usual form

$$\Delta_{\mathbf{k}} = -\sum_{\mathbf{k}'} V(\mathbf{k},\mathbf{k}')\frac{\Delta_{\mathbf{k}'}}{2E_{\mathbf{k}'}}[1-2f(E_{\mathbf{k}'})] \tag{115}$$

which extends Eq. (4) to finite temperature. Here, $V(\mathbf{k},\mathbf{k}')$ denotes the matrix element of the nucleon–nucleon force, $E_{\mathbf{k}} = \sqrt{\xi_{\mathbf{k}}^2 + \Delta_{\mathbf{k}}^2}$ the quasiparticle energy, with $\xi_{\mathbf{k}} = \varepsilon_{\mathbf{k}} - \mu$ and $f(E) = 1/(e^{E/T}+1)$ the Fermi function. In Ref. [16], a separable form of the Paris force [422] was used for $V(\mathbf{k},\mathbf{k}')$, reproducing nucleon–nucleon phase shifts and the deuteron binding energy. The density-dependent nucleon single-particle energies $\varepsilon_{\mathbf{k}}$ were obtained within the Brückner–Hartree–Fock (BHF) approach.

We recall from Section 2.1 that the BCS occupation numbers at finite temperature are given by the expression:

$$n_{\mathbf{k}} = \frac{1}{2}\left(1 - \frac{\xi_{\mathbf{k}}}{E_{\mathbf{k}}}[1-2f(E_{\mathbf{k}})]\right). \tag{116}$$

Similarly to what was done in Section 1.2, multiplying both sides of Eq. (115) by $\xi_{\mathbf{k}}[1-2f(E_{\mathbf{k}})]/2E_{\mathbf{k}} = 1-2n_{\mathbf{k}}$ and defining $\kappa_{\mathbf{k}} = \Delta_{\mathbf{k}}[1-2f(E_{\mathbf{k}})]/2E_{\mathbf{k}}$, one recovers Eq. (5) also at finite temperature, in the form:

$$2\varepsilon_{\mathbf{k}}\kappa_{\mathbf{k}} + (1-2n_{\mathbf{k}})\sum_{\mathbf{k}'} V(\mathbf{k},\mathbf{k}')\kappa_{\mathbf{k}'} = 2\mu\,\kappa_{\mathbf{k}}\,. \tag{117}$$

As discussed in Section 1.2 for the zero-temperature case, this shows that in the low-density limit, where $\varepsilon_{\mathbf{k}} \to k^2/(2m)$ and $n_{\mathbf{k}} \to 0$, the gap equation reduces to the Schrödinger equation, and the pairing tensor $\kappa_{\mathbf{k}}$ coincides with the deuteron wave function, whose eigenvalue 2μ tends towards (minus) the deuteron binding energy -2.2 MeV . Note, however, that this argument holds only at zero temperature. For any fixed non-zero temperature, the low-density limit corresponds to the classical limit whereby $\mu \to -\infty$, such that the gap equation has only the trivial solution $\Delta_{\mathbf{k}} = 0$ [i.e., $\kappa_{\mathbf{k}} = 0$].

Fig. 32(a) shows the S-wave and D-wave components of the pairing tensor $\kappa(r)$ (defined as the Fourier transform of $\kappa_{\mathbf{p}}$) as a function of r at zero temperature for four different densities n. The typical oscillatory behavior of the Cooper pair wave function results at higher densities. As the density decreases, on the other hand, the Cooper pair wave function reduces to the bound-state wave function of the free deuteron.

These results can be used to determine the size ξ_{pair} of the deuteron in matter [cf. Eq. (6) of Section 1.3], according to the expression [14,423]:

$$\xi_{\text{pair}}^2 = \frac{\int d\mathbf{r}\, r^2 |\kappa(r)|^2}{\int d\mathbf{r}\, |\kappa(r)|^2} = \frac{\sum_{\mathbf{k}} |\nabla_{\mathbf{k}}\kappa_{\mathbf{k}}|^2}{\sum_{\mathbf{k}} |\kappa_{\mathbf{k}}|^2}\,. \tag{118}$$

Results for the deuteron size as function of the density are shown in Fig. 32(b). In the lower curve (dashed line), free single-particle energies $p^2/(2m)$ were used, while the upper curve (solid line) was obtained with BHF single-particle energies $\varepsilon_{\mathbf{k}}$. Note how the deuteron size first shrinks with increasing density until it reaches a minimum at $n \sim 0.036$ fm^{-3}, after which it starts to increase. This initial size shrinking was also noticed in a more general context in Ref. [424]. A qualitatively similar behavior was already revealed in 1970, when the deuteron size was calculated as a function of the distance to the α-particle in ^{6}Li [425]. Note further that, although the deuteron size initially shrinks, it gets monotonously less bound with increasing

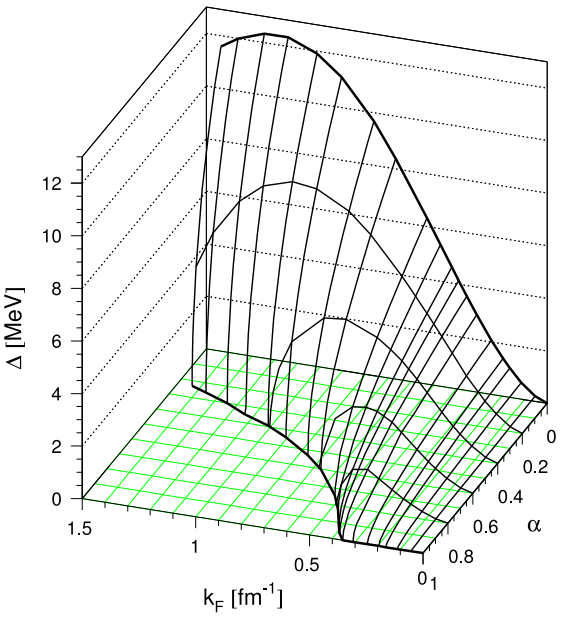

Fig. 33. Gap as a function of $k_F = (3\pi^2 n/2)^{1/3}$ (where $n = n_n + n_p$) and asymmetry $\alpha = (n_n - n_p)/(n_n + n_p)$.
Source: Reproduced from Ref. [23].

density. Neglecting the BHF mean field and the wave vector dependence of $V(\mathbf{k}, \mathbf{k}')$ at low wave vectors, one can show from Eq. (117) that, to linear order in the density, the chemical potential is given by $\mu = \mu_D + \pi n/(2mp_D)$ where $\mu_D = -1.1$ MeV is one half of (minus) the free deuteron binding energy and $p_D = \sqrt{2m|\mu_D|}$.

5.2. Asymmetric nuclear matter and the BCS–BEC crossover

Thus far we have considered only symmetric nuclear matter, with equal densities of protons and neutrons. However, in astrophysical situations such as proto-neutron stars, there is usually a strong neutron excess. It is thus important to consider also the asymmetric (i.e., isospin imbalanced) situation when there are more neutrons than protons. Formally, this is completely analogous to the situation of pairing between spin ↑ and ↓ in a spin-imbalanced (polarized) system discussed in Section 2.6. Here, for the sake of illustration, we concentrate on the blocking effect (breached-pair solution) and leave aside the FFLO solution and phase separation. [Recall, however, from Section 2.6 that, at least for the contact potential, the breached-pair solution corresponds to a physically stable phase only in the BEC limit.]

A first study of this type, which considers the blocking effect due to unpaired neutrons, was undertaken in Ref. [23], where the *pn* gap was studied as a function of asymmetry and density. It was found that asymmetry quenches the gap in the weak-coupling BCS regime, but that it does not play a role in the strong-coupling (low-density) regime. This is understandable since in this regime the system will form a BEC of deuterons and a Fermi sea of the remaining neutrons. At sufficiently low density, the surrounding neutrons will not perturb the deuteron bound state. Fig. 33 shows the gap as a function of $k_F = (3\pi^2 n/2)^{1/3}$, where $n = n_p + n_n$ is the total density, and of the asymmetry $\alpha = (n_n - n_p)/(n_n + n_p)$. In these calculations, the Argonne V_{14} interaction [426] and free single-particle energies were used. One sees that even at very large asymmetries (i.e., $n_n \gg n_p$) there remains a finite gap in the $k_F \to 0$ region, while in the weak-coupling regime (larger k_F) pairing does not survive past some critical asymmetry.

Analytically, this can be shown as follows. In the strong-coupling limit, where the chemical potential is negative and for very low densities tends to $\mu_D = -E_B/2 \sim -1.1$ MeV , the gap and particle number equations somehow exchange their roles as already noted in Section 2.3. The gap equation goes over into the Schrödinger equation for the deuteron, while the gap can be determined from the number equation in the following way. Consider, for example, the density of the protons given by

$$n_p = \frac{(2m)^{3/2}}{2\pi^2} \int_{\varepsilon_{\min}}^{\infty} d\varepsilon \sqrt{\varepsilon} \frac{1}{2} \left[1 - \frac{\varepsilon - \mu}{\sqrt{(\varepsilon - \mu)^2 + \Delta^2}} \right], \tag{119}$$

where the integral over $\mathbf{k}$ has been transformed in an integral over $\varepsilon = \mathbf{k}^2/(2m)$ and $\varepsilon_{\min} = \mu + \delta\varepsilon$ is the energy below which the neutron states are fully occupied while the proton states are empty (at zero temperature), cf. Fig. 4(b). In the $n \to 0$ limit, the width of this region tends towards zero. In addition, since $\mu \to \mu_D$ and $\Delta \ll |\mu_D|$, one can expand the expression within

brackets up to order $(\Delta/\mu_D)^2$. The resulting integral can be performed analytically and one obtains $n_p \sim (n_\mu/2)(\Delta/\mu_D)^2$, where $n_\mu = (2m|\mu_D|)^{3/2}/(8\pi) \sim 0.00049\ \mathrm{fm}^{-3}$. Writing the asymmetry as $\alpha = 1 - 2n_p/n$, one ends up with the following low-density result for the gap [23]

$$\frac{\Delta}{|\mu_D|} = \sqrt{\frac{n(1-\alpha)}{n_\mu}}\,, \tag{120}$$

which confirms that in strong coupling the gap persists for any asymmetry, as seen in Fig. 33.

In weak coupling the situation is different. As shown in Fig. 4(a), the proton occupation numbers are now zero in a window $\mu \pm \delta\varepsilon$ with $\delta\varepsilon = \sqrt{\delta\mu^2 - \Delta^2}$, where $\delta\mu = (\mu_p - \mu_n)/2$ is half the difference between the chemical potentials (analogous to $h = (\mu_\uparrow - \mu_\downarrow)/2$ of Section 2.6). For the gap equation, using a contact interaction with a coupling constant v_0 and a cutoff ε_c instead of the regularization of Eq. (47), one obtains:

$$1 = -\frac{(2m)^{3/2}v_0}{8\pi^2}\int_{-\mu}^{\varepsilon_c-\mu} d\xi\,\Theta(|\xi| - \delta\varepsilon)\sqrt{\frac{\xi+\mu}{\xi^2+\Delta^2}} \tag{121}$$

where $\xi = \varepsilon - \mu$. This integral can be done with the usual approximations valid in the weak-coupling limit. Comparing the result with the corresponding weak-coupling result in the symmetric ($\delta\mu = 0$) case, one finds:

$$\sqrt{\delta\varepsilon^2 + \Delta^2} + \delta\varepsilon = \Delta_0\,, \tag{122}$$

where Δ_0 is the gap in symmetric matter with the same value of μ. One obtains eventually:

$$\Delta = \Delta_0\sqrt{1 - \frac{2\delta\varepsilon}{\Delta_0}}\,. \tag{123}$$

From this result one sees that the gap decreases very rapidly and disappears when $2\delta\varepsilon = \Delta_0$, i.e., when the width of the window reaches the size of the gap in symmetric matter. Since $\Delta_0 \ll \mu$ in weak coupling, one can expand the asymmetry α to leading order in $\delta\varepsilon/\mu$, with the result $\alpha = 3\delta\varepsilon/(2\mu)$. Inserting this into Eq. (123), one concludes that the gap vanishes continuously, although with infinite slope, when [23]

$$\alpha_{\max} = \frac{3\Delta_0}{4\mu}\,, \tag{124}$$

as it can be seen in Fig. 33 for large values of k_F. Concerning further the dependence of Δ on $\delta\mu$, the asymmetry sets in and the gap starts to decrease only after the window $\delta\varepsilon$ opens up, that is, when $\delta\mu$ reaches Δ_0. But then, while $\delta\varepsilon$ and the asymmetry α increase, $\delta\mu$ *decreases* as one can show with the help of above expressions, and the gap eventually vanishes when $\delta\mu = \delta\varepsilon = \Delta_0/2$ [23]. This corresponds to the re-entrant behavior already found by Sarma [101] for condensed matter systems long time ago. As it was argued in Section 2.6, however, this unphysical behavior is eliminated when the FFLO phase or phase separation are considered. For nuclear matter this was done, for instance, in Ref. [427].

5.3. Proton–neutron correlations at finite temperature

Finite-temperature effects are very important in heavy-ion collisions and supernova matter, when low-density nuclear matter can be produced. As discussed in Section 3, the BCS theory is not suitable for the calculation of the critical temperature T_c in the BEC and crossover regimes, because of the existence of pair correlations (that give rise to pre-formed non-condensed pairs in the pseudo-gap phase above T_c). In nuclear matter, pair fluctuations were first studied in Ref. [193] within the ZS approach discussed in Section 3.5.

To reduce the complexity of the calculation, we follow Refs. [22,26,193] and consider a separable potential. In its simplest form, the potential in a given interaction channel α can be written in the form:

$$V_\alpha(k,k') = -\lambda_\alpha v(k)v(k')\,, \tag{125}$$

where k and k' are in- and out-going wave vectors in the center-of-mass frame of the two nucleons, $-\lambda_\alpha$ is the coupling constant, and $v(k)$ is a form factor (which, for instance, in the case of the Yamaguchi potential [428], has the form $v(k) = 1/(k^2+\beta^2)$). In this way, the expression for the t-matrix (with the diagrams shown in Fig. 8(b)) becomes analytic up to a quadrature like in the case of a contact interaction (cf. Eqs. (55) and (57)), leading to the following expressions:

$$\Gamma_\alpha(k,k',Q,\omega) = \frac{V_\alpha(k,k')}{1 - J_\alpha(Q,\omega)} \tag{126}$$

where Q and ω are the total wave vector and energy, respectively, and

$$J_\alpha(Q,\omega) = \int \frac{d\mathbf{k}}{(2\pi)^3}V_\alpha(k,k)\frac{1 - f(\xi_{\mathbf{Q}/2+\mathbf{k}}) - f(\xi_{\mathbf{Q}/2-\mathbf{k}})}{\omega - \xi_{\mathbf{Q}/2+\mathbf{k}} - \xi_{\mathbf{Q}/2-\mathbf{k}} + i0}\,. \tag{127}$$

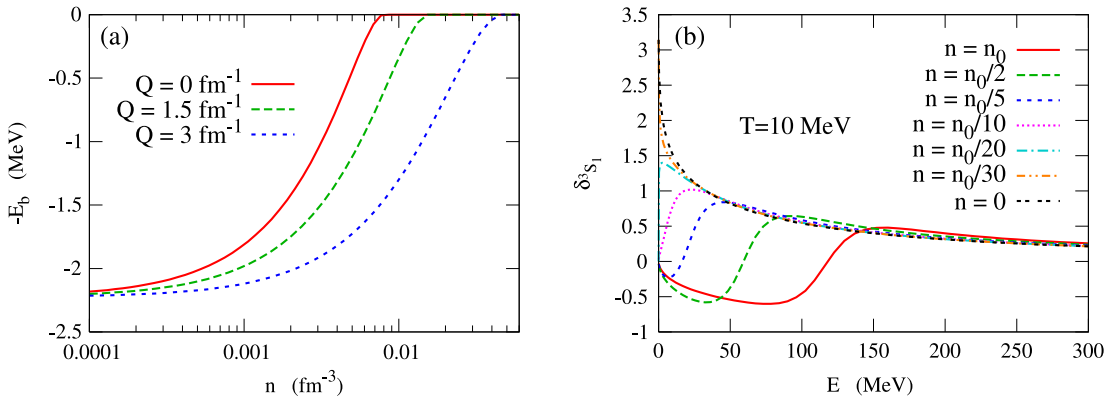

Fig. 34. (a) In-medium deuteron binding energy E_b as a function of the density n for different deuteron wave vectors Q at a fixed temperature of $T = 10$ MeV. (b) In-medium scattering phase shift in the $^3S_1$ channel for $Q = 0$ as a function of $E = k^2/m^*$ for different densities ($n_0 = 0.17$ fm^{-3} is the saturation density of nuclear matter) and $T = 10$ MeV.
Source: Adapted from Ref. [26].

The form factor makes this integral finite and no regularization procedure is needed. Concerning the single-particle energies $\xi_{\mathbf{k}}$ that enter the expression (127), different approximations have been used in the literature. In Ref. [22], the wave-vector dependence of the mean field was neglected and the constant shift was absorbed in an effective chemical potential μ^*, yielding $\xi_{\mathbf{k}} = k^2/2m - \mu^*$. In Ref. [26], the wave-vector dependent mean field was instead calculated with the D1 Gogny force [91] in Hartree–Fock (HF) approximation and then expanded up to second order, yielding $\xi_{\mathbf{k}} = k^2/2m^* - \mu^*$ (effective mass approximation).

Note that in the $^3S_1$ channel, the t-matrix (126) can have a pole at an energy $\omega_b(Q)$ below the two-particle threshold $\omega_0(Q) = Q^2/4m^* - 2\mu^*$. This pole corresponds to the deuteron bound state, and one can define the in-medium binding energy of the deuteron as $E_b = \omega_0 - \omega_b$. Owing to Pauli blocking, the deuteron gets less bound with increasing density, but this effect is weaker for a deuteron that moves with respect to the medium, as it can be seen from Fig. 34(a). The wave vector above which the deuteron is bound is called the Mott wave vector $Q_{\rm Mott}$ [193]. At very low density, the deuteron is always bound and $Q_{\rm Mott} = 0$. The density at which the bound state at $Q = 0$ disappears at a given temperature is called the Mott density. The in-medium nucleon–nucleon phase shifts δ_α can readily be obtained from $1/(1 - J_\alpha) = e^{i\delta_\alpha}/|1 - J_\alpha|$. As an example, Fig. 34(b) shows the phase shift in the $^3S_1$ channel for $Q = 0$ at different densities, as function of the energy $E = \omega + 2\mu^* = k^2/m^*$. One sees that at higher densities, for instance at $n \geq n_0/5$ ($n_0 = 0.17$ fm^{-3} being the saturation density of nuclear matter), the phase shift is negative in the low-energy region and then becomes positive as the energy increases. The energy where the phase shift crosses zero is $\omega = 0$, i.e., $E = 2\mu^*$. At lower densities, when μ^* is negative, the phase shift is positive at low energy. At some very low density, the value of the phase shift at $E = 0$ changes from 0 to π. This happens precisely at the density below which the deuteron is bound, in analogy with what is required in vacuum by Levinson's theorem (see, e.g., Ref. [429]).

Like in the NSR approach, the self-energy Σ is given by the diagram shown of Fig. 8(a), with an important difference, however, as explained in Section 3.5. In the NSR approach, the thin lines of Fig. 8 represent the bare single-particle propagator G_0, while here they represent the HF propagator $G_{\rm HF}$ which contains the HF single-particle energies $\xi_{\mathbf{k}}$ instead of the free ones $k^2/2m - \mu$. The Dyson equation now reads $G^{-1} = G_{\rm HF}^{-1} - \tilde{\Sigma}$, where $\tilde{\Sigma}$ is the self-energy with the HF mean field subtracted. A caution is in order at this point. On the one hand, the density-dependent Gogny force is supposed to take already into account the correlation effects on the single-particle energies $\xi_{\mathbf{k}}$. On the other hand, when calculating Σ with the t-matrix (126), including only the channels $\alpha = {}^3S_1$ (deuteron) and $\alpha = {}^1S_0$ which are most relevant for pairing correlations, one cannot expect Σ to give the correct quasi-particle energies. For this reason, it is convenient to subtract the full energy shift generated by the self-energy, by setting

$$\tilde{\Sigma}(\mathbf{k}, \omega) = \Sigma(\mathbf{k}, \omega) - \Sigma(k, \xi_{\mathbf{k}}), \tag{128}$$

which allows for a clear separation of dynamic correlation effects encoded in the energy dependence of $\tilde{\Sigma}$ and effects from the mean-field shift contained in $\xi_{\mathbf{k}}$.

To discuss the correlation correction to the density as a function of μ, one starts from the expression

$$n(T, \mu) = -4T \sum_{\nu, \mathbf{k}} G(k, i\omega_\nu) \tag{129}$$

where the factor of 4 comes from the sum over spin and isospin. If the Dyson equation is again truncated at first order, such that $G \approx G_{\rm HF} + G_{\rm HF}^2 \tilde{\Sigma}$, one can write the total density as in Eq. (92) as a sum of the HF density $n_{\rm HF}$ plus corrections in the

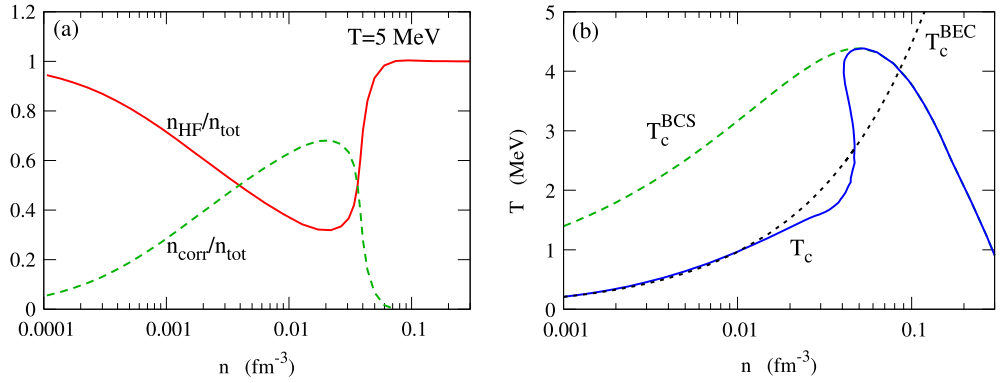

Fig. 35. (a) HF (solid line) and correlation (dashed line) contributions to the total density $n_{\rm tot} = n_{\rm HF} + n_{\rm corr}$ for $T = 5$ MeV as a function of the total density. (b) Critical temperature (solid line) as a function of density interpolating between BCS (long-dashed line) and BEC (short-dashed line) critical temperatures in symmetric nuclear matter.
Source: Adapted from Ref. [26].

form [22,26,193]:

$$n = n_{\rm HF} + n_{\rm corr} = n_{\rm HF} + n_{\rm bound} + n_{\rm scatt}\,. \tag{130}$$

Here, the bound-state contribution reads

$$n_{\rm bound} = 6\int_{|\mathbf{Q}|>Q_{\rm Mott}} \frac{d\mathbf{Q}}{(2\pi)^3} b(\omega_b(Q)) \tag{131}$$

where $b(\omega) = 1/(e^{\omega/T}-1)$ is the Bose function. This term gives the nucleon density corresponding to a Bose gas of deuterons. The factor of 6 takes into account that the deuteron has 3 spin projections and each deuteron contains 2 nucleons. In addition, the scattering-state contribution reads:

$$n_{\rm scatt} = -6\int_{|\mathbf{Q}|>Q_{\rm Mott}} \frac{d\mathbf{Q}}{(2\pi)^3} b(\omega_0(Q)) - 6\sum_{\alpha={}^3S_1,\,{}^1S_0} \int \frac{d\mathbf{Q}}{(2\pi)^3} \int_{\omega_0(Q)}^{\infty} \frac{d\omega}{\pi} \left(\frac{d}{d\omega} b(\omega)\right) \left(\delta_\alpha - \tfrac{1}{2}\sin 2\delta_\alpha\right)\,. \tag{132}$$

As an example of the importance of the correlation contribution to the density, Fig. 35(a) shows the composition of the system at temperature $T = 5$ MeV . One sees that the correlation contribution to the total density is important at low density ($n < n_0/4$). When $n = 0.02$ fm^{-3}, the correlated part is even larger than the HF part, meaning that most of the nucleons are in correlated pairs in this density region. With increasing temperature, the ratio of the correlated density to the total density decreases, but the density region with sizeable nucleon correlations is enlarged. Note that the correlation contribution is not separated into bound and scattering state contributions since, taken separately, they are not very meaningful, as discussed in Ref. [193]. For instance, if the temperature is much larger than the deuteron binding energy, the first term of the scattering-state contribution (132) almost exactly cancels the bound-state contribution (131).

For given chemical potential μ, the critical temperature T_c is obtained from the Thouless criterion, which in the present case reads $J_{^3S_1}(Q = 0, \omega = 0) = 1$. When one calculates T_c as a function of the density, the corrections $n_{\rm bound}$ and $n_{\rm scatt}$ are crucial in the strong-coupling regime, since only with these corrections one recovers the critical temperature $T_c^{BEC} = \pi/m(n/6\zeta(3/2))^{2/3}$ for the Bose–Einstein condensation of deuterons in the low-density limit. At higher densities, the result interpolates between $T_c^{\rm BEC}$ and the BCS critical temperature $T_c^{\rm BCS}$, as shown in Fig. 35(b). Note further that, in some range of densities, T_c as a function of n is double-valued. This is a consequence of the first-order liquid–gas phase transition of nuclear matter. We will discuss this phenomenon in detail in Section 5.4.

As discussed in Section 3.3, the pre-critical pair fluctuations lead to the formation of a pseudo-gap. For the case of low-density nuclear matter, the single-particle spectral function and the pseudo-gap in the level density (which corresponds to the density of states in condensed matter) were studied in Ref. [30]. In this work, the authors consider again the t-matrix approximation to the self-energy of Fig. 8(a). After analytic continuation, the imaginary part of the retarded self-energy reads:

$$\mathrm{Im}\,\Sigma(1,\omega) = \sum_2 \mathrm{Im}\,\Gamma(12,12,\omega+\xi_2+i0)[f(\xi_2)+b(\omega+\xi_2)] \tag{133}$$

where the short-hand notation "1" stands for wave vector $\mathbf{k}_1$, spin σ_1, and isospin τ_1 quantum numbers (and analogously for "2"). The real part is obtained from the imaginary part according to the Kramers–Kronig relation. Here, Γ is again calculated with the separable Yamaguchi potential (125), however, with the single-particle energies $\xi_k = k^2/2m + U(k) - \mu$ obtained

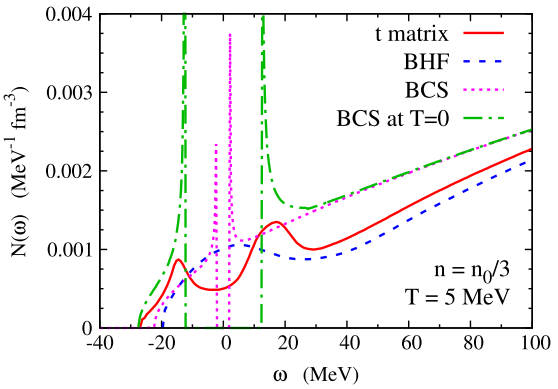

Fig. 36. Level density for $T = 5$ MeV and $n = n_0/3$ within the quasiparticle approximation, using $U(k)$ from the t-matrix approach (solid line) and from the BHF approximation (dashed line). For comparison, BCS results for $T = 5$ MeV (dotted line) and $T = 0$ (dot-dashed line) are also shown.
Source: Adapted from Ref. [30].

by a self-consistent Galitskii–Feynman calculation from the real part of the self-energy, i.e., $U(k) = \text{Re}\,\Sigma(k, \xi_k)$. Note that this is different from the Brückner–Hartree–Fock (BHF) approach [95], where the "backward" (hole–hole) contributions are discarded [i.e., the factor $(1 - f_1 - f_2)$ in the numerator of Eq. (127) is replaced by $(1 - f_1)(1 - f_2)$]. As we will see, this is important since the BHF approximation entails unphysical results for the level density.

Using the quasi-particle approximation, whereby the full spectral function in Eq. (81) is replaced by $A(k, \omega) = \delta(\omega - \xi_k)$, one obtains the level density from the expression:

$$N(\omega) = \left[\frac{1}{k^2}\frac{\partial \xi_k}{\partial k}\right]^{-1} \qquad \text{calculated at } \xi_k = \omega\,. \tag{134}$$

Fig. 36 shows the formation of the pseudo-gap in the level density approaching the critical temperature from above, for low particle density $n = n_0/3$. Note that when $T = 5$ MeV the BHF calculation yields an opposite behavior compared to the t-matrix approach, underlining the necessity to incorporate the hole–hole contribution. Fig. 36 also shows the standard BCS gap (dotted line) in the level density, which is quite small owing to the closeness of $T = 5$ MeV to the critical value $T_c^{\text{BCS}} = 5.08$ MeV of BCS theory. With the full theory, the critical temperature is instead $T_c = 4.34$ MeV and the calculation is performed in the normal-fluid regime. The full line shows that the pair fluctuations lead to a pseudo-gap, with a strong depletion of the level density around the Fermi energy. However, the pseudo-gap effect is overestimated in the quasi-particle approximation. If one calculates the level density from the full spectral function $A(k, \omega) = -1/\pi\ \text{Im}[1/(\omega - k^2/2m - \Sigma(k, \omega) + \mu)]$, the depletion in the level density is still present but it is somewhat weaker than that shown in Fig. 36 (cf. Fig. 2 of Ref. [30]). Note the overall similarity with the results presented in Fig. 13(c) for a contact potential.

5.4. Effect of pairing on the liquid–gas transition in symmetric nuclear matter

In symmetric nuclear matter one cannot pass continuously from the BEC to the BCS side, because, at intermediate densities, homogeneous nuclear matter is thermodynamically unstable and transforms into an inhomogeneous mixture of "gas" (dilute) and "liquid" (dense) phases (for a review, see, e.g., Ref. [430]). This occurs already at the HF level, but the inclusion of the correlated density in Eq. (130) has sizeable effects on the phase diagram.

We begin by discussing the relation between the density n and the chemical potential μ. Fig. 37(a) shows n as a function of μ for different temperatures, where the dashed lines represent the HF results n_{HF} (obtained with the Gogny force [91]) and the solid lines include the correction n_{corr} due to pair correlations (cf. Eq. (130)). This comparison shows that, for given chemical potential, the correlations increase the density. In the high-density region, the results with and without correlations converge to the same value, implying that the correlations fade away at high density as expected. For example, at $T = 5$ MeV, the two results coincide starting from $n = 0.07$ fm^{-3}. This is a consequence of the Mott mechanism, as discussed at length in Ref. [193]. As mentioned in Section 5.3, the critical number density where the bound state (at $Q = 0$) disappears is called Mott density. When the temperature changes from 5 MeV to 10, 15.9, and 20 MeV, the Mott density changes from 0.07 fm^{-3} to 0.12, 0.18, and 0.22 fm^{-3}, implying that the mean-field approximation is valid in the high-density region. Below this region, the contribution of the nucleon–nucleon correlations is important.

From Fig. 37(a) one also sees that, below a certain critical temperature $T_c^{\text{liq–gas}} = 15.9$ MeV (which has nothing to do with the superfluid critical temperature), n is no longer a single-valued function of μ. Therefore, the curves in Fig. 37(a) are generated in practice by making a loop over the HF density and not over μ. The presence of a region of densities where the chemical potential decreases with increasing density is a typical feature of a liquid–gas phase transition. In the present framework, the liquid–gas critical temperature coincides with the mean-field result [431,432]. This is an artifact of the

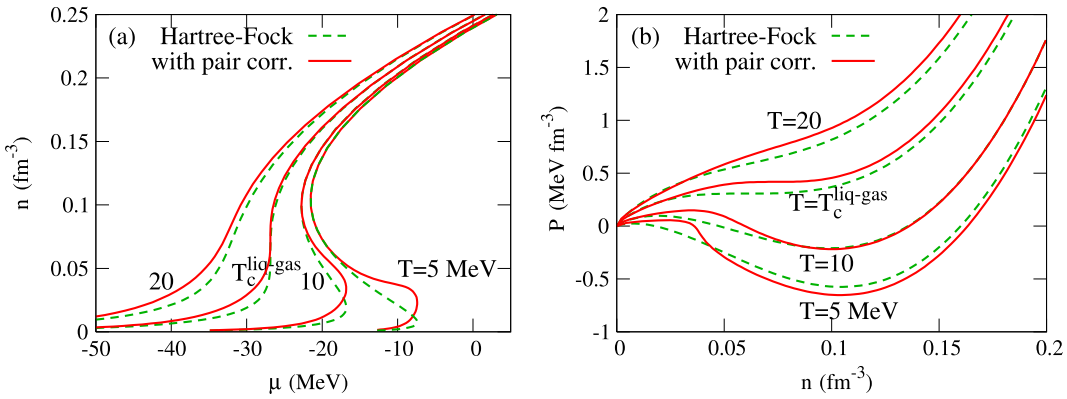

Fig. 37. (a) Density of symmetric nuclear matter at $T = 20$, 15.9, 10, and 5 MeV (from left to right) as a function of the chemical potential. (b) Corresponding pressure as function of the density. The dashed lines are Gogny HF results, while the solid lines include the pair correlations in the normal phase.
Source: Adapted from Ref. [26].

perturbative treatment of correlation effects, as explained in Section 5.3. In a more complete (self-consistent) treatment, $T_c^{\text{liq–gas}}$ should be reduced when deuteron (and heavier) clusters are included, as shown in Ref. [192].

To determine the boundary of this first-order phase transition, one needs to consider the pressure. In principle, one can get the pressure $P(T, \mu)$, as a function of temperature and chemical potential, from the number density $n(T, \mu)$ by integrating the thermodynamic relation $n = (\partial P/\partial \mu)_T$ over μ:

$$P(T, \mu) = \int_{-\infty}^{\mu} n(T, \mu')d\mu' . \tag{135}$$

However, this procedure has to be modified in the temperature range below $T_c^{\text{liq–gas}}$, where n is not a single-valued function of μ. In this region, one can obtain the pressure by transforming the integral over μ into an integral over n_{HF} as follows:

$$P(T, n_{\text{HF}}) = \int_0^{n_{\text{HF}}} n(T, n'_{\text{HF}}) \left(\frac{\partial \mu}{\partial n'_{\text{HF}}} \right)_T dn'_{\text{HF}} . \tag{136}$$

Since μ is a single-valued function of n_{HF} (cf. dashed line in Fig. 37(a)), this integral is well defined.

The resulting pressure is shown in Fig. 37(b) as a function of the density, where again the solid lines are the full results including pair correlations and the dashed lines are HF results. The main effect of the nucleon–nucleon correlations is to increase the pressure at very low densities, with the exception of the case $T = 5$ MeV for which the pressure at high densities is lower than the HF result.

From Fig. 37(b) one sees that there is a density region where $\partial P/\partial n < 0$. In this so-called spinodal region, small density fluctuations grow exponentially, resulting in phase separation (visible as multi-fragmentation in heavy-ion collisions). The boundaries of the spinodal region can be obtained from the zeros of $\partial P/\partial n$ (or, equivalently, of $\partial \mu/\partial n$) and are shown as the thick solid line in Fig. 38. Outside the spinodal region, there is a region in the phase diagram where the system is metastable and it is energetically favorable to phase separate. The coexistence region of the liquid and gas phases of nuclear matter are determined by the conditions for chemical and mechanical equilibrium:

$$P(T, n_1) = P(T, n_2) \qquad \text{and} \qquad \mu(T, n_1) = \mu(T, n_2) . \tag{137}$$

The result is shown in Fig. 38 as the thin solid line. Note that, within the present approach, the high-density boundary of the coexistence region cannot be computed for $T < 4.5$ MeV, because the calculation of the pressure at a given density n from Eq. (136) necessitates the calculation of all densities $n' < n$. This would, in fact, include the density at $n = 0.05$ fm^{-3} where the superfluid T_c reaches its maximum of about 4.5 MeV (cf. Fig. 35(b)).

For comparison, the corresponding mean-field results for the phase boundaries are presented in Fig. 38(a) (dashed lines), which coincide with Fig. 6 of Ref. [432]. Comparing the results with and without correlations, one sees that the correlations decrease the phase-transition temperature in the low-density region and reduce the unstable region of the liquid–gas phase transition considerably. This is an expected result, since the presence of deuterons in the gas can be considered as a first step towards the formation of liquid droplets. In the high-density region, the effect of the correlations is almost negligible, which is also plausible because there the deuteron is unbound. The stabilization effect is probably even stronger for α-particle condensation (to be discussed in Section 5.8) than for deuterons, since α particles are about seven times more strongly bound than deuterons.

In Fig. 38(b), the superfluid critical temperature T_c (dashed line), the liquid–gas coexistence region (thin line), and the spinodal instability region (thick line) have been combined in a single phase diagram. As explained above, the present

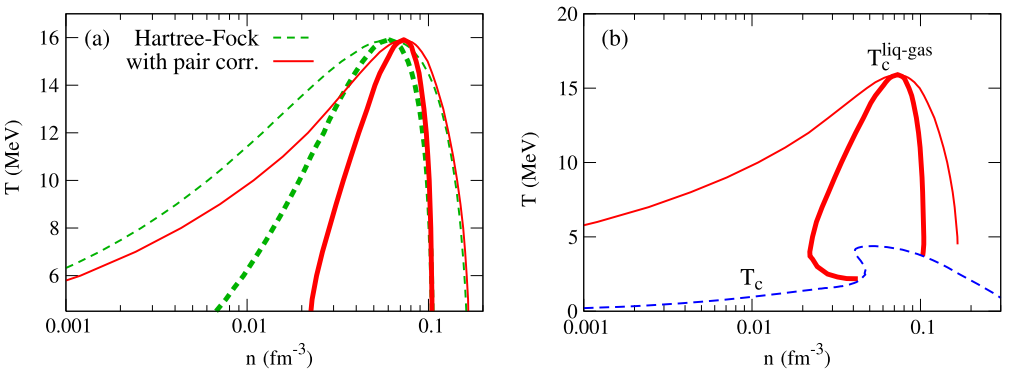

Fig. 38. (a) The liquid–gas phase diagram of symmetric nuclear matter as a function of density and temperature (for $T \geq 4.5$ MeV). The thin lines are the boundary of the coexistence region, while the thick lines are the boundary of the spinodal region. Solid lines: with correlations; dashed lines: mean field results. (b) Combination of the liquid–gas phase diagram of (a) and the superfluid phase diagram shown in Fig. 35(b). Upper thin line: limits of the coexistence region; thick line: spinodal region in the normal phase, dashed line: transition to the superfluid phase.
Source: Adapted from Ref. [26].

approach does not allow one to calculate the liquid–gas coexistence curve for $T < 4.5$ MeV . However, extrapolating the thin solid curve to lower temperatures and recalling that at $T = 0$ the liquid phase becomes stable at saturation density, it is clear that the coexistence curve will cross the superfluid T_c curve at $n \sim n_0$, implying that homogeneous nuclear matter with pairing is stable above this density, as one would expect. From the results of Ref. [433] one can presume that the liquid–gas coexistence region will be slightly reduced below the superfluid critical temperature, but this effect should be almost negligible in the case of symmetric nuclear matter considered here [433,434]. At low densities, superfluid matter is never stable, because the superfluid T_c curve remains always below the coexistence curve.

The spinodal curve, given by the thick line of Fig. 38, can be calculated until it reaches the superfluid region. One thus concludes that superfluid nuclear matter is metastable below $n \sim 0.045$ fm^{-3} and above $n \sim 0.1$ fm^{-3}. Note that, at low density, the density region where the gas phase is metastable is strongly enlarged by correlations, especially when approaching the superfluid transition temperature. This confirms that the correlations have a stabilizing effect with respect to phase separation, even though the intermediate region of the BCS–BEC crossover still lies in the unstable region of the liquid–gas phase transition. Note that also at $T = 0$ symmetric nuclear matter is not stable at sub-saturation densities, but the exact boundaries of the spinodal region are not yet known.

5.5. Neutron–neutron pairing at zero temperature

In the *nn* case, the BEC side of the BCS–BEC crossover cannot be realized because there is no *nn* bound state. As a matter of fact, it is generally believed that two neutrons are nearly bound (although experimentally the possibility of an extremely weakly bound state is not excluded). As a consequence, the S-wave scattering length $a_{nn} = -18.5$ fm [435] is quite large compared to the range of the *nn* interaction, which is only of the order of $R \sim 1$ fm. Hence, at low density the situation $R < 1/k_F < |a_{nn}|$ can be realized, similarly to trapped atoms near the unitary limit. With increasing density, however, the finite range of the interaction plays an increasingly important role. The effect of the effective range on the equation of state was studied within a t-matrix theory in Ref. [436]. The finite range of the interaction leads to a reduction of pairing correlations at higher density, so that one passes from the strongly interacting to the BCS regime.

It is assumed that in the inner crust of neutron stars there is a dilute gas of neutrons coexisting with a Coulomb lattice of dense nuclear clusters (for a review, see, e.g., Ref. [437]). The density of the neutron gas varies continuously from 0 to ∼0.08 fm^{-1} as one goes deeper into the star. The distance between the heavy clusters can be very large (up to more than 100 fm) and the neutron gas can be approximately regarded as uniform. The *nn* pairing in this gas can have important observable consequences on the cooling of the star [438].

Several studies in the low-density limit of *nn* pairing have been performed. In Ref. [34], the BCS gap equation (115) was solved for the case of pure neutron matter. For the interaction $V(\mathbf{k}, \mathbf{k}')$, the D1 Gogny force [91] and the so-called G3RS force [439] were used. While the former is a density-dependent effective in-medium interaction, the latter is a bare nucleon–nucleon force, which is relatively simple but reproduces the *nn* scattering phase shifts in the $^1S_0$ channel. The single-particle energies ξ_k were calculated with the Gogny HF mean field. It should, however, be mentioned that the Gogny force in the $^1S_0$ channel is also density independent and relatively close to the bare force (with scattering length −13.5 fm).

Fig. 39(a) shows the *nn* pairing tensor as a function of position r for various densities. In the zero-density limit, the wave function looks like that of a bound state although there is only a resonance very close to zero energy. In Fig. 39(b), the *nn* coherence length (pair size) is shown as a function of density. Although qualitatively it looks similar to the *pn* case of Fig. 32(b), the important difference is that, in the zero-density limit, the coherence length of the *nn* pairs diverges (since there is no *nn* bound state) while the coherence length of *pn* pairs approaches the deuteron rms radius. Note also that the

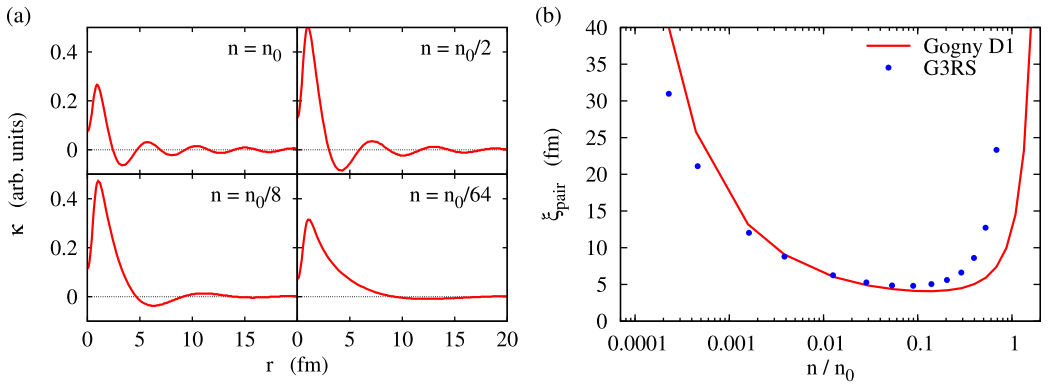

Fig. 39. (a) Pairing tensor in coordinate space as a function of r in neutron matter for various densities ($n_0 = 0.085$ fm^{-3} is half the saturation density of symmetric nuclear matter). (b) Coherence length of the *nn* Cooper pair in neutron matter as a function of the density.
Source: Adapted from Ref. [34].

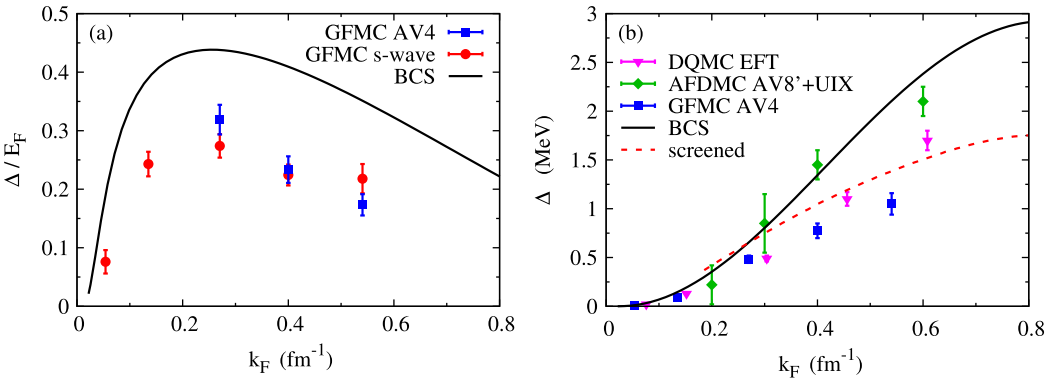

Fig. 40. (a) Ratio Δ/E_F and (b) gap Δ in neutron matter as a function of the Fermi wave vector k_F, as obtained in different QMC calculations (symbols): variational and Green's function Monte Carlo (GFMC) [36]; determinantal quantum Monte Carlo (DQMC) [35]; auxiliary field diffusion Monte Carlo (AFDMC) [443]. For comparison, the BCS results (solid line) and results of Ref. [189] that include screening corrections (dashed line) are also shown.
Source: Adapted from Ref. [36].

minimal size of the *nn* Cooper pair stays slightly above the *pn* one. Similar results were found using relativistic mean-field (RMF) single-particle energies and the Bonn-B potential in the gap equation [440].

The nuclear pairing problem is further complicated by the fact that the nuclear force contains a three-body piece, which is not very well known. Recently, a *nn* pairing calculation was performed in Ref. [441] including two-body and three-body forces obtained from chiral perturbation theory. According to this study, the (repulsive) three-body force does not give rise to a very strong reduction of the gap in neutron matter. As with other well tested phenomenological pairing forces like the Gogny D1S force [91], one obtains a gap which culminates at ∼2.5 MeV at $k_F \sim 0.8$ fm^{-1}. In a recent study of the *nn* gap [442], extensive numerical investigations of the $^1S_0$ gap (and the $^3P_2 - {}^3F_2$ one) were performed in the BCS approach using chiral effective field theory also including three body forces, with the aim of assessing the uncertainty of the *nn* gap in BCS approximation. These results confirm the earlier findings, with the conclusion that at the BCS level the uncertainties are not important (at least, as far as the $^1S_0$ *nn* gaps are concerned).

Low-density neutron matter was also studied with more sophisticated Quantum-Monte-Carlo (QMC) approaches. These are ab-initio calculations that adopt a realistic nucleon–nucleon interaction. As an example, Fig. 40(a) shows the ratio Δ/E_F of the gap to the Fermi energy $E_F = k_F^2/(2m)$ obtained by the variational and Green's function Monte-Carlo (GFMC) method of Ref. [36]. The blue squares were obtained with the AV4 interaction, a simplified version of the Argonne V_{18} interaction keeping *s* and *p* wave contributions, while the red circles were obtained keeping only the *s*-wave interaction. As expected, the gap is entirely determined by the *s*-wave interaction at these low densities. It appears that the QMC results for Δ/E_F are suppressed compared to the BCS ones (solid line). Even with this suppression, the maximum value of Δ/E_F of about 0.3 is reached at $k_F \sim 0.27$ fm^{-1}, corresponding to a very low density of ∼0.0007 fm^{-3}. This ratio corresponds to a strong coupling situation, with $(k_F a_{nn})^{-1} \sim -0.2$, which is close to, but not precisely at, the unitary limit. At higher densities, $(k_F a_{nn})^{-1}$ gets even closer to zero, but the finite range of the interaction leads to a strong reduction of the gap. As a consequence, high-density neutron matter is again in the weak-coupling (BCS) regime. In Fig. 40(b), the gap Δ of the GFMC calculations of Ref. [36] (squares) is compared with the results of other QMC calculations. The determinantal quantum Monte-Carlo (DQMC)

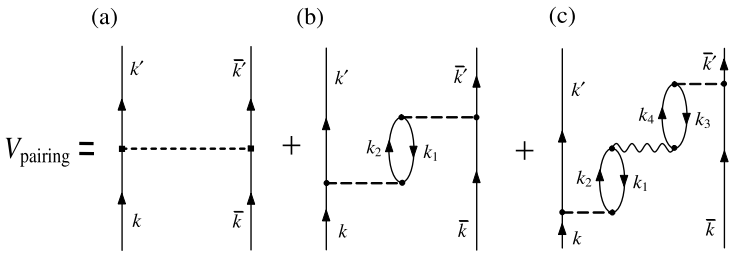

Fig. 41. Diagrams for the pairing interaction with screening from bubble exchanges.

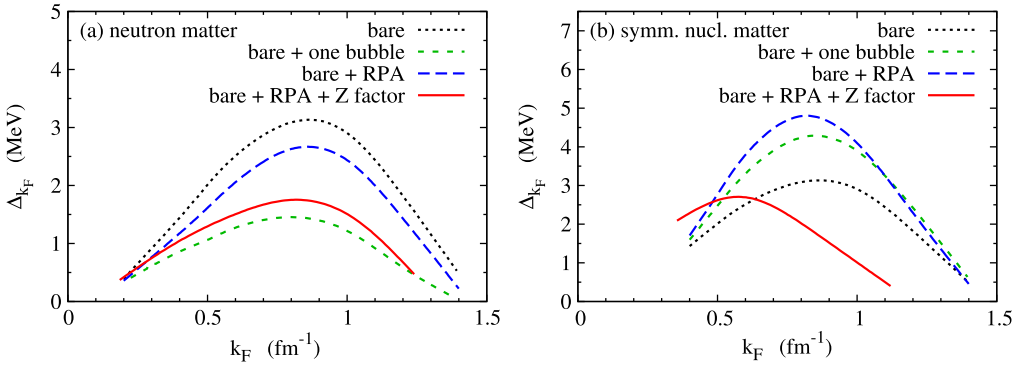

Fig. 42. Neutron–neutron pairing gaps in the $^1S_0$ channel for (a) neutron matter and (b) symmetric nuclear matter obtained with different approximations. Dashed line: using only the bare interaction of Fig. 41(a); short-dashed line: including the one bubble exchange of Fig. 41(a) and (b); long-dashed line: including the full RPA in the screened interaction of Fig. 41(a), (b), and (c); solid line: including the Z factors in addition to the fully screened interaction. *Source:* Data taken from Ref. [189].

results of Ref. [35] (triangles), obtained with a low-momentum interaction derived from pionless effective-field theory (EFT), agrees at low density very well with the GFMC results of Ref. [36] and also shows a suppression with respect to the BCS gap (solid line). This suppression is mainly a consequence of the particle–hole fluctuations, analogous to the Gor'kov–Melik-Barkhudarov (GMB) corrections discussed in Section 3.4 for a contact interaction. These screening effects, which are missing in the BCS approach, are in principle automatically included in the exact QMC calculations. Surprisingly, the auxiliary field diffusion Monte-Carlo (AFDMC) calculation of Ref. [443] (diamonds), which uses a more complete interaction (AV8' two-body plus Urbana IX three-body force), shows almost no suppression of the gap with respect to the BCS result. As pointed out in Ref. [36], this discrepancy between the AFDMC results of Ref. [443] and the other QMC results may be due to the trial wave function used in Ref. [443].

The inclusion of screening (or anti-screening) corrections is a delicate task. Only a few theoretical studies in infinite nuclear and neutron matters exist (see, e.g., Ref. [444] and references therein). The reason is that nuclear systems are strongly interacting, while medium polarization can only be tackled perturbatively for technical reasons. A step towards a non-perturbative treatment of screening, based on a renormalization group approach, was made in Ref. [445], leading to a very strong suppression of the gap. The fact that the gap, like in nuclear matter, depends exponentially on any uncertainty of the effective pairing force makes a reliable prediction very difficult. In any case, one has to go beyond the lowest-order GMB approach (see Section 3.4). Nonetheless, the results obtained in Ref. [189] with screening corrections are quite close to the Monte-Carlo results in neutron matter (see dashed line in Fig. 40(b)). It is therefore worth explaining how pairing is affected by medium polarization in neutron matter and symmetric nuclear matter. One of the subtle points is that one has to treat polarization effects consistently in the pairing force and nucleon self-energies. This is because quite often strong cancellations of both contributions occur. The screening terms which we refer to are depicted in Fig. 41. Here, diagram (a) corresponds to the bare force (Born term), while diagrams (b) and (c) stand for the whole bubble series (RPA). The bubbles are attached to the particle–particle lines via the G-matrix [446,447]. The corresponding gap equation is given in Eq. (91). There is, however, a problem with the calculation of the multi-bubble contributions. The particle–hole interaction in the bubble series can be approximated by the Landau parameters. However, as a consequence of the liquid–gas instability, there appears the well-known low-density singularity of the RPA in nuclear matter (with Landau parameter $F_0 = -1$). This problem, discussed in Ref. [448] (see also references therein) is remedied by dressing the vertex insertions according to the Babu–Brown induced-interaction theory [449]. The results are shown in Fig. 42 for (a) neutron matter and (b) symmetric nuclear matter. The red solid lines should be considered as the final results.

As already mentioned, the gap in neutron matter compares quite well with the QMC results of Ref. [36]. One may extrapolate from this that also the gap in symmetric nuclear matter is quite reliable. However, the strong shift of the

peak position towards lower density is slightly suspicious, also because this feature is not seen in any of the more phenomenological approaches. If true, this feature would imply that, at saturation, there is practically a vanishing neutron–neutron gap in symmetric nuclear matter. Nevertheless, this does not necessarily mean that in finite nuclei the superfluid properties are not well reproduced, since there an average over whole volume and surface is performed.

It is also interesting to see from Fig. 42 that, concerning the induced force, in symmetric nuclear matter there is actually anti-screening while in neutron matter there is screening. This stems from the fact that, contrary to neutron matter, also proton bubbles can be exchanged which have an attractive effect. Only when in addition the dynamic mean field corrections (i.e., the Z-factors defined in Eq. (90)) are included, the final gap becomes quenched.

More recently [450], the induced pairing interaction was calculated at various asymmetries. The screening in neutron matter goes smoothly over to anti-screening in symmetric nuclear matter. About half way in between there is practically total cancellation between screening and anti-screening and only the mean field remains active. However, so far the corresponding gaps have not yet been calculated.

5.6. Neutron matter at finite temperature

At finite temperature, the correlated density of Eq. (130) has to be included in the calculation of T_c as a function of n, as discussed in Sections 3.1 and 5.3. This was done, e.g., in Ref. [37], where an effective low-momentum interaction $V_{\text{low-}k}$ was used [451]. Since this interaction is not separable, the calculation of the t-matrix, the critical temperature, and the correlated density is slightly more involved than with a separable potential.

The technique used in Ref. [37] is based on the so-called Weinberg eigenvalues [452]. The starting point is the integral equation for the nn t-matrix, of the form:

$$\Gamma(\mathbf{k}, \mathbf{k}', \mathbf{Q}, \omega) = V(\mathbf{k}, \mathbf{k}') + \int \frac{d\mathbf{k}''}{(2\pi)^3} V(\mathbf{k}, \mathbf{k}'') G_0^{(2)}(\mathbf{k}'', \mathbf{Q}, \omega) \Gamma(\mathbf{k}'', \mathbf{k}', \mathbf{Q}, \omega) \,. \tag{138}$$

Here, $\mathbf{Q}$ is the total wave vector of the pair, $\mathbf{k}$ and $\mathbf{k}'$ are the initial and final wave vectors in the center-of-mass frame, and

$$G_0^{(2)}(\mathbf{k}, \mathbf{Q}, \omega) = \frac{1 - f(\xi_{\mathbf{Q}/2+\mathbf{k}}) - f(\xi_{\mathbf{Q}/2-\mathbf{k}})}{\omega - \xi_{\mathbf{Q}/2+\mathbf{k}} - \xi_{\mathbf{Q}/2-\mathbf{k}} + i0} \tag{139}$$

is the (retarded) non-interacting two-particle propagator in the medium with $\xi_{\mathbf{k}} = k^2/2m - \mu$. Eq. (138) can be readily solved in the basis where the operator $VG_0^{(2)}$ is diagonal, which implies finding the (generally complex) eigenvalues η_ν that correspond to the eigenfunctions ψ_ν, such that:

$$\int \frac{d\mathbf{k}'}{(2\pi)^3} V(\mathbf{k}, \mathbf{k}') G_0^{(2)}(\mathbf{k}', \mathbf{Q}, \omega) \psi_\nu(\mathbf{k}', \mathbf{Q}, \omega) = \eta_\nu(Q, \omega) \psi_\nu(\mathbf{k}, \mathbf{Q}, \omega) \,. \tag{140}$$

In the S-wave case here considered, the eigenvectors depend only on $Q = |\mathbf{Q}|$ and $k = |\mathbf{k}|$, but not on the angle between $\mathbf{Q}$ and $\mathbf{k}$, such that $G_0^{(2)}$ can be averaged over this angle. The critical temperature can then be obtained from the condition $\eta_\nu(Q = 0, \omega = 0) = 1$, since this corresponds to a pole in the t matrix.

To obtain the correction to the density, the Dyson series of the single-particle Green's function can be truncated to first order like in the original NSR approach, by writing $G \approx G_0 + G_0^2(\Sigma - \Sigma_1)$ where the self-energy Σ is again calculated within the t-matrix approximation (cf. Fig. 8(a)). Note that the first-order (HF) contribution Σ_1 has been subtracted, assuming that it is already included in the single-particle energies (cf. discussion in Section 5.3). In this case, one can write the density as $n = n_{\text{free}} + n_{\text{corr}} - n_1$, where the correlation contribution can be expressed in terms of the Weinberg eigenvalues η_ν, in the form

$$n_{\text{corr}} = -\frac{\partial}{\partial \mu} \int \frac{Q^2 dQ}{2\pi^2} \int \frac{d\omega}{\pi} b(\omega) \, \text{Im} \sum_\nu \log(1 - \eta_\nu(Q, \omega)) \,, \tag{141}$$

while the correction from the HF term is given by:

$$n_1 = 2 \int \frac{d\mathbf{k}}{(2\pi)^3} \frac{\partial f(\xi_{\mathbf{k}})}{\partial \xi_{\mathbf{k}}} \Sigma_1(k) \,. \tag{142}$$

Fig. 43 shows the resulting dependence of T_c on n via the dimensionless parameter $(k_F a_{nn})^{-1}$(with $k_F = (3\pi^2 n)^{1/3}$). The results obtained by the BCS theory (dashed line) and the original NSR approach with a contact interaction (dotted line) are also shown for comparison. In the figure, the limits $(k_F a_{nn})^{-1} \to -\infty$ and $(k_F a_{nn})^{-1} \to 0$ correspond to low and high density, respectively. In both limits, neutron matter is in the BCS phase: at low density, because $a_{nn} < 0$ is finite; at high density, because of the finite range of the interaction [24]. The maximum of T_c/E_F is reached for $(k_F a_{nn})^{-1} \sim -0.2$, which corresponds to a density of ~ 0.0007 fm^{-3} $\sim 0.004\, n_0$ (which is approximately where also the ratio Δ/E_F is maximum, cf. Fig. 40(a)). Such a dilute neutron gas exists probably between the nuclear clusters in certain regions of the inner crust of neutron stars. One can say that, at this density, the neutron gas is very close to the unitary limit. Note however that, as it was the case for the gap (cf. Figs. 40 and 42), also the critical temperature is expected to be lowered by GMB-like screening corrections [172,189] which were not included here.

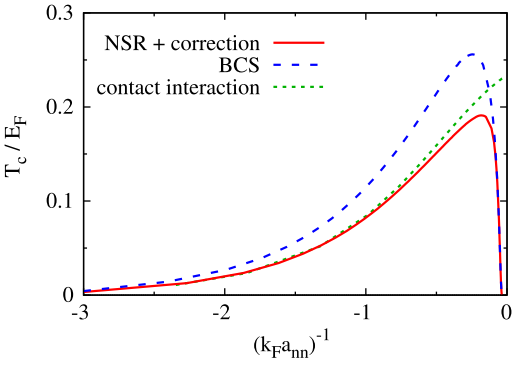

Fig. 43. Solid line: critical temperature of neutron matter in units of the Fermi energy, as a function of the dimensionless parameter $(k_F a_{nn})^{-1}$, obtained within the NSR approach adapted to neutron matter [37]. For comparison, the dashed line shows the BCS result and the dotted line the NSR result for a contact interaction.
Source: Adapted from Ref. [37].

5.7. Short-range correlations and generalized nuclear contact

In contrast to ultra-cold atoms, the inter-particle distance and the interaction range in nuclei are not separated by orders of magnitude and, therefore, one cannot expect to find a clean $1/k^4$ tail in the occupation numbers [453]. As a consequence, there is no nuclear analog of the Tan's relations of Section 4.5. Nevertheless, the contact formalism has been generalized to the nuclear physics context.

As pointed out in Ref. [453], a kind of universality of short-range proton–neutron correlations was already observed more than 60 years ago. Namely, it was found that the cross section for the nuclear photoeffect at photon energies above 150 MeV is approximately given by [454]

$$\sigma = L\frac{NZ}{A}\sigma_d\,, \tag{143}$$

where σ_d is the photodisintegration cross section of the deuteron. This suggests that the photon is absorbed by a correlated proton–neutron pair whose wave function is similar to that of the deuteron at short distances. The so-called Levinger constant $L \approx 6$ is universal in the sense that it is roughly the same for all nuclei, and it has been recently related to the contact [453,455].

Since in nuclear physics there is not only spin but also isospin, one has now two contacts C_s and C_t depending on whether the pair is in a spin singlet ($S = 0, T = 1$) or triplet ($S = 1, T = 0$ as the deuteron) state. In terms of the contacts C_s and C_t, the Levinger constant L can be written as [453]

$$L = \frac{a_t}{8\pi}\frac{A}{NZ}(C_s + C_t)\,, \tag{144}$$

where a_t is the *pn* scattering length in the triplet channel.

Although the *s* wave is dominant at short distances, a generalization of the contact formalism to higher partial waves was presented in Ref. [456]. In that work, the momentum distributions of light nuclei, obtained in variational Quantum Monte-Carlo calculations, were analyzed. It was found that the large wave-vector tails become universal, although not proportional to $1/k^4$, for $k \gtrsim 4$ fm^{-1}, in contrast to Ref. [457] where a universal $1/k^4$ behavior was found in the range 1.6 fm$^{-1} \lesssim k \lesssim$ 3.2 fm^{-1}.

Also inelastic electron scattering experiments were interpreted in terms of the contact [458]. It was observed that for each high-momentum proton knocked out of the nucleus, most of the time another nucleon is knocked out with momentum back-to-back to the first one, confirming the picture of short-range two-body correlations. Interestingly, *np* correlations are about 20 times stronger than *pp* correlations. Hence, in a neutron-rich nucleus, the probability to be in the large wave-vector tail of the distribution is higher for protons than for neutrons.

5.8. Quartet BEC with applications to nuclear systems: alpha condensation in infinite nuclear matter

The possibility of quartet (that is, α-particle) condensation in nuclear systems has come to the forefront only in recent years. This may be due to the fact that the problem of quartet condensation (the condensation of four tightly correlated fermion) is technically far more difficult than pairing. In addition, the BCS–BEC transition for quartets is very different (as we shall see) from the pair case, to the extent that the weak-coupling BCS-like regime of long coherence length does not exist for quartets. Rather, at high density quartets dissolve into two Cooper pairs.

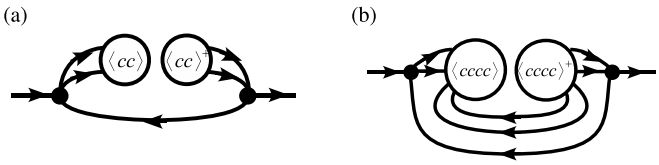

Fig. 44. Single-particle mass operator in case of pairing (a) and quartetting (b).

Quartets are present in nuclear systems, while they are much rarer in other fields of physics. One knows that two excitons in semiconductors can form a bound state and the question has been raised in the past whether bi-excitons can condense [459]. In future cold-atom devices, it might be possible to trap four different species of fermions which, with the help of Fano-Feshbach resonances, could form quartets (note that four different fermions are necessary to form quartets owing to Pauli principle). Theoretical models have already been treated and a quartet phase predicted in this context [28,460].

We begin the theoretical description of quartet condensation, by briefly recalling what is done in the standard S-wave pairing. In the equation for the pairing tensor (anomalous average) $\kappa_{\mathbf{k}_1\mathbf{k}_2} = \langle c_{\mathbf{k}_1} c_{\mathbf{k}_2}\rangle$ (with spin and isospin dependence suppressed)

$$\kappa_{\mathbf{k}_1\mathbf{k}_2} = \frac{1 - n_{\mathbf{k}_1} - n_{\mathbf{k}_2}}{\varepsilon_{\mathbf{k}_1} + \varepsilon_{\mathbf{k}_2} - 2\mu} \sum_{\mathbf{k}'_1\mathbf{k}'_2} \langle \mathbf{k}_1\mathbf{k}_2|V|\mathbf{k}'_1\mathbf{k}'_2\rangle \kappa_{\mathbf{k}'_1\mathbf{k}'_2}\,, \tag{145}$$

where $\varepsilon_{\mathbf{k}}$ is the kinetic energy (possibly, with a HF shift) and $\langle \mathbf{k}_1\mathbf{k}_2|V|\mathbf{k}'_1\mathbf{k}'_2\rangle = \delta(\mathbf{Q} - \mathbf{Q}')V(\mathbf{k} - \mathbf{k}')$ is the matrix element of the force with $\mathbf{Q} = \mathbf{k}_1 + \mathbf{k}_2$ and $\mathbf{k} = (\mathbf{k}_1 - \mathbf{k}_2)/2$ the center-of-mass and relative wave vectors, respectively, one recognizes the two-particle Bethe–Salpeter equation, taken at the eigenvalue $E = 2\mu$. For pairs at rest (that is, with $\mathbf{Q} = 0$), inserting the standard BCS expression (116) for the occupation numbers leads to the gap equation (115).

The idea is to proceed in an analogous way for quartets. With the short-hand notation introduced after Eq. (133), the in-medium four-fermion Bethe–Salpeter equation for the quartet order parameter $K(1234) = \langle c_1 c_2 c_3 c_4\rangle$ reads [461]:

$$(\varepsilon_1 + \varepsilon_2 + \varepsilon_3 + \varepsilon_4 - 4\mu)K(1234) = (1 - n_1 - n_2)\sum_{1'2'} \langle 12|V|1'2'\rangle K(1'2'34) + \text{permutations}\,. \tag{146}$$

Although the above equation is a rather straightforward extension of the pairing to the quartet one, the crux lies in the problem of finding the single-particle occupation numbers $n_{\mathbf{k}}$ in the quartet case. To this end, it is again convenient to proceed in analogy with the pairing case. Eliminating there the anomalous Green's function from the 2×2 set of Gor'kov equations [95], the retarded mass operator in the Dyson equation for the normal Green's function takes the form:

$$M_{1,1'} = \frac{|\Delta_1|^2}{\omega + \xi_1}\delta_{1,1'} \tag{147}$$

where $\xi_1 = \varepsilon_1 - \mu$ and the gap is defined by

$$\Delta_1 = \sum_2 \langle 1\bar{1}|V|2\bar{2}\rangle \langle c_2 c_{\bar{2}}\rangle\,, \tag{148}$$

"$\bar{1}$" being the time reversed state of "1". The graphical representation of Eq. (147) is given in Fig. 44(a).

In the case of quartets, the derivation of a single-particle mass operator is more involved, and we give here only the final expression (for a detailed derivation, see Refs. [461,462]):

$$M^{\text{quartet}}_{1,1}(\omega) = \sum_{234} \frac{\Delta_{1234}[\bar{f}_2\bar{f}_3\bar{f}_4 + f_2 f_3 f_4]\Delta^*_{1234}}{\omega + \xi_2 + \xi_3 + \xi_4} \tag{149}$$

where $f_i = f(\xi_i)$ is the Fermi function and $\bar{f} = 1 - f$. In addition, the quartet gap matrix is given by:

$$\Delta_{1234} = \sum_{1'2'} \langle 12|V|1'2'\rangle \langle c_{1'} c_{2'} c_3 c_4\rangle. \tag{150}$$

The quartet mass operator (149) is also depicted in Fig. 44(b).

Although the derivation of Eqs. (149) and (150) is slightly intricate, the final result looks rather plausible on physical grounds. For instance, the three backward going fermion lines in Fig. 44(b) give rise to the Fermi occupation factors in the numerator of Eq. (150). This makes a marked difference with pairing (cf. Fig. 44(a)), where only a single fermion line with $\bar{f} + f = 1$ appears. Once the mass operator has been obtained, the occupation number can be calculated via the standard procedure and the system of equations for the quartet order parameter is closed.

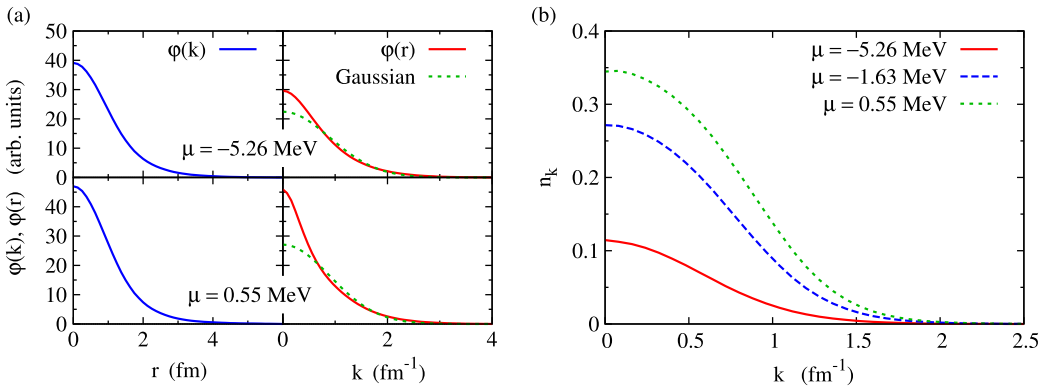

Fig. 45. (a) Single-particle wave functions φ in position (left) and wave-vector (right) space for two different chemical potentials at zero temperature. A Gaussian function is also shown for comparison (dashed line). (b) Single-particle occupation numbers n_k vs k.
Source: Data taken from Ref. [461].

For the moment we concentrate on the case $T = 0$. Even in this case, solving numerically this complicated non-linear set of four-body equations by brute force is out of question. Luckily, there exists a very efficient and simplifying approximation that comes to the rescue. In nuclear physics, it is known that, because of its strong binding, it is a good approximation to treat an α particle in mean field as long as it is projected on good total momentum. In Eq. (150), one can therefore make the ansatz (see also Ref. [463]):

$$\langle c_1 c_2 c_3 c_4 \rangle \rightarrow \varphi(\mathbf{k}_1)\,\varphi(\mathbf{k}_2)\,\varphi(\mathbf{k}_3)\,\varphi(\mathbf{k}_4)\,\delta(\mathbf{k}_1 + \mathbf{k}_2 + \mathbf{k}_3 + \mathbf{k}_4)\,, \tag{151}$$

where φ is a 0S single-particle wave function in wave-vector space (the spin–isospin singlet wave function is again suppressed). This ansatz, which is an eigenstate of the total momentum operator with eigenvalue $\mathbf{K} = 0$, makes the problem manageable, since it reduces the calculation to the self-consistent determination of $\varphi(\mathbf{k})$. Below, an example will be given where the high efficiency of the product ansatz is demonstrated. Note, however, that the bare nucleon–nucleon force cannot be used with the mean-field ansatz (151). It is thus convenient to take a separable potential with two parameters (strength and range), which can be adjusted to energy and radius of a free α particle. Fig. 45(a) shows the single-particle wave function in position and wave-vector space for two values of the chemical potential. For the larger chemical potential, one sees the wave function deviates considerably from a Gaussian. It is also found that, for slightly positive μ, the system of equations has no longer solution and self-consistency cannot be achieved.

The evolution of the occupation number n_k with μ (density) shown in Fig. 45(b) is very interesting. At slightly positive μ where the system has no longer solution, the occupation number is still far from unity. The largest occupation number one obtains lies at around $n_{\mathbf{k}=0} \sim 0.35$. This result is completely different from the BCS–BEC crossover in the pairing case, when μ can vary from negative to positive values and the occupation number saturates at unity for μ well inside the positive region, see Section 1.2. This shows that, in the case of quartetting, the system is still far from the regime of weak coupling and large coherence length, when the equations that describe it stop having solution. From the extension of the wave functions one also sees that the size of the α particles has barely increased. Before giving an explanation for this behavior, we consider the critical temperature for which the breakdown of the solution is more clearly seen.

To determine the critical temperature for the onset of quartet condensation, the equation for the order parameter (146) has to be linearized, by replacing the correlated occupation number $n_{\mathbf{k}}$ therein by the free Fermi–Dirac distribution $f_{\mathbf{k}}$ at finite temperature. Determining the temperature where the equation is satisfied gives the desired critical temperature T_c^α. This is the Thouless criterion for the critical temperature of pairing [173], transposed to the quartet case. Fig. 46 shows the evolution of T_c^α as a function of the chemical potential and density [464], and explicitly demonstrates the excellent performance of the momentum-projected mean-field ansatz for the quartet order parameter. The crosses correspond to the full solution of Eq. (146) in the linearized finite-temperature regime with the rather realistic Malfliet–Tjon bare nucleon–nucleon potential [465] using the Faddeev–Yakubovsky method, while the continuous line corresponds to the projected mean-field solution (the full solution is available only for negative chemical potentials). One clearly sees the breakdown of quartetting at small positive μ, while pn pairing (in the deuteron channel) continues smoothly into the large μ region. [The occurrence of the breakdown of T_c^α at a somewhat larger positive μ with respect to the full solution of the quartet gap equation with the ansatz (151) at $T = 0$, may be due to the fact that here we are at finite temperature — see also the discussion below.] Note that the density n_0 in Fig. 46(b) is the uncorrelated one. Actually, a calculation *à la* Nozières and Schmitt-Rink for the quartet case is still missing. Therefore, no plot can be shown for T_c, as a function of the correlated density, as it was the case for deuteron pairing, see Fig. 35(b).

It is worth mentioning that in the isospin polarized case with more neutrons than protons, pn pairing is much more affected than quartetting (due to the much stronger binding of the α particle) and finally loses against α condensation [466].

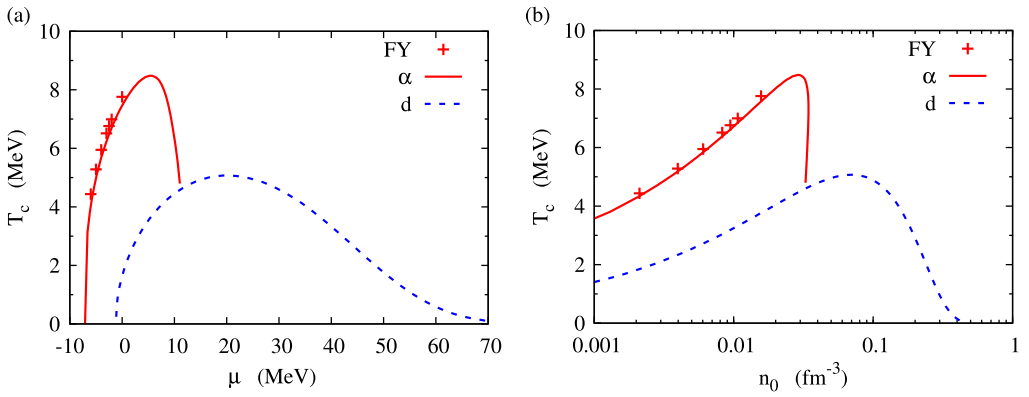

Fig. 46. Critical temperatures for the condensation of α particle (with binding energy $E_B/A \sim 7.1$ MeV — solid lines) and of deuteron (with $E_B/A \sim 1.1$ MeV — dashed lines), as a function (a) of the chemical potential μ and (b) of the uncorrelated density n_0 (see also Ref. [27]). The crosses were obtained by solving the linearized version of Eq. (146) with the Faddeev–Yakubovsky (FY) method.
Source: Adapted from Ref. [464].

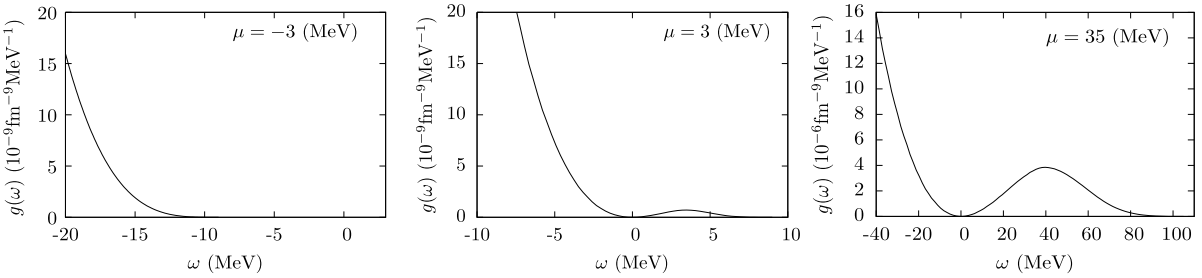

Fig. 47. 3h-level density $g_{3h}(\omega)$ for three different values of the chemical potential μ.
Source: Reproduced from Ref. [461].

As a consequence, in the quartetting case, and contrary to the pairing case, the dissolution of α particles seems to occur quite abruptly as a function of density, although it is still unknown whether this is an abrupt transition or a (rather sharp) crossover. It could be possible that α particles coexist with (pn, nn, or pp) Cooper pairing at somewhat positive values of μ (higher density) and disappear asymptotically much faster than deuteron pairing. Nevertheless, a phase transition from α condensation to Cooper pairing cannot be excluded and the breakdown of the solution at $T = 0$ at small positive μ, discussed above, hints at a quantum phase transition with the density as control parameter. To settle this question, the equation for the quartet order parameter should be formulated at the outset in terms of BCS quasi-particles and solved as a function of density. This is a complicated problem to be addressed in the future.

The above difference between pairing and quartetting has to do with the different level densities involved in the two systems. In the pairing case, the single-particle mass operator contains only a single particle (hole) line propagator and the level density is given by:

$$g_{1h}(\omega) = -\frac{1}{\pi}\,\mathrm{Im}\int\frac{d\mathbf{k}}{(2\pi)^3}\frac{\bar{f}_{\mathbf{k}}+f_{\mathbf{k}}}{\omega+\xi_{\mathbf{k}}+i\eta} = \int\frac{d\mathbf{k}}{(2\pi)^3}\delta(\omega+\xi_{\mathbf{k}})\,. \tag{152}$$

In the case of three fermions, as is the case of quartetting, the corresponding level density is instead given by (see also Ref. [467]):

$$g_{3h}(\omega) = -\frac{1}{\pi}\,\mathrm{Im}\,\mathrm{Tr}\,\frac{\bar{f}_1\bar{f}_2\bar{f}_3+f_1f_2f_3}{\omega+\xi_1+\xi_2+\xi_3+i\eta} = \mathrm{Tr}(\bar{f}_1\bar{f}_2\bar{f}_3+f_1f_2f_3)\,\delta(\omega+\xi_1+\xi_2+\xi_3)\,. \tag{153}$$

Fig. 47 gives the results of $g_{3h}(\omega)$ for negative and positive values of μ at $T = 0$. The interesting case is $\mu > 0$, for which phase-space constraint and energy conservation cannot be fulfilled simultaneously at the Fermi level (which corresponds to $\omega = 0$) and the level density is zero there. This is just the point where quartetting should build up, but if the level density is zero, there cannot be quartetting. In the case of pairing, on the other hand, there is no phase space restriction and the level density is finite at the Fermi level. For negative μ, $f(\xi_{\mathbf{k}})$ vanishes at $T = 0$ and is exponentially small at finite T, in such a way that there is no fundamental difference between $1h$ and $3h$ level densities. This explains the striking difference between pairing and quartetting in the weak-coupling regime. The same reasoning holds when considering the in-medium four-body

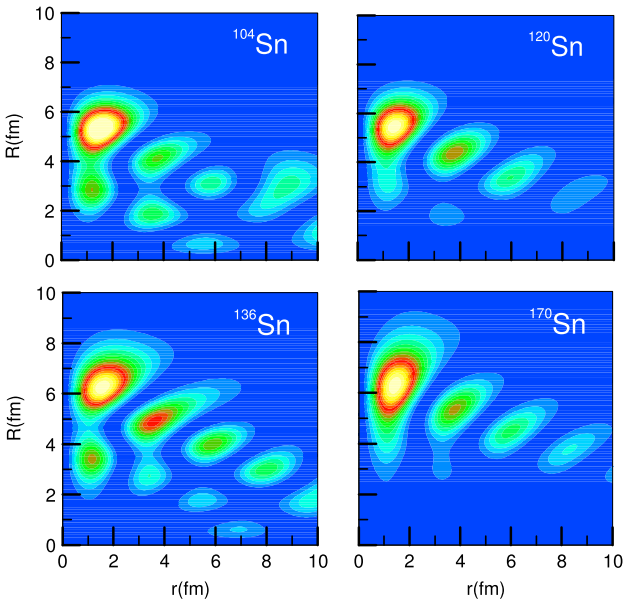

Fig. 48. Square of the pairing tensor, multiplied by R^2r^2, as a function of relative (r) and center-of-mass (R) coordinates, in different Sn isotopes. *Source:* Reproduced from Ref. [471].

equation (146). The relevant in-medium four-fermion level density is also zero at 4μ for $\mu > 0$. Actually, the only case of an in-medium n-fermion level density which remains finite at the Fermi energy is (besides $n = 1$) the $n = 2$ case when the center-of-mass wave vector is zero, see Ref. [468]. That is why pairing is such a special case, different from condensation of all higher clusters. At finite temperature, on the other hand, the level densities no longer pass through zero and only a strong depression may occur at the Fermi energy. This is probably the reason why the breakdown of the critical temperature is slightly less abrupt than what happens at $T = 0$.

5.9. A glimpse at finite nuclei

We end up this Section on nuclear systems by briefly considering the situation of the BCS–BEC crossover and alpha condensation in finite nuclei. The proton–neutron (deuteron like) pairing in heavier nuclei is very elusive, and a considerable activity is going on about this subject at present. For asymmetric nuclei, the suppression of *pn*-pairing can be understood in terms of what we have seen from the infinite-matter study. For $N \sim Z$ nuclei, on the other hand, one would expect to find *pn* pairing because the bare proton–neutron attraction is stronger than the proton–proton or neutron–neutron one. However, these different pairing channels enter in competition with each other and it is not clear which one prevails. Recent publications of interest on this subject can be found in Refs. [469,470].

The situation is different if one considers single Cooper pairs in light nuclei (in this case, even though one cannot speak about BEC, yet the strong coupling limit may manifest itself). For example, the nucleus ^{6}Li in its ground state has a strong $\alpha+d$ cluster structure. Because of the small number of nucleons, quite sophisticated Resonating Group Method (RGM) calculations could be performed in the past [472,473]. It is interesting to note that, similar to Fig. 32, as a function of distance from the α particle the deuteron first shrinks before it enters the inner part of the α. For this reason, the situation is qualitatively similar to the infinite-matter case. A similar situation may occur for ^{18}F = ^{16}O + d, where ^{18}F has the quantum numbers of the deuteron in its ground state as is the case also for ^{42}Sc = ^{40}Ca + d. However, no studies concerning the strong coupling features of these systems are reported. Even though one may think that adding more deuterons to doubly magic nuclei would enhance the condensate aspect, two deuterons form an α particle which is about seven times more strongly bound. This fact may also obscure the *pn*-pairing in the $N \sim Z$ nuclei.

Important *nn* correlations have been discussed in very neutron-rich nuclei, close to the neutron drip line, where a so-called neutron skin develops. The neutron Cooper pairs turn out to be spatially localized at the surface of those nuclei, thus inducing a spatial asymmetry. What is important for this effect to occur is that the gap field is built up of states with even *and* odd parity. This can happen either when the value of the gap englobes different major shells or when an intruder single particle state invades a shell of opposite parity. Typical studies of this effect can be found in Refs. [471,475–477]. This spatial concentration of *nn* Cooper pairs in those nuclei (as shown in Fig. 48) can be considered as a signature for the transition from weak to strong coupling, as discussed in Section 5.5.

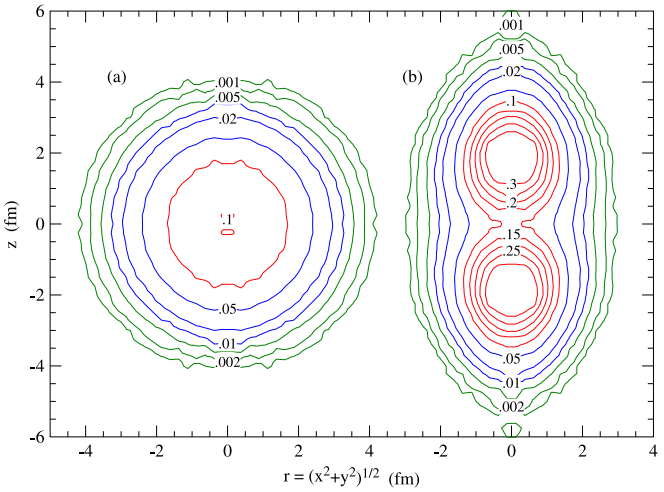

Fig. 49. QMC result for the density distribution of ^{8}Be in its ground state, (a) in the laboratory frame and (b) in the intrinsic frame: The nucleus clearly consists of two α clusters.
Source: Adapted from Ref. [474].

To summarize, in finite nuclei no clear evidence has been seen thus far of strong coupling and the BCS–BEC crossover in the deuteron channel, but these effects may play a certain role in compact stellar objects. Concerning *nn* pairing in neutron-rich nuclei, some transition from weak to strong coupling can actually be revealed.

The BEC of α particles in nuclei has been widely discussed over the last ten years. Usually, the ground states of nuclei are too compact to allow for α particles to form (the only exception being ^{8}Be, see Fig. 49). At least in lighter nuclei, however, there exist long lived states with a dilute density (about a factor 3–4 smaller than the ordinary density of nuclei), which allows for the appearance of α particles with little mutual overlap, forming an almost ideal Bose gas. One notable state of this kind is the first excited 0^+ state at 7.65 MeV in ^{12}C, called the Hoyle state. Because of the abundance of ^{12}C in the universe (giving rise to life on earth), the astrophysicist Fred Hoyle predicted in 1952 [478] that in stars the triple α reaction $\alpha+\alpha+\alpha\rightarrow{}^{12}\mathrm{C}^{*}$ must be accelerated due to the existence of an excited state in ^{12}C at the right resonating energy, which he predicted to be very close to the value 7.65 MeV measured by Fowler a couple of years later [479]. It turns out that this state can be described to a good approximation as a state of low density, where all three α particles are "condensed" with their center-of-mass motion in the same 0*S* bosonic mean-field orbit [29]. It seems that this is not the only $n\alpha$ nucleus exhibiting such an "exotic" state. A good candidate is the sixth 0^+ state in ^{16}O at 15.1 MeV [29]. There may be α gas states in even heavier nuclei as well. Intense experimental activity is presently going on in this field. There also exist speculations that in heavier nuclei a surface layer of condensed α particles may exist [480] and α clustering certainly also exists in nuclei with spontaneous α decay [481].

On the theoretical side, in small systems like nuclei one must deal with a number-conserving condensate ansatz. In Ref. [483], the following variational ansatz was made for the Hoyle state with, for instance, three α particles:

$$\Psi_{3\alpha}=\mathcal{A}[\phi(\alpha_1)\phi(\alpha_2)\phi(\alpha_3)] \tag{154}$$

where $\phi(\alpha_i)$ the four-nucleon wave function of the ith α particle and $\mathcal{A}$ the antisymmetrization operator with respect to all the 12 nucleons. Note the analogy of the expression (154) with a number-projected BCS wave function. Generalization of this ansatz to more than three α particles is straightforward. As mentioned in Section 5.8, the α particle can be well described by a mean-field wave function as long as the center-of-mass motion is correctly separated. It is also well known that for light nuclei, harmonic oscillator wave functions with the oscillator length as parameter are excellent variational functions. The following ansatz was thus made in Ref. [483]:

$$\phi(\alpha_i)\propto\exp\left[-\frac{2}{B^2}\mathbf{R}_i^2\right]\varphi(\alpha_i) \tag{155}$$

where $\mathbf{R}_i$ is the center-of-mass coordinate of the ith α particle and

$$\varphi(\alpha_i)\propto\exp\left[-\frac{1}{2}\sum_{k,l=1}^{4}(\mathbf{r}_{i,k}-\mathbf{r}_{i,l})^2/(8b^2)\right] \tag{156}$$

is a translationally invariant "intrinsic" α-particle wave function. Here, the only variational parameters are then the widths B and b. It generally turns out that, for α-particle gas states, the width of the intrinsic α-particle wave function stays close to

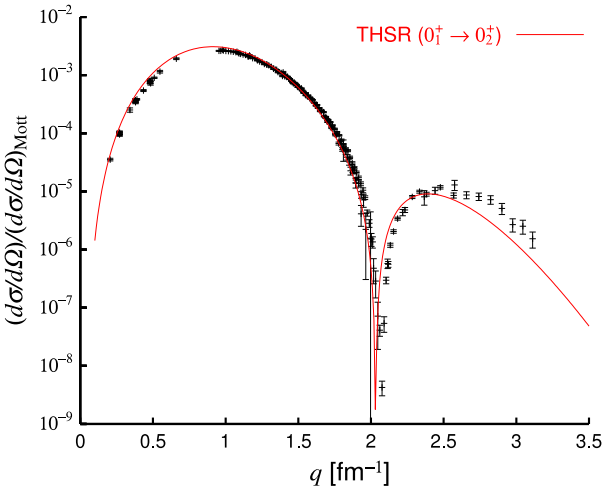

Fig. 50. Inelastic form factor calculated with the THSR wave function (BEC) and the one of Kamimura et al. [472,473]. The two results are on top of each other. Experimental data are from Ref. [482]
Source: Courtesy of Y. Funaki.

its free value $b = 1.35$ fm, whereas B is much larger since the center-of-mass covers the whole nuclear volume. Performing the antisymmetrization and minimizing the energy with respect to B for fixed b, under the condition that the Hoyle state is orthogonal to the ground state, yields a single α-condensate 12-nucleon wave function. Because of the Gaussian form of the center-of-mass motion of each α, also the total center-of-mass can eventually be eliminated, so that the 12-nucleon 3α-cluster wave function is totally translationally invariant. The Hamiltonian used contains two-body and three-body effective forces of Gaussian type, whose parameters were adjusted many years before the description of the Hoyle state from $\alpha - \alpha$ scattering data and the properties of a single free α particle [484]. The Coulomb force was also included. In this way, all measured properties of the Hoyle state have been reproduced from a parameter-free theory with only a single variational parameter B. Among those properties we mention, for instance, the inelastic form factor from the ground to the Hoyle state obtained from electron scattering experiments [485], as shown in Fig. 50. This inelastic form factor is quite sensitive to the size of the Hoyle state. Its rms radius was obtained to be 3.8 fm, which, when compared with that of the ground state of 2.4 fm, implies a volume increase by a factor 3–4, thus confirming the low-density gas-like quartet structure of the Hoyle state which is similar to the one of ^{8}Be shown in Fig. 49 but with one additional α particle. Since quartetting was found to exist only at low density also in nuclear matter, one can assume that the Hoyle state (and possibly more α gas states in other nuclei) is a precursor to macroscopic quartet condensation. This should be considered in analogy to pairing, for which it is known that only a handful of Cooper pairs gives rise in superfluid nuclei to what can be considered as precursor to macroscopic neutron superfluidity in neutron stars.

A number-conserving quartet wave function does not necessarily imply that condensation occurs. One convenient way to theoretically investigate this question is to construct the single α-particle density matrix $n(\mathbf{R}, \mathbf{R}')$, by integrating out from the density matrix of the total system all intrinsic coordinates and all center-of-mass coordinates but one. The diagonalization of this matrix yields the occupation probabilities of the various α orbits. It was found that in the Hoyle state the three α particles are to over 70% in the lowest 0S orbit, the remaining orbits having an occupancy reduced by at least a factor of ten. In contrast, the occupancies of the ^{12}C ground states are equally distributed [29]. At least theoretically, this result represents a clear signature that to a large extent the Hoyle state can be considered as an α condensate. However, the effect of anti-symmetrization is to scatter the α particles out of the condensate 30% of the time, which by itself is an interesting effect. Fig. 51 shows the probability distributions of the α occupancies for the ground and Hoyle states.

Although more could be said about α clustering and α condensation in nuclei, we have given only a short overview of the present situation in finite nuclei because this report mainly concentrates on phenomena occurring in infinite matter. Recent more complete reviews on the subject can be found in Refs. [486,487].

6. Concluding remarks

Quite generally, "crossover" is a term that describes a situation when a system goes from being in one phase to being in another phase as a certain parameter is changed, without encountering a phase transition in between. For the BCS–BEC crossover, this means that by tuning the inter-particle interaction (or the density) the system goes from a BCS state where pairs of (opposite spin) fermions are described by Fermi statistics, to a BEC state where two-fermion dimers are described by Bose statistics. In this way, by freezing out the internal degrees of freedom of the fermion pairs, the statistics of fermions

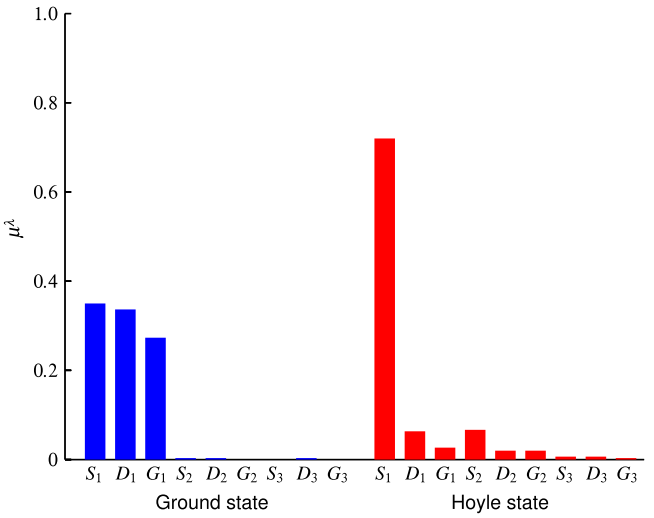

Fig. 51. Single α occupation probabilities for ground (left) and Hoyle state (right). The ground state complies with the pure shell model where the occupation is uniform, while in the Hoyle state the 0S occupancy is by over 70% at least a factor of ten larger than in all other states.
Source: Reproduced from Ref. [29].

smoothly merges with the statistics of bosons. As a consequence, the BCS and BEC paradigms are not fully distinct from each other but rather are the two extrema of a continuum.

It appears fair to say that the BCS–BEC crossover should be considered one of the major scientific achievements that have occurred during the last several years. For this reason, our scope here has been to provide a detailed and as much as possible comprehensive review of the physics of the BCS–BEC crossover, and to apply it to the physical systems for which (the ultra-cold Fermi gases) this crossover has been explicitly realized experimentally, or for which (the nuclear systems) the crossover scenario is found consistent with various aspects of its phenomenology, or indirectly accessed from close analogy with ultra-cold gases. For both systems, we have focused on the aspects of maximum cross interest. For this reason, less attention was paid to topics that are of more specific interest to the separate systems, such as the effects of the trapping potential in ultra-cold gases or the pairing in finite nuclei.

Even within these restrictions, the topics covered by this paper are not exhaustive and important aspects have unavoidably been left out. In particular, special mention deserve the radio-frequency spectroscopy that was originally introduced to measure the pairing gap in the condensed state [247,488], and the thermodynamics of the gas cloud from which the equation of state was extracted [183,260]. From the theoretical side, emphasis was not given to the results obtained via functional-integral approaches [44,45,489] or quantum Monte Carlo methods [38,39]. Rather, a diagrammatic approach was preferred, because it can be more directly connected to one's physical intuition and can also be more readily subject to targeted improvements.

Additional interest in the BCS–BEC crossover comes from particle physics (and, in particular, from quark–gluon plasma, see, e.g., Refs. [490,491]). In the ultimate analysis, this cross interest from different fields of physics to the BCS–BEC crossover is due to the fact that strongly-coupled quantum Fermi systems, even though they are described by different microscopic theories, share the basic feature of having the same kind of spontaneously broken symmetry [492,493]. Superconductors make thus no exception to the interest in the BCS–BEC crossover. As mentioned in Section 1.1, actually the first motivation for introducing the BCS–BEC crossover originated in condensed matter. Nowadays, there is growing direct evidence for the occurrence of this crossover in two-band superconductors with iron-based materials [494], for which it was possible to detect the collapse of the small Fermi surface pocket, with the related single-particle dispersion in the condensed state becoming an inverted parabola (as discussed in Section 3.3 in the context of ultra-cold gases). Electron–hole bilayers appear also as promising candidates for the realization of the BCS–BEC crossover in condensed matter systems [495–498]. It is thus possible that in the near future the BCS–BEC crossover might be under the spotlight also in condensed matter, the field where it was originally envisaged. On the other hand, condensation of quartets, very relevant for nuclear systems, may in the future also be investigated with ultra-cold atoms when the trapping of four different fermion species will be achieved. Definitely, the exploration of the BCS–BEC crossover in ultra-cold Fermi gases and nuclear systems, which has been reviewed here, has enriched us with concepts, tools, and results that will be extremely precious for the investigations of this phenomenon in a broader range of contexts, in the years to come.

Acknowledgments

The authors are grateful to M. Baldo and U. Lombardo for discussions on Section 5, and to A. Perali for bringing Ref. [494] to their attention.

References

[1] J. Bardeen, L.N. Cooper, J.R. Schrieffer, Theory of superconductivity, Phys. Rev. 108 (1957) 1175–1204.
[2] M.R. Schafroth, S.T. Butler, J.M. Blatt, Quasi-chemical equilibrium model for superconductivity, Helv. Phys. Acta 30 (1957) 93–134.
[3] L.V. Keldysh, Y.V. Kopaev, Possible instability of the semimetallic state toward Coulomb interaction, Sov. Phys.—Solid State 6 (1965) 2219–2224; Fiz. Tverd. Tela (Leningrad) 6 (1964) 2791.
[4] V.N. Popov, Theory of a Bose gas produced by bound states of Fermi particles, Sov. Phys.—JETP 23 (1966) 1034–1039; Zh. Eksp. Teor. Fiz. 36 (1966) 1550-1558.
[5] D.M. Eagles, Possible pairing without superconductivity at low carrier concentrations in bulk and thin-film superconducting semiconductors, Phys. Rev. 186 (1969) 456–463.
[6] A.J. Leggett, Diatomic molecules and Cooper pairs, in: A. Pekalski, R. Przystawa (Eds.), Modern Trends in the Theory of Condensed Matter, in: Lecture Notes in Physics, vol. 115, Springer-Verlag, Berlin, 1980, p. 13.
[7] P. Nozières, S. Schmitt-Rink, Bose condensation in an attractive fermion gas: From weak to strong coupling superconductivity, J. Low Temp. Phys. 59 (1985) 195–211.
[8] M. Randeria, J.-M. Duan, L.-Y. Shieh, Bound states, Cooper pairing, and Bose condensation in two dimensions, Phys. Rev. Lett. 62 (1989) 981–984.
[9] M. Randeria, J.-M. Duan, L.-Y. Shieh, Superconductivity in a two-dimensional Fermi gas: Evolution from Cooper pairing to Bose condensation, Phys. Rev. B 41 (1990) 327–343.
[10] R. Micnas, J. Ranninger, S. Robaszkiewicz, Superconductivity in narrow-band systems with local nonretarded attractive interactions, Rev. Modern Phys. 62 (1990) 113–171.
[11] M. Randeria, N. Trivedi, A. Moreo, R.T. Scalettar, Pairing and spin gap in the normal state of short coherence length superconductors, Phys. Rev. Lett. 69 (1992) 2001–2004.
[12] M. Drechsler, W. Zwerger, Crossover from BCS-superconductivity to Bose-condensation, Ann. Phys. 504 (1992) 15–23.
[13] R. Haussmann, Crossover from BCS superconductivity to Bose-Einstein condensation: A self-consistent theory, Z. Phys. B 91 (1993) 291–308.
[14] F. Pistolesi, G.C. Strinati, Evolution from BCS superconductivity to Bose condensation: Role of the parameter $k_F\xi$, Phys. Rev. B 49 (1994) 6356–6359.
[15] M. Casas, J.M. Getino, M. de Llano, A. Puente, R.M. Quick, H. Rubio, D.M. van der Walt, BCS-Bose model of exotic superconductors: Generalized coherence length, Phys. Rev. B 50 (1994) 15945–15952.
[16] M. Baldo, U. Lombardo, P. Schuck, Deuteron formation in expanding nuclear matter from a strong coupling BCS approach, Phys. Rev. C 52 (1995) 975–985.
[17] M. Inguscio, W. Ketterle, C. Salomon (Eds.), Ultra-Cold Fermi Gases, in: Proceedings of the International School of Physics "Enrico Fermi", vol. CLXIV, IOS Press, Amsterdam, 2007.
[18] W. Zwerger (Ed.), The BCS-BEC Crossover and the Unitary Fermi Gas, in: Lecture Notes in Physics, vol. 863, Springer-Verlag, Berlin, 2012.
[19] G.A. Baker, The MBX challenge competition: a neutron matter model, in: R.F. Bishop, K.A. Gernoth, N.R. Walet, Y. Xian (Eds.), the Proceedings of the 10th International Conference Recent Progress in Many-Body Theories, in: Series on Advances in Quantum Many-Body theory, vol. 3, World Scientific, Singapore, 2000, pp. 15–20.
[20] G.A. Baker, Neutron matter model, Phys. Rev. C 60 (1999) 054311.
[21] T. Alm, B.L. Friman, G. Röpke, H. Schulz, Pairing instability in hot asymmetric nuclear matter, Nuclear Phys. A 551 (1993) 45–53.
[22] H. Stein, A. Schnell, T. Alm, G. Röpke, Correlations and pairing in nuclear matter within the Nozières-Schmitt-Rink approach, Z. Phys. A 351 (1995) 295–299.
[23] U. Lombardo, P. Nozières, P. Schuck, H.-J. Schulze, A. Sedrakian, Transition from BCS pairing to Bose-Einstein condensation in low-density asymmetric nuclear matter, Phys. Rev. C 64 (2001) 064314.
[24] N. Andrenacci, A. Perali, P. Pieri, G.C. Strinati, Density-induced BCS to Bose-Einstein crossover, Phys. Rev. B 60 (1999) 12410–12418.
[25] S. Heckel, P.P. Schneider, A. Sedrakian, Light nuclei in supernova envelopes: A quasiparticle gas model, Phys. Rev. C 80 (2009) 015805.
[26] M. Jin, M. Urban, P. Schuck, BEC-BCS crossover and the liquid-gas phase transition in hot and dense nuclear matter, Phys. Rev. C 82 (2010) 024911.
[27] G. Röpke, A. Schnell, P. Schuck, P. Nozières, Four-particle condensate in strongly coupled fermion systems, Phys. Rev. Lett. 80 (1998) 3177–3180.
[28] S. Capponi, G. Roux, P. Azaria, E. Boulat, P. Lecheminant, Confinement versus deconfinement of Cooper pairs in one-dimensional spin-3/2 fermionic cold atoms, Phys. Rev. B 75 (2007) 100503(R).
[29] T. Yamada, Y. Funaki, H. Horiuchi, G. Röpke, P. Schuck, A. Tohsaki, Nuclear alpha-particle condensates, in: C. Beck (Ed.), Clusters in Nuclei, Vol. 2, in: Lecture Notes in Physics, vol. 848, Springer-Verlag, Berlin, 2012, p. 229.
[30] A. Schnell, G. Röpke, P. Schuck, Precritical pair fluctuations and formation of a pseudogap in low-density nuclear matter, Phys. Rev. Lett. 83 (1999) 1926–1929.
[31] J.T. Stewart, J.P. Gaebler, D.S. Jin, Using photoemission spectroscopy to probe a strongly interacting Fermi gas, Nature 454 (2008) 744–747.
[32] J.P. Gaebler, J.T. Stewart, T.E. Drake, D.S. Jin, A. Perali, P. Pieri, G.C. Strinati, Observation of pseudogap behaviour in a strongly interacting Fermi gas, Nat. Phys. 6 (2010) 569–573.
[33] M. Feld, B. Fröhlich, E. Vogt, M. Koschorreck, M. Köhl, Observation of a pairing pseudogap in a two-dimensional Fermi gas, Nature 480 (2011) 75–78.
[34] M. Matsuo, Spatial structure of neutron Cooper pair in low density uniform matter, Phys. Rev. C 73 (2006) 044309.
[35] T. Abe, R. Seki, Lattice calculation of thermal properties of low-density neutron matter with pionless *NN* effective field theory, Phys. Rev. C 79 (2009) 054002.
[36] A. Gezerlis, J. Carlson, Low-density neutron matter, Phys. Rev. C 81 (2010) 025803.
[37] S. Ramanan, M. Urban, BEC-BCS crossover in neutron matter with renormalization-group-based effective interactions, Phys. Rev. C 88 (2013) 054315.
[38] A. Bulgac, The unitary Fermi gas: from Monte Carlo to density functionals, in: W. Zwerger (Ed.), The BCS-BEC Crossover and the Unitary Fermi Gas, in: Lecture Notes in Physics, vol. 863, Springer-Verlag, Berlin, 2012, pp. 305–374.
[39] J. Carlson, S. Gandolfi, A. Gezerlis, Quantum Monte Carlo approaches to nuclear and atomic physics, Prog. Theor. Exp. Phys. 2012 (2012) 01A209.
[40] S. Diehl, S. Floerchinger, H. Gies, J. Pawlowkski, C. Wetterich, Functional renormalization group approach to the BCS-BEC crossover, Ann. Phys. 522 (2010) 615–656.
[41] Y. Nishida, D. Son, Unitary Fermi gas, ϵ expansion, and nonrelativistic conformal field theories, in: W. Zwerger (Ed.), The BCS-BEC Crossover and the Unitary Fermi Gas, in: Lecture Notes in Physics, vol. 863, Springer-Verlag, Berlin, 2012, pp. 305–374.
[42] X.-J. Liu, Virial expansion for a strongly correlated Fermi system and its application to ultracold atomic Fermi gases, Phys. Rep. 524 (2013) 37–83.
[43] F. Pistolesi, G.C. Strinati, Evolution from BCS superconductivity to Bose condensation: Calculation of the zero-temperature phase coherence length, Phys. Rev. B 53 (1996) 15168–15192.
[44] H. Hu, X.-J. Liu, P.D. Drummond, Equation of state of a superfluid Fermi gas in the BCS-BEC crossover, Europhys. Lett. 74 (2006) 574–580.
[45] R.B. Diener, R. Sensarma, M. Randeria, Quantum fluctuations in the superfluid state of the BCS-BEC crossover, Phys. Rev. A 77 (2008) 023626.
[46] M. Randeria, E. Taylor, Crossover from Bardeen-Cooper-Schrieffer to Bose-Einstein condensation and the unitary Fermi gas, Ann. Rev. Cond. Matt. Phys. 5 (2014) 209–232.
[47] L. Pitaevskii, S. Stringari, Bose-Einstein Condensation and Superfluidity, Oxford University Press, Oxford, 2016.

[48] W. Zwerger, Strongly interacting Fermi gases, in: M. Inguscio, W. Ketterle, S. Stringari, G. Roati (Eds.), Quantum Matter at Ultralow Temperatures, in: Proceedings of the International School of Physics "Enrico Fermi", vol. 191, IOS Press, Amsterdam, 2016, pp. 63–142.
[49] C. Chin, R. Grimm, P. Julienne, E. Tiesinga, Feshbach resonances in ultracold gases, Rev. Modern Phys. 82 (2010) 1225–1286.
[50] K. Gubbels, H. Stoof, Imbalanced Fermi gases at unitarity, Phys. Rep. 525 (2013) 255–313.
[51] S. Giorgini, L.P. Pitaevskii, S. Stringari, Theory of ultracold atomic Fermi gases, Rev. Modern Phys. 80 (2008) 1215–1274.
[52] L. Radzihovsky, D.E. Sheehy, Imbalanced Feshbach-resonant Fermi gases, Rep. Progr. Phys. 73 (2010) 076501.
[53] F. Chevy, C. Mora, Ultra-cold polarized Fermi gases, Rep. Progr. Phys. 73 (2010) 112401.
[54] Q. Chen, J. Stajic, S. Tan, K. Levin, BCS-BEC crossover: From high temperature superconductors to ultracold superfluids, Phys. Rep. 412 (2005) 1–88.
[55] D. Brink, R. Broglia, Nuclear superfluidity: pairing in finite systems, in: Cambridge Monographs on Particle Physics, Nuclear Physics and Cosmology, vol. 24, Cambridge University Press, Cambridge, 2005.
[56] D.J. Dean, M. Hjorth-Jensen, Pairing in nuclear systems: from neutron stars to finite nuclei, Rev. Modern Phys. 75 (2003) 607–656.
[57] A. Gezerlis, C.J. Pethick, A. Schwenk, Pairing and superfluidity of nucleons in neutron stars, in: K.-H. Bennemann, J.B. Ketterson (Eds.), Novel Superfluids, Vol. 2, in: International Series of Monographs on Physics, vol. 157, Oxford University Press, 2014, p. 580.
[58] J.R. Schrieffer, Theory of Superconductivity, Benjamin, New York, 1964.
[59] P. Ring, P. Schuck, The Nuclear Many Body Problem, Springer-Verlag, Berlin, 1980.
[60] A. Spuntarelli, P. Pieri, G.C. Strinati, Solution of the Bogoliubov-de Gennes equations at zero temperature throughout the BCS-BEC crossover: Josephson and related effects, Phys. Rep. 488 (2010) 111–167.
[61] H.A. Mook, J.W. Lynn, R.M. Nicklow, Temperature dependence of the magnetic excitations in Nickel, Phys. Rev. Lett. 30 (1973) 556–559.
[62] F. Marsiglio, J.E. Hirsch, Hole superconductivity and the high-T_c oxides, Phys. Rev. B 41 (1990) 6435–6456.
[63] F. Palestini, G.C. Strinati, Temperature dependence of the pair coherence and healing lengths for a fermionic superfluid throughout the BCS-BEC crossover, Phys. Rev. B 89 (2014) 224508.
[64] L.N. Cooper, Bound electron pairs in a degenerate Fermi gas, Phys. Rev. 104 (1956) 1189–1190.
[65] E. Garrido, P. Sarriguren, E. Moya de Guerra, U. Lombardo, P. Schuck, H.J. Schulze, Nuclear pairing in the $t = 0$ channel reexamined, Phys. Rev. C 63 (2001) 037304.
[66] A. Bulgac, Y. Yu, Renormalization of the Hartree-Fock-Bogoliubov equations in the case of a zero range pairing interaction, Phys. Rev. Lett. 88 (2002) 042504.
[67] Y. Yu, A. Bulgac, Energy density functional approach to superfluid nuclei, Phys. Rev. Lett. 90 (2003) 222501.
[68] C.A.R. Sá de Melo, M. Randeria, J.R. Engelbrecht, Crossover from BCS to Bose superconductivity: Transition temperature and time-dependent Ginzburg-Landau theory, Phys. Rev. Lett. 71 (1993) 3202–3205.
[69] C.A. Regal, D.S. Jin, Measurement of positive and negative scattering lengths in a Fermi gas of atoms, Phys. Rev. Lett. 90 (2003) 230404.
[70] R.M. Carter, M. Casas, J.M. Getino, M. de Llano, A. Puente, H. Rubio, D.M. van der Walt, Coherence lengths for three-dimensional superconductors in the BCS-Bose picture, Phys. Rev. B 52 (1995) 16149–16154.
[71] M. Marini, F. Pistolesi, G.C. Strinati, Evolution from BCS superconductivity to Bose condensation: analytic results for the crossover in three dimensions, Eur. Phys. J. B 1 (1998) 151–159.
[72] T. Papenbrock, G.F. Bertsch, Pairing in low-density Fermi gases, Phys. Rev. C 59 (1999) 2052–2055.
[73] L. Salasnich, N. Manini, A. Parola, Condensate fraction of a Fermi gas in the BCS-BEC crossover, Phys. Rev. A 72 (2005) 023621.
[74] G.C. Strinati, A survey on the crossover from BCS superconductivity to Bose-Einstein condensation, Phys. Essays 13 (2000) 427–436.
[75] P.G. De Gennes, Superconductivity of Metals and Alloys, Benjamin, New York, 1966 (Chapter 5).
[76] G. Bruun, Y. Castin, R. Dum, K. Burnett, BCS theory for trapped ultracold fermions, Eur. Phys. J. D 7 (1999) 433–439.
[77] M. Grasso, M. Urban, Hartree-Fock-Bogoliubov theory versus local-density approximation for superfluid trapped fermionic atoms, Phys. Rev. A 68 (2003) 033610.
[78] S. Simonucci, P. Pieri, G.C. Strinati, Temperature dependence of a vortex in a superfluid Fermi gas, Phys. Rev. B 87 (2013) 214507.
[79] P. Pieri, G.C. Strinati, Derivation of the Gross-Pitaevskii equation for condensed bosons from the Bogoliubov-de Gennes equations for superfluid fermions, Phys. Rev. Lett. 91 (2003) 030401.
[80] Y. Ohashi, A. Griffin, Single-particle excitations in a trapped gas of Fermi atoms in the BCS-BEC crossover region, Phys. Rev. A 72 (2005) 013601.
[81] P. Castorina, M. Grasso, M. Oertel, M. Urban, D. Zappalà, Nonstandard pairing in asymmetric trapped Fermi gases, Phys. Rev. A 72 (2005) 025601.
[82] L.M. Jensen, J. Kinnunen, P. Törmä, Non-BCS superfluidity in trapped ultracold Fermi gases, Phys. Rev. A 76 (2007) 033620.
[83] N. Nygaard, G.M. Bruun, C.W. Clark, D.L. Feder, Microscopic structure of a vortex line in a dilute superfluid Fermi gas, Phys. Rev. Lett. 90 (2003) 210402.
[84] R. Sensarma, M. Randeria, T.-L. Ho, Vortices in superfluid Fermi gases through the BEC to BCS crossover, Phys. Rev. Lett. 96 (2006) 090403.
[85] A. Bulgac, Y. Yu, Vortex state in a strongly coupled dilute atomic fermionic superfluid, Phys. Rev. Lett. 91 (2003) 190404.
[86] A. Bulgac, Local density approximation for systems with pairing correlations, Phys. Rev. C 65 (2002) 051305.
[87] A. Bulgac, Local-density-functional theory for superfluid fermionic systems: The unitary gas, Phys. Rev. A 76 (2007) 040502.
[88] A. Bulgac, M.M. Forbes, Unitary Fermi Supersolid: The Larkin-Ovchinnikov Phase, Phys. Rev. Lett. 101 (2008) 215301.
[89] D.L. Feder, Vortex arrays in a rotating superfluid Fermi gas, Phys. Rev. Lett. 93 (2004) 200406.
[90] G. Tonini, F. Werner, Y. Castin, Formation of a vortex lattice in a rotating BCS Fermi gas, Eur. Phys. J. D 39 (2006) 283–294.
[91] J. Dechargé, D. Gogny, Hartree-Fock-Bogolyubov calculations with the D1 effective interaction on spherical nuclei, Phys. Rev. C 21 (1980) 1568–1593.
[92] M. Bender, P.-H. Heenen, P.-G. Reinhard, Self-consistent mean-field models for nuclear structure, Rev. Modern Phys. 75 (2003) 121–180.
[93] D. Vretenar, A.V. Afanasjev, G.A. Lalazissis, P. Ring, Relativistic Hartree-Bogoliubov theory: static and dynamic aspects of exotic nuclear structure, Phys. Rep. 409 (2005) 101–259.
[94] J. Erler, P. Klüpfel, P.-G. Reinhard, Self-consistent nuclear mean-field models: example Skyrme-Hartree-Fock, J. Phys. G 38 (2011) 033101.
[95] A.L. Fetter, J.D. Walecka, Quantum Theory of Many-Particle Systems, McGraw-Hill, New York, 1971.
[96] L.P. Gor'kov, Microscopic derivation of the Ginzburg-Landau equations in the theory of superconductivity, Sov. Phys.—JETP 9 (1959) 1364–1367; Zh. Eksp. Teor. Fiz. 36 (1959) 1918-1923.
[97] M.A. Baranov, D.S. Petrov, Critical temperature and Ginzburg-Landau equation for a trapped Fermi gas, Phys. Rev. A 58 (1998) R801–R804.
[98] S. Simonucci, G.C. Strinati, Equation for the superfluid gap obtained by coarse graining the Bogoliubov—de Gennes equations throughout the BCS-BEC crossover, Phys. Rev. B 89 (2014) 054511.
[99] A.M. Clogston, Upper limit for the critical field in hard superconductors, Phys. Rev. Lett. 9 (1962) 266–267.
[100] B.S. Chandrasekhar, A note on the maximum critical field of high-field superconductors, Appl. Phys. Lett. 1 (1962) 7–8.
[101] G. Sarma, On the influence of a uniform exchange field acting on the spins of the conduction electrons in a superconductor, J. Phys. Chem. Solids 24 (1963) 1029–1032.
[102] P. Fulde, R.A. Ferrell, Superconductivity in a strong spin-exchange field, Phys. Rev. 135 (1964) A550–A563.
[103] A.I. Larkin, Y.N. Ovchinnikov, Nonuniform state of superconductors, Sov. Phys.—JETP 20 (1965) 762–769; Zh. Eksp. Teor. Fiz. 47 (1964) 1136-1146.
[104] Y. Matsuda, H. Shimahara, Fulde-Ferrell-Larkin-Ovchinnikov state in heavy fermion superconductors, J. Phys. Soc. Japan 76 (2007) 051005.
[105] A. Sedrakian, T. Alm, U. Lombardo, Superfluidity in asymmetric nuclear matter, Phys. Rev. C 55 (1997) R582–R584.

[106] R. Casalbuoni, G. Nardulli, Inhomogeneous superconductivity in condensed matter and QCD, Rev. Modern Phys. 76 (2004) 263–320.
[107] M.G. Alford, A. Schmitt, K. Rajagopal, T. Schäfer, Color superconductivity in dense quark matter, Rev. Modern Phys. 80 (2008) 1455–1515.
[108] M.W. Zwierlein, A. Schirotzek, C.H. Schunck, W. Ketterle, Fermionic superfluidity with imbalanced spin populations, Science 311 (2006) 492–496.
[109] G.B. Partridge, W. Li, R.I. Kamar, Y.-a. Liao, R.G. Hulet, Pairing and phase separation in a polarized Fermi gas, Science 311 (2006) 503–505.
[110] W.V. Liu, F. Wilczek, Interior gap superfluidity, Phys. Rev. Lett. 90 (2003) 047002.
[111] E. Gubankova, W.V. Liu, F. Wilczek, Breached pairing superfluidity: Possible realization in QCD, Phys. Rev. Lett. 91 (2003) 032001.
[112] M. McNeil Forbes, E. Gubankova, W.V. Liu, F. Wilczek, Stability criteria for breached-pair superfluidity, Phys. Rev. Lett. 94 (2005) 017001.
[113] S. Takada, T. Izuyama, Superconductivity in a molecular field. I, Progr. Theoret. Phys. 41 (1969) 635–663.
[114] G. Eilenberger, Transformation of Gorkov's equation for type II superconductors into transport-like equations, Z. Phys. 214 (1968) 195–213.
[115] A.I. Larkin, Y.N. Ovchinnikov, Quasiclassical method in the theory of superconductivity, Sov. Phys.—JETP 55 (1968) 1200–1205; Zh. Eksp. Teor. Fiz. 55 (1968) 2262-2272.
[116] S. Matsuo, S. Higashitani, Y. Nagato, K. Nagai, Phase diagram of the Fulde-Ferrell-Larkin-Ovchinnikov state in a three-dimensional superconductor, J. Phys. Soc. Japan 67 (1998) 280–289.
[117] C. Mora, R. Combescot, Transition to Fulde-Ferrell-Larkin-Ovchinnikov phases in three dimensions: A quasiclassical investigation at low temperature with Fourier expansion, Phys. Rev. B 71 (2005) 214504.
[118] A.I. Buzdin, H. Kachkachi, Generalized Ginzburg-Landau theory for nonuniform FFLO superconductors, Phys. Lett. A 225 (1997) 341–348.
[119] M. Houzet, Y. Meurdesoif, O. Coste, A. Buzdin, Structure of the non-uniform Fulde-Ferrell-Larkin-Ovchinnikov state in 3D superconductors, Physica C 316 (1999) 89–96.
[120] R. Combescot, C. Mora, Transition to Fulde-Ferrel-Larkin-Ovchinnikov phases near the tricritical point: an analytical study, Eur. Phys. J. B 28 (2002) 397–406.
[121] J.A. Bowers, K. Rajagopal, Crystallography of color superconductivity, Phys. Rev. D 66 (2002) 065002.
[122] K. Machida, H. Nakanishi, Superconductivity under a ferromagnetic molecular field, Phys. Rev. B 30 (1984) 122–133.
[123] A.I. Buzdin, V.V. Tugushev, Phase diagrams of electronic and superconducting transitions to soliton lattice states, Sov. Phys.—JETP 58 (1983) 428–433; Zh. Eksp. Teor. Fiz. 85 (1983) 735–745.
[124] A.I. Buzdin, S.V. Polonskii, Nonuniform state in quasi-1D superconductor, Sov. Phys.—JETP 66 (1987) 422–429; Zh. Eksp. Teor. Fiz. 93 (1987) 747–761.
[125] P.F. Bedaque, H. Caldas, G. Rupak, Phase separation in asymmetrical fermion superfluids, Phys. Rev. Lett. 91 (2003) 247002.
[126] S.-T. Wu, S. Yip, Superfluidity in the interior-gap states, Phys. Rev. A 67 (2003) 053603.
[127] D.T. Son, M.A. Stephanov, Phase diagram of a cold polarized Fermi gas, Phys. Rev. A 74 (2006) 013614.
[128] M. Iskin, C.A.R. Sá de Melo, Two-species fermion mixtures with population imbalance, Phys. Rev. Lett. 97 (2006) 100404.
[129] K.B. Gubbels, M.W.J. Romans, H.T.C. Stoof, Sarma phase in trapped unbalanced Fermi gases, Phys. Rev. Lett. 97 (2006) 210402.
[130] Q. Chen, Y. He, C.-C. Chien, K. Levin, Stability conditions and phase diagrams for two-component Fermi gases with population imbalance, Phys. Rev. A 74 (2006) 063603.
[131] C.-H. Pao, S.-T. Wu, S.-K. Yip, Superfluid stability in the BEC-BCS crossover, Phys. Rev. B 73 (2006) 132506;
C.-H. Pao, S.-T. Wu, S.-K. Yip, Phys. Rev. B 74 (2006) 189901 (erratum).
[132] S. Pilati, S. Giorgini, Phase separation in a polarized Fermi gas at zero temperature, Phys. Rev. Lett. 100 (2008) 030401.
[133] D.E. Sheehy, L. Radzihovsky, BEC-BCS crossover, phase transitions and phase separation in polarized resonantly-paired superfluids, Ann. Phys. 322 (2007) 1790–1924.
[134] P. Pieri, G.C. Strinati, Trapped fermions with density imbalance in the Bose-Einstein condensate limit, Phys. Rev. Lett. 96 (2006) 150404.
[135] N. Yoshida, S.-K. Yip, Larkin-Ovchinnikov state in resonant Fermi gas, Phys. Rev. A 75 (2007) 063601.
[136] C.-H. Pao, S.-K. Yip, Phase diagram of asymmetric Fermi gas across Feshbach resonance, J. Phys. Conf. Ser. 150 (2009) 032078.
[137] Y.-I. Shin, C.H. Schunck, A. Schirotzek, W. Ketterle, Phase diagram of a two-component Fermi gas with resonant interactions, Nature 451 (2008) 689–693.
[138] T. Kashimura, R. Watanabe, Y. Ohashi, Spin susceptibility and fluctuation corrections in the BCS-BEC crossover regime of an ultracold Fermi gas, Phys. Rev. A 86 (2012) 043622.
[139] A. Tartari, Phase Diagram of a Two-Component Fermi Gas with Density Imbalance Throughout the BCS-BEC Crossover, (Ph.D. thesis), University of Camerino, 2011.
[140] M.M. Parish, F.M. Marchetti, A. Lamacraft, B.D. Simons, Finite-temperature phase diagram of a polarized Fermi condensate, Nat. Phys. 3 (2007) 124–128.
[141] V.M. Galitskii, The energy spectrum of a non-ideal Fermi gas, Sov. Phys.—JETP 7 (1958) 104–112; Zh. Eksp. Teor. Fiz. 34 (1958) 151-162.
[142] A. Vagov, H. Schomerus, A. Shanenko, Generalized Galitskii approach for the vertex function of a Fermi gas with resonant interaction, Phys. Rev. B 76 (2007) 214513.
[143] T. Enss, Quantum critical transport in the unitary Fermi gas, Phys. Rev. A 86 (2012) 013616.
[144] J.W. Serene, Stability of two-dimensional Fermi liquids against pair fluctuations with large total momentum, Phys. Rev. B 40 (1989) 10873–10877.
[145] G.D. Mahan, Many-Particle Physics, third ed., Kluwer Academic/ Plenum Publishers, New York, 2000.
[146] M. Urban, P. Schuck, Occupation numbers in strongly polarized Fermi gases and the Luttinger theorem, Phys. Rev. A 90 (2014) 023632.
[147] P. Schuck, H.-J. Schulze, N. Van Giai, M. Zverev, Two-dimensional electron gas in an improved random-phase approximation, Phys. Rev. B 67 (2003) 233404.
[148] R. Haussmann, Properties of a Fermi liquid at the superfluid transition in the crossover region between BCS superconductivity and Bose-Einstein condensation, Phys. Rev. B 49 (1994) 12975–12983.
[149] P. Pieri, G.C. Strinati, Strong-coupling limit in the evolution from BCS superconductivity to Bose-Einstein condensation, Phys. Rev. B 61 (2000) 15370–15381.
[150] A. Perali, P. Pieri, G.C. Strinati, C. Castellani, Pseudogap and spectral function from superconducting fluctuations to the bosonic limit, Phys. Rev. B 66 (2002) 024510.
[151] P. Pieri, L. Pisani, G.C. Strinati, BCS-BEC crossover at finite temperature in the broken-symmetry phase, Phys. Rev. B 70 (2004) 094508.
[152] P. Pieri, L. Pisani, G.C. Strinati, Comparison between a diagrammatic theory for the BCS-BEC crossover and quantum Monte Carlo results, Phys. Rev. B 72 (2005) 012506.
[153] P. Pieri, L. Pisani, G.C. Strinati, Pairing fluctuation effects on the single-particle spectra for the superconducting state, Phys. Rev. Lett. 92 (2004) 110401.
[154] N. Andrenacci, P. Pieri, G.C. Strinati, Evolution from BCS superconductivity to Bose-Einstein condensation: Current correlation function in the broken-symmetry phase, Phys. Rev. B 68 (2003) 144507.
[155] N. Prokof'ev, B. Svistunov, Bold diagrammatic Monte Carlo: A generic sign-problem tolerant technique for polaron models and possibly interacting many-body problems, Phys. Rev. B 77 (2008) 125101.
[156] B. Jankó, J. Maly, K. Levin, Pseudogap effects induced by resonant pair scattering, Phys. Rev. B 56 (1997) R11407–R11410.
[157] I. Kosztin, Q. Chen, B. Jankó, K. Levin, Relationship between the pseudo- and superconducting gaps: Effects of residual pairing correlations below T_c, Phys. Rev. B 58 (1998) R5936–R5939.

[158] Q. Chen, I. Kosztin, B. Jankó, K. Levin, Pairing fluctuation theory of superconducting properties in underdoped to overdoped cuprates, Phys. Rev. Lett. 81 (1998) 4708–4711.
[159] R. Haussmann, W. Rantner, S. Cerrito, W. Zwerger, Thermodynamics of the BCS-BEC crossover, Phys. Rev. A 75 (2007) 023610.
[160] R. Zimmermann, H. Stolz, The mass action law in two-component Fermi systems revisited: Excitons and electron-hole pairs, Phys. Status Solidi b 131 (1985) 151–164.
[161] H. Hu, X.-J. Liu, P.D. Drummond, Comparative study of strong-coupling theories of a trapped Fermi gas at unitarity, Phys. Rev. A 77 (2008) 061605.
[162] C.-C. Chien, H. Guo, Y. He, K. Levin, Comparative study of BCS-BEC crossover theories above T_c: The nature of the pseudogap in ultracold atomic Fermi gases, Phys. Rev. A 81 (2010) 023622.
[163] R. Combescot, S. Giraud, Normal state of highly polarized fermi gases: Full many-body treatment, Phys. Rev. Lett. 101 (2008) 050404.
[164] J.R. Engelbrecht, M. Randeria, C.A.R. Sá de Melo, BCS to Bose crossover: Broken-symmetry state, Phys. Rev. B 55 (1997) 15153–15156.
[165] N.F. Mott, Conduction in non-crystalline materials, Phil. Mag. 19 (1969) 835–852.
[166] F. Palestini, A. Perali, P. Pieri, G.C. Strinati, Dispersions, weights, and widths of the single-particle spectral function in the normal phase of a Fermi gas, Phys. Rev. B 85 (2012) 024517.
[167] F. Palestini, A. Perali, P. Pieri, G.C. Strinati, Temperature and coupling dependence of the universal contact intensity for an ultracold Fermi gas, Phys. Rev. A 82 (2010) 021605(R).
[168] S. Tsuchiya, R. Watanabe, Y. Ohashi, Pseudogap temperature and effects of a harmonic trap in the BCS-BEC crossover regime of an ultracold Fermi gas, Phys. Rev. A 84 (2011) 043647.
[169] T. Kashimura, R. Watanabe, Y. Ohashi, Pseudogap phenomenon and effects of population imbalance in the normal state of a unitary Fermi gas, Phys. Rev. A 89 (2014) 013618.
[170] F. Marsiglio, P. Pieri, A. Perali, F. Palestini, G.C. Strinati, Pairing effects in the normal phase of a two-dimensional Fermi gas, Phys. Rev. B 91 (2015) 054509.
[171] A. Perali, F. Palestini, P. Pieri, G.C. Strinati, J.T. Stewart, J.P. Gaebler, T.E. Drake, D.S. Jin, Evolution of the normal state of a strongly interacting Fermi gas from a pseudogap phase to a molecular Bose gas, Phys. Rev. Lett. 106 (2011) 060402.
[172] L.P. Gor'kov, T.K. Melik-Barkhudarov, Contribution to the theory of superfluidity in an imperfect Fermi gas, Sov. Phys.—JETP 13 (1961) 1018–1022; Zh. Eksp. Teor. Fiz. 40 (1961) 1452-1458.
[173] D.J. Thouless, Perturbation theory in statistical mechanics and the theory of superconductivity, Ann. Phys. 10 (1960) 553–588.
[174] N.M. Hugenholtz, D. Pines, Ground-state energy and excitation spectrum of a system of interacting bosons, Phys. Rev. 116 (1959) 489–506.
[175] A. Bulgac, J.E. Drut, P. Magierski, Spin 1/2 fermions in the unitary regime: A superfluid of a new type, Phys. Rev. Lett. 96 (2006) 090404.
[176] Z.-Q. Yu, K. Huang, L. Yin, Induced interaction in a Fermi gas with a BEC-BCS crossover, Phys. Rev. A 79 (2009) 053636.
[177] X.-X. Ruan, H. Gong, L. Du, W.-M. Sun, H.-S. Zong, Effect of the induced interaction on the superfluid-transition temperature of ultracold Fermi gases within the T-matrix approximation, Phys. Rev. A 87 (2013) 043608.
[178] S. Floerchinger, M. Scherer, S. Diehl, C. Wetterich, Particle-hole fluctuations in BCS-BEC crossover, Phys. Rev. B 78 (2008) 174528.
[179] S. Floerchinger, M.M. Scherer, C. Wetterich, Modified Fermi sphere, pairing gap, and critical temperature for the BCS-BEC crossover, Phys. Rev. A 81 (2010) 063619.
[180] Y. Tanizaki, G. Fejős, T. Hatsuda, Fermionic functional renormalization group approach to superfluid phase transition, Prog. Theor. Exp. Phys. 2014 (2014) 043I01.
[181] L. Pisani, A. Perali, P. Pieri, G.C. Strinati, Entanglement between pairing and screening in the Gorkov-Melik-Barkhudarov correction to the critical temperature throughout the BCS-BEC crossover, Phys. Rev. B 97 (2018) 014528.
[182] S. Nascimbène, N. Navon, K.J. Jiang, F. Chevy, C. Salomon, Exploring the thermodynamics of a universal Fermi gas, Nature 463 (2010) 1057–1060.
[183] M.J.H. Ku, A.T. Sommer, L.W. Cheuk, M.W. Zwierlein, Revealing the superfluid lambda transition in the universal thermodynamics of a unitary Fermi gas, Science 335 (2012) 563–567.
[184] E. Burovski, N. Prokof'ev, B. Svistunov, M. Troyer, Critical temperature and thermodynamics of attractive fermions at unitarity, Phys. Rev. Lett. 96 (2006) 160402.
[185] E. Burovski, E. Kozik, N. Prokof'ev, B. Svistunov, M. Troyer, Critical temperature curve in BEC-BCS crossover, Phys. Rev. Lett. 101 (2008) 090402.
[186] O. Goulko, M. Wingate, Thermodynamics of balanced and slightly spin-imbalanced Fermi gases at unitarity, Phys. Rev. A 82 (2010) 053621.
[187] H.-J. Schulze, A. Polls, A. Ramos, Pairing with polarization effects in low-density neutron matter, Phys. Rev. C 63 (2001) 044310.
[188] H. Heiselberg, C.J. Pethick, H. Smith, L. Viverit, Influence of induced interactions on the superfluid transition in dilute Fermi gases, Phys. Rev. Lett. 85 (2000) 2418–2421.
[189] L.G. Cao, U. Lombardo, P. Schuck, Screening effects in superfluid nuclear and neutron matter within Brueckner theory, Phys. Rev. C 74 (2006) 064301.
[190] M. Baldo, A. Grasso, Dispersive effects in neutron matter superfluidity, Phys. Lett. B 485 (2000) 115–120.
[191] G. Röpke, L. Münchow, H. Schulz, Particle clustering and Mott transitions in nuclear matter at finite temperature, Nuclear Phys. A 379 (1982) 536–552.
[192] G. Röpke, M. Schmidt, L. Münchow, H. Schulz, Particle clustering and Mott transition in nuclear matter at finite temperature (II) Self-consistent ladder Hartree-Fock approximation and model calculations for cluster abundances and the phase diagram, Nuclear Phys. A 399 (1983) 587–602.
[193] M. Schmidt, G. Röpke, H. Schulz, Generalized Beth-Uhlenbeck approach for hot nuclear matter, Ann. Phys. 202 (1990) 57–99.
[194] P.-A. Pantel, D. Davesne, M. Urban, Polarized Fermi gases at finite temperature in the BCS-BEC crossover, Phys. Rev. A 90 (2014) 053629; P.-A. Pantel, D. Davesne, M. Urban, Phys. Rev. A 94 (2016) 019901 (erratum).
[195] D.S. Petrov, C. Salomon, G.V. Shlyapnikov, Weakly bound dimers of fermionic atoms, Phys. Rev. Lett. 93 (2004) 090404.
[196] D.S. Petrov, C. Salomon, G.V. Shlyapnikov, Scattering properties of weakly bound dimers of fermionic atoms, Phys. Rev. A 71 (2005) 012708.
[197] I.V. Brodsky, A.V. Klaptsov, M.Y. Kagan, R. Combescot, X. Leyronas, Bound states of three and four resonantly interacting particles, JETP Lett. 82 (2005) 273–278.
[198] I.V. Brodsky, M.Y. Kagan, A.V. Klaptsov, R. Combescot, X. Leyronas, Exact diagrammatic approach for dimer-dimer scattering and bound states of three and four resonantly interacting particles, Phys. Rev. A 73 (2006) 032724.
[199] S. Elhatisari, K. Katterjohn, D. Lee, U.-G. Meiner, G. Rupak, Universal dimer-dimer scattering in lattice effective field theory, Phys. Lett. B 768 (2017) 337–344.
[200] A. Deltuva, Universality in fermionic dimer-dimer scattering, Phys. Rev. A 96 (2017) 022701.
[201] J. von Stecher, C.H. Greene, D. Blume, Energetics and structural properties of trapped two-component Fermi gases, Phys. Rev. A 77 (2008) 043619.
[202] J.P. D'Incao, S.T. Rittenhouse, N.P. Mehta, C.H. Greene, Dimer-dimer collisions at finite energies in two-component Fermi gases, Phys. Rev. A 79 (2009) 030501.
[203] F. Alzetto, R. Combescot, X. Leyronas, Dimer-dimer scattering length for fermions with different masses: Analytical study for large mass ratio, Phys. Rev. A 87 (2013) 022704.
[204] F. Wilczek, Origins of mass, Open Phys. 10 (2012) 1021–1037. arXiv:1206.7114.
[205] A. Deltuva, A.C. Fonseca, Deuteron–deuteron scattering above four-nucleon breakup threshold, Phys. Lett. B 742 (2015) 285–289.
[206] X.-J. Liu, H. Hu, BCS-BEC crossover in an asymmetric two-component Fermi gas, Europhys. Lett. 75 (2006) 364–370.

[207] T. Kashimura, R. Watanabe, Y. Ohashi, Magnetic properties and strong-coupling corrections in an ultracold Fermi gas with population imbalance, J. Low. Temp. Phys. 171 (2013) 355–361.
[208] J. Maly, K. Levin, D.Z. Liu, Coulomb correlations and pseudogap effects in a preformed pair model for the cuprates, Phys. Rev. B 54 (1996) R15657–R15660.
[209] Y. Ohashi, On the Fulde-Ferrell State in spatially isotropic superconductors, J. Phys. Soc. Japan 71 (2002) 2625–2628.
[210] H. Shimahara, Phase fluctuations and Kosterlitz-Thouless transition in two-dimensional Fulde-Ferrell-Larkin-Ovchinnikov superconductors, J. Phys. Soc. Japan 67 (1998) 1872–1875.
[211] H. Shimahara, Stability of Fulde-Ferrell-Larkin-Ovchinnikov state in type-II superconductors against the phase fluctuations, Physica B 259–261 (1999) 492–493.
[212] L. Radzihovsky, A. Vishwanath, Quantum liquid crystals in an imbalanced Fermi gas: Fluctuations and fractional vortices in Larkin-Ovchinnikov States, Phys. Rev. Lett. 103 (2009) 010404.
[213] L. Radzihovsky, Fluctuations and phase transitions in Larkin-Ovchinnikov liquid-crystal states of a population-imbalanced resonant Fermi gas, Phys. Rev. A 84 (2011) 023611.
[214] P. Jakubczyk, Renormalization theory for the Fulde-Ferrell-Larkin-Ovchinnikov states at $T > 0$, Phys. Rev. A 95 (2017) 063626.
[215] K. Gubbels, H. Stoof, Renormalization group theory for the imbalanced Fermi gas, Phys. Rev. Lett. 100 (2008) 140407.
[216] Y. He, C.-C. Chien, Q. Chen, K. Levin, Thermodynamics and superfluid density in BCS-BEC crossover with and without population imbalance, Phys. Rev. B 76 (2007) 224516.
[217] I. Boettcher, J. Braun, T.K. Herbst, J.M. Pawlowski, D. Roscher, C. Wetterich, Phase structure of spin-imbalanced unitary Fermi gases, Phys. Rev. A 91 (2015) 013610.
[218] J.M. Luttinger, Fermi surface and some simple equilibrium properties of a system of interacting fermions, Phys. Rev. 119 (1960) 1153–1163.
[219] I. Bloch, J. Dalibard, W. Zwerger, Many-body physics with ultracold gases, Rev. Modern Phys. 80 (2008) 885–964.
[220] U. Fano, Sullo spettro di assorbimento dei gas nobili presso il limite dello spettro d'arco, Nuovo Cimento 12 (1935) 154–161.
[221] U. Fano, Effects of configuration interaction on intensities and phase shifts, Phys. Rev. 124 (1961) 1866–1878.
[222] H. Feshbach, A unified theory of nuclear reactions. II, Ann. Phys. 19 (1962) 287–313.
[223] S. Simonucci, P. Pieri, G.C. Strinati, Broad vs. narrow Fano-Feshbach resonances in the BCS-BEC crossover with trapped Fermi atoms, Europhys. Lett. 69 (2005) 713–718.
[224] M. Holland, S.J.J.M.F. Kokkelmans, M.L. Chiofalo, R. Walser, Resonance superfluidity in a quantum degenerate Fermi gas, Phys. Rev. Lett. 87 (2001) 120406.
[225] Y. Ohashi, A. Griffin, BCS-BEC crossover in a gas of Fermi atoms with a Feshbach resonance, Phys. Rev. Lett. 89 (2002) 130402.
[226] G.M. Falco, H.T.C. Stoof, Crossover temperature of Bose-Einstein condensation in an atomic Fermi gas, Phys. Rev. Lett. 92 (2004) 130401.
[227] G.M. Bruun, C.J. Pethick, Effective theory of Feshbach resonances and many-body properties of Fermi gases, Phys. Rev. Lett. 92 (2004) 140404.
[228] J. Stajic, J.N. Milstein, Q. Chen, M.L. Chiofalo, M.J. Holland, K. Levin, Nature of superfluidity in ultracold Fermi gases near Feshbach resonances, Phys. Rev. A 69 (2004) 063610.
[229] S. Diehl, C. Wetterich, Universality in phase transitions for ultracold fermionic atoms, Phys. Rev. A 73 (2006) 033615.
[230] C. Pethick, H. Smith, Bose-Einstein Condensation in Dilute Gases, Cambridge University Press, Cambridge, 2008.
[231] A. Perali, P. Pieri, G.C. Strinati, Shrinking of a condensed fermionic cloud in a trap approaching the Bose-Einstein condensation limit, Phys. Rev. A 68 (2003) 031601.
[232] A. Perali, P. Pieri, L. Pisani, G.C. Strinati, BCS-BEC crossover at finite temperature for superfluid trapped Fermi atoms, Phys. Rev. Lett. 92 (2004) 220404.
[233] R. Haussmann, W. Zwerger, Thermodynamics of a trapped unitary Fermi gas, Phys. Rev. A 78 (2008) 063602.
[234] Y. Shin, C.H. Schunck, A. Schirotzek, W. Ketterle, Tomographic rf spectroscopy of a trapped Fermi gas at unitarity, Phys. Rev. Lett. 99 (2007) 090403.
[235] T.-L. Ho, Q. Zhou, Obtaining the phase diagram and thermodynamic quantities of bulk systems from the densities of trapped gases, Nat. Phys. 6 (2010) 131–134.
[236] C.A. Regal, C. Ticknor, J.L. Bohn, D.S. Jin, Creation of ultracold molecules from a Fermi gas of atoms, Nature 424 (2003) 47–50.
[237] K.E. Strecker, G.B. Partridge, R.G. Hulet, Conversion of an atomic Fermi gas to a long-lived molecular Bose gas, Phys. Rev. Lett. 91 (2003) 080406.
[238] J. Cubizolles, T. Bourdel, S.J.J.M.F. Kokkelmans, G.V. Shlyapnikov, C. Salomon, Production of long-lived ultracold Li_2 molecules from a Fermi gas, Phys. Rev. Lett. 91 (2003) 240401.
[239] S. Jochim, M. Bartenstein, A. Altmeyer, G. Hendl, C. Chin, J. Hecker Denschlag, R. Grimm, Pure gas of optically trapped molecules created from fermionic atoms, Phys. Rev. Lett. 91 (2003) 240402.
[240] M. Greiner, C.A. Regal, D.S. Jin, Emergence of a molecular Bose-Einstein condensate from a Fermi gas, Nature 426 (2003) 537–540.
[241] S. Jochim, M. Bartenstein, A. Altmeyer, G. Hendl, S. Riedl, C. Chin, J. Hecker Denschlag, R. Grimm, Bose-Einstein condensation of molecules, Science 302 (2003) 2101–2103.
[242] M.W. Zwierlein, C.A. Stan, C.H. Schunck, S.M.F. Raupach, S. Gupta, Z. Hadzibabic, W. Ketterle, Observation of Bose-Einstein condensation of molecules, Phys. Rev. Lett. 91 (2003) 250401.
[243] C.A. Regal, M. Greiner, D.S. Jin, Observation of resonance condensation of fermionic atom pairs, Phys. Rev. Lett. 92 (2004) 040403.
[244] M.W. Zwierlein, C.A. Stan, C.H. Schunck, S.M.F. Raupach, A.J. Kerman, W. Ketterle, Condensation of pairs of fermionic atoms near a Feshbach resonance, Phys. Rev. Lett. 92 (2004) 120403.
[245] A. Perali, P. Pieri, G.C. Strinati, Extracting the condensate density from projection experiments with Fermi gases, Phys. Rev. Lett. 95 (2005) 010407.
[246] M.W. Zwierlein, C.H. Schunck, C.A. Stan, S.M.F. Raupach, W. Ketterle, Formation dynamics of a fermion pair condensate, Phys. Rev. Lett. 94 (2005) 180401.
[247] C. Chin, M. Bartenstein, A. Altmeyer, S. Riedl, S. Jochim, J. Hecker Denschlag, R. Grimm, Observation of the pairing gap in a strongly interacting Fermi gas, Science 305 (2004) 1128–1130.
[248] M. Greiner, C.A. Regal, D.S. Jin, Probing the excitation spectrum of a Fermi gas in the BCS-BEC crossover regime, Phys. Rev. Lett. 94 (2005) 070403.
[249] A. Schirotzek, Y.-i. Shin, C.H. Schunck, W. Ketterle, Determination of the superfluid gap in atomic Fermi gases by quasiparticle spectroscopy, Phys. Rev. Lett. 101 (2008) 140403.
[250] J. Kinast, S.L. Hemmer, M.E. Gehm, A. Turlapov, J.E. Thomas, Evidence for superfluidity in a resonantly interacting Fermi gas, Phys. Rev. Lett. 92 (2004) 150402.
[251] M. Bartenstein, A. Altmeyer, S. Riedl, S. Jochim, C. Chin, J. Hecker Denschlag, R. Grimm, Collective excitations of a degenerate gas at the BEC-BCS crossover, Phys. Rev. Lett. 92 (2004) 203201.
[252] J. Kinast, A. Turlapov, J.E. Thomas, Breakdown of hydrodynamics in the radial breathing mode of a strongly interacting Fermi gas, Phys. Rev. A 70 (2004) 051401.
[253] A. Altmeyer, S. Riedl, C. Kohstall, M.J. Wright, R. Geursen, M. Bartenstein, C. Chin, J. Hecker Denschlag, R. Grimm, Precision measurements of collective oscillations in the BEC-BCS crossover, Phys. Rev. Lett. 98 (2007) 040401.
[254] S. Riedl, E. Sanchez Guajardo, C. Kohstall, A. Altmeyer, M. Wright, J. Hecker Denschlag, R. Grimm, G. Bruun, H. Smith, Collective oscillations of a Fermi gas in the unitarity limit: temperature effects and role of pair correlations, Phys. Rev. A 78 (2008) 053609.

[255] A. Altmeyer, S. Riedl, M.J. Wright, C. Kohstall, J. Hecker Denschlag, R. Grimm, Dynamics of a strongly interacting Fermi gas: The radial quadrupole mode, Phys. Rev. A 76 (2007) 033610.
[256] M.J. Wright, S. Riedl, A. Altmeyer, C. Kohstall, E.R. Sanchez Guajardo, J. Hecker Denschlag, R. Grimm, Finite-temperature collective dynamics of a Fermi gas in the BEC-BCS crossover, Phys. Rev. Lett. 99 (2007) 150403.
[257] M.K. Tey, L.A. Sidorenkov, E.R. Sanchez Guajardo, R. Grimm, M.J.H. Ku, M.W. Zwierlein, Y.-H. Hou, L. Pitaevskii, S. Stringari, Collective modes in a unitary Fermi gas across the superfluid phase transition, Phys. Rev. Lett. 110 (2013) 055303.
[258] J. Kinast, A. Turlapov, J.E. Thomas, Q. Chen, J. Stajic, K. Levin, Heat capacity of a strongly interacting Fermi gas, Science 307 (2005) 1296–1299.
[259] L. Luo, B. Clancy, J. Joseph, J. Kinast, J.E. Thomas, Measurement of the entropy and critical temperature of a strongly interacting Fermi gas, Phys. Rev. Lett. 98 (2007) 080402.
[260] N. Navon, S. Nascimbène, F. Chevy, C. Salomon, The equation of state of a low-temperature Fermi gas with tunable interactions, Science 328 (2010) 729–732.
[261] M. Horikoshi, S. Nakajima, M. Ueda, T. Mukaiyama, Measurement of universal thermodynamic functions for a unitary Fermi gas, Science 327 (2010) 442–445.
[262] G.B. Partridge, K.E. Strecker, R.I. Kamar, M.W. Jack, R.G. Hulet, Molecular probe of pairing in the BEC-BCS crossover, Phys. Rev. Lett. 95 (2005) 020404.
[263] M. Greiner, C.A. Regal, J.T. Stewart, D.S. Jin, Probing pair-correlated fermionic atoms through correlations in atom shot noise, Phys. Rev. Lett. 94 (2005) 110401.
[264] E. Altman, E. Demler, M.D. Lukin, Probing many-body states of ultracold atoms via noise correlations, Phys. Rev. A 70 (2004) 013603.
[265] M.W. Zwierlein, J.R. Abo-Shaeer, A. Schirotzek, C.H. Schunck, W. Ketterle, Vortices and superfluidity in a strongly interacting Fermi gas, Nature 435 (2005) 1047–1051.
[266] Y. Shin, M.W. Zwierlein, C.H. Schunck, A. Schirotzek, W. Ketterle, Observation of phase separation in a strongly interacting imbalanced Fermi gas, Phys. Rev. Lett. 97 (2006) 030401.
[267] M.W. Zwierlein, C.H. Schunck, A. Schirotzek, W. Ketterle, Direct observation of the superfluid phase transition in ultracold Fermi gases, Nature 442 (2006) 54–58.
[268] Y.-i. Shin, A. Schirotzek, C.H. Schunck, W. Ketterle, Realization of a strongly interacting Bose-Fermi mixture from a two-component Fermi gas, Phys. Rev. Lett. 101 (2008) 070404.
[269] B.A. Olsen, M.C. Revelle, J.A. Fry, D.E. Sheehy, R.G. Hulet, Phase diagram of a strongly interacting spin-imbalanced Fermi gas, Phys. Rev. A 92 (2015) 063616.
[270] J. Joseph, B. Clancy, L. Luo, J. Kinast, A. Turlapov, J.E. Thomas, Measurement of sound velocity in a Fermi gas near a Feshbach resonance, Phys. Rev. Lett. 98 (2007) 170401.
[271] L.A. Sidorenkov, M.K. Tey, R. Grimm, Y.-H. Hou, L. Pitaevskii, S. Stringari, Second sound and the superfluid fraction in a Fermi gas with resonant interactions, Nature 498 (2013) 78–81.
[272] D. Miller, J. Chin, C. Stan, Y. Liu, W. Setiawan, C. Sanner, W. Ketterle, Critical velocity for superfluid flow across the BEC-BCS crossover, Phys. Rev. Lett. 99 (2007) 070402.
[273] W. Weimer, K. Morgener, V.P. Singh, J. Siegl, K. Hueck, N. Luick, L. Mathey, H. Moritz, Critical velocity in the BEC-BCS crossover, Phys. Rev. Lett. 114 (2015) 095301.
[274] C.H. Schunck, Y.-i. Shin, A. Schirotzek, W. Ketterle, Determination of the fermion pair size in a resonantly interacting superfluid, Nature 454 (2008) 739–743.
[275] J.T. Stewart, J.P. Gaebler, T.E. Drake, D.S. Jin, Verification of universal relations in a strongly interacting Fermi gas, Phys. Rev. Lett. 104 (2010) 235301.
[276] E. Kuhnle, H. Hu, X.-J. Liu, P. Dyke, M. Mark, P. Drummond, P. Hannaford, C. Vale, Universal behavior of pair correlations in a strongly interacting Fermi gas, Phys. Rev. Lett. 105 (2010) 070402.
[277] E. Kuhnle, S. Hoinka, P. Dyke, H. Hu, P. Hannaford, C. Vale, Temperature dependence of the universal contact parameter in a unitary Fermi gas, Phys. Rev. Lett. 106 (2011) 170402.
[278] Y. Sagi, T.E. Drake, R. Paudel, D.S. Jin, Measurement of the homogeneous contact of a unitary Fermi gas, Phys. Rev. Lett. 109 (2012) 220402.
[279] S. Hoinka, M. Lingham, K. Fenech, H. Hu, C. Vale, J. Drut, S. Gandolfi, Precise determination of the structure factor and contact in a unitary Fermi gas, Phys. Rev. Lett. 110 (2013) 055305.
[280] C. Cao, E. Elliott, J. Joseph, H. Wu, J. Petricka, T. Schäfer, J. Thomas, Universal quantum viscosity in a unitary Fermi gas, Science 331 (2011) 58–61.
[281] E. Elliott, J. Joseph, J. Thomas, Anomalous minimum in the shear viscosity of a Fermi gas, Phys. Rev. Lett. 113 (2014) 020406.
[282] J.A. Joseph, E. Elliott, J.E. Thomas, Shear viscosity of a unitary Fermi gas near the superfluid phase transition, Phys. Rev. Lett. 115 (2015) 020401.
[283] M. Bluhm, J. Hou, T. Schäfer, Determination of the density and temperature dependence of the shear viscosity of a unitary Fermi gas based on hydrodynamic flow, Phys. Rev. Lett. 119 (2017) 065302.
[284] P.K. Kovtun, D.T. Son, A.O. Starinets, Viscosity in strongly interacting quantum field theories from black hole physics, Phys. Rev. Lett. 94 (2005) 111601.
[285] C. Sanner, E. Su, A. Keshet, W. Huang, J. Gillen, R. Gommers, W. Ketterle, Speckle imaging of spin fluctuations in a strongly interacting Fermi gas, Phys. Rev. Lett. 106 (2011) 010402.
[286] S. Hoinka, M. Lingham, M. Delehaye, C.J. Vale, Dynamic spin response of a strongly interacting Fermi gas, Phys. Rev. Lett. 109 (2012) 050403.
[287] M.G. Lingham, K. Fenech, S. Hoinka, C.J. Vale, Local observation of pair condensation in a Fermi gas at unitarity, Phys. Rev. Lett. 112 (2014) 100404.
[288] S. Riedl, E.R. Sanchez Guajardo, C. Kohstall, J. Hecker Denschlag, Superfluid quenching of the moment of inertia in a strongly interacting Fermi gas, New J. Phys. 13 (2011) 035003.
[289] D. Husmann, S. Uchino, S. Krinner, M. Lebrat, T. Giamarchi, T. Esslinger, J.-P. Brantut, Connecting strongly correlated superfluids by a quantum point contact, Science 350 (2015) 1498–1501.
[290] G. Valtolina, A. Burchianti, A. Amico, E. Neri, K. Xhani, J.A. Seman, A. Trombettoni, A. Smerzi, M. Zaccanti, M. Inguscio, G. Roati, Josephson effect in fermionic superfluids across the BEC-BCS crossover, Science 350 (2015) 1505–1508.
[291] B. Fröhlich, M. Feld, E. Vogt, M. Koschorreck, W. Zwerger, M. Köhl, Radio-frequency spectroscopy of a strongly interacting two-dimensional Fermi gas, Phys. Rev. Lett. 106 (2011) 105301.
[292] A.T. Sommer, L.W. Cheuk, M.J.H. Ku, W.S. Bakr, M.W. Zwierlein, Evolution of fermion pairing from three to two dimensions, Phys. Rev. Lett. 108 (2012) 045302.
[293] E. Vogt, M. Feld, B. Fröhlich, D. Pertot, M. Koschorreck, M. Köhl, Scale invariance and viscosity of a two-dimensional Fermi gas, Phys. Rev. Lett. 108 (2012) 070404.
[294] V. Makhalov, K. Martiyanov, A. Turlapov, Ground-state pressure of quasi-2D Fermi and Bose gases, Phys. Rev. Lett. 112 (2014) 045301.
[295] W. Ong, C. Cheng, I. Arakelyan, J.E. Thomas, Spin-imbalanced quasi-two-dimensional Fermi gases, Phys. Rev. Lett. 114 (2015) 110403.
[296] M.G. Ries, A.N. Wenz, G. Zürn, L. Bayha, I. Boettcher, D. Kedar, P.A. Murthy, M. Neidig, T. Lompe, S. Jochim, Observation of pair condensation in the quasi-2D BEC-BCS crossover, Phys. Rev. Lett. 114 (2015) 230401.
[297] P.A. Murthy, I. Boettcher, L. Bayha, M. Holzmann, D. Kedar, M. Neidig, M.G. Ries, A.N. Wenz, G. Zürn, S. Jochim, Observation of the Berezinskii-Kosterlitz-Thouless phase transition in an ultracold Fermi gas, Phys. Rev. Lett. 115 (2015) 010401.

[298] K. Fenech, P. Dyke, T. Peppler, M.G. Lingham, S. Hoinka, H. Hu, C.J. Vale, Thermodynamics of an attractive 2D Fermi gas, Phys. Rev. Lett. 116 (2016) 045302.
[299] I. Boettcher, L. Bayha, D. Kedar, P.A. Murthy, M. Neidig, M.G. Ries, A.N. Wenz, G. Zürn, S. Jochim, T. Enss, Equation of state of ultracold fermions in the 2D BEC-BCS crossover region, Phys. Rev. Lett. 116 (2016) 045303.
[300] Y.-a. Liao, A.S.C. Rittner, T. Paprotta, W. Li, G.B. Partridge, R.G. Hulet, S.K. Baur, E.J. Mueller, Spin-imbalance in a one-dimensional Fermi gas, Nature 467 (2010) 567–569.
[301] G. Orso, Attractive Fermi gases with unequal spin populations in highly elongated traps, Phys. Rev. Lett. 98 (2007) 070402.
[302] J.R. Taylor, Scattering Theory: The Quantum Theory of Nonrelativistic Collisions, Dover Publications, Mineola, N.Y., 1972, 2006 (Chapter 6-c).
[303] T.-L. Ho, Universal thermodynamics of degenerate quantum gases in the unitarity limit, Phys. Rev. Lett. 92 (2004) 090402.
[304] A. Perali, P. Pieri, G.C. Strinati, Quantitative comparison between theoretical predictions and experimental results for the BCS-BEC crossover, Phys. Rev. Lett. 93 (2004) 100404.
[305] M.E. Gehm, S.L. Hemmer, S.R. Granade, K.M. O'Hara, J.E. Thomas, Mechanical stability of a strongly interacting Fermi gas of atoms, Phys. Rev. A 68 (2003) 011401.
[306] M. Bartenstein, A. Altmeyer, S. Riedl, S. Jochim, C. Chin, J. Hecker Denschlag, R. Grimm, Crossover from a molecular Bose-Einstein condensate to a degenerate Fermi gas, Phys. Rev. Lett. 92 (2004) 120401.
[307] Y. Nishida, D.T. Son, ϵ expansion for a Fermi gas at infinite scattering length, Phys. Rev. Lett. 97 (2006) 050403.
[308] Y. Nishida, D.T. Son, Fermi gas near unitarity around four and two spatial dimensions, Phys. Rev. A 75 (2007) 063617.
[309] Y. Nishida, Ground-state energy of the unitary Fermi gas from the ϵ expansion, Phys. Rev. A 79 (2009) 013627.
[310] M.Y. Veillette, D.E. Sheehy, L. Radzihovsky, Large-N expansion for unitary superfluid Fermi gases, Phys. Rev. A 75 (2007) 043614.
[311] S. Diehl, H. Gies, J.M. Pawlowski, C. Wetterich, Flow equations for the BCS-BEC crossover, Phys. Rev. A 76 (2007) 021602.
[312] L. Bartosch, P. Kopietz, A. Ferraz, Renormalization of the BCS-BEC crossover by order-parameter fluctuations, Phys. Rev. B 80 (2009) 104514.
[313] Z. Nussinov, S. Nussinov, The BCS-BEC crossover in arbitrary dimensions, 2004. arXiv:0410597.
[314] Y. Nishida, Unitary Fermi gas at finite temperature in the ϵ expansion, Phys. Rev. A 75 (2007) 063618.
[315] P. Nikolić, S. Sachdev, Renormalization-group fixed points, universal phase diagram, and $1/N$ expansion for quantum liquids with interactions near the unitarity limit, Phys. Rev. A 75 (2007) 033608.
[316] W. Metzner, M. Salmhofer, C. Honerkamp, V. Meden, K. Schönhammer, Functional renormalization group approach to correlated fermion systems, Rev. Modern Phys. 84 (2012) 299–352.
[317] E. Beth, G.E. Uhlenbeck, The quantum theory of the non-ideal gas. II. Behaviour at low temperatures, Physica 4 (1937) 915–924.
[318] X.-J. Liu, H. Hu, P.D. Drummond, Virial expansion for a strongly correlated Fermi gas, Phys. Rev. Lett. 102 (2009) 160401.
[319] D.B. Kaplan, S. Sun, New field-theoretic method for the virial expansion, Phys. Rev. Lett. 107 (2011) 030601.
[320] X. Leyronas, Virial expansion with Feynman diagrams, Phys. Rev. A 84 (2011) 053633.
[321] D. Rakshit, K.M. Daily, D. Blume, Natural and unnatural parity states of small trapped equal-mass two-component Fermi gases at unitarity and fourth-order virial coefficient, Phys. Rev. A 85 (2012) 033634.
[322] V. Ngampruetikorn, M.M. Parish, J. Levinsen, High-temperature limit of the resonant Fermi gas, Phys. Rev. A 91 (2015) 013606.
[323] Y. Yan, D. Blume, Path-integral Monte Carlo determination of the fourth-order virial coefficient for a unitary two-component Fermi gas with zero-range interactions, Phys. Rev. Lett. 116 (2016) 230401.
[324] J. Carlson, S. Gandolfi, Predicting energies of small clusters from the inhomogeneous unitary Fermi gas, Phys. Rev. A 90 (2014) 011601.
[325] D. Blume, J. von Stecher, C.H. Greene, Universal properties of a trapped two-component Fermi gas at unitarity, Phys. Rev. Lett. 99 (2007) 233201.
[326] X.Y. Yin, D. Blume, Trapped unitary two-component Fermi gases with up to ten particles, Phys. Rev. A 92 (2015) 013608.
[327] S.Y. Chang, G.F. Bertsch, Unitary Fermi gas in a harmonic trap, Phys. Rev. A 76 (2007) 021603.
[328] M.G. Endres, D.B. Kaplan, J.-W. Lee, A.N. Nicholson, Lattice Monte Carlo calculations for unitary fermions in a harmonic trap, Phys. Rev. A 84 (2011) 043644.
[329] D. Lee, Ground-state energy of spin-$\frac{1}{2}$ fermions in the unitary limit, Phys. Rev. B 73 (2006) 115112.
[330] J. Carlson, S.-Y. Chang, V.R. Pandharipande, K.E. Schmidt, Superfluid Fermi gases with large scattering length, Phys. Rev. Lett. 91 (2003) 050401.
[331] D. Lee, Ground state energy at unitarity, Phys. Rev. C 78 (2008) 024001.
[332] G.E. Astrakharchik, J. Boronat, J. Casulleras, S. Giorgini, Equation of state of a Fermi gas in the BEC-BCS crossover: A quantum Monte Carlo study, Phys. Rev. Lett. 93 (2004) 200404.
[333] J. Carlson, S. Reddy, Asymmetric two-component fermion systems in strong coupling, Phys. Rev. Lett. 95 (2005) 060401.
[334] A.J. Morris, P. López Ríos, R.J. Needs, Ultracold atoms at unitarity within quantum Monte Carlo methods, Phys. Rev. A 81 (2010) 033619.
[335] M. McNeil Forbes, S. Gandolfi, A. Gezerlis, Resonantly interacting fermions in a box, Phys. Rev. Lett. 106 (2011) 235303.
[336] X. Li, J. Kolorenč, L. Mitas, Atomic Fermi gas in the unitary limit by quantum Monte Carlo methods: Effects of the interaction range, Phys. Rev. A 84 (2011) 023615.
[337] M.G. Endres, D.B. Kaplan, J.-W. Lee, A.N. Nicholson, Lattice Monte Carlo calculations for unitary fermions in a finite box, Phys. Rev. A 87 (2013) 023615.
[338] J. Carlson, S. Gandolfi, K.E. Schmidt, S. Zhang, Auxiliary-field quantum Monte Carlo method for strongly paired fermions, Phys. Rev. A 84 (2011) 061602.
[339] K.M. O'Hara, S.L. Hemmer, M.E. Gehm, S.R. Granade, J.E. Thomas, Observation of a strongly interacting degenerate Fermi gas of atoms, Science 298 (2002) 2179–2182.
[340] T. Bourdel, L. Khaykovich, J. Cubizolles, J. Zhang, F. Chevy, M. Teichmann, L. Tarruell, S.J.J.M.F. Kokkelmans, C. Salomon, Experimental study of the BEC-BCS crossover region in lithium 6, Phys. Rev. Lett. 93 (2004) 050401.
[341] J.T. Stewart, J.P. Gaebler, C.A. Regal, D.S. Jin, Potential energy of a ^{40}K Fermi gas in the BCS-BEC crossover, Phys. Rev. Lett. 97 (2006) 220406.
[342] L. Luo, J.E. Thomas, Thermodynamic measurements in a strongly interacting Fermi gas, J. Low Temp. Phys. 154 (2009) 1–29.
[343] G. Zürn, T. Lompe, A.N. Wenz, S. Jochim, P.S. Julienne, J.M. Hutson, Precise characterization of ^{6}Li Feshbach resonances using trap-sideband-resolved RF spectroscopy of weakly bound molecules, Phys. Rev. Lett. 110 (2013) 135301.
[344] J. Carlson, S. Reddy, Superfluid pairing gap in strong coupling, Phys. Rev. Lett. 100 (2008) 150403.
[345] A. Bulgac, J.E. Drut, P. Magierski, Quantum Monte Carlo simulations of the BCS-BEC crossover at finite temperature, Phys. Rev. A 78 (2008) 023625.
[346] J.E. Drut, T.A. Lähde, G. Wlazłowski, P. Magierski, Equation of state of the unitary Fermi gas: An update on lattice calculations, Phys. Rev. A 85 (2012) 051601.
[347] J.E. Drut, T.A. Lähde, T. Ten, Momentum distribution and contact of the unitary Fermi gas, Phys. Rev. Lett. 106 (2011) 205302.
[348] P. Magierski, G. Wlazłowski, A. Bulgac, Onset of a pseudogap regime in ultracold Fermi gases, Phys. Rev. Lett. 107 (2011) 145304.
[349] G. Wlazłowski, P. Magierski, J.E. Drut, A. Bulgac, K.J. Roche, Cooper pairing above the critical temperature in a unitary Fermi gas, Phys. Rev. Lett. 110 (2013) 090401.
[350] G. Wlazłowski, P. Magierski, J.E. Drut, Shear viscosity of a unitary Fermi gas, Phys. Rev. Lett. 109 (2012) 020406.
[351] G. Wlazłowski, P. Magierski, A. Bulgac, K.J. Roche, Temperature evolution of the shear viscosity in a unitary Fermi gas, Phys. Rev. A 88 (2013) 013639.
[352] G. Wlazłowski, W. Quan, A. Bulgac, Perfect-fluid behavior of a dilute Fermi gas near unitary, Phys. Rev. A 92 (2015) 063628.

[353] E. Burovski, N. Prokof'ev, B. Svistunov, M. Troyer, The Fermi-Hubbard model at unitarity, New J. Phys. 8 (2006) 153.
[354] K. Van Houcke, F. Werner, E. Kozik, N. Prokof'ev, B. Svistunov, M.J.H. Ku, A.T. Sommer, L.W. Cheuk, A. Schirotzek, M.W. Zwierlein, Feynman diagrams versus Fermi-gas Feynman emulator, Nat. Phys 8 (2012) 366–370.
[355] E. Kozik, M. Ferrero, A. Georges, Nonexistence of the Luttinger-Ward functional and misleading convergence of skeleton diagrammatic series for Hubbard-like models, Phys. Rev. Lett. 114 (2015) 156402.
[356] R. Rossi, F. Werner, Skeleton series and multivaluedness of the self-energy functional in zero space-time dimensions, J. Phys. A 48 (2015) 485202.
[357] R. Rossi, F. Werner, N. Prokof'ev, B. Svistunov, Shifted-action expansion and applicability of dressed diagrammatic schemes, Phys. Rev. B 93 (2016) 161102.
[358] A. Spuntarelli, P. Pieri, G.C. Strinati, Josephson effect throughout the BCS-BEC crossover, Phys. Rev. Lett. 99 (2007) 040401.
[359] S. Tan, Energetics of a strongly correlated Fermi gas, Ann. Phys. 323 (2008) 2952–2970.
[360] S. Tan, Large momentum part of a strongly correlated Fermi gas, Ann. Phys. 323 (2008) 2971–2986.
[361] S. Tan, Generalized virial theorem and pressure relation for a strongly correlated Fermi gas, Ann. Phys. 323 (2008) 2987–2990.
[362] E. Braaten, L. Platter, Exact relations for a strongly interacting Fermi gas from the operator product expansion, Phys. Rev. Lett. 100 (2008) 205301.
[363] E. Braaten, D. Kang, L. Platter, Universal relations for a strongly interacting Fermi gas near a Feshbach resonance, Phys. Rev. A 78 (2008) 053606.
[364] R. Combescot, F. Alzetto, X. Leyronas, Particle distribution tail and related energy formula, Phys. Rev. A 79 (2009) 053640.
[365] E. Braaten, Universal relations for fermions with large scattering length, in: W. Zwerger (Ed.), The BCS-BEC Crossover and the Unitary Fermi Gas, in: Lecture Notes in Physics, vol. 863, Springer-Verlag, Berlin, 2012, pp. 193–231.
[366] P. Pieri, A. Perali, G.C. Strinati, Enhanced paraconductivity-like fluctuations in the radiofrequency spectra of ultracold Fermi atoms, Nat. Phys. 5 (2009) 736–740.
[367] E. Braaten, D. Kang, L. Platter, Short-time operator product expansion for rf spectroscopy of a strongly interacting Fermi gas, Phys. Rev. Lett. 104 (2010) 223004.
[368] H. Hu, X.-J. Liu, P.D. Drummond, Static structure factor of a strongly correlated Fermi gas at large momenta, Europhys. Lett. 91 (2010) 20005.
[369] F. Werner, L. Tarruell, Y. Castin, Number of closed-channel molecules in the BEC-BCS crossover, Eur. Phys. J. B 68 (2009) 401–415.
[370] S. Zhang, A.J. Leggett, Universal properties of the ultracold Fermi gas, Phys. Rev. A 79 (2009) 023601.
[371] K. Van Houcke, F. Werner, E. Kozik, N. Prokof'ev, B. Svistunov, Contact and momentum distribution of the unitary Fermi gas by bold diagrammatic Monte Carlo, 2013. arXiv:1303.6245.
[372] Z. Yu, G.M. Bruun, G. Baym, Short-range correlations and entropy in ultracold-atom Fermi gases, Phys. Rev. A 80 (2009) 023615.
[373] M. Sun, X. Leyronas, High-temperature expansion for interacting fermions, Phys. Rev. A 92 (2015) 053611.
[374] R. Combescot, X. Leyronas, M.Y. Kagan, Self-consistent theory for molecular instabilities in a normal degenerate Fermi gas in the BEC-BCS crossover, Phys. Rev. A 73 (2006) 023618.
[375] P. Pieri, G.C. Strinati, Popov approximation for composite bosons in the BCS-BEC crossover, Phys. Rev. B 71 (2005) 094520.
[376] T. Enss, R. Haussmann, W. Zwerger, Viscosity and scale invariance in the unitary Fermi gas, Ann. Phys. 326 (2011) 770–796.
[377] H. Hu, X.-J. Liu, P.D. Drummond, Universal contact of strongly interacting fermions at finite temperatures, New J. Phys. 13 (2011) 035007.
[378] I. Boettcher, S. Diehl, J.M. Pawlowski, C. Wetterich, Tan contact and universal high momentum behavior of the fermion propagator in the BCS-BEC crossover, Phys. Rev. A 87 (2013) 023606.
[379] Y.Y. Chen, Y.Z. Jiang, X.W. Guan, Q. Zhou, Critical behaviours of contact near phase transitions, Nature Commun. 5 (2014) 5140.
[380] B. Josephson, Possible new effects in superconductive tunnelling, Phys. Lett. 1 (1962) 251–253.
[381] A. Barone, G. Paternò, Physics and Applications of the Josephson Effect, John Wiley & Sons, New York, 1982.
[382] A.A. Abrikosov, L.P. Gorkov, I.E. Dzyaloshinski, Methods of Quantum Field Theory in Statistical Physics, Dover, New York, 1975.
[383] P. Engels, C. Atherton, Stationary and nonstationary fluid flow of a Bose-Einstein condensate through a penetrable barrier, Phys. Rev. Lett. 99 (2007) 160405.
[384] C. Menotti, P. Pedri, S. Stringari, Expansion of an interacting Fermi gas, Phys. Rev. Lett. 89 (2002) 250402.
[385] S. Stringari, Collective excitations of a trapped Bose-condensed gas, Phys. Rev. Lett. 77 (1996) 2360–2363.
[386] M.A. Baranov, D.S. Petrov, Low-energy collective excitations in a superfluid trapped Fermi gas, Phys. Rev. A 62 (2000) 041601.
[387] M. Cozzini, S. Stringari, Fermi gases in slowly rotating traps: Superfluid versus collisional hydrodynamics, Phys. Rev. Lett. 91 (2003) 070401.
[388] F. Dalfovo, S. Giorgini, L.P. Pitaevskii, S. Stringari, Theory of Bose-Einstein condensation in trapped gases, Rev. Modern Phys. 71 (1999) 463–512.
[389] M. Urban, P. Schuck, Dynamics of a trapped Fermi gas in the BCS phase, Phys. Rev. A 73 (2006) 013621.
[390] L.P. Pitaevskii, E.M. Lifshitz, Physical kinetics, in: Landau-Lifshitz Course of Theoretical Physics, vol. 10, Pergamon Press, 1981.
[391] G.M. Bruun, B.R. Mottelson, Low energy collective modes of a superfluid trapped atomic Fermi gas, Phys. Rev. Lett. 87 (2001) 270403.
[392] M. Grasso, E. Khan, M. Urban, Temperature dependence and finite-size effects in collective modes of superfluid-trapped Fermi gases, Phys. Rev. A 72 (2005) 043617.
[393] R. Combescot, X. Leyronas, Comment on "Collective excitations of a degenerate gas at the BEC-BCS crossover", Phys. Rev. Lett. 93 (2004) 138901.
[394] R. Combescot, M.Y. Kagan, S. Stringari, Collective mode of homogeneous superfluid Fermi gases in the BEC-BCS crossover, Phys. Rev. A 74 (2006) 042717.
[395] N. Bogoliubov, V. Tolmachev, D. Shirkov, A new method in the theory of superconductivity, Consultants Bureau, New York, 1959.
[396] P.W. Anderson, Random-phase approximation in the theory of superconductivity, Phys. Rev. 112 (1958) 1900–1916.
[397] M. McNeil Forbes, R. Sharma, Validating simple dynamical simulations of the unitary Fermi gas, Phys. Rev. A 90 (2014) 043638.
[398] N. Martin, M. Urban, Collective modes in a superfluid neutron gas within the quasiparticle random-phase approximation, Phys. Rev. C 90 (2014) 065805.
[399] E. Taylor, A. Griffin, Two-fluid hydrodynamic modes in a trapped superfluid gas, Phys. Rev. A 72 (2005) 053630.
[400] O. Betbeder-Matibet, P. Nozières, Transport equations in clean superconductors, Ann. Phys. 51 (1969) 392–417.
[401] M. Urban, Coupling of hydrodynamics and quasiparticle motion in collective modes of superfluid trapped Fermi gases, Phys. Rev. A 75 (2007) 053607.
[402] M. Urban, Radial quadrupole and scissors modes in trapped Fermi gases across the BCS phase transition, Phys. Rev. A 78 (2008) 053619.
[403] P.-A. Pantel, D. Davesne, M. Urban, Numerical solution of the Boltzmann equation for trapped Fermi gases with in-medium effects, Phys. Rev. A 91 (2015) 013627.
[404] F. Toschi, P. Vignolo, S. Succi, M.P. Tosi, Dynamics of trapped two-component Fermi gas: Temperature dependence of the transition from collisionless to collisional regime, Phys. Rev. A 67 (2003) 041605.
[405] P. Massignan, G.M. Bruun, H. Smith, Viscous relaxation and collective oscillations in a trapped Fermi gas near the unitarity limit, Phys. Rev. A 71 (2005) 033607.
[406] S. Chiacchiera, T. Lepers, D. Davesne, M. Urban, Collective modes of trapped Fermi gases with in-medium interaction, Phys. Rev. A 79 (2009) 033613.
[407] T. Lepers, D. Davesne, S. Chiacchiera, M. Urban, Numerical solution of the Boltzmann equation for the collective modes of trapped Fermi gases, Phys. Rev. A 82 (2010) 023609.
[408] S. Chiacchiera, T. Lepers, D. Davesne, M. Urban, Role of fourth-order phase-space moments in collective modes of trapped Fermi gases, Phys. Rev. A 84 (2011) 043634.

[409] G.M. Bruun, H. Smith, Viscosity and thermal relaxation for a resonantly interacting Fermi gas, Phys. Rev. A 72 (2005) 043605.
[410] M. Bluhm, T. Schäfer, Medium effects and the shear viscosity of the dilute Fermi gas away from the conformal limit, Phys. Rev. A 90 (2014) 063615.
[411] M. Farine, P. Schuck, X. Viñas, Moment of inertia of a trapped superfluid gas of atomic fermions, Phys. Rev. A 62 (2000) 013608.
[412] M. Durand, P. Schuck, J. Kunz, Semiclassical description of currents in normal and superfluid rotating nuclei, Nuclear Phys. A 439 (1985) 263.
[413] A.B. Migdal, Superfluidity and the moments of inertia of nuclei, Nuclear Phys. 13 (1959) 655–674.
[414] M. Urban, Two-fluid model for a rotating trapped Fermi gas in the BCS phase, Phys. Rev. A 71 (2005) 033611.
[415] M. Urban, P. Schuck, Slow rotation of a superfluid trapped Fermi gas, Phys. Rev. A 67 (2003) 033611.
[416] I. Bausmerth, A. Recati, S. Stringari, Destroying superfluidity by rotating a Fermi gas at unitarity, Phys. Rev. Lett. 100 (2008) 070401.
[417] M. Urban, P. Schuck, Pair breaking in rotating Fermi gases, Phys. Rev. A 78 (2008) 011601.
[418] S. Simonucci, P. Pieri, G.C. Strinati, Vortex arrays in neutral trapped Fermi gases through the BCS-BEC crossover, Nat. Phys. 11 (2015) 941–945.
[419] P. Nozières, D. Pines, The Theory of Quantum Liquids: Superfluid Bose Liquids, Addison-Wesley, Reading, 1990.
[420] G.F. Bertsch, T. Papenbrock, Yrast line for weakly interacting trapped bosons, Phys. Rev. Lett. 83 (1999) 5412–5414.
[421] A. Bohr, B. Mottelson, Nuclear Structure. Vol. 1: Single-Particle Motion, Benjamin, New York, 1969.
[422] J. Haidenbauer, W. Plessas, Separable representation of the Paris nucleon-nucleon potential, Phys. Rev. C 30 (1984) 1822–1839.
[423] U. Lombardo, P. Schuck, Size shrinking of deuterons in very dilute superfluid nuclear matter, Phys. Rev. C 63 (2001) 038201.
[424] N. Andrenacci, P. Pieri, G.C. Strinati, Size shrinking of composite bosons for increasing density in the BCS to Bose-Einstein crossover, Eur. Phys. J. B 13 (2000) 637–642.
[425] K. Itonaga, H. Bandō, On the contraction of deuteron cluster in Li6, Progr. Theoret. Phys. 44 (1970) 1232–1241.
[426] R.B. Wiringa, R.A. Smith, T.L. Ainsworth, Nucleon-nucleon potentials with and without $\Delta(1232)$ degrees of freedom, Phys. Rev. C 29 (1984) 1207–1221.
[427] M. Stein, A. Sedrakian, X.-G. Huang, J.W. Clark, BCS-BEC crossovers and unconventional phases in dilute nuclear matter, Phys. Rev. C 90 (2014) 065804.
[428] Y. Yamaguchi, Two-nucleon problem when the potential is nonlocal but separable, Phys. Rev. 95 (1954) 1628–1634.
[429] J.R. Taylor, Scattering Theory: The Quantum Theory of Nonrelativistic Collisions, Dover Publications, Mineola, N.Y., 1972, 2006 (Chapter 12-e).
[430] P. Chomaz, M. Colonna, J. Randrup, Nuclear spinodal fragmentation, Phys. Rep. 389 (2004) 263–440.
[431] H.-Q. Song, G.-D. Zheng, R.-K. Su, Critical phenomena in nuclear matter with Gogny interaction, J. Phys. G: Nucl. Phys. 16 (1990) 1861–1871.
[432] J. Ventura, A. Polls, X. Viñas, S. Hernandez, M. Pi, Thermodynamic instabilities of nuclear matter at finite temperature with finite range effective interactions, Nuclear Phys. A 545 (1992) 247–257.
[433] H. Stein, C. Porthun, G. Röpke, Liquid-gas binodal anomaly for systems with pairing transition, Eur. Phys. J. B 2 (1998) 393–398.
[434] R.K. Su, S.D. Yang, T.T.S. Kuo, Liquid-gas and superconducting phase transitions of nuclear matter calculated with real time Green's function methods and Skyrme interactions, Phys. Rev. C 35 (1987) 1539–1550.
[435] A. Gårdestig, Extracting the neutron-neutron scattering length — recent developments, J. Phys. G 36 (2009) 053001.
[436] A. Schwenk, C.J. Pethick, Resonant Fermi gases with a large effective range, Phys. Rev. Lett. 95 (2005) 160401.
[437] N. Chamel, P. Haensel, Physics of neutron star crusts, Living Rev. Relativ. 11 (2008) 10. http://dx.doi.org/10.1007/lrr-2008-10.
[438] M. Fortin, F. Grill, J. Margueron, D. Page, N. Sandulescu, Thermalization time and specific heat of the neutron stars crust, Phys. Rev. C 82 (2010) 065804.
[439] R. Tamagaki, Potential models of nuclear forces at small distances, Progr. Theoret. Phys. 39 (1968) 91–107.
[440] B.Y. Sun, H. Toki, J. Meng, Relativistic description of BCS-BEC crossover in nuclear matter, Phys. Lett. B 683 (2010) 134–139.
[441] S. Maurizio, J.W. Holt, P. Finelli, Nuclear pairing from microscopic forces: Singlet channels and higher-partial waves, Phys. Rev. C 90 (2014) 044003.
[442] C. Drischler, T. Krüger, K. Hebeler, A. Schwenk, Pairing in neutron matter: new uncertainty estimates and three-body forces, Phys. Rev. C 95 (2017) 024302.
[443] S. Gandolfi, A.Y. Illarionov, S. Fantoni, F. Pederiva, K.E. Schmidt, Equation of state of superfluid neutron matter and the calculation of the $^1S_0$ pairing gap, Phys. Rev. Lett. 101 (2008) 132501.
[444] A. Schwenk, B. Friman, Polarization contributions to the spin dependence of the effective interaction in neutron matter, Phys. Rev. Lett. 92 (2004) 082501.
[445] A. Schwenk, B. Friman, G.E. Brown, Renormalization group approach to neutron matter: quasiparticle interactions, superfluid gaps and the equation of state, Nuclear Phys. A 713 (2003) 191–216.
[446] K.A. Brueckner, Two-body forces and nuclear saturation. III. Details of the structure of the nucleus, Phys. Rev. 97 (1955) 1353–1366.
[447] B.D. Day, Elements of the Brueckner-Goldstone theory of nuclear matter, Rev. Modern Phys. 39 (1967) 719–744.
[448] U. Lombardo, H.-J. Schulze, Superfluidity in neutron star matter, in: D. Blaschke, A. Sedrakian, N.K. Glendenning (Eds.), Physics of Neutron Star Interiors, Springer, Berlin, 2001, pp. 30–53.
[449] S. Babu, G.E. Brown, Quasiparticle interaction in liquid ^{3}He, Ann. Phys. 78 (1973) 1–38.
[450] S.S. Zhang, L.G. Cao, U. Lombardo, P. Schuck, Medium polarization in asymmetric nuclear matter, Phys. Rev. C 93 (2016) 044329.
[451] S.K. Bogner, R.J. Furnstahl, S. Ramanan, A. Schwenk, Low-momentum interactions with smooth cutoffs, Nuclear Phys. A 784 (2007) 79–103.
[452] S. Weinberg, Quasiparticles and the Born series, Phys. Rev. 131 (1963) 440–460.
[453] R. Weiss, B. Bazak, N. Barnea, Nuclear neutron-proton contact and the photoabsorption cross section, Phys. Rev. Lett. 114 (2015) 012501.
[454] J.S. Levinger, The high energy nuclear photoeffect, Phys. Rev. 84 (1951) 43–51.
[455] R. Weiss, B. Bazak, N. Barnea, The generalized nuclear contact and its application to the photoabsorption cross-section, Eur. Phys. J. A 52 (2016) 92.
[456] R. Weiss, B. Bazak, N. Barnea, Generalized nuclear contacts and momentum distributions, Phys. Rev. C 92 (2015) 054311.
[457] O. Hen, L.B. Weinstein, E. Piasetzky, G.A. Miller, M.M. Sargsian, Y. Sagi, Correlated fermions in nuclei and ultracold atomic gases, Phys. Rev. C 92 (2015) 045205.
[458] O. Hen, et al., Momentum sharing in imbalanced Fermi systems, Science 346 (2014) 614–617.
[459] P. Nozières, D. Saint James, Particle vs. pair condensation in attractive Bose liquids, J. Phys. (Paris) 43 (1982) 1133–1148.
[460] S. Capponi, G. Roux, P. Lecheminant, P. Azaria, E. Boulat, S.R. White, Molecular superfluid phase in systems of one-dimensional multicomponent fermionic cold atoms, Phys. Rev. A 77 (2008) 013624.
[461] T. Sogo, G. Röpke, P. Schuck, Many-body approach for quartet condensation in strong coupling, Phys. Rev. C 81 (2010) 064310.
[462] P. Schuck, Y. Funaki, H. Horiuchi, G. Röpke, A. Tohsaki, T. Yamada, Theory for quartet condensation in Fermi systems with applications to nuclei and nuclear matter, J. Phys. Conf. Ser. 529 (2014) 012014.
[463] H. Kamei, K. Miyake, On quartet superfluidity of Fermionic atomic gas, J. Phys. Soc. Japan 74 (2005) 1911–1913.
[464] T. Sogo, R. Lazauskas, G. Röpke, P. Schuck, Critical temperature for α-particle condensation within a momentum-projected mean-field approach, Phys. Rev. C 79 (2009) 051301.
[465] R.A. Malfliet, J.A. Tjon, Solution of the Faddeev equations for the triton problem using local two-particle interactions, Nuclear Phys. A 127 (1969) 161–168.
[466] T. Sogo, G. Röpke, P. Schuck, Critical temperature for α-particle condensation in asymmetric nuclear matter, Phys. Rev. C 82 (2010) 034322.
[467] A.H. Blin, R.W. Hasse, B. Hiller, P. Schuck, C. Yannouleas, On the evaluation of semiclassical nuclear many-particle many-hole level densities, Nuclear Phys. A 456 (1986) 109–133.

[468] C. Xu, Z. Ren, G. Röpke, P. Schuck, Y. Funaki, H. Horiuchi, A. Tohsaki, T. Yamada, B. Zhou, α-decay width of ^{212}Po from a quartetting wave function approach, Phys. Rev. C 93 (2016) 011306.
[469] B. Bulthuis, A. Gezerlis, Probing mixed-spin pairing in heavy nuclei, Phys. Rev. C 93 (2016) 014312.
[470] A. Gezerlis, G.F. Bertsch, Y.L. Luo, Mixed-Spin pairing condensates in heavy nuclei, Phys. Rev. Lett. 106 (2011) 252502.
[471] N. Pillet, N. Sandulescu, P. Schuck, Generic strong coupling behavior of Cooper pairs on the surface of superfluid nuclei, Phys. Rev. C 76 (2007) 024310.
[472] Y. Fukushima, M. Kamimura, Suppl. J. Phys. Soc. Jpn. 44 (1978) 225.
[473] M. Kamimura, Transition densities between the 0_1^+, 2_1^+, 4_1^+, 0_2^+, 2_2^+, 1_1 and 3_1 states in ^{12}C derived from the three-alpha resonating-group wave functions, Nuclear Phys. A 351 (1981) 456–480.
[474] R.B. Wiringa, S.C. Pieper, J. Carlson, V.R. Pandharipande, Quantum Monte Carlo calculations of $A = 8$ nuclei, Phys. Rev. C 62 (2000) 014001.
[475] M. Matsuo, K. Mizuyama, Y. Serizawa, Di-neutron correlation and soft dipole excitation in medium mass neutron-rich nuclei near drip line, Phys. Rev. C 71 (2005) 064326.
[476] N. Pillet, N. Sandulescu, P. Schuck, J.-F. Berger, Two-particle spatial correlations in superfluid nuclei, Phys. Rev. C 81 (2010) 034307.
[477] K. Hagino, H. Sagawa, P. Schuck, Cooper pair sizes in ^{11}Li and in superfluid nuclei: a puzzle?, J. Phys. G 37 (2010) 064040.
[478] F. Hoyle, On nuclear reactions occuring in very hot stars. I. The synthesis of elements from carbon to nickel, Astrophys. J. Suppl. 1 (1954) 121–146.
[479] C.W. Cook, W.A. Fowler, C.C. Lauritsen, T. Lauritsen, B^{12}, C^{12}, and the red giants, Phys. Rev. 107 (1957) 508–515.
[480] Y. Funaki, H. Horiuchi, W. von Oertzen, G. Röpke, P. Schuck, A. Tohsaki, T. Yamada, Concepts of nuclear α-particle condensation, Phys. Rev. C 80 (2009) 064326.
[481] G. Röpke, P. Schuck, Y. Funaki, H. Horiuchi, Z. Ren, A. Tohsaki, C. Xu, T. Yamada, B. Zhou, Nuclear clusters bound to doubly magic nuclei: The case of ^{212}Po, Phys. Rev. C 90 (2014) 034304.
[482] M. Chernykh, H. Feldmeier, T. Neff, P. von Neumann-Cosel, A. Richter, Structure of the Hoyle state in ^{12}C, Phys. Rev. Lett. 98 (2007) 032501.
[483] A. Tohsaki, H. Horiuchi, P. Schuck, G. Röpke, Alpha cluster condensation in ^{12}C and ^{16}O, Phys. Rev. Lett. 87 (2001) 192501.
[484] A. Tohsaki, New effective internucleon forces in microscopic α-cluster model, Phys. Rev. C 49 (1994) 1814–1817.
[485] Y. Funaki, A. Tohsaki, H. Horiuchi, P. Schuck, G. Röpke, Inelastic form factors to alpha-particle condensate states in ^{12}C and ^{16}O: What can we learn?, Eur. Phys. J. A 28 (2006) 259–263.
[486] P. Schuck, Y. Funaki, H. Horiuchi, G. Röpke, A. Tohsaki, T. Yamada, Alpha particle clusters and their condensation in nuclear systems, Phys. Scr. 91 (2016) 123001.
[487] A. Tohsaki, H. Horiuchi, P. Schuck, G. Röpke, Status of α-particle condensate structure of the Hoyle state, Rev. Modern Phys. 89 (2017) 011002.
[488] P. Törma, Physics of ultracold Fermi gases revealed by spectroscopies, Phys. Scr. 91 (2016) 043006.
[489] L. Salasnich, F. Toigo, Zero-point energy of ultracold atoms, Phys. Rep. 640 (2016) 1–29.
[490] G. Baym, B.L. Friman, J.-P. Blaizot, M. Soyeur, W. Czyż, Hydrodynamics of ultra-relativistic heavy ion collisions, Nuclear Phys. A 407 (1983) 541–570.
[491] N. Yamamoto, M. Tachibana, T. Hatsuda, G. Baym, Phase structure, collective modes, and the axial anomaly in dense QCD, Phys. Rev. D 76 (2007) 074001.
[492] Y. Nambu, Quasi-particles and gauge invariance in the theory of superconductivity, Phys. Rev. 117 (1960) 648–663.
[493] C.N. Yang, Concept of off-diagonal long-range order and the quantum phases of liquid He and of superconductors, Rev. Modern Phys. 34 (1962) 694–704.
[494] Y. Lubashevsky, E. Lahoud, K. Chashka, D. Podolsky, A. Kanigel, Shallow pockets and very strong coupling superconductivity in $FeSe_xTe_{1-x}$, Nat. Phys. 8 (2012) 309–312.
[495] P. Pieri, D. Neilson, G.C. Strinati, Effects of density imbalance on the BCS-BEC crossover in semiconductor electron-hole bilayers, Phys. Rev. B 75 (2007) 113301.
[496] A. Perali, D. Neilson, A.R. Hamilton, High-temperature superfluidity in double-bilayer graphene, Phys. Rev. Lett. 110 (2013) 146803.
[497] J.I.A. Li, T. Taniguchi, K. Watanabe, J. Hone, A. Levchenko, C.R. Dean, Negative Coulomb drag in double bilayer graphene, Phys. Rev. Lett. 117 (2016) 046802.
[498] K. Lee, J. Xue, D.C. Dillen, K. Watanabe, T. Taniguchi, E. Tutuc, Giant frictional drag in double bilayer graphene heterostructures, Phys. Rev. Lett. 117 (2016) 046803.